Structural evolution of continental rifting, quantitative analysis of fault populations: insights from the central Kenya rift, central and north main Ethiopian rift

Ahmad Khalil Mustafa Shmela

Submitted in accordance with the requirements for the degree of
Doctor of Philosophy

The University of Leeds
School of Earth and Environment
Institute of Geophysics and Tectonics

April 2018

Declaration

The candidate confirms that the work submitted is his own and that appropriate credit has been given where reference has been made to the work of others.

Acknowledgements

Certainly, all praise and thanks are due purely to Allah who guided me and granted me the capacity and patience to accomplish this work.

I would like to express my deep gratitude to my academic supervisors, Prof. Douglas Paton and Dr. Richard Collier for their continuous guidance, support and encouragement that were essential for the completion of this this PhD researches. I would like to extend my sincere gratitude to Dr. Emma Bramham, for kindly sharing with me her MATLAB code and for providing genuine support and encouragement when things were feeling rather bleak. I would also thank Dr. Paul Markwick for offering constructive discussions and view on my research.

Special thanks and appreciation goes to my official financial sponsor, Libyan Ministry of High Education and Scientific Research for granting me this Scholarships to pursue my doctoral degree, and without this continuous support, it would have never been possible to be on this route of science.

And last but not least, I would indeed like to express my sincere respect and gratitude to my wife Fatma for her patience, encouragement and appreciation throughout this journey of my PhD study, and also for her amazing efforts in looking after our children especially when I had to be away from home. I would never forget to thank my children Nour, Riem, Anas, Maha, Rahaf and Roaa for supporting me and being a continues source of hope to move forward. Thank you all very much indeed!

Abstract

The aim of the current research is to provide new insights into the evolution of normal faults and their implications on continental rift evolution in order to inform our understanding of the north to south rift propagation of the east African rift system (EARS). Therefore, three different rift segments representing different stages of continental rifting have been selected along the EARS, namely; the central Kenya rift representing an early stage of continental rifting, the central main Ethiopian rift (CMER) as an intermediate stage and the northern Ethiopian rift (NMER) exemplifying a late stage. Digital Elevation Model DEM with 30m horizontal resolution and Google Earth images are the main data used for this study. A large dataset of fault size attributes of the present-day fault geometry was built from 2130 faults scarps that were identified and manually mapped from DEM surface of the three areas, in order to conduct a quantitative and statistical analysis on scaling relations of fault populations, spatial strain distribution and to assess the role of pre-existing structures on fault development. Estimations of extensional strain along the three rift segments revealed a general progressive increase of strain from south to north. In the central Kenya rift, fault length and throw populations exhibited a power-law distribution, the fractal dimension of fault throw populations showed a decrease with increasing strain, while the fractal dimension of fault length populations remained almost constant, which may imply that the fault system in this central Kenya rift develop in accordance to near constant length fault growth model. Analysis of the spatial distribution of strain exhibits a rather distributed faulting deformation in the southernmost part of the central Kenya rift, and more localized deformation on rift flanks towards the north. As for the central main Ethiopian rift (CMER) and the

northern main Ethiopian rift (NMER), the cumulative distributions for length and displacement populations fit to both exponential and log-normal functions, which is a function of limited crustal layers thickness. The observed decrease of average fault lengths and increasing average fault throws and D/L ratio in the NMER as opposed to the CMER may have occurred after reaching the maximum fault length at an earlier stage of development, which would again be in line with the coherent fault model. The domain of deformation moved from being rather localized at and near rift margins in the southern segment (CMER) to a more distributed domain of faulting deformation across the northern rift segment (NMER). This is in contrast to domains of deformation observed in the central Kenya rift as we move from south to north. The possible influence of the underlying Precambrian basement structures on the orientation of Cenozoic fault on the surface has been investigated and discussed in the light of existing experimental models, and that suggests the presence of basement influence in the central Kenya rift, whereas such influence is not as evident within the CMER and NMER segments. Generally, in the present thesis, the quantitative and statistical analysis of scaling properties of fault populations in the EARS demonstrates how these properties can provide new insights into the evolution of different stages of continental rifting.

Table of Contents

List of Figures

List of Tables

Chapte 1. Introduction

1.1 Introduction

Over the past several decades, tectonic evolution of continental rifting within the East African rift system has been the focus of enormous detailed crustal and lithospheric studies within different rift basins. Understanding the evolution of extensional fault is very important for many practical applications, such as earthquake hazard assessment (Childs et al., 2009, Soliva et al., 2006) and the production of oil from faulted reservoirs, as faults can behave as both barriers and/or conduits for fluid flow (Morley, 1990, Dawers et al., 1993, Finkbeiner et al., 1997, Faulkner et al., 2010) . The EARS is one of the few locations on Earth where the full evolution of continental rifting can be observed and analysed (Hayward and Ebinger, 1996, Corti, 2009, Agostini et al., 2011a). The eastern branch of the EARS is seismically relatively quiet (e.g. Morley and Ngenoh, 1999c) as opposed to the western branch that represents a continental rift in the early stages of development (e.g. Ebinger, 1989b). However, numerous small earthquakes affect the eastern branch, and data from the central Kenya rift shows a clustering of earthquake events beneath this region (Tongue et al., 1994) (Tongue et al. 1994).

A complete record of the brittle deformation in continental rifting evolves from deformation dominated by fault assisted rifting in the early stages of extension into magma assisted-rifting during continental break-up (e.g. Hayward and Ebinger, 1996, Ebinger, 2005, Corti, 2009, Agostini et al., 2011b, Keir et al., 2013), the early phase of continental rifting is characterized by half-graben

formation governed by large border faults that accommodate a significant amount of deformation and dominate basin geometry (Cowie and Scholz, 1992a, Cowie and Scholz, 1992b, Cowie et al., 1995, Nicol et al., 1997, Meyer et al., 2002, Walsh et al., 2003b, Corti, 2009). The transitional phase of continental rifting occurs with increasing strain that leads to an incipient migration of deformation from rift borders to rift axis where some internal faults start to emerge in the rift commonly accompanied with some magmatism (Hayward and Ebinger, 1996, Agostini et al., 2011b). The late or mature phase of continental rifting involves localization of deformation within the rift axis, which gives rise to volcano-tectonic segments, and deformation being distributed across a large number of small-offset normal faults that occupy the weakened lithosphere within rift axis(Hayward and Ebinger, 1996, Keir et al., 2006, Corti, 2009, Agostini et al., 2011b).

It has been thought that continental rifts including the EARS are not randomly distributed but tend to follow the trend of pre-existing weakness zones, and avoiding stronger regions (e.g. Morley, 1999 a, Petit and Ebinger, 2000, Ziegler and Cloetingh, 2004). Existence of inherited underlying structures are thought to have contributed to the evolution of east African rift system and influenced the normal fault growth and their geometry (Rosendahl 1987, Morley 1999 a, Ebinger, Yemane et al. 2000). Moreover, faults produced as a result of the up-dip propagation of pre-existing structures may follow the coherent fault model (Jackson and Rotevatn, 2013, Giba et al., 2012).

Since its discovery, mid last century, the eastern branch of the EARS has been the focus of detailed investigations included: rift evolution (e.g. Baker and Wohlenberg, 1971, Baker et al., 1972, McConnell, 1972, Logatchev et al.,

1972, Strecker et al., 1990, Morley et al., 1992, Bosworth, 1994, Ebinger, 2005, Corti, 2009, Agostini et al., 2011b, Corti, 2012), deep structure influence on rift evolution (e.g. Smith and Mosley, 1993, Hautot et al., 2000, Stuart et al., 2006, Maguire et al., 2006, Kogan et al., 2012), structure assisted by magmatism (e.g. King, 1978, Karson and Curtis, 1989, Daly et al., 1989, Pavoni, 1992, Keir et al., 2006, Le Gall et al., 2008, Muirhead et al., 2016). This enormous number of previous research studies has concentrated on individual rift segments of continental rifting in EARS, and have contributed to the body of knowledge of long term evolution of continental rifting in terms of deep subsurface dynamic processes. However, there is still a need to characterize the surface expression of rift evolution and describe the evolution of surface faults in this region, there is still also a lack of sufficient understanding of the north-south rift propagation in the EARS.

The overall aim of the current research is to investigating the surface brittle deformation in three rift segments along the EARS in order to inform our understanding on how this continental rifting evolves from south to north. The three selected areas represent three different stages of continental rifting as follow; the central Kenya rift represents the early continental rifting phase, the central main Ethiopian rift, (CMER) exemplifies the transitional stage of continental rifting, and the northern main Ethiopian rift (NMER) that represents a late stage of continental rifting.

Moreover, In order to understand rift evolution, it is fundamental to understand the evolution of normal faulting associated with rifting and extension processes through answering the following research questions:

- How do fault populations evolve with increasing strain in different stages of continental rifting?
- What is the spatial distribution of extensional brittle strain manifested by normal faults within the entire study area?
- Which fault growth model best describes the fault evolution in these three rift segments?
- Is there any influence of pre-existing underlying structures on the present day geometry of surface faults?

Digital elevation models DEM combined with satellite images (Google Earth) are the main data used for this study. They a means for quantifying the upper crust brittle deformation over large areas of Earth's surface and over long periods of time, this approach is particularly useful in areas with limited or no seismic data such as the eastern branch of east African rift system. Thus the idea is to identify and map all fault scarps that appear on DEM surface, in order to build up a detailed dataset for attributes of the present-day fault geometry in order to conduct quantitative and statistical analysis on scaling relations of fault populations and discuss results with reference to the published literature so that we get a better insight into the evolution of normal faults and their implications on continental rift evolution as a whole.

A fault population is a system that includes all faults having full range of lengths, spacing, displacement distributions, and other characteristics that record the progressive evolution of a deformed domain. fault populations are thought to be self-organizing in such a way that their physical, geometric, and statistical characteristics evolve with increasing deformation of a given region e.g. (Cowie et al., 1995, Cladouhos and Marrett, 1996, Ackermann et al., 2001,

Meyer et al., 2002). The approach used in the current study for the purpose of understanding the development of continental rifting, through investigating normal fault evolution with regard to increasing strain, is similar to that used by Poulimenos (2000), Soliva and Schultz (2008), and Nixon et al. (2014).

Investigation of scaling relations of fault population involve statistical characterization of fault size attributes (fault trace length, fault throw, fault spacing, the relationship between displacement and length, and strain accommodated by faulting) to provide quantitative description of fault evolution. This approach has been used in numerous studies including 1) assessment of fault growth models (Cowie and Scholz, 1992c, Schultz and Fossen, 2002, Cowie and Scholz, 1992b, Cowie and Scholz, 1992a) 2) prediction of fault geometries (Walsh et al., 2003a, Soliva and Benedicto, 2004) 3) Understanding the structural evolution by dividing a region into subsets of structures based upon their statistical distribution (Schlische et al., 1996, Ackermann and Schlische, 1997), and 4) understanding rift evolution(Gupta and Scholz, 2000a, Soliva and Schultz, 2008).

Continental rifts are thought to form around zones of weaknesses within the lithosphere (such as ancient orogenic belts), avoiding stronger formations, and propagate following the trend of inherited structures in the basement (e.g. Versfelt and Rosendahl, 1989, Petit and Ebinger, 2000, Ziegler and Cloetingh, 2004).Heterogeneities in the pre-existing underlying structures are known to influence normal fault growth and geometry (Walsh et al., 2002b, Morley, 1999b), and faults produced as a result of the up-dip propagation of pre-existing structures may follow the coherent fault model (Jackson and Rotevatn, 2013, Giba et al., 2012). Chapter 6 of this research lays the ground-work for

future analysis through offering a new idea for a preliminary method to reconstruct the possible original location of eroded footwalls of faults.

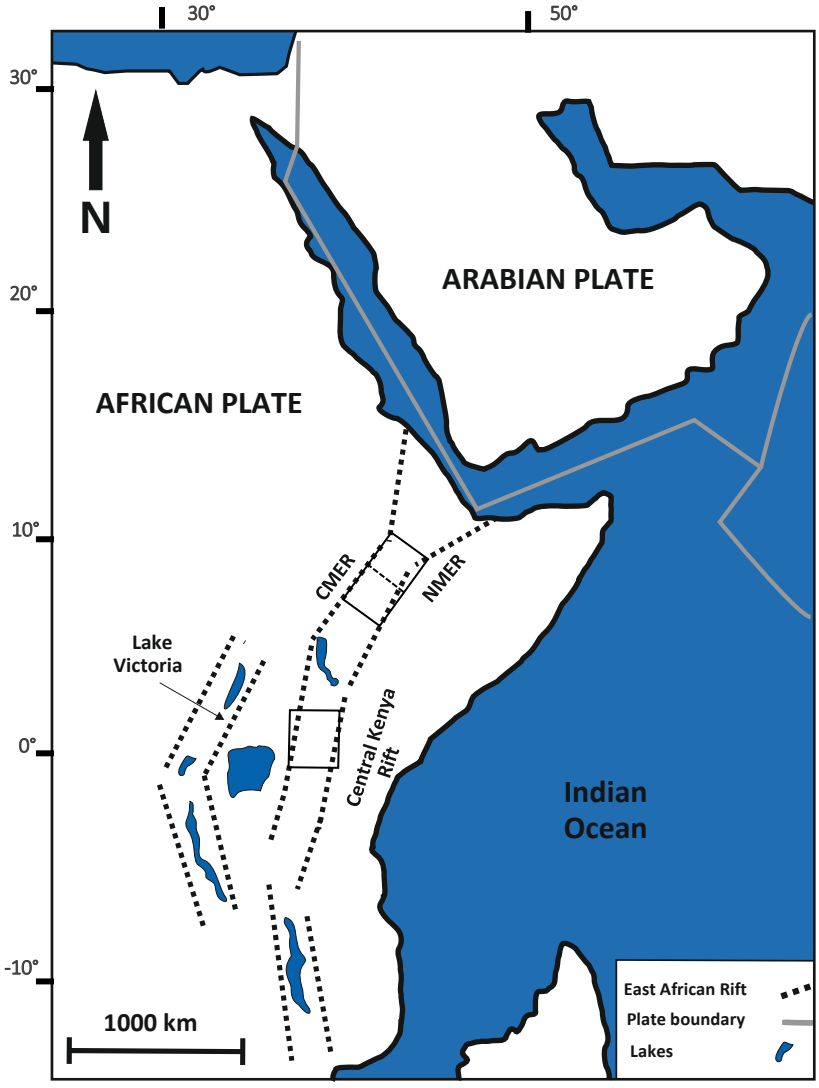

Figure 1.1 Locations of the three study areas the within the main Ethiopian Rift MER), CMER: central MER, NMER: northern MER

1.2 Hypothesis

This present research aims to test three hypotheses:

1) Increasing tensional stresses caused by divergent tectonic movements is the process leading to continental break-up and the creation of new oceanic lithosphere (Hayward and Ebinger, 1996, Corti et al., 2003, Ebinger, 2005, Maguire et al., 2006, Corti, 2009, Agostini et al., 2011b). Consequently continental deformation occurs as a result of increasing strain as demonstrated by (Poulimenos, 2000), (Soliva and Schultz, 2008) and (Nixon et al., 2014) . Moreover, it has been demonstrated that the evolution of continental rifting increases northward as observed in the North Ethiopian Rift–Afar transition area (Soliva and Schultz, 2008) and the Main Ethiopian Rifts (Hayward and Ebinger, 1996, Agostini et al., 2011b). Therefore, the first hypotheses of this research is to test whether there is a Northward increase of total strain in rift segments along the EARS.

2) Average fault trace length is larger in the late stage of continental rifting exemplified in the NMER segment as opposed to the prior transitional stage in the CMER. This hypotheses is based upon the observation from the model of Ackermann et al. (2001) that fault length increases with increasing strain.

3) Heterogeneities in the pre-existing underlying structures are thought to influence normal fault growth and geometry (Walsh et al., 2002b, Morley, 1999b). Hence, the second hypotheses of this research assumes that local fault orientations of fault populations are influenced by the underlying basement structures at depth.

1.3 Objectives

The objectives that will be used to help answer the research questions and achieve the aim of this research are:

- Using ASTER DEM data to identify and map faults scarps from DEM topographic surface in the study areas.
- Measure fault geometries including, fault orientation, fault trace length, fault vertical displacement (throw), fault spacing and fault displacement\length ratio.
- Measure heave related strain and displacement related strain for fault populations to determine the contribution of different fault populations to the strain accommodation and the trend of extensional strain along the rifts.
- Mapping and quantifying the spatial heterogeneity of extensional strain and faulting in different fault populations and relate that to the deformation along the rift.
- Examine the relationship between fault lengths and their vertical displacement.
- Investigate displacement\length scaling relations of isolated faults to infer their growth mechanism.
- Examine the fault size populations by using cumulative frequency distribution with respect to the amount of extensional strain to deduce any patterns of fault growth within fault populations and their implication on the evolution of the rift.
- Synthesis and discuss fault parameters analysis in the light of published literature to infer which fault growth models best describe normal fault evolution in each rift segment.
- Compare and contrast results from the three rift zones; the central Kenya rift, the central main Ethiopian rift (CMER) and the northern Ethiopian rift (NMER).

- Capture pre-existing fabrics from structural maps found in previously published studies.
- Constructing rose diagrams for azimuths of fault populations in each rift segment, the regional stress direction and pre-existing structures.
- Extraction of the drainage networks from DEM for the three rift segments.

1.4 Significance of the research

The importance of the current study is exemplified in:

- Characterize the north to south surface deformation of rift evolution in three phases of continental rifting along the EARS.
- Using DEM data to analyse the upper crust brittle deformation of continental rift evolution in a reginal context within the EARS, due to the lack of adequate subsurface data (i.e. seismic data).
- Examine normal fault populations both in terms of throws and lengths in 2D (map view), which allows a better explanation of deformation in continental rifting to be made, whereas enormous other studies of this kind examine the brittle deformation by analysing normal fault populations in cross-sectional view 1D with emphasis on fault lengths but not fault throws.
- A large dataset of fault size parameters collected in three rift zones from 2130 fault scarps.

1.5 Thesis outline

Chapter 1: introduces the evolution of continental rifting and the importance of understanding the evolution of normal faulting associated with rifting and extension processes, this chapter also states rational of the research, problem statement, research questions, aims and objectives of this research, significance of the research, hypothesis and the layout of the structure of this thesis.

Chapter 2: Presents a summary of previous work on key structural processes involved in continental rifting, and highlights theories and methods involved in analysing and quantifying the upper crust brittle deformation and gives an overview of the key fault growth models. This chapter also describes the methodology used for data acquisition, mapping of fault length and fault throw through digital elevation model (DEM) surfaces. The fault datasets are described including their length, throw, orientation and displacement length ratio.

Chapter 3: Introduces the tectonic and geological setting of the central Kenya rift, describes the three defined zones of fault populations to be investigated, and estimates the extensional strain and analyse the spatial heterogeneity of extensional strain and fault frequency. This chapter also quantitatively describes and investigates fault size attributes (length and throw) of fault populations measured in 2-dimensions and discusses implications for fault growth and rift evolution.

Chapter 4: Introduces the tectonic and geological setting of the CMER and the NMER segments, estimates the extensional strain and examines the

spatial heterogeneity of extensional strain and fault frequency, quantitatively describes and investigate fault size attributes (length, throw and spacing) of fault populations measured in map view of DEM surface and Synthesis and discusses the fault scaling properties and their implications for fault growth and rift evolution.

Chapter 5: addresses the specific question of whether there is any influence of the pre-existing underlying structures on the present day geometry of surface faults. This chapter presents qualitative and quantitative assessment of the relationship between faults orientations at the surface, extension direction and pre-existing structures in the basement, the obtained results were then correlated with existing sandbox models to assess the possible influence of pre-existing structures.

Chapter 6: Is an attempt to propose a preliminary method to interpret and define the likely original position of eroded footwall blocks of the Quaternary faults in continental rifting, and qualitatively assess how good the initial estimations of extensional strain are in the three study areas.

Chapter 7: Synthesises and discusses key results from the previous chapters, and compares and contrasts results from the three studied rift segments in order to provide an overview of the implications for the evolution of fault system and the rifting as a whole. This chapter also summarizes conclusions reached in each chapter and discuss recommendations for future work.

Chapte 2. Background & fault dataset

2.1 Background

2.1.1 Regional geology of the east African rift.

The East African Rift System (EARS) is the largest continental rift system on Earth and has long been considered an ideal place to analyse the progressive evolution of continental rifting (e.g. Hayward and Ebinger, 1996, Morley and Ngenoh, 1999c, Chorowicz, 2005, Ebinger, 2005, Corti, 2009, Agostini et al., 2011a). The EARS, first described in 1921 by Gregory, constitutes, with the Red Sea and the Gulf of Aden, the Afar triple junction (McKenzie and Morgan, 1969). It has bisected into two branches as it moves from the Ethiopian part towards the south (Figure 2.1), and the development of the EARS is governed by inherited fabrics where extensional deformation is localized along mobile belts and suture zones as they tend to be weaker than the surrounding areas (Petit and Ebinger, 2000). The Eastern and Western branches alike trace pre-existing mobile belts and branch around the Archean Tanzania Craton (McConnell, 1972), while in the Main Ethiopian Rift, rifting localize deformation along a suture zone (Keranen and Klemperer, 2008).

It has been demonstrated in a number of previous studies e.g. McConnell (1972), Chorowicz (2005) and (Achauer et al., 1992) that the East African rift system is affected by localized extensional force in the continental lithosphere produced by divergent tectonic movements. According to these studies, the ductile properties of lithospheric mantle allowed ductile thinning of the crust, and encouraging the rise of asthenosphere mantle to the base of the lithosphere, whereas faulting and subsidence (grabens) were the result of the

brittle crust response to further mantle extension, forming elongate, narrows rifts.

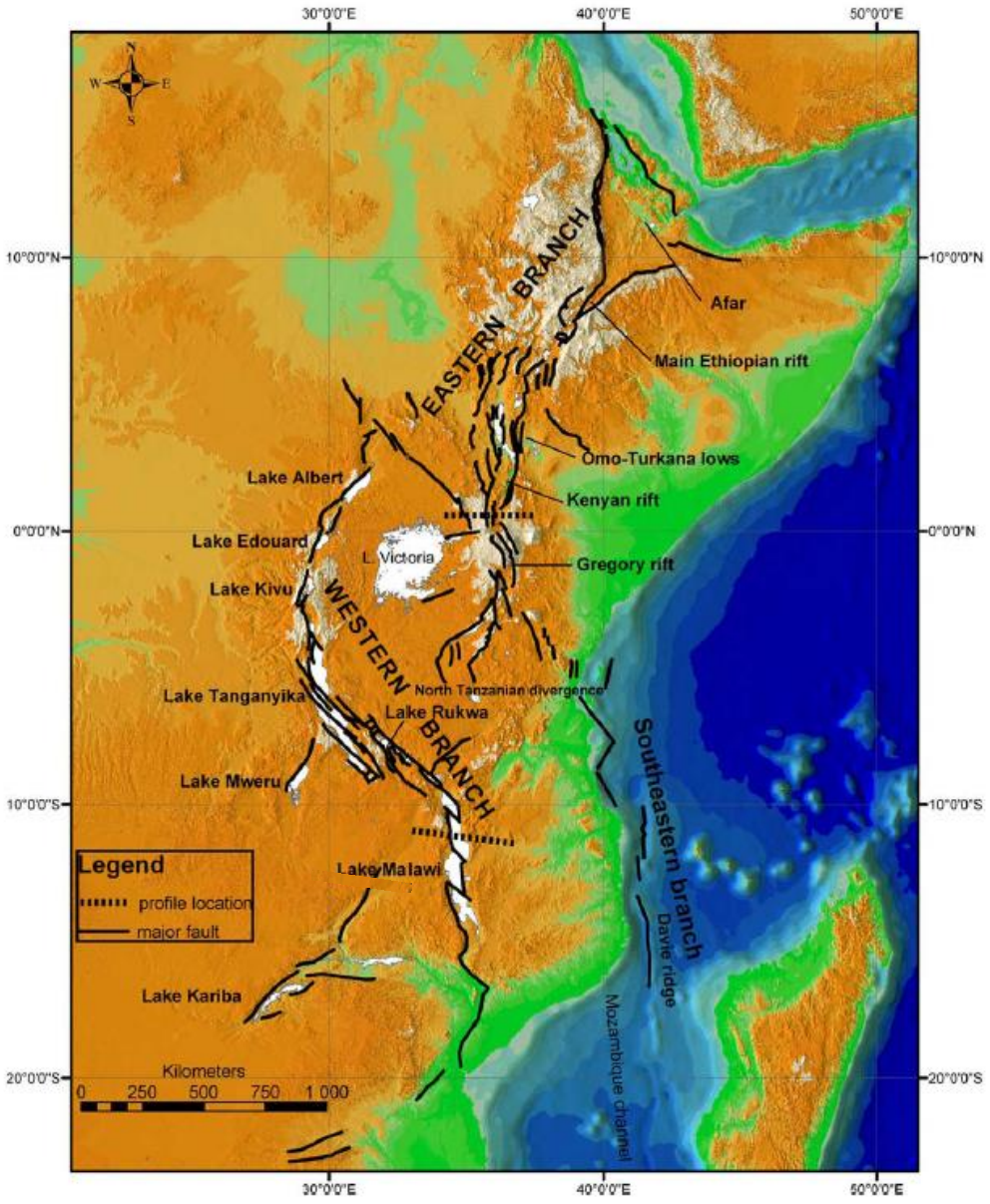

Figure 2.1. The eastern and western branches of EARS and their distinct rift zones from **(Chorowicz, 2005)**.

It has been reported that the thickness of the brittle crustal layer is a major factor that control the fault system geometry, therefore, fault system attributes including size distribution, displacement length relation and spacing, are dependent on the brittle rock layer thickness (Cowie et al., 1994, Cowie, 1998a, Odling et al., 1999, Ackermann et al., 2001, Schultz and Fossen, 2002, Soliva and Benedicto, 2004, Soliva and Schultz, 2008). Velocity model along the rift axis of the MER and Afar region (Figure 2.2) shows that the crust thickness gradually thins to the north, from ~33–35 km at the northern MER–Central MER boundary to ~24–26 km in southern Afar (e.g.Mackenzie et al., 2005, Maguire et al., 2006, Stuart et al., 2006, Keranen and Klemperer, 2008). There is also a northward decrease in the effective elastic thickness from ~20 km in the MER to ~6 km beneath Northern Afar (Hayward and Ebinger, 1996). The elastic thickness is modify by the duration of heating from below from a mantle plume and/or stretching, as well as the volume of magmatic material accreted to the lithosphere (Ebinger et al., 1999). Estimates of elastic plate thickness were found to be 21-36 km in Kenya, and Ethiopian rifts that include are severely faulted and commonly volcanically active (Ebinger et al., 1989).

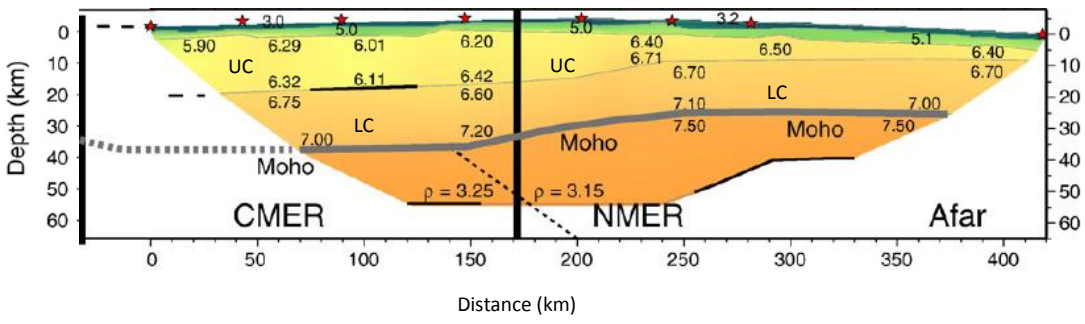

Figure 2.2 Cross-sections across Velocity model along the rift depicting thinning of the crust layer northward, modified from (Keranen and Klemperer, 2008, Maguire et al., 2006)

The eastern branch, which is the focus of this research runs over a distance of 2200 km, from the Afar triangle in the north, through the main Ethiopian rift, the Turkana lows, the Kenyan (Gregory) rifts, and ends in the basins of the North-Tanzanian divergence in the south. Geological, geochemical and geophysical constraints indicate that magmatism and tectonism vary significantly with depth and along strike (Karson and Curtis, 1989, Chorowicz, 2005). The eastern branch exhibits faulting and several volcanoes refer back to the Quaternary age and large volumes of basaltic (mafic and silicic) lavas and pyroclastic erupted through fractures superimposing materials of Miocene and Pliocene volcanism (Omenda, 2010).

Volcanic activity arose firstly in the Ethiopian rift (49 Ma), followed by the Kenya rift (30-24 Ma), and most recently in the western rift (12 Ma) (Olsen, 1995). It has been shown that the volume of rift related volcanism is much greater in the Ethiopian and Kenyan rift than in western rift, and the large volume of flood basalt in Ethiopia supports that suggestion that the original crust has been extensively replaced by magmatic products (Mohr, 1989).

Rift structure in the eastern branch of EARS take place in broad and complex areas that are topographically low, in Afar southern Ethiopia, Northern Kenya, and Northern Tanzania (Olsen, 1995). Estimates of the magnitude of extension across some portions of the eastern branch, beneath the rift lakes where seismic reflection data are available show the amount of extension to be 10% or less (Karson and Curtis, 1989).

The Ethiopian and Kenyan portions of the EARS show little seismic activity except around the Afar Triple Junction, the west of the Gregory Rift close to Lake Victoria, and in northern Tanzania. Micro-earthquake studies in these

areas show high levels of seismicity along the floor of central rift valley at depths of 4 to 10 km. these micro-earthquakes match well with active surface faults, many of which are associated with hot springs and geysers (Fairhead and Stuart, 1982, Rykounov et al., 1972, Pointing et al., 1985). The micro-earthquakes that happen at a superficial depth reflects that the brittle extension is limited to a few kilometers of the upper lithosphere, and ductile creep may occur at relatively shallow depths where strain is accommodated along low-angle faults or by the intrusion of magma bodies (Karson and Curtis, 1989).

2.1.2 Basic concepts of continental rifting

2.1.2.1 Extensional tectonics and lithospheric development

Initiation and growth of continental rifting are thought to be caused by extension of the Earth's crust and lithospheric mantle. Continental rifts have been defined as elongate basins constrained by opposite dipping normal faults, involving a thinning mechanism of the Earth's crust and lithosphere, leading eventually to splitting the continent and forming new mid ocean ridge and sea floor spreading (Hayward and Ebinger, 1996, Corti et al., 2003, Ebinger, 2005, Maguire et al., 2006, Corti, 2009, Agostini et al., 2011b). Nevertheless, this process may not always come to its end due to deactivation of the extensional process. According to the models of McConnell (1972) and (Bott and Hinze, 1995), the fundamental mechanism for continental rifting is reliant on high heat flow causing expansion, upward bending and extension of the lithospheric mantle. In the East African Rift for example, volcanism has

been suggested to result from up-welling of mantle material along narrow dyke-like channels (Harris, 1969, Jakovlev et al., 2008). The heat is derived from radioactive decay in the mantle and in a way that is similar to penetrative convection (Elder, 1966, McConnell, 1972, Achauer et al., 1992) .

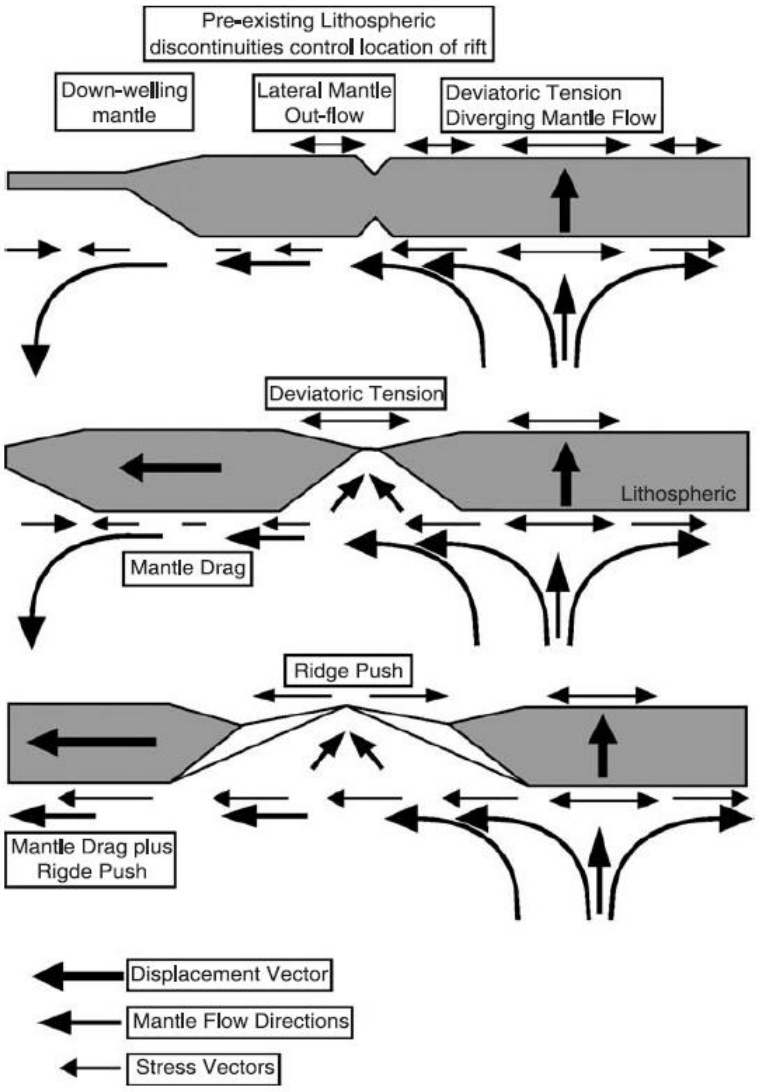

Figure 2.3. Diagram illustrating the interaction of forces exerted by movement and interaction of lithospheric plates on the base of the lithosphere, and tensional stress above upwelling mantle convection from **(Ziegler and Cloetingh, 2004)**.

Rift duration before the final split-up of continental crust is believed to vary between 9 and 280 Ma. The geometry of rift systems is normally strongly influenced by lithospheric structures beneath it (Ziegler and Cloetingh, 2004), and the resulting margins geometry (width and symmetry) and volcanism are highly variable due to variations in initial rheological or thermal structure of the lithosphere, strain rate, rift kinematics, presence of inherited pre-existing fabrics, magmatic melting from the uprising asthenosphere and development of large detachment faults (Corti et al., 2003). Those rifts that reach the stage of continental breakup are thought to be controlled by the movement and interaction of lithospheric plates and frictional forces imposed by slap pull and mental drag (McConnell, 1972), and the movements of convection currents on the base of the lithosphere (Bott and Kusznir, 1979, Bott, 1993, ZIEGLER, 1993). Ziegler and Cloetingh (2004) pointed out that these forces along with tensional stresses of lithosphere of young orogenic belts, above upwelling mantle convection cells and mantle plumes (Bott, 1993), interact together to overcome the strength of the lithosphere and cause rifting (Figure 2.3)

Numerical models of Buck (1991) and analogue models of Brun (1999) have shown that deformation caused by continental extension can take one of two forms due to the initial strength of the lithosphere; either as; narrow rifting that is thought to be caused by strong lithosphere (where the width of the rift valley is narrower than the lithospheric thickness range between 50–100 km, as typically represented in EARS) or as wide rifting that is associated with extension of weak lithospheres (when extension is accommodated by the development of horsts and grabens distributed over areas much wider than lithospheric thickness, and up to 1000 km, as exemplified in the Basin and Range region of Western United States) (Brun, 1999).

2.1.2.2 Rifting and pre-existing structures

It has been widely demonstrated that continental rifts are not arbitrarily distributed but rift segments are inclined to propagate following the trend of inherited weaknesses of pre-existing fabric of the lithosphere (such as ancient orogenic belts), avoiding stronger formations (e.g. Versfelt and Rosendahl, 1989, Petit and Ebinger, 2000, Ziegler and Cloetingh, 2004). Rift architecture is often related to the reviving of former pre-Cambrian weakness in the Earth's crust and lithosphere. The pre-existing crustal and lithosphere discontinuities regardless of their age (young orogenic belts, old Precambrian shields) are prone to tensional reactivation, which control the location of rifts, the structural style of rifts, and localization and distribution of crustal strain (e.g. Janssen et al., 1995, Bellahsen and Daniel, 2005, Corti, 2009, Agostini et al., 2009, Agostini et al., 2011a, Corti, 2012). Moreover, Results from the numerical models of Brune (2014) indicate that rifting prefers oblique reactivation of mechanically weak zones, at an angle to far-field stresses.

It has been supported by several analog models that rift localization may be influenced by pre-existing weakness (Figure 2.4). In an experiment containing a 4-layer lithosphere, including a central 3-layer weakness zone, the lithospheric strength is weakened by inhibition of the lateral continuity of the strong lithospheric mantle and its replacement with weak crustal material (Callot et al., 2001, 2002, Corti, 2012). The lithospheric strength is further weakened by thermal variations resulting from channelling and ponding of plume-related deep hot materials in correspondence to pre-existing mobile belts (Ebinger and Sleep, 1998, Corti et al., 2003). These circumstances restricted normal faulting and lithospheric thinning to follow the weak zone (Figure 2.4).

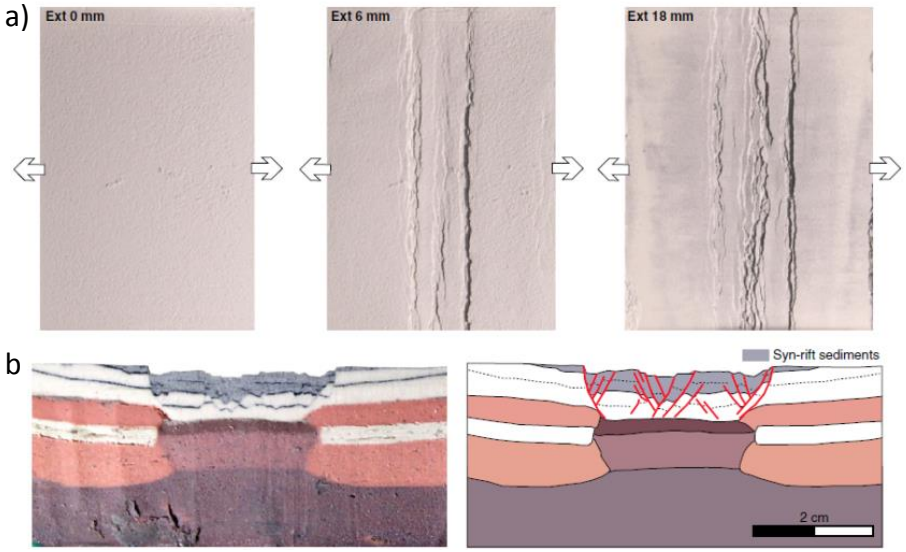

Figure 2.4. Analog model of typical evolution of 4-layer experiment containing a central 3-layer weakness zone a): top view photos of the surface of the model during progressive extension. B): Cross-section of the model shown as photo (left) and line-drawing (right) of structures (Corti, 2012).

2.1.3 Basic concepts of faulting

2.1.3.1 Fault length-displacement relationship

It has been largely accepted that the relationship between vertical displacement and fault length provides crucial information on the growth of faults through time (e.g. Walsh and Watterson, 1988, Cowie and Scholz, 1992b). Moreover, this relationship also enables the total brittle strain in a fault rock volume to be calculated (Scholz and Cowie, 1990, Marrett and Allmendinger, 1991). The relationship between a fault length (L) and its maximum displacement (Dmax) involves a state of fault growth over geologic time, due to accumulation of displacement on faults, which increases the strain concentration at the fault tips, and therefore causes them to grow in length to maintain the scaling relationship (Walsh and Watterson, 1988, Scholz and

Cowie, 1990, Cowie and Scholz, 1992b). Faults growing by such a model follow a self-similar behaviour over several orders of magnitude and maintain a linear relationship between displacement and length, (e.g. Cowie and Scholz, 1992c, Soliva and Schultz, 2008). The strong correlation between fault size attributes indicated in several studies (Walsh and Watterson, 1988, Peacock and Sanderson, 1991, Gillespie et al., 1992, Cowie and Scholz, 1992a, Cartwright et al., 1995, Cowie, 1998a, Kim and Sanderson, 2005, Childs et al., 2009); suggest that these attributes constrain and depend on one another, therefore knowledge of one or two key attributes can provide insight into the values and relationships among the others.

It has generally been assumed that there is a proportional relationship between the fault length (L) and the maximum displacement (D) as follow:

$$D = cL^n \qquad (Eq. 1)$$

Where c is a constant relating to material properties n is the exponent value, which ranges from 0.5 to 2.0 for tectonic fault systems; n=0.5 (Fossen and Hesthammer, 1997), n=1.0 (Cowie and Scholz, 1992a, Dawers et al., 1993, Schlische et al., 1996), n=1.5 (Marrett and Allmendinger, 1991, Gillespie et al., 1992) and n=2.0 (Watterson, 1986, Walsh and Watterson, 1988), The n value of fault Displacement/Length data is of interest and has implications on the way in which faults grow and what fault model best describes the growth of faults.

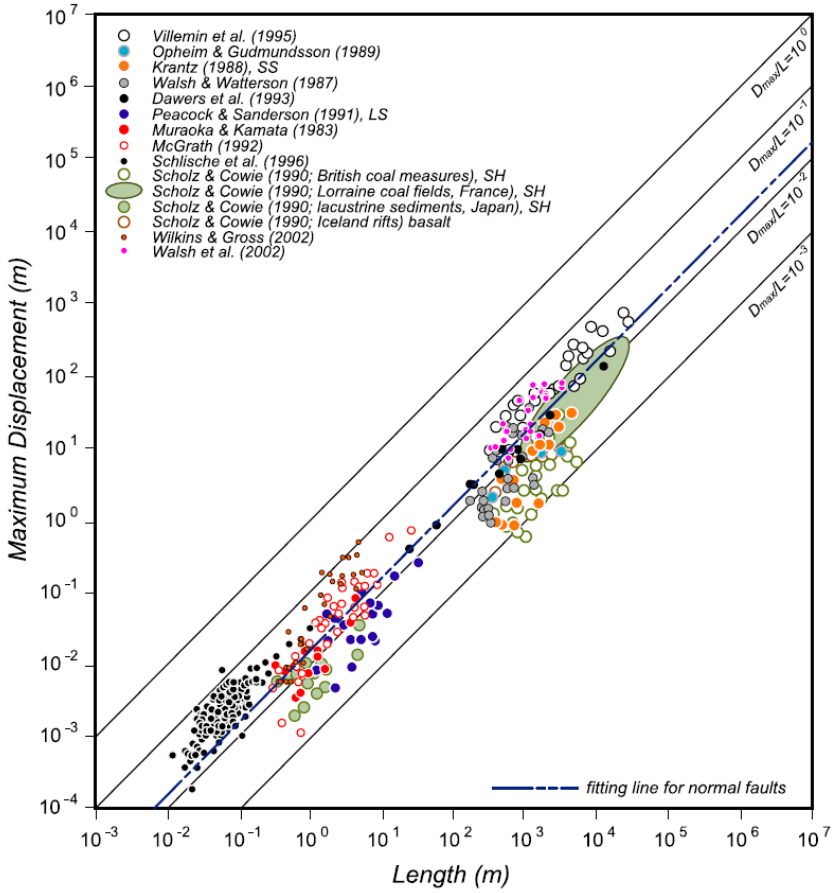

Figure 2.5 A plots of maximum displacement (dmax) against fault length (L) for normal faults from**(Kim and Sanderson, 2005)**

There has still been a controversy over whether the scaling relationship between dmax /L is linear (n=1.0), where faults exhibit a self-similar or scale invariant geometry which is independent of scale, or nonlinear (n=>1.0) where faults are scale-dependent. It has been observed in a number of studies such as Kim and Sanderson (2005) for normal faults (Figure 2.5) that there is typically large scattering associated with the linear relationship. The D/L relationship is affected by potential sources of scattering that have long been attributed to: measurement errors, sampling of faults in different lithology and effects of fault linkage (Walsh and Watterson, 1988, Cowie and Scholz, 1992a, Gillespie et al., 1992, Cartwright et al., 1995, Kim and Sanderson, 2005).

2.1.3.2 Scaling laws

Scaling relations of fault displacement–length (D-L) as well as displacement distributions have been studied in recent decades in order to understand growth history of fault populations (Cowie and Scholz, 1992a, Dawers et al., 1993, Schultz and Fossen, 2002, Soliva and Schultz, 2008). The scaling relations between fault geometry (D-L) has been used to suggest a number of fault growth models such as Walsh and Watterson (1988), Cartwright et al. (1995) and Walsh et al. (2002a).

Fault population data, such as trace-length, spacing and displacement can be analysed by cumulative frequency distribution (CFD), in most instances, those attributes are best described either by simple power-laws or exponential fit distribution (Cladouhos and Marrett, 1996, Gupta and Scholz, 2000, Cowie et al., 1995, Cowie and Scholz, 1992c, Cowie and Scholz, 1992b, Cowie and Scholz, 1992a), depending on the tectonic setting of the region (Cowie et al., 1994, Scholz and Shaw, 1999).

Power-law distribution is the most commonly observed scaling function for the distribution of fault displacements (Pickering et al., 1996). Moreover, differences in the exponent of power law scaling distributions between fault populations is due to variations in the amount of strain accommodated by fault systems, and it is also associated with the fault nucleation, growth and amalgamation, which define the main stages of fault evolution (Ackermann et al., 2001, Cowie et al., 1995). Therefore, scaling relations of fault size population showing power-law distribution is used to assess the amount of deformation and highlight the contribution of different fault size to the strain accommodation.

Many fault offset populations plot along a more or less straight line in the log-log plot (Figure 2.6), which implies a power-law distribution or self-similar relation. This is described mathematically as*:*

$$N=aS^{-D} \qquad (Eq.\ 2)$$

Where *S* could be displacement, throw or heave, *N* is the cumulative number of fault offset, and *a* is a constant. *D* is an exponent, and it describes the fractal dimension of slope of the straight segment (e.g. Poulimenos, 2000).

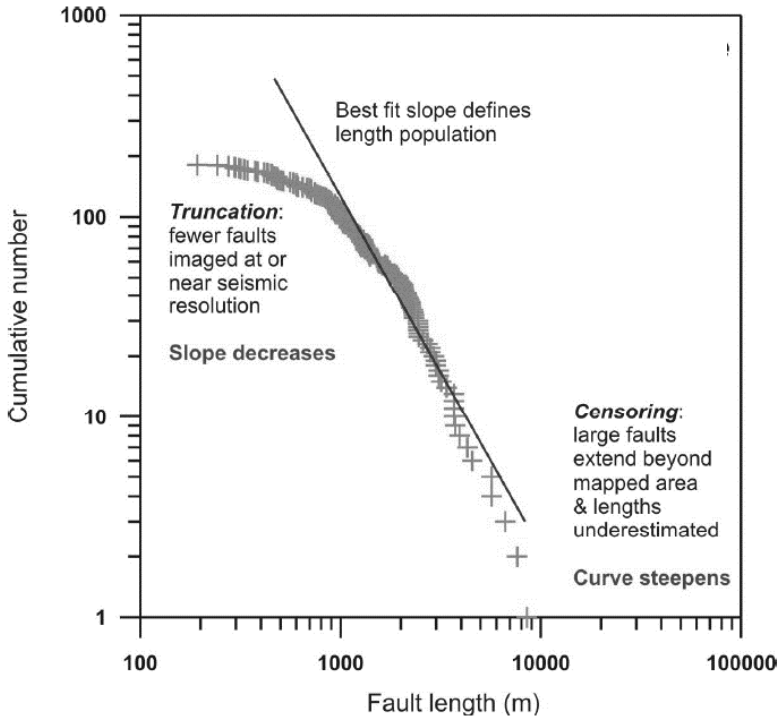

Figure 2.6 Schematic example of power-law distribution in log-log plot, showing truncation and censoring effects.

The straight segments (Figure 2.6) are truncated by curved segments at each end, due to truncation effect (underrepresentation of small faults that are below the resolution of observation) at the upper part of the curve, and censoring effect at the lower part of the curve as a result of large faults

extending beyond the scale of observation (Pickering et al., 1995, Bonnet et al., 2001).

Power function exponent of fault trace length populations can also be used to differentiate interacting normal faults from non-interacting faults based on power scaling exponent for fault trace-length data plotted on a cumulative distribution plot. Vallianatos and Sammonds (2011) derived a q-factor (Eq. 73 based on the power scaling exponent of a CDF fit to the fault trace-length data plotted on a CNL plot. If a q-parameter is close to one, the fault system is considered to be independent or non-interactive, whereas a q-parameter close to two indicates highly interacting fault systems.

$$q \approx 1+1/c \qquad \text{(Eq. 3)}$$

Where C is the power law exponent of fault trace length population.

Other scaling laws such as exponential and log-normal distribution (Figure 2.7). It has been generally recognized that resolution and finite size effects on a power law population can result in a distribution that appear to be exponential or log normal (Bonnet et al., 2001). Thus, with the rise of scaling concepts in earth sciences, power law distributions have been favoured over log-normal distributions because of their greater physical significance (Barton and Zoback, 1992).

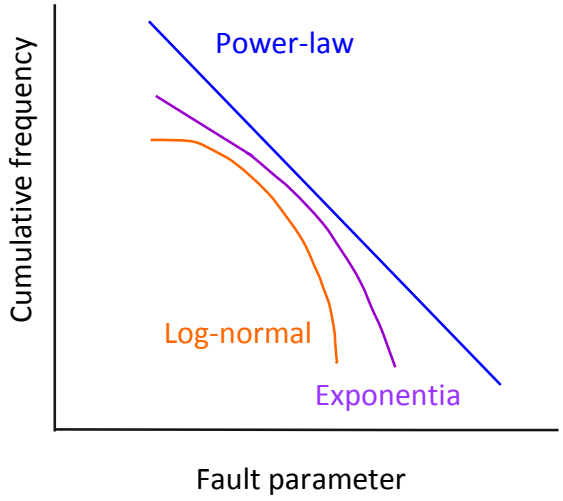

Figure 2.7. Log-log illustration of common scaling laws used in geoscience

2.1.3.3 Scaling properties analysis in previous studies

A previous quantitative study by Soliva and Schultz (2008) in the Main Ethiopian Rift-Afar has examined the scaling relation of fault populations and identified fault systems within the extensional setting that are deformed in two different patterns, known as; (1) localized strain deformation, which occur at rift border zones that show large-scale fault linkage and a power law size distribution. This power law distribution reflects scale-invariant (self-similar) behaviour of growth between fault length and fault displacement (Scholz and Cowie, 1990, Schlische et al., 1996), where strain is localized along a few large faults accumulating around 50% of the total strain (Scholz and Cowie, 1990, Walsh et al., 1991), and a large number of relatively small faults in a contributing to the strain accommodation (Walsh et al., 1991). (2) Distributed strain deformation that take place when strain is more distributed within small scale fault linkage showing an exponential size distribution. Normal fault

populations that grow in confined brittle layers of finite thickness are characterized by faults growing in length with restricted fault displacement, due to limited layer thickness acting as mechanical barrier, leading to a horizontally distributed fault system (Soliva et al., 2006). In such setting, isolated faults are no longer self-similar in length and displacement distribution but are a scale-dependent distributed system, since the vertical growth is hindered, generally displaying plateaued displacement profiles that fit to an exponential size distribution (Figure 2.8) (Ackermann et al., 2001, Soliva and Benedicto, 2005, Soliva et al., 2006).

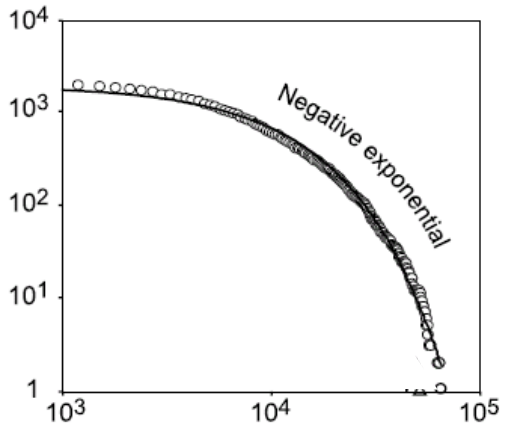

Figure 2.8 Schematic example of exponential distribution in a log-log plot, modified from **Soliva and Schultz (2008)**.

Scaling properties have also been used in quantitative analysis of faults within the Kino Sogo Fault Belt (KSFB) in Turkana rift, Northern Kenya by (Vétel et al., 2005). This work provided an analysis of the geometry and growth of the KSFB using data obtained from outcrop studies, remote sensing data and digital elevation models, this study found that this inner trough fault system accommodates very low strains (<1%). This fault system encompasses segmented fault populations with lengths of up to 40 km, and maximum throws of < 100 m, this under-displaced pattern of the fault system was attributed to

rapid propagation of fault length in response to the reactivation of inherited earlier underlying basement structures. Therefore, fault scaling properties, such as fault length distributions, show exponential distributions (Figure 2.8), contrasting the power-law scaling (Figure 2.6) typical of other fault systems because the displacement/length distribution is scale dependent.

2.1.3.4 Fault growth by segment linkage

The processes of fault interaction and linkage in normal faults have been described by several workers, where fault growth by linkage involve interaction of en echelon segments through ramp and relay zones, and fault displacement distribution is affected along fault length by fault interactions and linkage to form segmented faults (Peacock and Sanderson, 1991, Gillespie et al., 1992, Dawers et al., 1993, Peacock and Sanderson, 1994, Cartwright et al., 1995). Peacock & Sanderson (1991) suggested a model of fault growth (Figure 2.10), where relay structures (Figure 2.9) develop when two fault segment tips propagate and pass each other forming an overlapping configuration (Peacock and Sanderson, 1991) and the strain is transferred between the two Interacting faults (Walsh et al., 2002a, Walsh et al., 2003b). Relay ramps connect the footwall and the hanging wall of two parallel overlapping fault segments that interact within an area of reoriented bedding (Figure 2.9), formed by the decrease in displacement at the fault tips, At this stage, further lateral propagation is inhibited by the interaction of stress fields around the overlapping fault tips (Peacock and Sanderson, 1994, Hus et al., 2005). The limit by which a relay ramp can stand before it breaks is determined by the rheology and bed thickness of the ramp structure (Peacock and Sanderson, 1991, Hus et al., 2005).

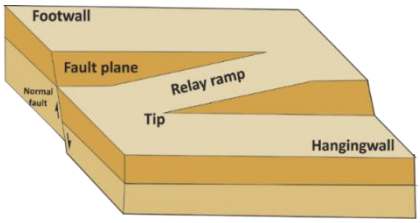

Figure 2.9: Block diagram showing the main features of a relay ramp. Modified from **(Peacock and Sanderson, 1994)**.

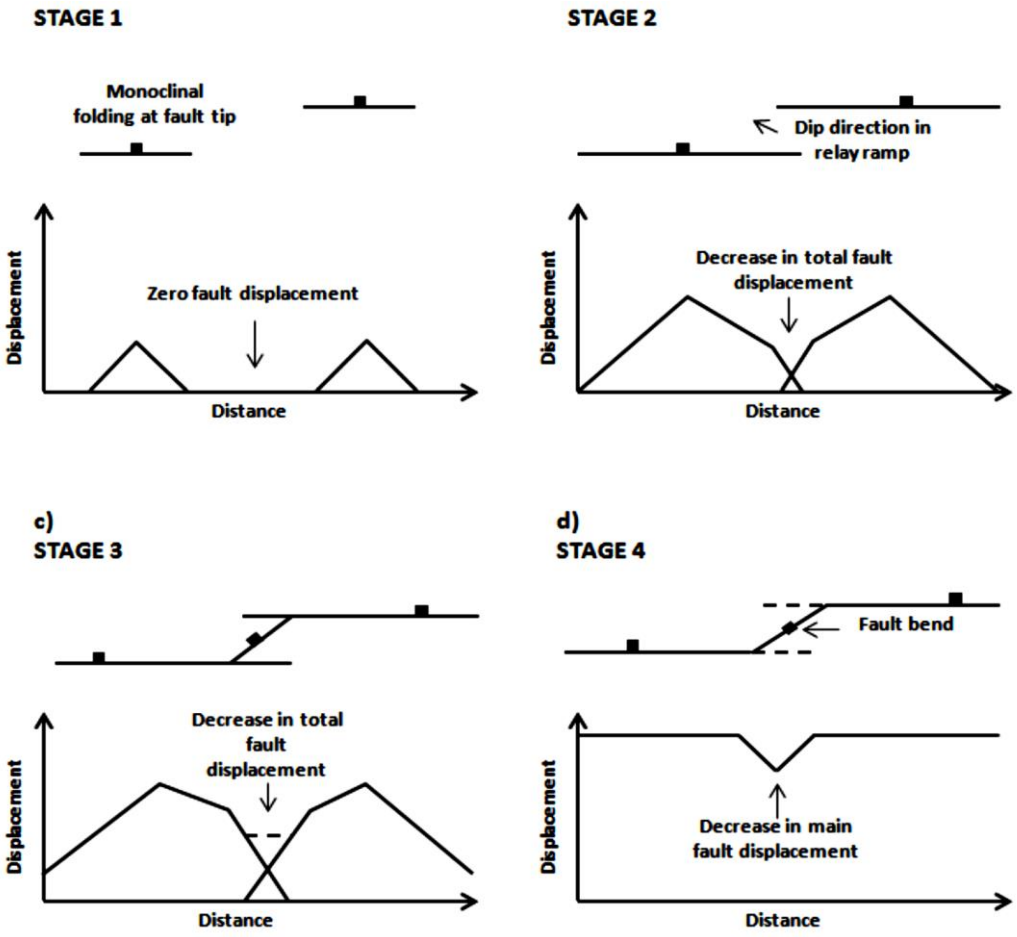

Figure 2.10: Diagrams of stages of displacement development with equivalent displacement-distance profiles. (Stage 1) The faults are isolated and do not overlap. (Stage 2) Initiation of relay ramp when the two faults overlap and displacement is transferred between the faults by rotation. (Stage 3) The relay ramp is hard linked. (Stage 4) The relay ramp is established, faults are hard linked and pre-existing fault tips are incorporated into the footwall and hanging-wall of the linked fault set **(Peacock and Sanderson, 1991)**.

2.1.3.5 Fault growth models

There are two widely competing models for fault initiation and growth. The first model is the isolated fault model in which length and displacement accrue synchronously throughout faulting, in a scale invariant manner, maintaining a constant Displacement/Length ratio (Figure 2.11) until the faults began to either interact or intersect with other faults (Watterson, 1986, Walsh and Watterson, 1988, Gillespie et al., 1992, Cowie and Scholz, 1992a, Cartwright et al., 1995, Peacock and Sanderson, 1996). This model suggests that as a volume of rock is subjected to increasing strain, a number of small distributed faults will begin to emerge as a single isolated, smooth continuous surface of displacement discontinuity (Kim and Sanderson, 2005). As the strain continues to increase, faults grow in length by propagation of individual faults towards adjacent small faults and begin to interact and link when their strain fields begin to overlap, propagation is then inhibited and displacement begins to accumulate at the expense of smaller faults due to their greater size (Cartwright et al., 1995, Gupta and Scholz, 2000a, Cowie et al., 2000, Kim and Sanderson, 2005, Bergen and Shaw, 2010). This process is thought to result in the creation of large localised faults, and the abandonment of small faults. The second model is the constant length model, this model suggests that normal faults grow by a rapid establishment of their near-final length prior to a prolonged period of significant displacement accumulation (Poulimenos, 2000, Meyer et al., 2002, Walsh et al., 2002a, Nicol et al., 2010, Jackson and Rotevatn, 2013), in this model, as stress is applied to the volume of rock, faults would initiate with low displacements but with lengths at or near maximum, this length would then remain fixed while displacement increases until what started as many small displacement faults is now only a few large

displacement faults that have accrued the majority of the strain in the volume. In this model, displacement/length ratio would increase as the strain increases (Figure 2.11), this proposed fault growth model is consistent with the coherent fault model (Walsh et al., 2003a, Childs et al., 2009), that suggests; what appears to be as individual fault segments in their initiation, are thought to be kinematically and geometrically interrelated to a larger coherent underlying fault structure (Giba et al., 2012).

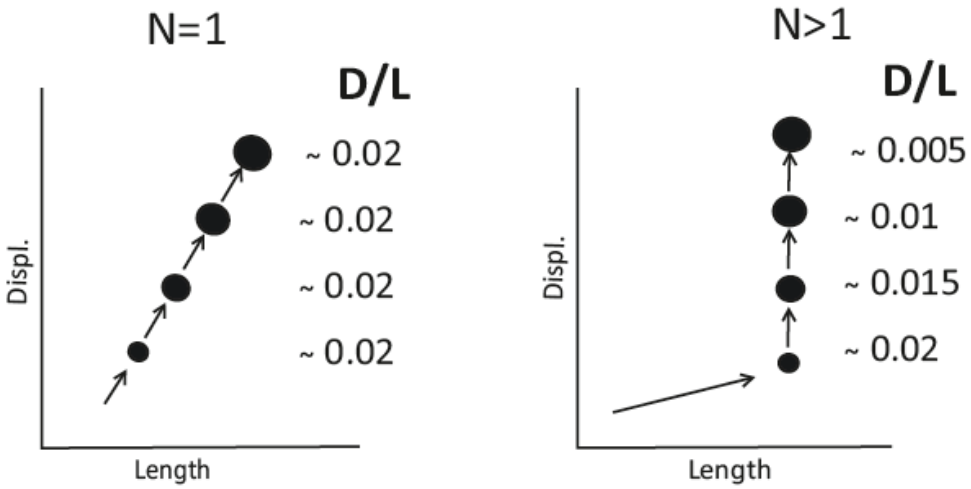

Figure 2.11. Illustration of isolated fault growth model (left) and constant-length fault model (right), modified from **(Nicol et al., 2016)**.

2.1.4 Concepts of fault analysis

2.1.4.1 Fault sampling methods

One-Dimensional (1-D), two-Dimensional (2-D) and three-Dimensional (3-D) methods; are the common methods of collecting fault attributes. The current study only 1D and 2D were used. A one-dimensional sample can be obtained by making measurements along a linear traverse (also known as a line section or a scan line) drawn on a map, satellite image, along a single horizon on a seismic line or from a borehole. The 1D data is easy to collect and their results can be easily comparable between different data sources (McCaffrey et al., 2003b). Fault/fracture parameters such as throw, length, spacing and fault heaves can be collected along 1D line transects. Two dimensional data of Fault/fracture parameters such as throw and length can be measured at a variety of scales from scaled maps, air-photographs, and satellite images, maps containing fault /fracture traces and seismic data. (McCaffrey et al., 2003b).

2.1.4.2 Step plots

The spatial distribution of fault attributes can also be investigated along 1-dimensional line transects by plotting the cumulative parameter values against distance along the fault. If strain is accommodated by a large number of evenly-spaced small faults, then the graph approaches a straight line (low variance), If the strain is focussed on a few larger faults, then there are large steps in the graph and a larger variance can be quantified from the graphical data (Figure 2.12), see also (e.g. Nixon et al., 2014).

2.1.4.3 Coefficient of variation (Cv)

The coefficient of variation, Cv, is a method for characterising fault/fracture spacing that can be used as an index of clustering. Cv is defined as the ratio of the standard deviation to the mean of fault spacing that expresses the degree of clustering along a 1-dimensional line transect e.g. (Gillespie et al., 2001). If the standard deviation and mean are equal, then Cv = 1 and fault/ fracture spacing's is randomly distributed along the line transect, and fit to an exponential distribution. If Cv > 1 then the fault /fracture spacing's is clustered, whereas, if the fracture spacing's is regularly (anti-clustered) distributed then Cv < 1 (e.g. Gillespie et al., 2001).

2.1.4.4 Kuiper's model

The spatial heterogeneity of brittle strain is quantified according to Kuiper's model (Kuiper, 1960) (Figure 2.12). By measuring two components in a 1D line; extensional strain (Vs) (fault heaves) and the fault frequency (Vf) represented by fault spacing. These components are then plotted in step plots of cumulative vales of fault heaves and fault spacing against distance and compared against a uniform distribution. The spatial heterogeneity (V) of extensional strain (Vs) is then quantified by measuring max and min deviation of cumulative vales of fault heaves from the uniform distribution (Figure 2.12) and divided by the cumulative total of fault heaves. The spatial heterogeneity (V) of fault frequency (Vf) is also quantified in the same way by measuring max and min deviation of cumulative vales of fault spacing from the uniform distribution and divided by the number of faults. Graphs with large steps and large variant gradient changes indicate high heterogeneity and localized deformation for both extensional strain Vs and faulting Vf, whereas, graphs

that show relatively uniform steps and less variant gradients represent less heterogeneity due to strain being distributed across a large number of relatively small faults segments that contribute to the strain accommodation. This method has been used in some recent studies such as (Nixon et al., 2014, Putz-Perrier and Sanderson, 2008b) to quantify the spatial heterogeneity.

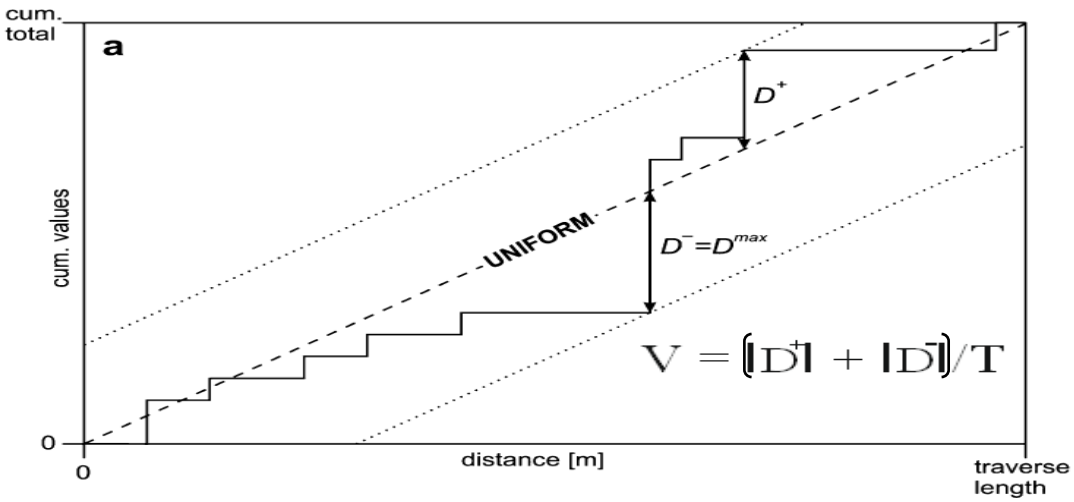

Figure 2.12. Kuiper's Test. (a) shows a cumulative graph over distance (solid line). D^+ & D^- are the maximum positive (upper dotted line) and negative (lower dotted line) deviations of the cumulative graph from the uniform distribution (dashed line), T = total heaves or number of faults modified from **(Putz-Perrier and Sanderson, 2008b)**.

2.2 Fault dataset

2.2.1 DEM data acquisition

Digital elevation models DEM combined with satellite images (Google Earth) are the main data used for the purpose of investigating the upper crust brittle deformation in the three study areas (the central Kenya rift, the central MER and the Northern MER). The DEM data for the study areas were downloaded from the USGS website (https://lpdaac.usgs.gov/) through Advanced Space-borne Thermal Emission and Reflection Radiometer (ASTER) data with ground resolution of 30 mx30 m and vertical resolution of 20 m to provide information on the morphology of surface faults. Google earth optical spectrum imagery with a resolution of about 15 m was used to aid in identification and verification of faults mapped from DEM (Figure 2.16).

The DEM data were brought into Move 2014.1 software for coordinate transformation into (WGS1984_UTM_Zone_37N) and format conversion from GeoTIFF format into Gocad ASCII. The latter format is therefore recognized in Schlumberger's Petrel 2013 software to obtain the 3D view of the DEM, as a shaded relief surface (figure 3.2) and (figure 3.4). To help tracing and mapping fault escarpments on the DEM surface a couple of techniques available in Petrel software were applied, including 3D rotation capability, illumination and edge detection, which is particularly useful in identifying where subtle changes in the surface topography occur, thereby enhancing confidence in the modelled fault network.

2.2.2 Sampling Fault and measurement of fault lengths and throw

The most commonly used measures of fault geometry are the fault length and the maximum displacement. The vertical displacement distribution along the fault trace (fault length) can provide important insights into fault formation and development, until recently displacement-length data were typically obtained from field measurements and seismic surveys (Cowie and Scholz, 1992a, Gillespie et al., 1992, Cartwright et al., 1995). However, remote sensing technology has offered data for the shape of the earth surface, and studies of faults are increasingly based on digital elevation models (DEMs) (Begg and Mouslopoulou, 2010) and other types of digital data.

From the DEM surfaces of the central Kenya rift, the central MER and the Northern MER, hundreds of discrete fault segments were readily distinguishable as individual topographic scarps across the study areas. The physical characteristics of surface faults that can be obtained from virtual topographic surfaces generated by DEM are; strike, relative dip direction, spatial distributions of faults, fault length, throw and linkage style.

On ASTER DEM data, it is not always a straightforward to confirm whether the topographic features are fault related rather than erosional or depositional structures. For most fault segments, trace lengths were measured at the generated surface from tip to tip with respect to the resolution provided by Aster DEM. However, a higher resolution may reveal different tip positions. Vertical exaggeration of x5 is used to facilitate tracing fault scarps.

Therefore, 2130 surface normal faults were identified from the three study areas with high degree of confidence and manually digitized by tracing the fault continuity along strike and picking points representing footwall cut-offs

shown as blue dots on blue lines in (Figure 2.15A -I). The continuity of footwall cut-off is sometimes interrupted by erosional fissures. The hanging wall cut-offs were also picked by tracing the lower horizontal line (fault line) at the bottom of the footwall that represent the hanging wall cut-off and picking points correspondent to those picked for the footwall cut-offs shown as pink dots on pink lines in (Figure 2.15). Fault length defined in this study is the horizontal exposed fault trace length along strike, this is a minimum value of the fault length due to the possibility of the hanging wall being partially filled with sediments and volcanic deposits. Fault trace displacement as mentioned in this study is the vertical offset of the fault defined by the scarp height, a mat lab code was used to measure fault throw by surveying the elevation deference between correspondent points exposed at the footwall crest and the hanging wall cut-off, fault length was also calculated using that code. The measured throw is the maximum value of the apparent throw for each fault, measured perpendicularly to the fault strike, sometimes referred to as apparent throw in this study. Fault throw and length attributes were obtained from three dimensional view of the DEM surface, while fault spacing attributes and fault heaves and throw were obtained from cross-sections (1D) drawn on 2D view of DEM surface.

The result was a database of fault attributes that describe several criteria of fault surface geometry including; fault trace length, maximum apparent throw, orientation, displacement\ length ratio in addition to some descriptive information such as location within the rift, isolated or segmented fault, and hanging-wall cut-off (buried/not buried/partial). A wide scale range of fault sizes populations have been obtained over the three rift segments with fault lengths extending from 272 m to 68615 m, with an average of 4526 m, and

fault throw ranging from 25 to 1561m, with an average of 124 m, and that allowed a detailed quantitative assessment of the scaling properties to be carried out for extensional faults in the study areas of interest.

2.2.3 Potential geological and resolution related errors.

Geological processes and/or sampling and mapping techniques may introduce errors that lead to underestimation of the true fault throw and the true fault trace-length. Hence, the data set presented in this study may be affected by those errors.

2.2.3.1 Geological errors

Picking the hanging wall cut-offs of fault scarp using DEM data representing virtual surfaces generated by satellite images is not always as straightforward as the footwall cut-off, because, in some cases, faults are parallel to each other with a very close spacing distance, which makes picking the hanging wall cut-off of the successive faults is not always possible, and second, the presence of monocline structures and accumulations of erosional or depositional sediment fills on the fault hanging wall also hinder following and picking the hanging wall cut-off. Moreover, fault blocks are normally eroded (Figure 2.13a), and in DEM surfaces, it is not always possible to determine how much erosion of the block has occurred. However, in theory, to estimate the original height of the footwall, the shape of the footwall side can be projected to an estimated original footwall crest before erosion (Figure 2.13b). For these reasons, what can be seen from scarp height is only the apparent fault throw. This partial exposure may introduce systematic error into throw measurements and strain estimations. Moreover, with accumulation of

erosional deposits between faults these faults appear as large segmented faults as opposed to linked faults, which may cause error in the fault trace-lengths.

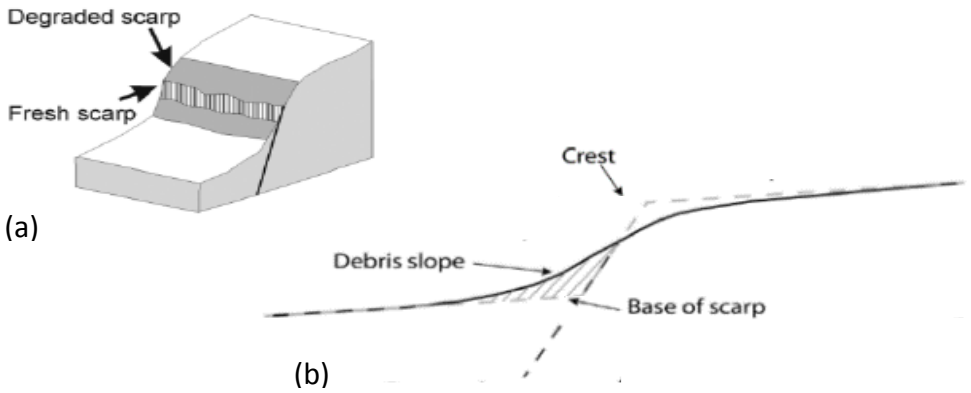

Figure 2.13: sketch showing composite fault scarp

2.2.3.2 Resolution errors

In the present study, where satellite data is used to trace a fault, there are relative errors associated with the horizontal and vertical resolution of the mapping technique, below which the fault length and displacement cannot be detected. Therefore, resolution refers to the minimum distance by which data can be recorded from the scanned scene. Horizontal resolution of ASTER DEM used in this study is 30 mx30 m, which is the spatial frequency at which data are modelled, which affects the measurement of fault trace length. Whereas vertical resolution in ASTER DEM is 20 m, which refers to how frequently the DEM can record a difference in elevation, which again affects measurement of fault throw for the dataset presented here, thus the error associated with fault trace length is greater than that of fault throw, meaning to say, the higher the resolution the more detailed the data are and vice versa.

The main effect of resolution is truncation that occurs because fault trace lengths below 30 m (found in fault tips) and fault heights (throws) below 20 m cut-offs are not resolvable, which lead to underestimation of these parameters. However, the effect of truncation is more significant on small size fault populations (Yielding et al., 1996, Walsh et al., 1996, Watterson et al., 1996). For the purpose of examining the surface deformation of continental rifting over a large area, this resolution is thought to be good enough, since the changes in normal fault geometries are relatively large in scale.

Furthermore, digitizing is the process of converting geological features either from satellite image, scanned image or a map into vector data by tracing the features. Therefore, two other possible errors can occur during the course of capturing the data that are caused jointly by the digitizing technique of the software used for digitizing (Petrel) and the interpretation of the geological features that involves the human eye and hand. Chapter 3 discusses in more detail and quantifies the resolution errors in the fault length and throw caused by the abovementioned factors combined.

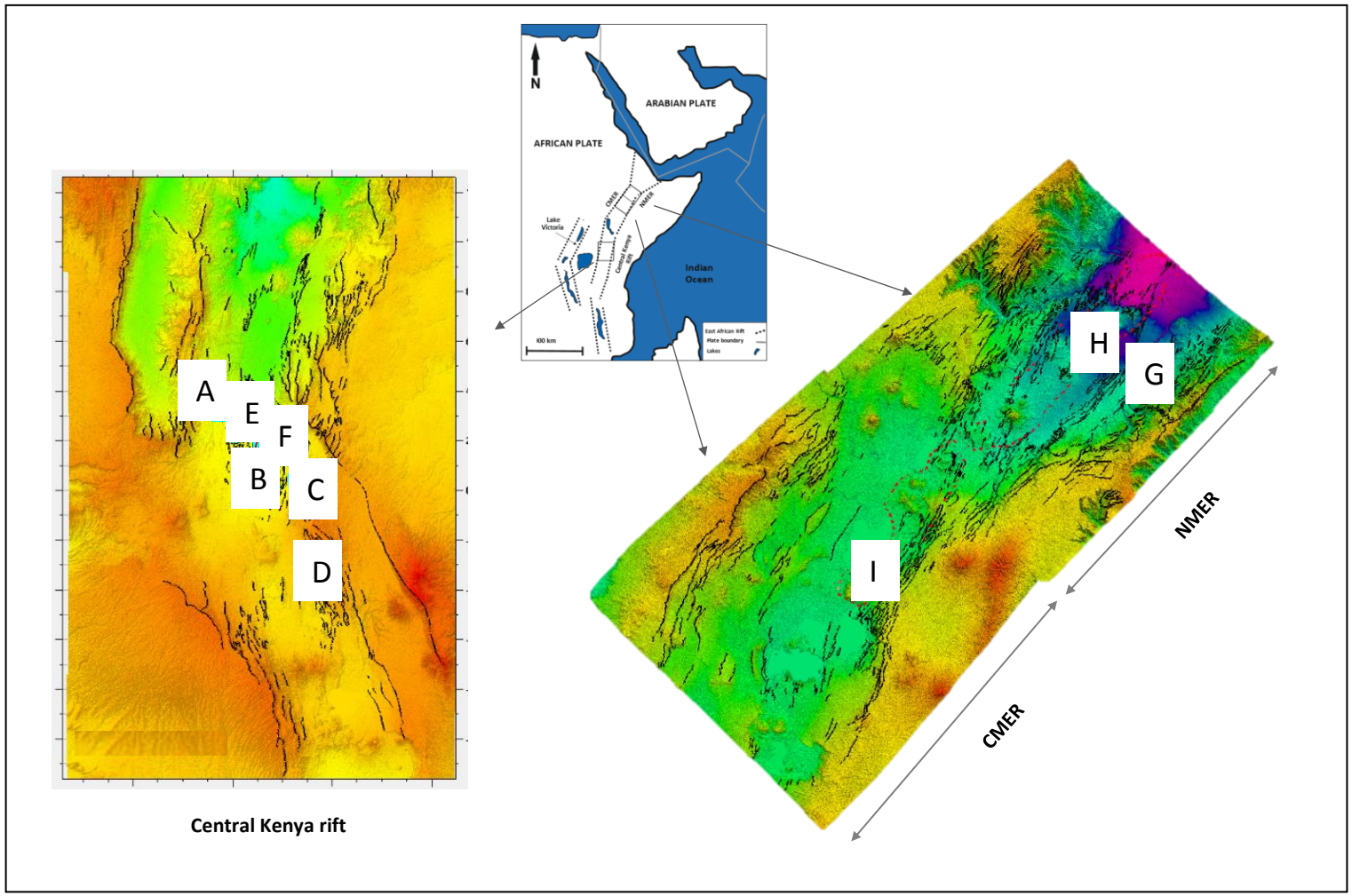

Figure 2.14 shows locations of examples of fault pickings showing Figure 2.15

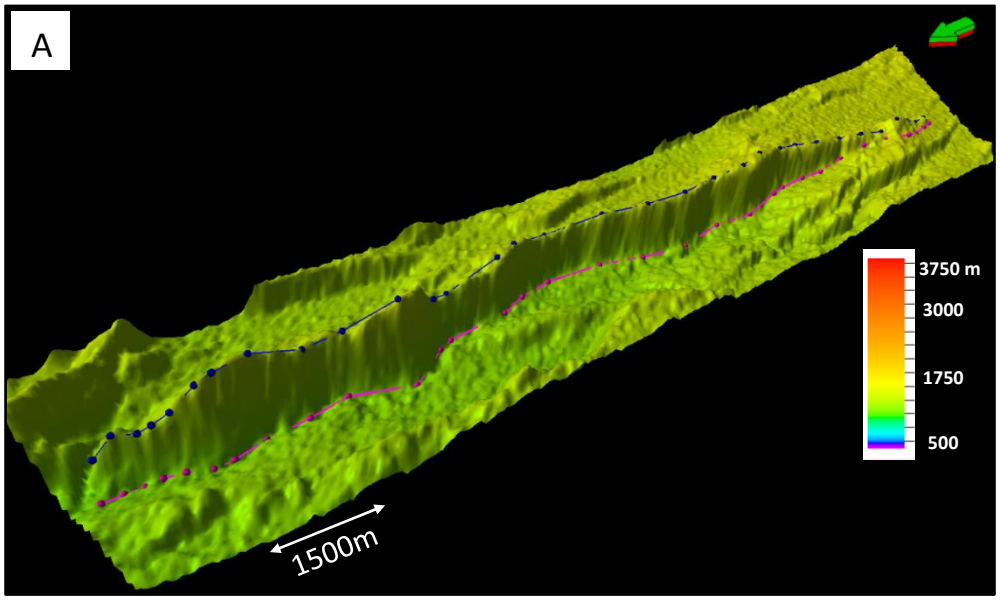

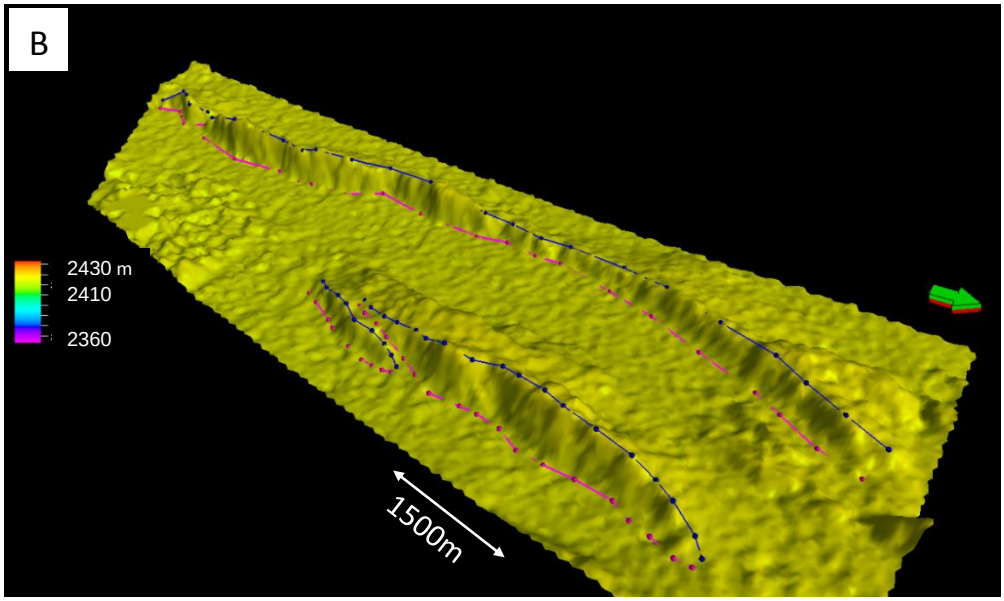

Figure 2.15 Examples of picks of fault foot-wall cut-off (blue line) and hanging-wall cut-off (pink line) on DEM surface, see for Figure **2.14** locations.

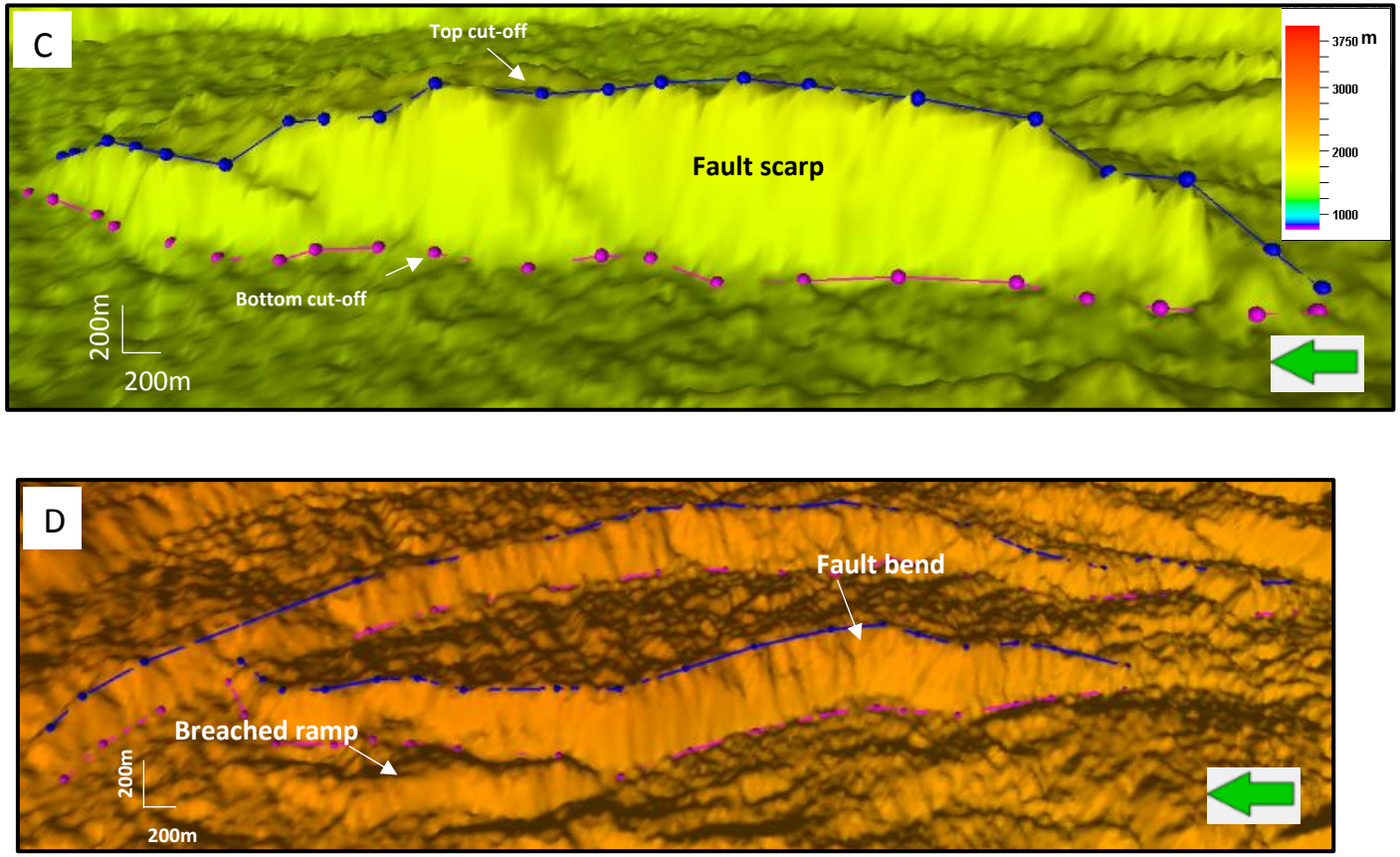

Figure 2.15 (continued)

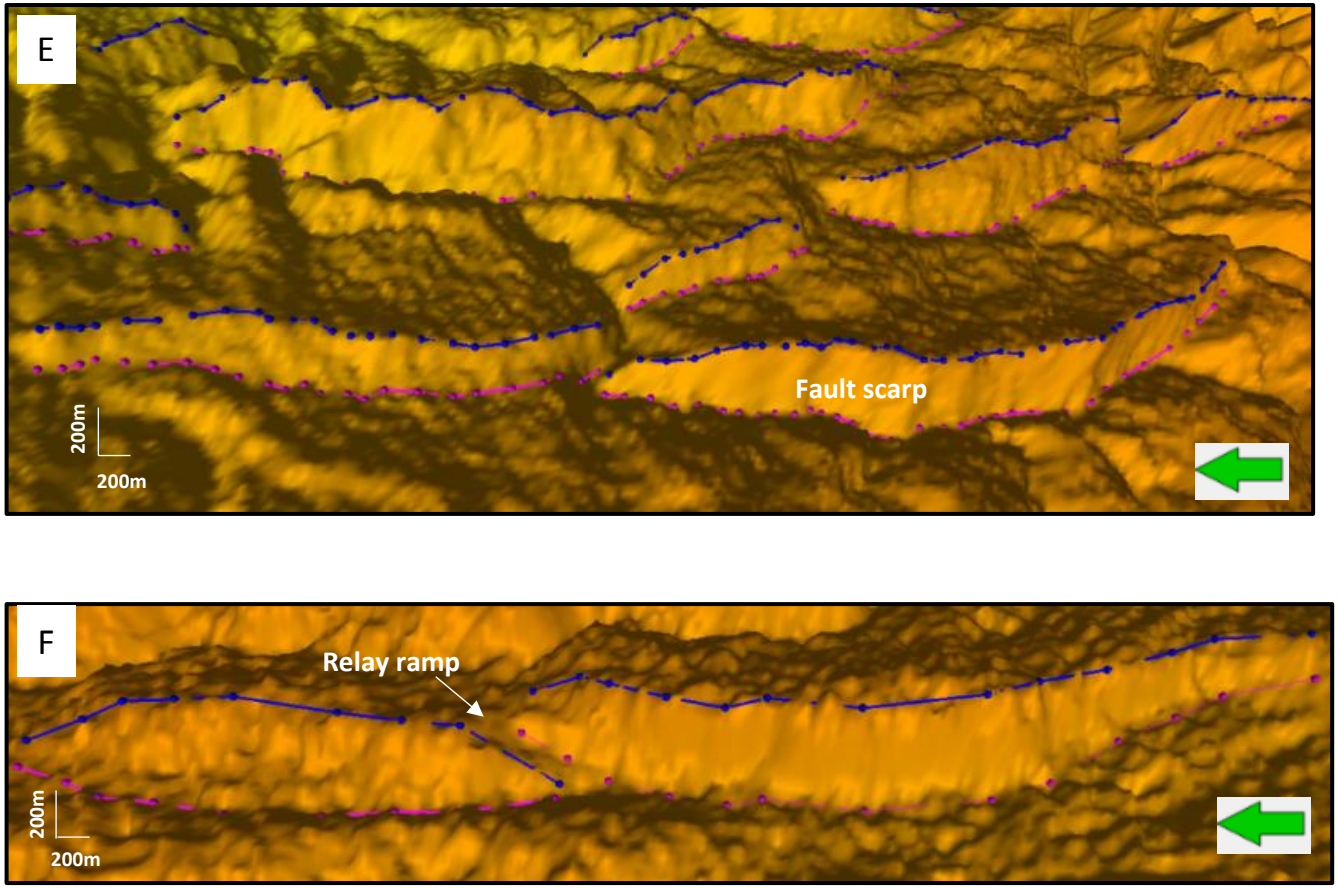

Figure 2.15 (continued)

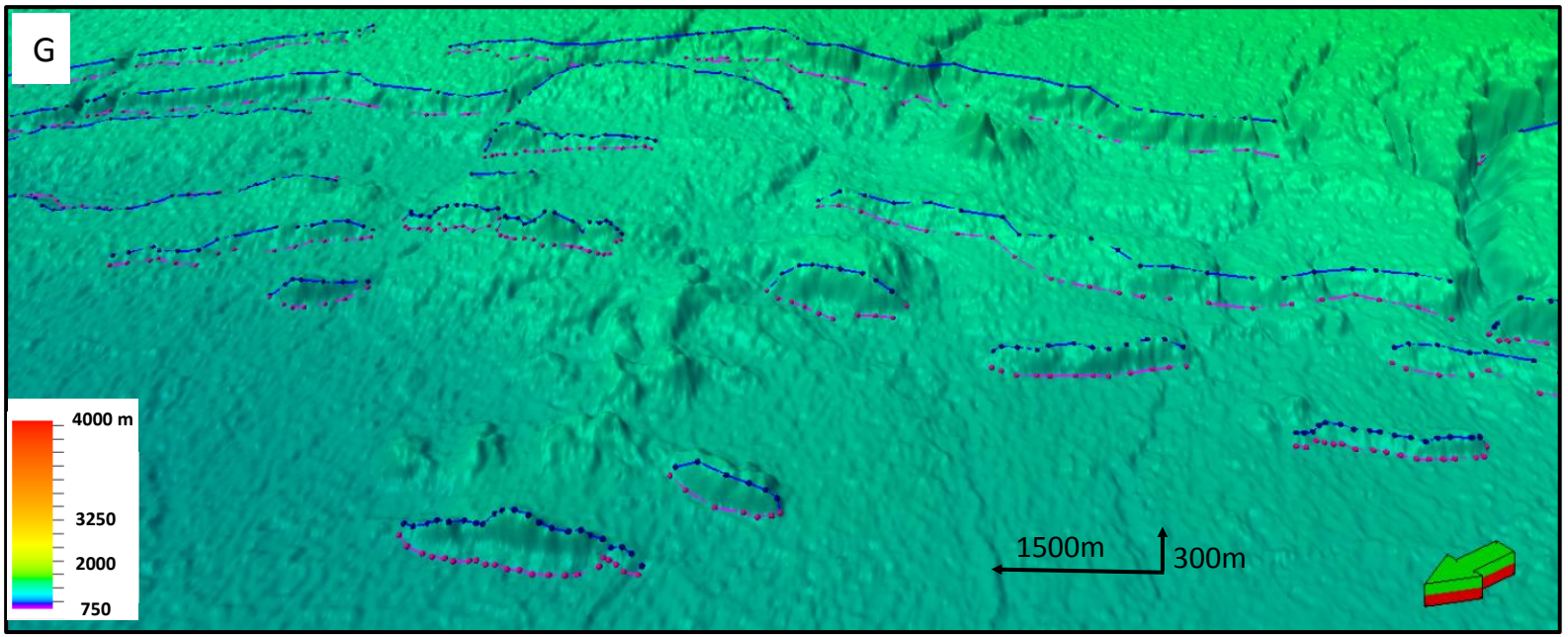

Figure 2.15 (continued)

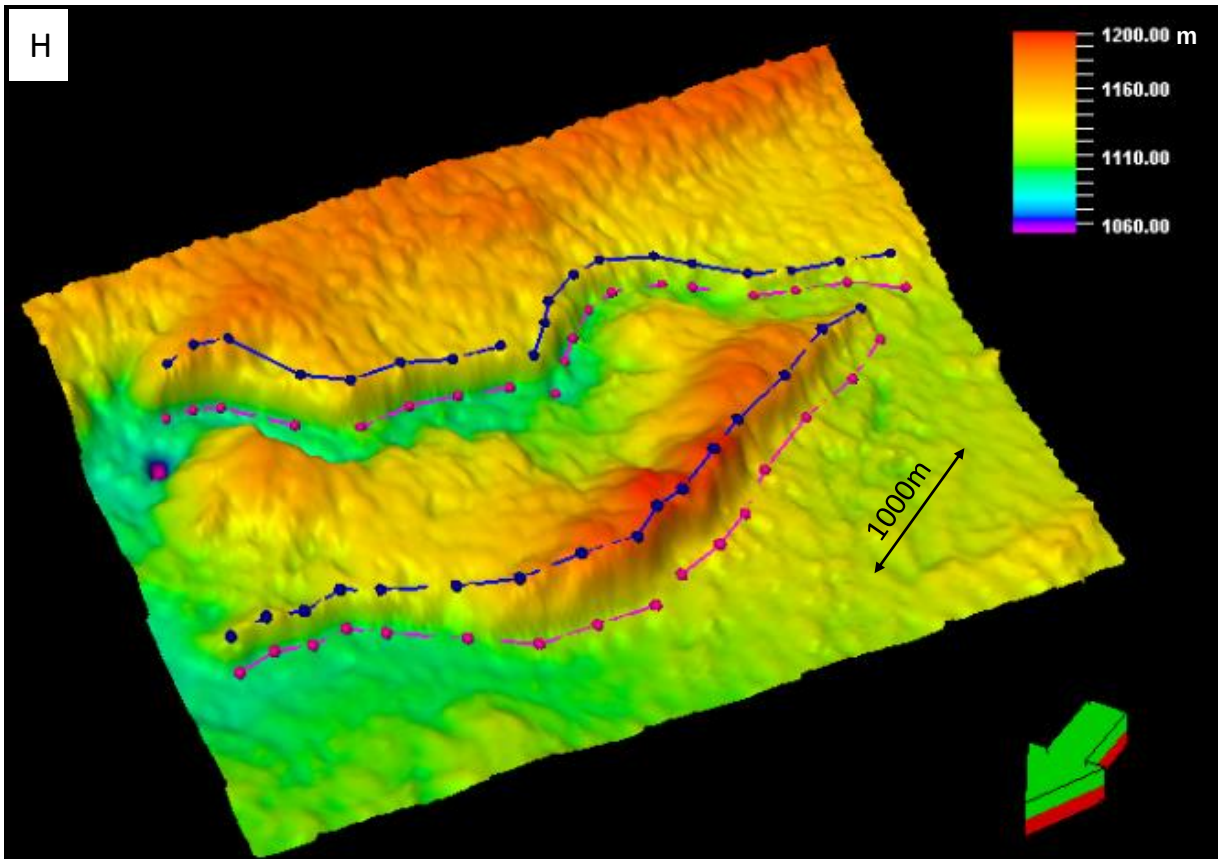

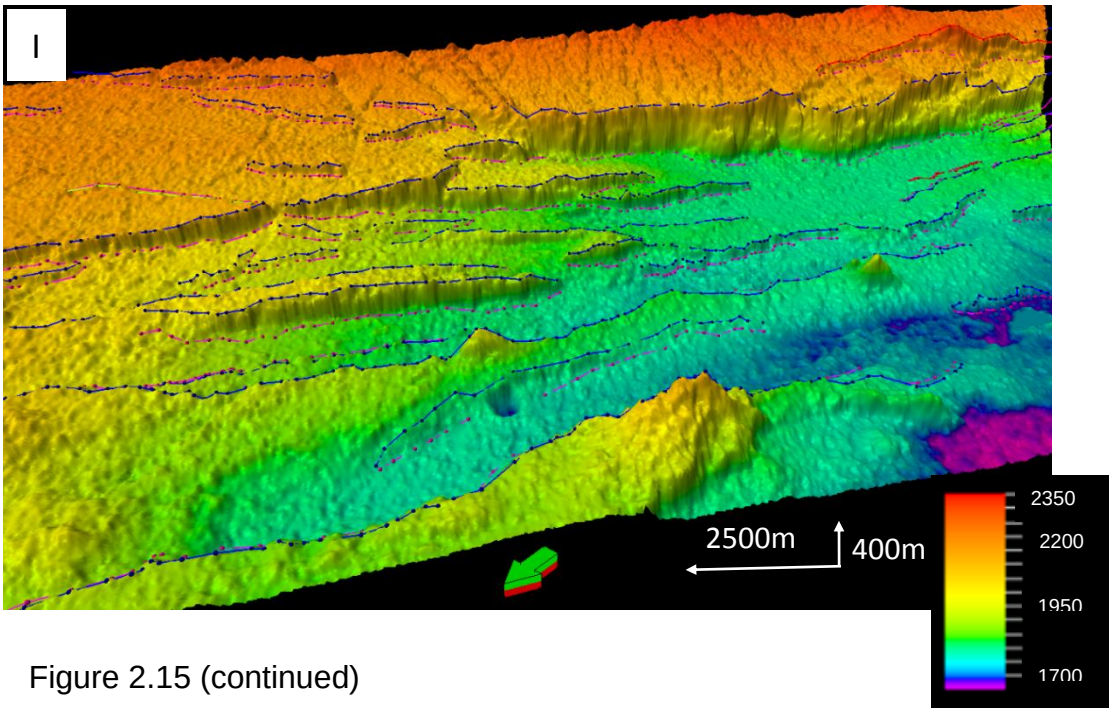

Figure 2.15 (continued)

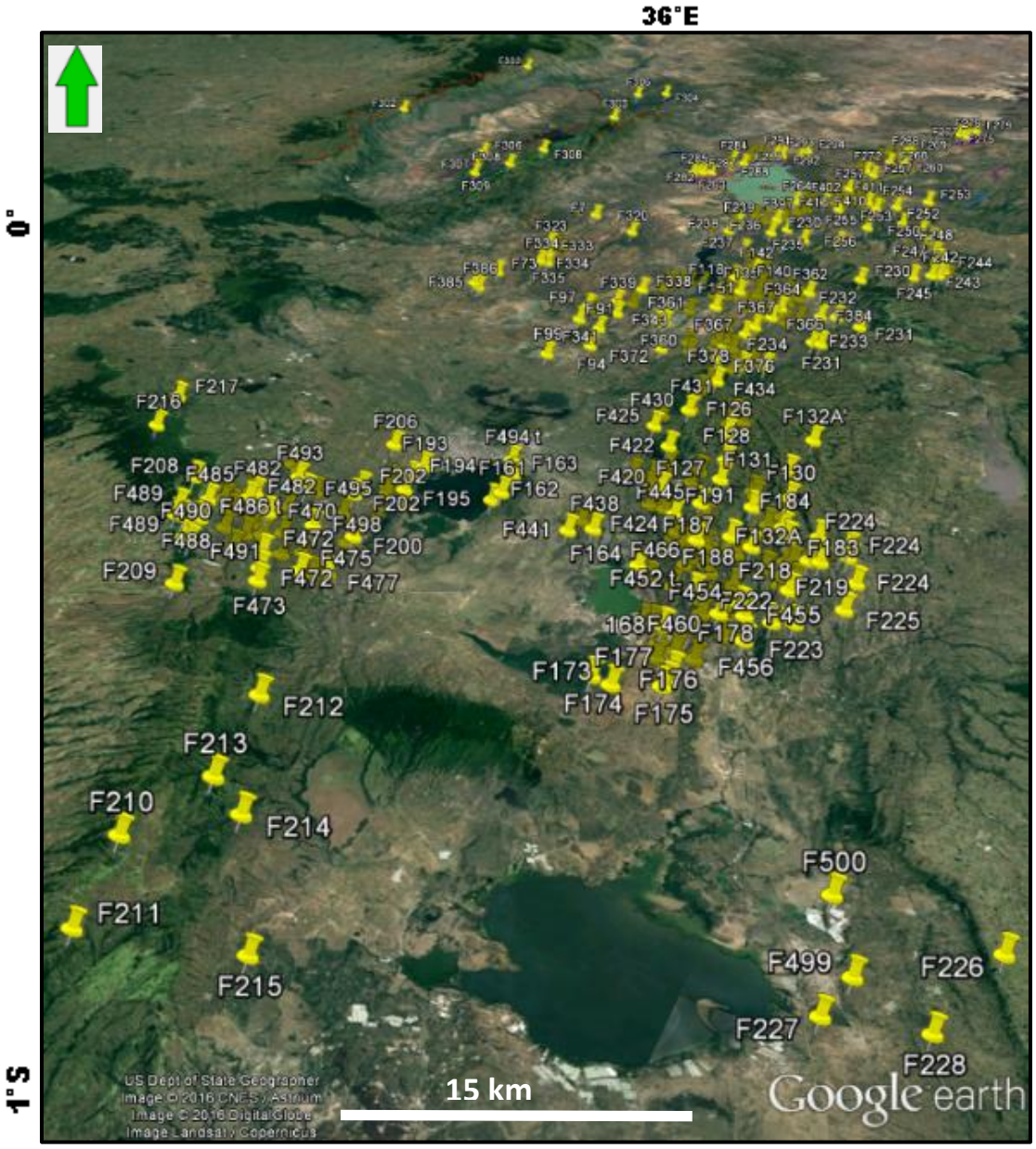

Figure 2.16. Google earth imagery used to verify fault scarps mapped from DEM

Chapte 3. Investigation of Rift evolution through examining scaling properties of fault populations within the central Kenya Rift

3.1 Introduction

Rifting is the process through which the continental lithosphere is modified by extension and related magmatic activity (e.g. Mariita and Keller, 2007, Corti, 2012). The central Kenya Rift is thought to symbolise a phase of an early continental Rifting (Baker and Wohlenberg, 1971) where the largest part of deformation being accommodated by boundary faults and almost absence of internal faults (e.g. Corti, 2009, Agostini et al., 2011b). The central and southern Kenya Rift segments formed along old zones of weakness at the contact between the Archean Tanzania craton and the Proterozoic Mozambique organic belt (e.g. Smith and Mosley, 1993, Mariita and Keller, 2007). Investigations into the surface deformation are crucial to understanding of processes associated with active regions. The investigation carried out in this chapter is part of a wider research effort that aims to understand evolution of extensional faults and how they relate to evolution of continental Rifting in three areas of the east African Rift system EARS, namely, the central Kenya Rift, the central main Ethiopian Rift (CMER) and the northern Ethiopian Rift (NMER). The purpose of this investigation is to contributing to the current knowledge of the north to south Rift propagation of continental Rifting in the east African Rift system EARS. Digital Elevation Model DEM with 30m horizontal resolution and Google Earth images are the main data used in this study to produce a detailed fault geometry dataset for surface faults defined

from DEM surface. 620 faults have been manually mapped using the methodology described in section (2.2.2). This part of the central Kenya Rift has been divided into three subzones of fault population (zone 1, zone 2 & zone 3) based upon their average range of fault orientations as NNE, NNE to NNW and NNW respectively. Therefore, using this new dataset of fault size attributes acquired from DEM data, this chapter quantitatively investigates fault scaling relations of three different fault populations within the central Kenya Rift in order to characterize the behaviour of fault growth and quantify the strain distribution along this region. Moreover, this chapter also tests the hypothesis that have been stated in chapter 1 (section 1.2) that the extensional strain increases from south to north.

3.2 Study area

The spatial extent of this study covers a portion of the central Kenya Rift located between Lat -1^0 to 1.05^0 and Long 35.5^0 to 36.7^0 that covers 240x150km of land, including Kerio and Baringo grabens in the north and Gregory graben in the centre and moving down to the southern part of the Rift at Nakuru- Naivasha basins (Figure 3.3).

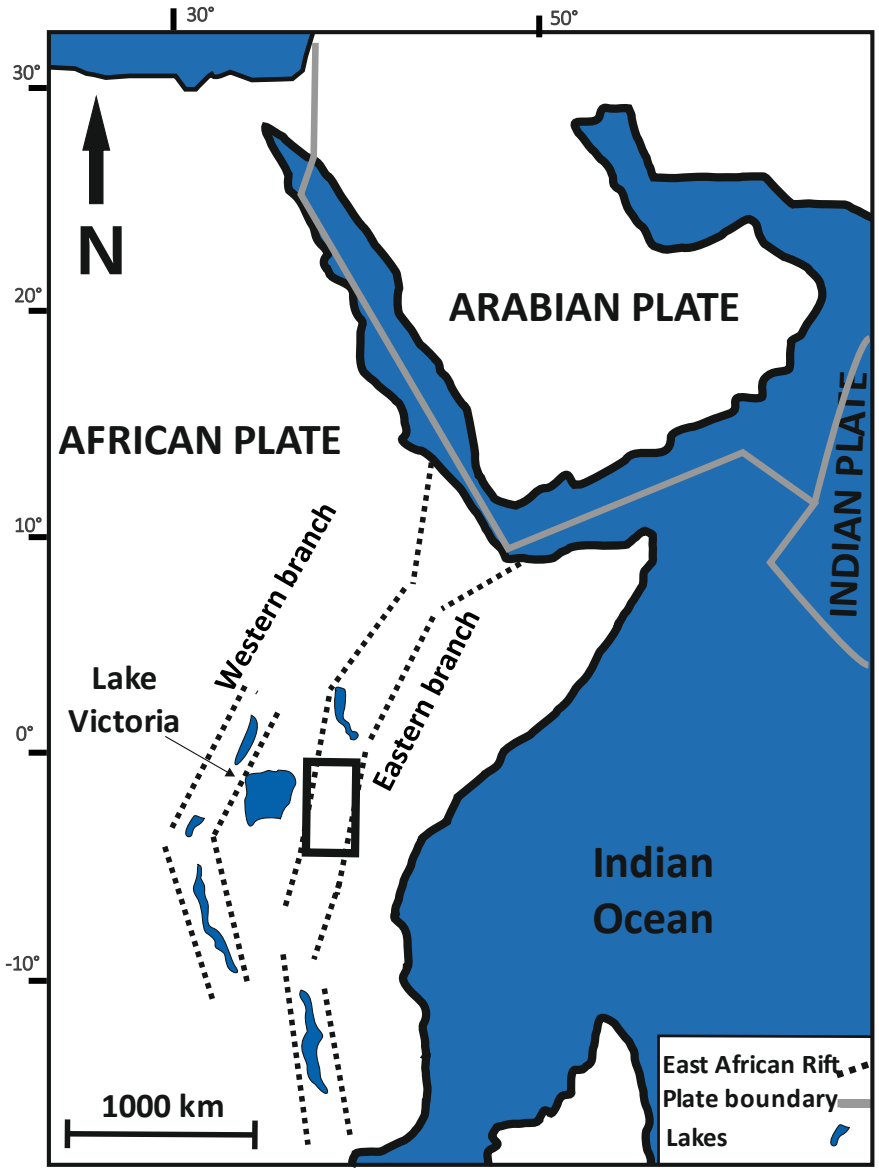

Figure 3.1: Location of study area (black rectangle)

3.3 Geological setting

3.3.1 Tectonic and Geology of the central Kenya Rift

It has been widely demonstrated that continental Rifts are not arbitrarily distributed but instead Rift segments are incline to propagate following the trend of inherited weaknesses of pre-existing fabric of the lithosphere (such as ancient orogenic belts) and avoiding stronger formations (Versfelt and Rosendahl, 1989, Petit and Ebinger, 2000, Ziegler and Cloetingh, 2004). The structure of the central Kenya Rift (Figure 3.2) follows the general north–south trend of the Mozambique mobile belt, and its location governed by the boundary between two contrasting types of lithosphere; the Archean Tanzanian craton and the Proterozoic Mozambique belt, the major boundary faults were also controlled by the older structure (Hetzel and Strecker, 1994, Smith and Mosley, 1993). Therefore, the extensional deformation can be localized along mobile belts and suture zones as they tend to be weaker than the surrounding areas (Petit and Ebinger, 2000).

Volcanism and Rifting started in the Kenya Rift around the early Miocene in the north in the Lake Turkana area and migrated southwards being active from around middle to late Miocene in the central segment (Baker et al., 1972, Smith and Mosley, 1993). The chronological fault formation in the central Kenya shows that the minor tilting and faulting happened after a basalt eruption in the central Kenya Rift at around 15 Ma, whereas, major faults were first formed between 12 and 7 Ma along the western flank of the Rift and dipped E-NE, and perhaps concurrent with major border faults dipping E along the Elgeyo and Nguruman escarpments (Jones and Lippard, 1979, Baker et al., 1988). The brittle crust is predominantly comprised of post-Miocene lavas,

the thickness of volcano-sedimentary infill in this region is ~4.5-5km (Hautot et al., 2000). The evolution of the Kenya Rift is thought to be influenced by the Precambrian basement structure, this Rift system developed on a strongly heterogeneous basement, exhibiting a series of Late Proterozoic, regional-scale NW-SE and NS trending ductile/brittle shear zones, which exist in the lithosphere beneath the Kenya Rift, and these pre-existing faults and shear zones represent a mechanical weakness both at upper and lower crustal levels (Daly et al., 1989, Maurin and Guiraud, 1993, Mosley, 1993). The Precambrian basement within the Rift valley is not exposed due to the cover by post-Miocene lavas, but it is well evident outside the Rift.

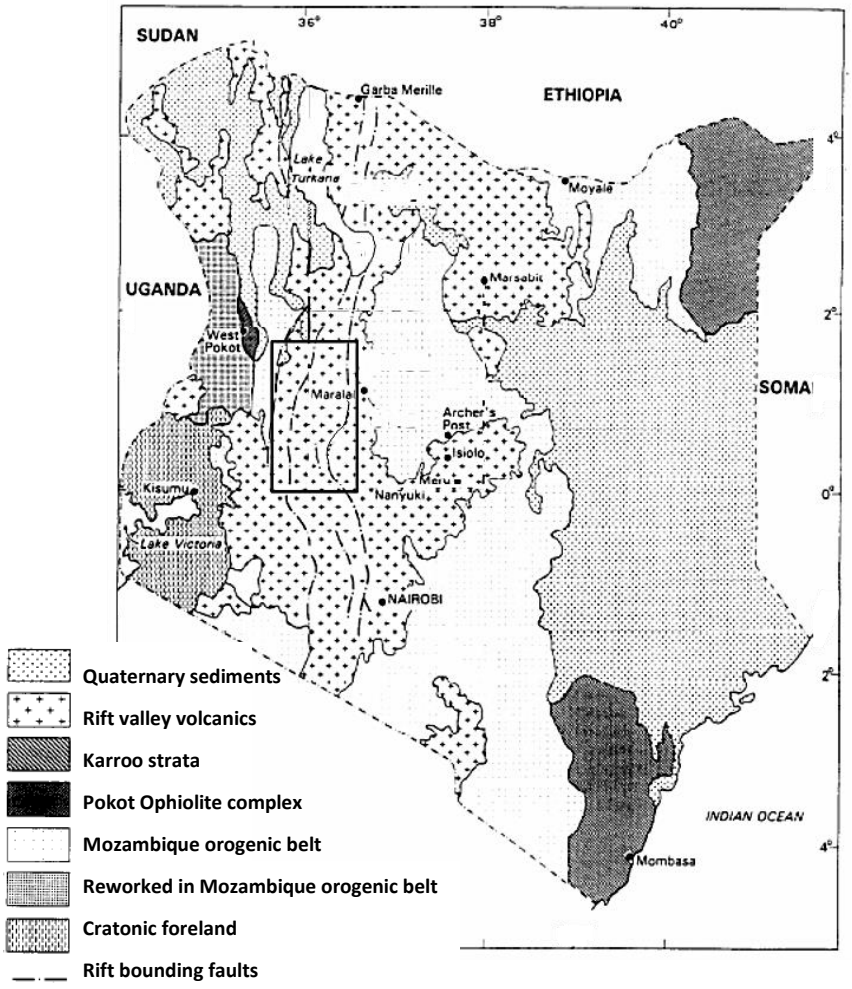

Figure 3.2 Map showing the geology of Kenya with study area showing in a rectangle after (Key et al., 1989).

3.3.2 Fault structure

The Kenya Rift is bounded by major normal faults forming the Nguruman, Mau, and Elgeyo escarpment on the western boundary and the Aberdare escarpment that escarpment constitutes the eastern boundary of the Kenya Rift (Figure 3.3). The Kenyan Rift follows the general north–south trend of the Mozambique Mobile Belt structure (Ebinger, 1989b) and corresponds to the Kenyan dome (Baker et al., 1972). The northern part of the central Kenyan Rift comprises two parallel Rift valleys at an elevation of 1050 m, the eastern Rift is known as the Kenyan Rift and the western one is called Kerio Rift, separated by the Kamasia horst and both orienting $N10^0E$ (Figure 3.3). Both Rift basins are west-dipping half-grabens, with major border faults at the Rifts shoulders, the Kerio Rift terminates west of Lake Bogoria, while the Kenyan Rift continues farther to the south and bending sharply at the Gregory Rift (Figure 3.3), this bend has been interpreted as the intersection with a large NW trending basement structure known as the Aswa lineament (Smith and Mosley, 1993, Chorowicz, 2005, Omenda, 2010).

The central segment of the Kenya is known as Gregory Rift (Figure 3.3) and is a complex graben that trends N-S along. It is 60 -70 km in width and bounded by en echelon arrangements of major normal faults. Fault escarpments are well defined and reach up to 2000m in height (Baker and Wohlenberg, 1971). This graben displays variety of orientations ranging from NNE-SSW to NNW-SSE (Smith and Mosley, 1993). The east-northeast-dipping normal faults was followed by antithetic faulting on west- and west-southwest-dipping normal faults concentrated along the Aberdare escarpment that had been formed by about 5.5 Ma (Baker et al., 1988) and converted the initial half graben into a full graben (Strecker et al., 1990). Overall, the

tectonostratigraphic evolution of these Rift sectors shows a successive migration of normal faulting from the boundary faults inwards toward the Rift valley , where the structural development has been characterized by a concentration of faulting associated with volcanism since late Pliocene era (Baker and Wohlenberg, 1971). Extensive step-fault platforms happen locally at both sides of the graben, the Rift valley also encompasses step-fault platforms and ramps (Griffiths, 1980). The major faults in the central Kenya Rift are antithetic in style and dominantly dipping eastwards (Baker and Wohlenberg, 1971, Baker et al., 1972).

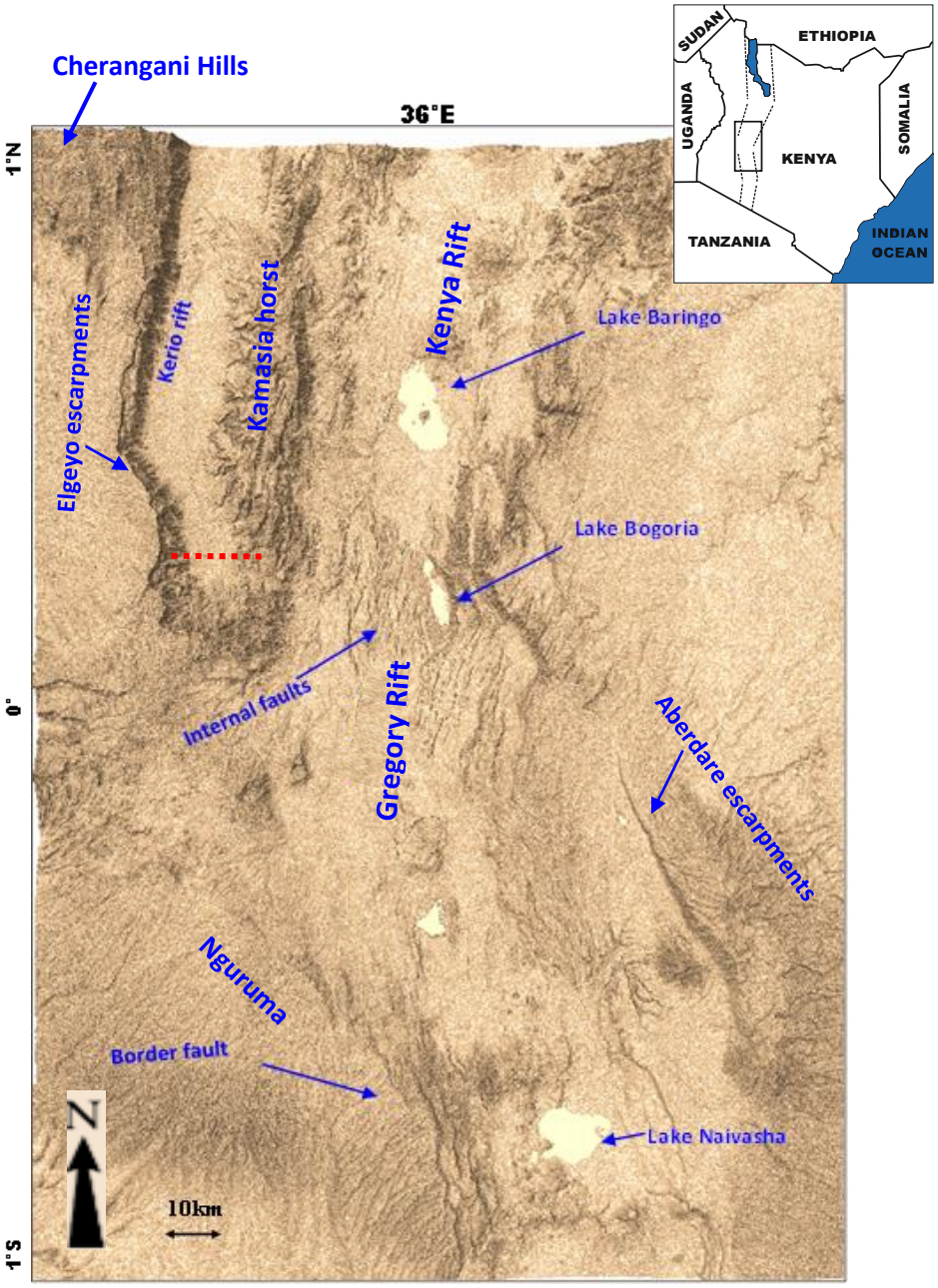

Figure 3.3: 3D shaded relief surface image generated from ASTER DEM, dashed red line is location of seismic line (see section **3.7.11**)

3.4 Method and Data Collection

The methodology used for data collection in this study area is described in detail in chapter 2 (section 2.2.2). Digital elevation models DEM combined with satellite images (i.e. Google Earth) are the main data used to create shaded relief surfaces for the study area in order to capture fault traces and measure fault lengths and throws as described in chapter 2 (section 2.2.2). A published geological map of Kenya (Survey of Kenya. 1959) was also used to compare faults identified from DEM with published ones. Fault attributes such as length, throw, fault orientation, aspect ratio (D\L), and position within the Rift have been obtained and analysed in the current chapter for a dataset of 620 fault traces from the central Kenya Rift.

3.5 Fault populations in the central Kenya Rift

3.5.1 Zones of fault populations

The study area was divided into three zones of fault populations based upon differences in the range of fault orientations in each fault population, initially visually observed. These sub areas are referred to as zones in this study (zone 1, zone 2 & zone 3) (Figure 3.4). The different fault orientations were afterward confirmed by the rose diagrams of the fault trends (Figure 3.4). there showed that fault population in zone 1 in the north of the study area is dominated by NNE striking faults, and fault population in zone2 in the central of the Rift is characterised by NNW to NNE fault trend, whereas zone3 in the south is characterised by NNW striking fault system. Chapter 5 discusses in detail the different fault orientation in relation to possible influence from the basement structure.

Therefore, to insure consistency for further analysis, three rectangles with the same area size of 62x90 km were drawn surrounding each zone based upon the range of fault orientation they display, these rectangles were defined perpendicular to the average strike of fault population in each zone (Figure 3.4).

The number of resolved faults within the study area varies, where the biggest number of faults are found in zone 2 with 295 faults concentrated in the Rift valley , followed by zone 1 that contain 149 faults, while zone 3 encompasses (177) faults.

The mapped faults were superimposed on the geological map of Kenya, which shows that the picked faults matched reasonably well with most major faults in the published map (Figure 3.5). Lack of complete correspondence is attributed to differences in resolution between the DEM data and the published geological map, where the first is 30 mx30 m resolution data obtained from recent remote sensing techniques and the latter is 1:3,000,000 map scales created in the year of 1959 using simple cartographic methods. Nevertheless, sampling errors could still be associated with both methods of mapping faults.

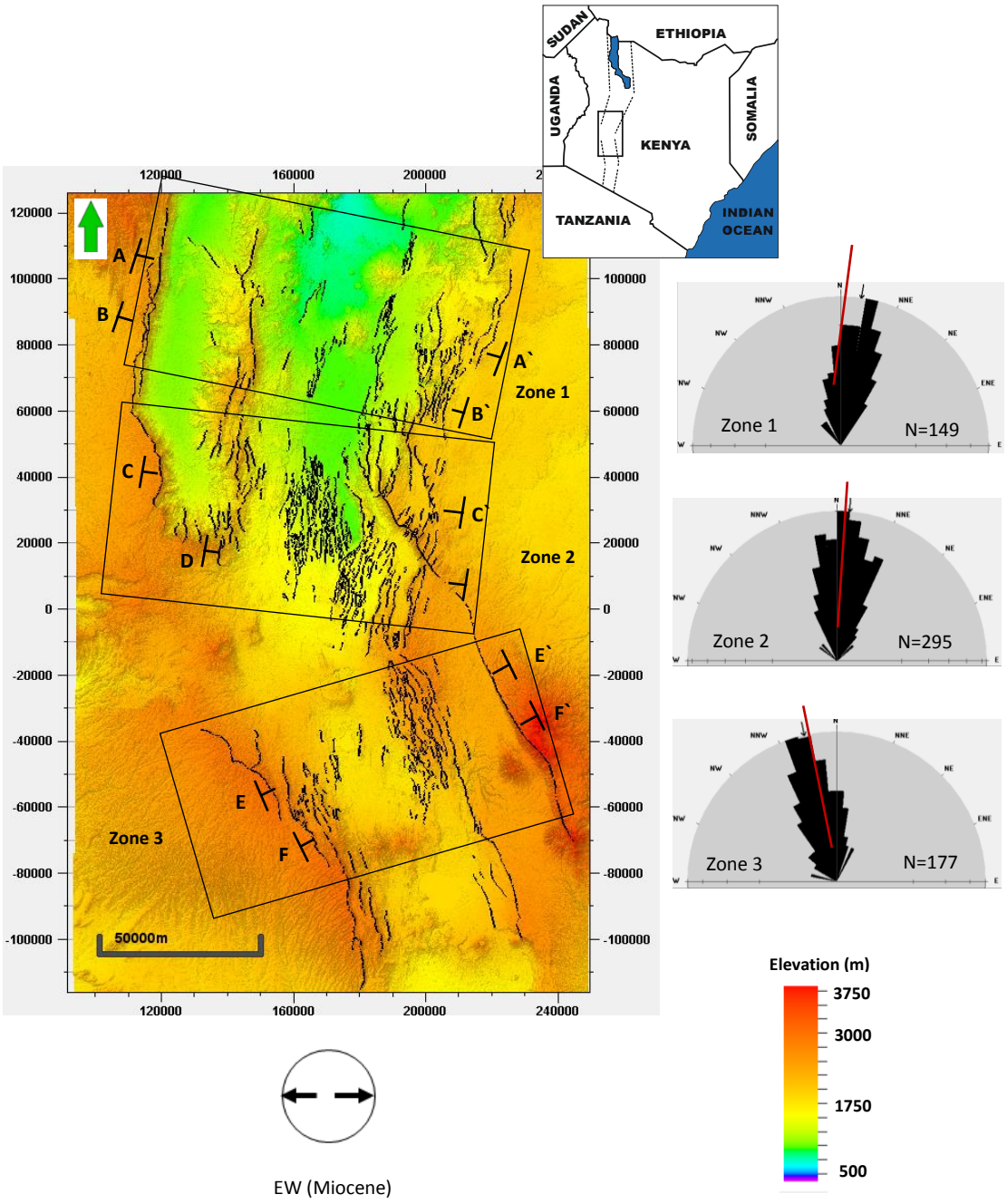

Figure 3.4 : The three zones defined within study area, cross-sections, opposite black arrows indicate extension direction and rose diagram with red line shows mean fault arrays orientation and dashed navy opposite arrows show least horizontal stress perpendicular to mean fault orientation (see section **3.5.2**).

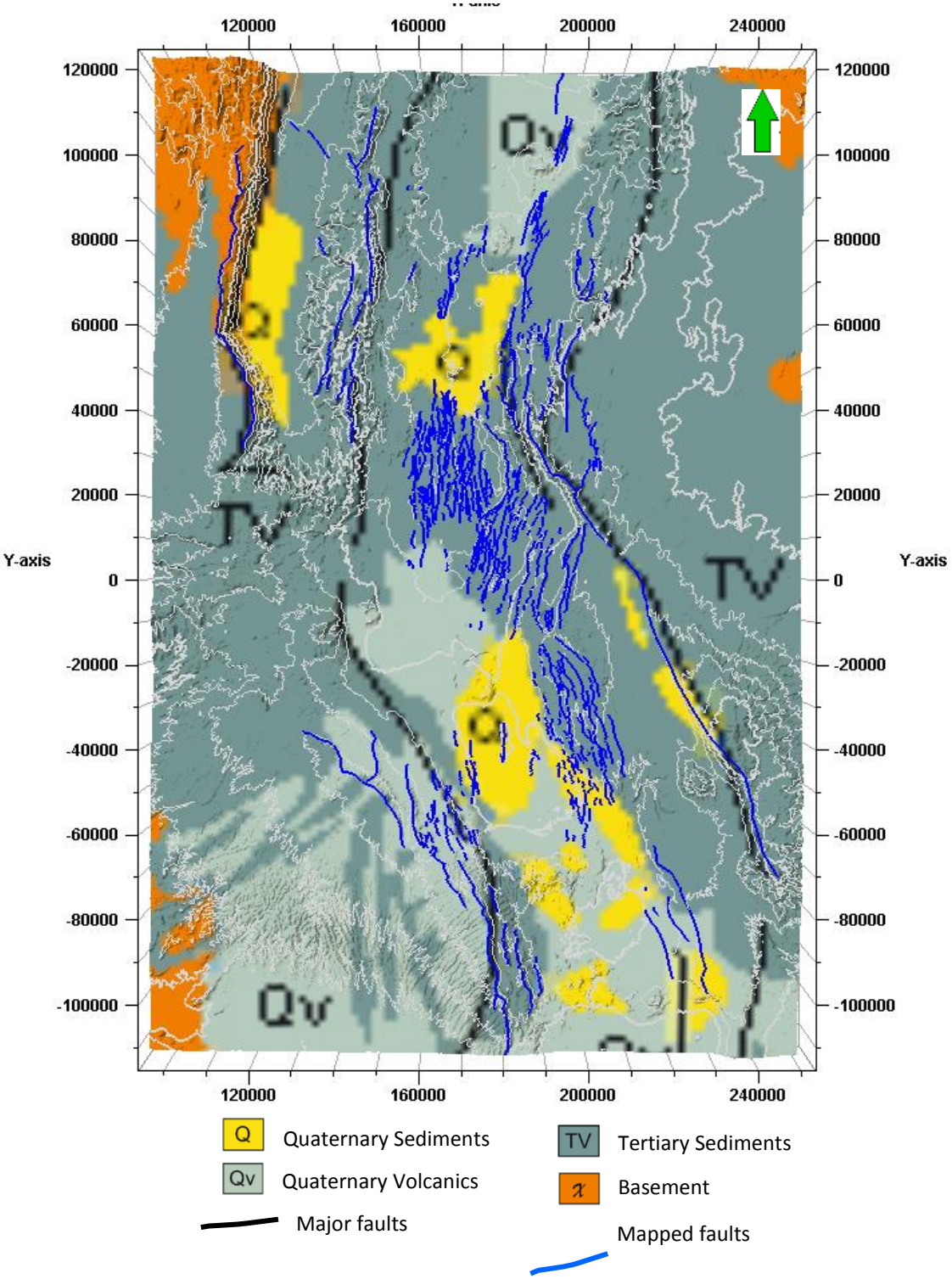

Figure 3.5: the 620 fault mapped in study area are shown in blue overlaying a geological map after Survey of Kenya. 1962

3.5.2 Fault geometry in the three zones

The 149 faults mapped in zone 1 in the north are characterized by a dominant NNE fault orientation with fault trace length ranging between 737– 47237 m and an average of 5162 m. The extent of the fault throw is 26 - 1561m with an average of 173 m. The Elgeyo fault escarpment (Figure 3.3) appears to be the only border fault forming the left shoulder of the Rift from the west that appear well developed in terms of fault linkage, whereas the eastern shoulder show relatively shorter parallel or subparallel en echelon patterns of border faults that form areas of interaction (Figure 3.6 & Figure 3.7e).

In the central part of the Rift (zone 2) faulting affects largely the Rift depression where patterns of fault interaction and linkage are observed, while deformation in the north (zone 1) and the south of the study area (zone3) is concentrated on the Rift margins (Figure 3.4). This reflects a different distribution of the brittle deformation across the Rift structure. In zone 2, the internal faults, are higher in number than the border faults, and the total number of faults mapped in this zone is the largest of all (295 fault) as opposed to zones 1 and 2 (Figure 3.4). Fault orientation of fault population in zone 2 straddle between NNW and NNE, with a range of fault trace length of 272- 46751 m and an average of 4583 m. The throw extends from 22 m to 1561 m with an average of 121 m.

The dense internal faults found in the Rift valley within zone2 are closely spaced and organized in en-echelon style, and exhibit different patterns of fault growth by segment linkage and relay ramp structures; (Figure 3.7a) shows faults that are physically overlap and begin to form open relay ramps, and linking the two fault segments in a soft linkage manner. Figure 3.7b exhibits another stage of fault interaction where two overlapping fault segments are

incipiently linked and start to break the relay ramp by through-going faults, the relay ramp in such a stage is referred to as linked relay ramp according to fault linkage model of Peacock and Sanderson (1991). A more evolved stage of fault interaction is shown in Figure 3.7c where the two overlapping fault segments propagate and fully linked by breaching or destroying the relay ramp, as by the reoriented fault segment tips, and the two fault segments are therefore hard linked. Figure 3.7d displays a fault trace that has fault bends that indicate a zone of former linkage but no remnants of breached ramps can be observed, all these observations are in accordance to fault linkage model by Peacock and Sanderson (1991). Moreover, some Y-shaped linkage structure have also been observed within the central zone (zone2), which forms when the relay ramp is breached through the propagation of the hanging-wall fault towards the footwall fault to produce two splay faults of similar length but different amounts of throw (Figure 3.7c).

Zone 3 in the southern part of the Rift is characterized by a narrower zone (20 km) of faults that encompass the fault population that dominantly strike NNW. Border faults in both sides of the Rift consist of a few large fault and a large number of shorter faults to the side of the Rift valley that appear to be in parallel and en-echelon structure (Figure 3.4) that exhibit signs of interaction and linkage, but there are not as clearly manifested as in zone 2 (Figure 3.7f). Comparing with zones 1 & 2, a small number of internal faults have been identified in the Rift valley from the total number of faults (177 fault) mapped in zone 3. These internal faults show a parallel pattern with a range of fault trace length of 629 -50477 m and an average of 4618 m, and vertical throw 24.0 - 1012 m and an average of 118 m.

Examples of topographic profiles (Figure 3.8) from three cross-sections (AA`, CC`& EE`) showed widening of the Rift valley and a gradual decline of elevation of the Rift from south to north, Rift valleys of Kero Rift and Kenya Rift in cross-section AA` for example representing lower parts of the Rift appear to more subject to fault scarp burial due to accumulation of erosional and volcanic sediments in them .The geological formations shown in the cross-sections depict extensive volcanic deposits of different ages along the Rift. Topography of the Rift valley decrease from 2000m in the south to 1000m in the north, this systematic decrease is interpreted to reflect increased lithospheric thinning and subsidence, as indicated by (Cowie et al., 2005).

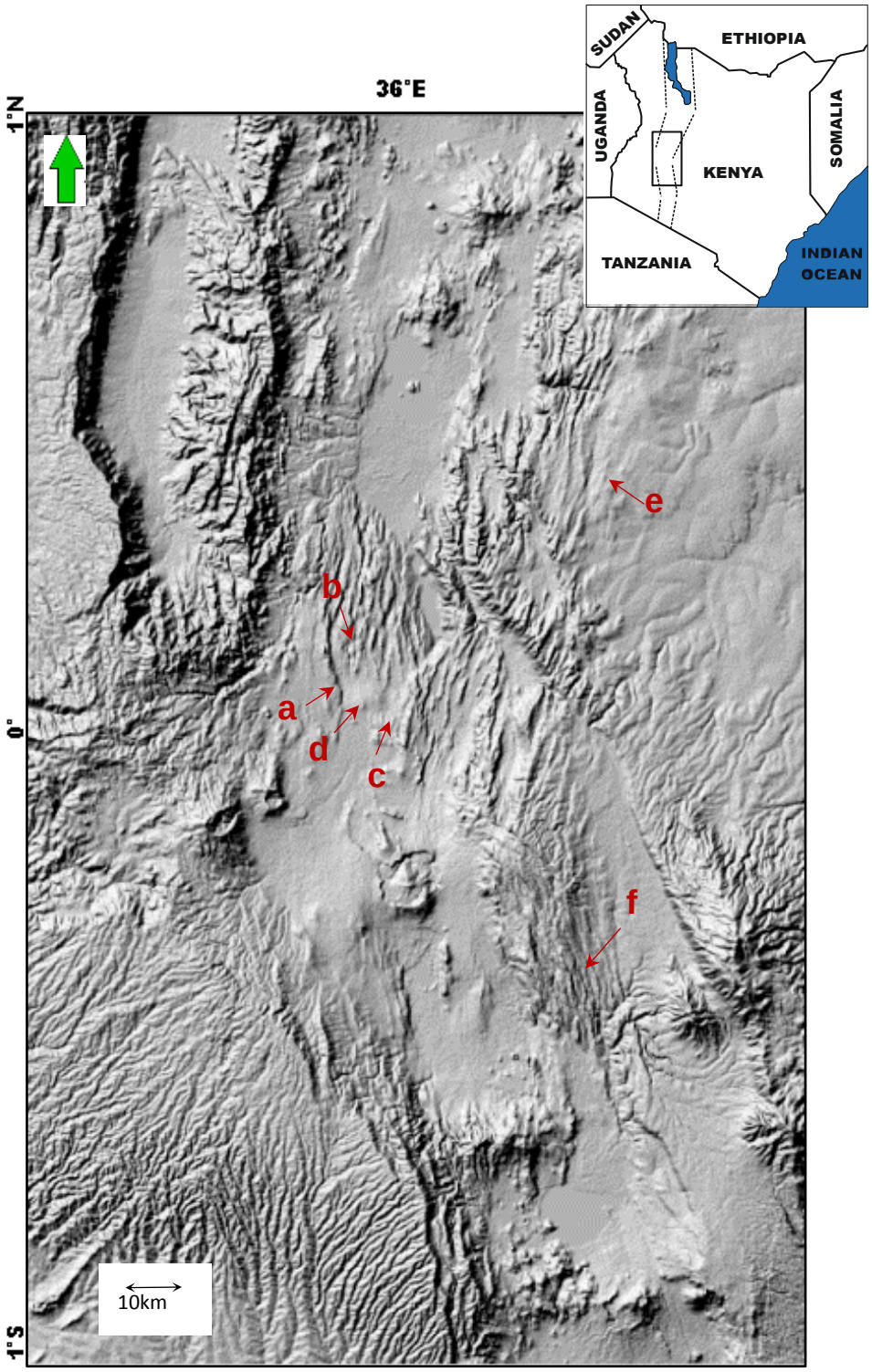

Figure 3.6: Locations of different stages of fault linkage, shown close-up in Figure **3.7**a - f

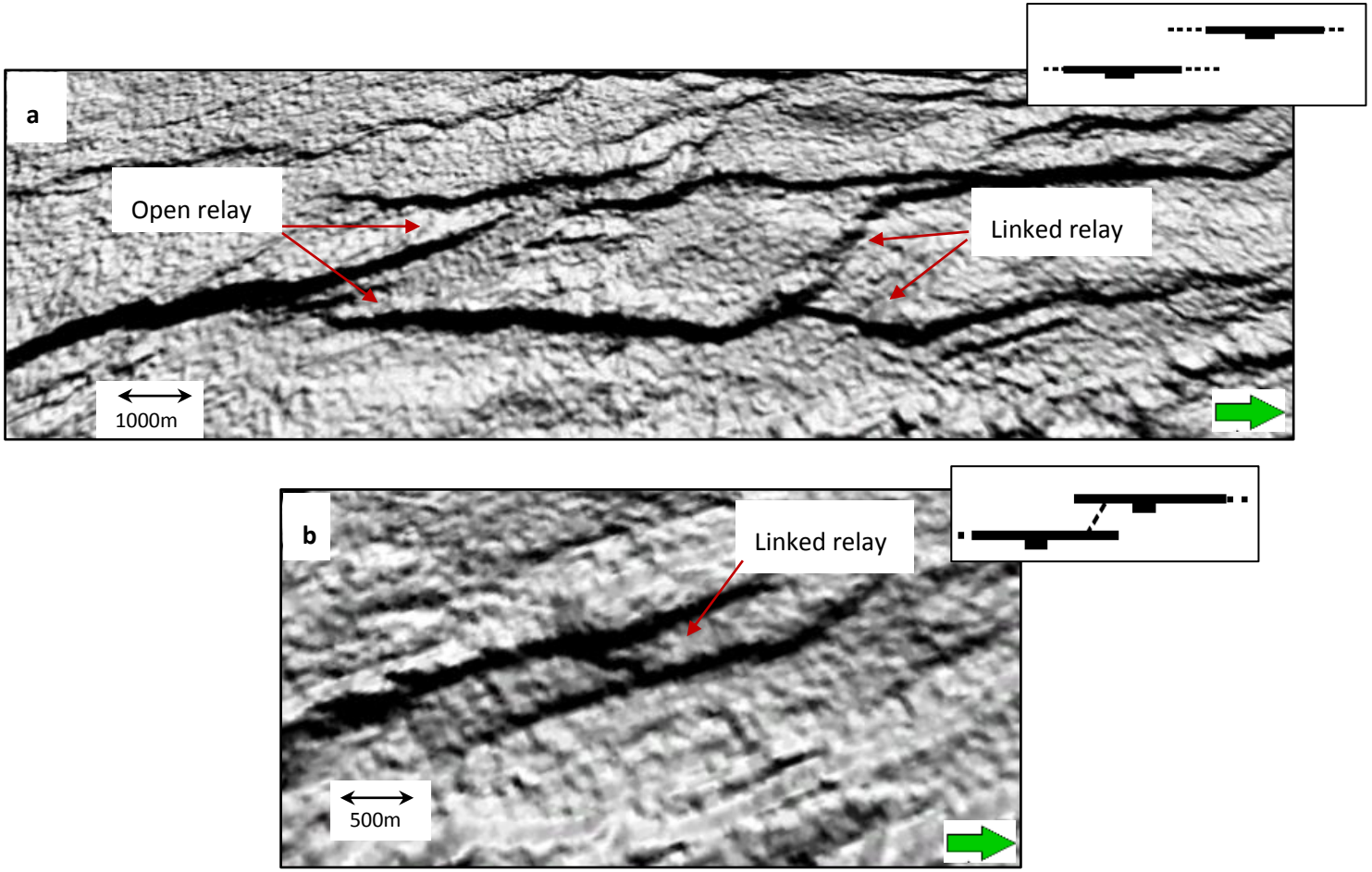

Figure 3.7. Different stages of fault linkage. (a & b) Open and linked relay ramps. (c) Breached the relay ramp. (d) Old fault linkage zone ramp marked by fault bend. (e) and (f) show parallel fault geometry with the absence of obvious fault interaction . Locations of interaction and linkage zones are shown in (Figure **3.6**).

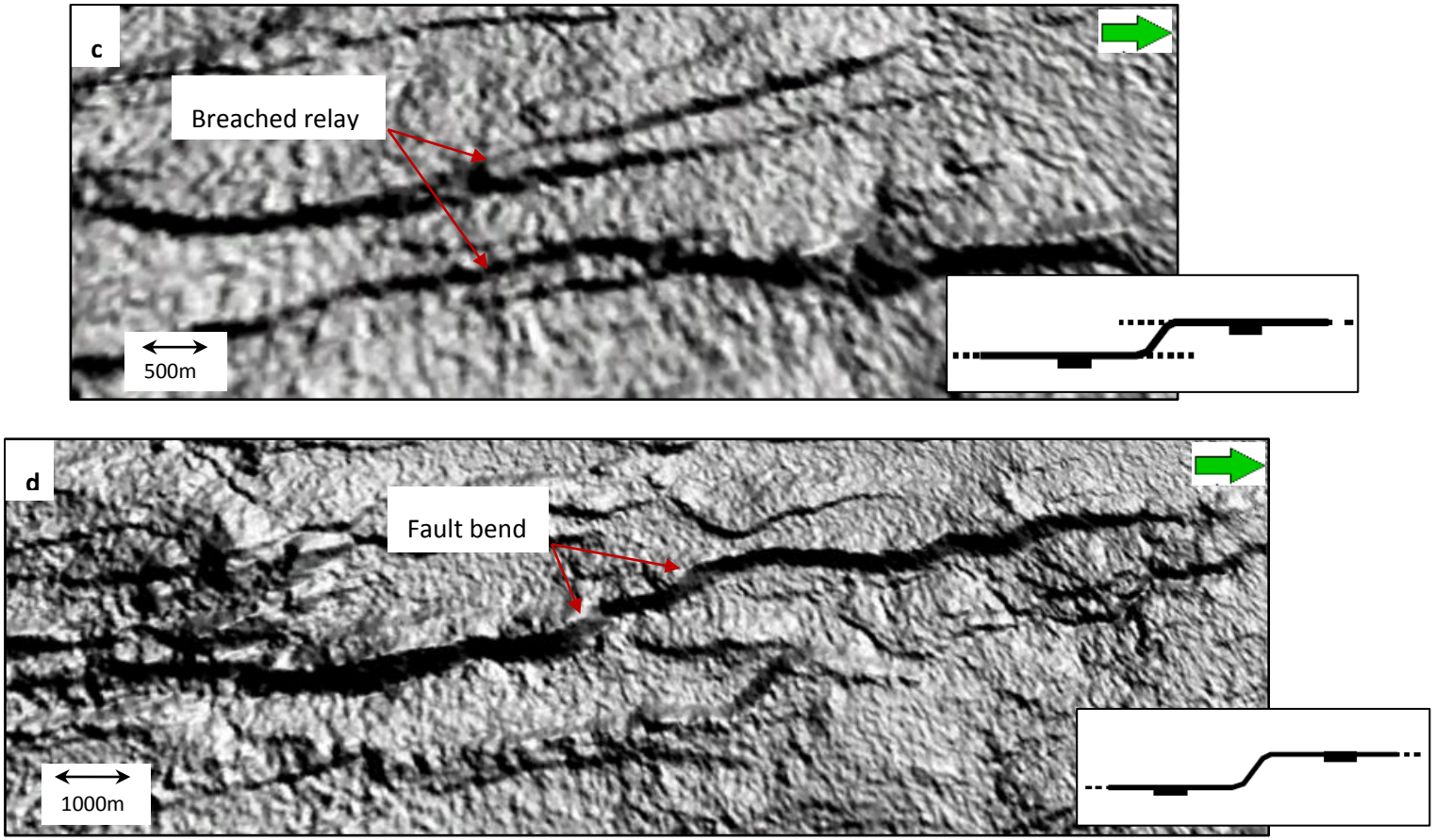

Figure 3.7 (continued).

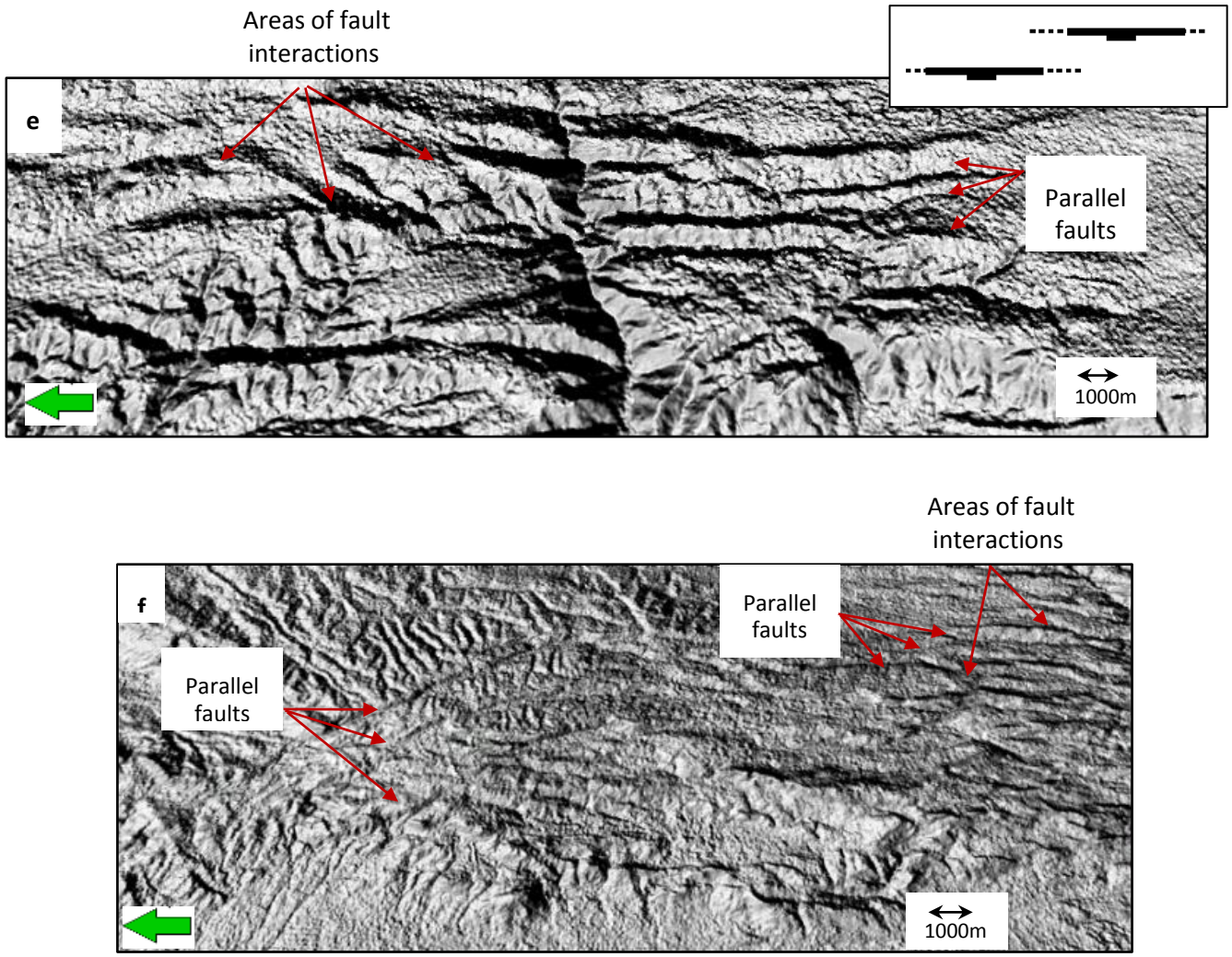

Figure 3.7 (continued).

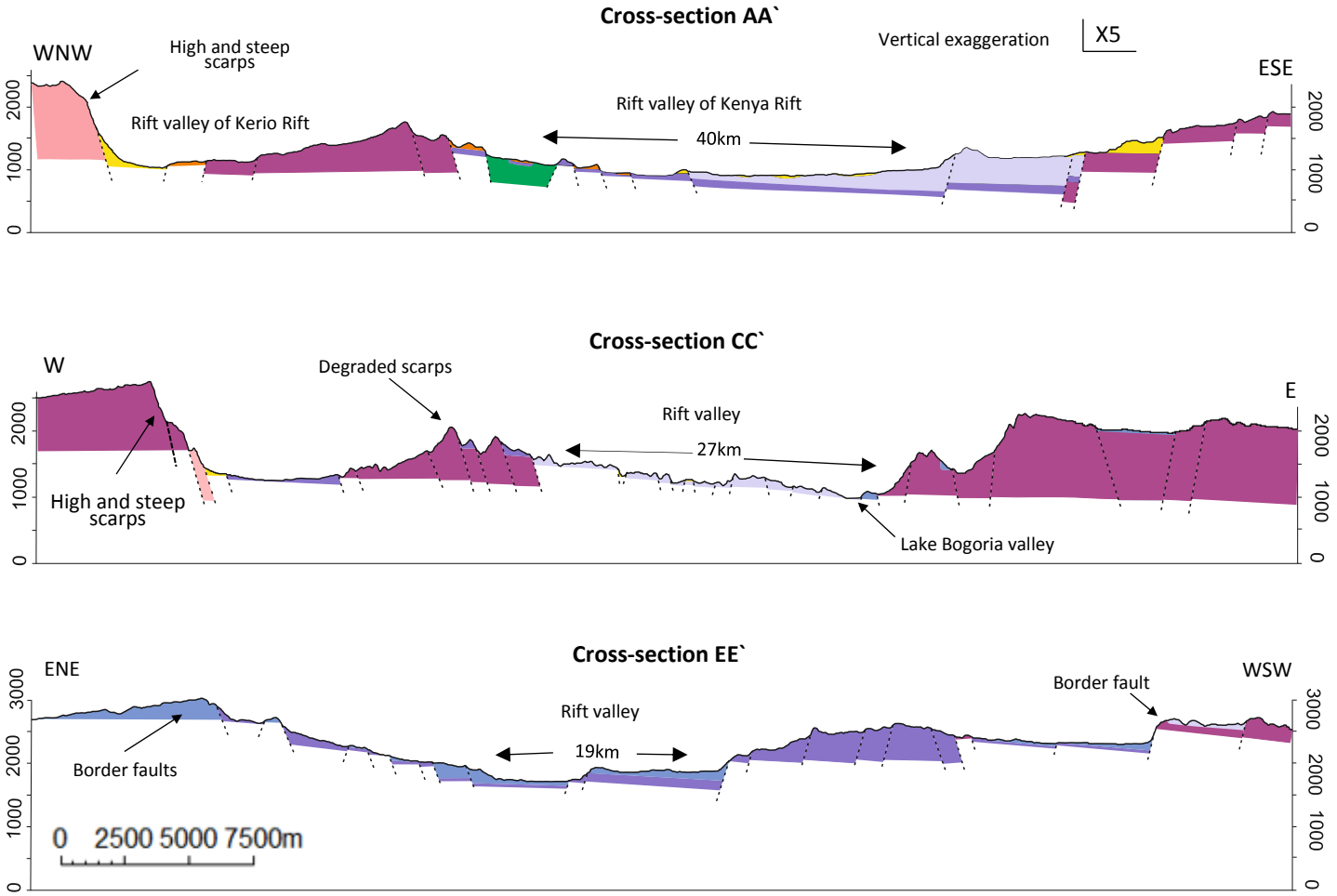

Figure 3.8 cross-sections AA`, BB` & CC` displaying the topographic profile, see Figure **3.4** for locations. Key of geological units is according to Geological map of Kenya (Ministry of energy of Kenya 1987).

Key for geological units shown in Figure 3.8

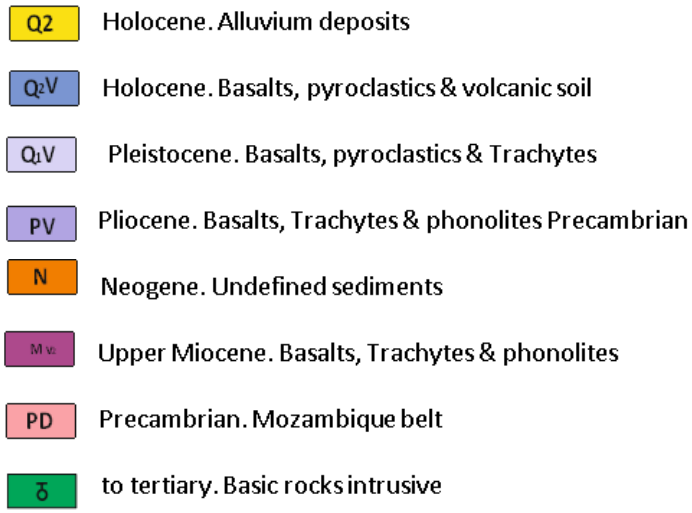

3.6 Strain accommodation

In order to understand the evolution of continental rifting, the way in which the strain is accommodate, has been examined in this section.

3.6.1 Strain estimations

The observed change in fault trend from south to north has inspired the idea to investigate these variations further by comparing the distribution of displacement and strain in the three zones. This section tests the first hypothesis that a northward increase of total strain exist in the study area (see section 1.2).

Extensional strain within the study area was examined along the Rift using cross-sections, and then the result of estimates were plotted together (Figure 3.10) to get a sense of the trend of the strain from south to north, and compare the contributions of different fault strike populations to the strain accommodation in the study area. Six cross-sections (shown as blacklines in Figure 3.4) were defined perpendicular to the average trend of fault population, across the study area, two cross-sections for each zone, cutting across ESE-WNW for cross-sections AA`, BB`, CC` DD` and ENE-WSW for cross-sections EE`& FF` shown in Figure 3.4 to estimate how much strain is accommodated at each zone.

In the absence of seismic data (apart from the one shown in section3.6.1) that would help better characterize fault offsets (heave and throw) (Figure 3.9), and in the presence of erosional and depositional sediment accumulating at the base of fault scarp and reducing the actual throw, the extensional strain has been estimated through both total heaves and throws.

The heave is the horizontal distance that a point moves during faulting and the throw is the vertical distance that a point moves during faulting (Figure 3.9). Measuring total heaves and throws provide different ways of characterizing the strain distribution but are geometrically related to one another and hence results of both estimations should be consistent. Therefore, estimating both total heaves and throws is used to correlate results and insure that the result is not biased by measurement errors in case of either heave or throw is measured.

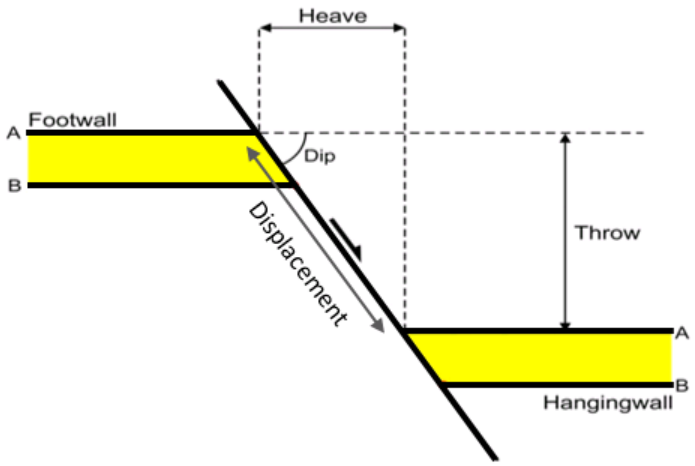

Figure 3.9 schematic diagram showing fault heave, throw and displacement.

The vertical separation (throw) at each fault intersected by a cross-section, was measured manually by measuring the distance between picks of hanging-wall and footwall cut-offs at each fault for all cross-sections. The total fault throw was then calculated by summing fault throw across each cross-section. The horizontal separation (heave) was estimated through measuring the horizontal distance between the hanging-wall and footwall cut-offs, measured perpendicular to the trace of the fault on the map view for all faults at each cross-section. The strain (total fault heave) was then estimated by summing

fault heaves across each cross-section. Estimations of strain from both heaves and throws were plotted in (Figure 3.10a & b) (Table 3.1), the two plots showed similar trend of increasing strain as we move from south to north zones.

The percentage of strain accommodated at each cross-section was defined by dividing the amount of strain of each transect by the total amount of strain estimated for the entire study area (Table 3.1). Moreover, the total extensional strain (ß-factor) accommodated by normal faults was also estimated along each cross-section, the total extensional strain is given by the original length of transect divided by the same original length minus the sum of the heaves.

Table 3.1 Total fault heaves and throws obtained from each cross-section (Figure **3.4**).

Zones	Zone1		Zone2		Zone3	
Cross-sections	AA`	BB`	CC`	DD`	EE`	FF `
Total heaves (m)	10748	8884	8882	6066	5896	5226
Total throws (m)	7389	6515	6234	4177	4006	3318
Extension value ß	1.11	1.11	1.13	1.16	1.09	1.08
Strain accommodated %	34	21	20	10	9	6
length of cross-sections (Km)	107	92	78	44	83	70

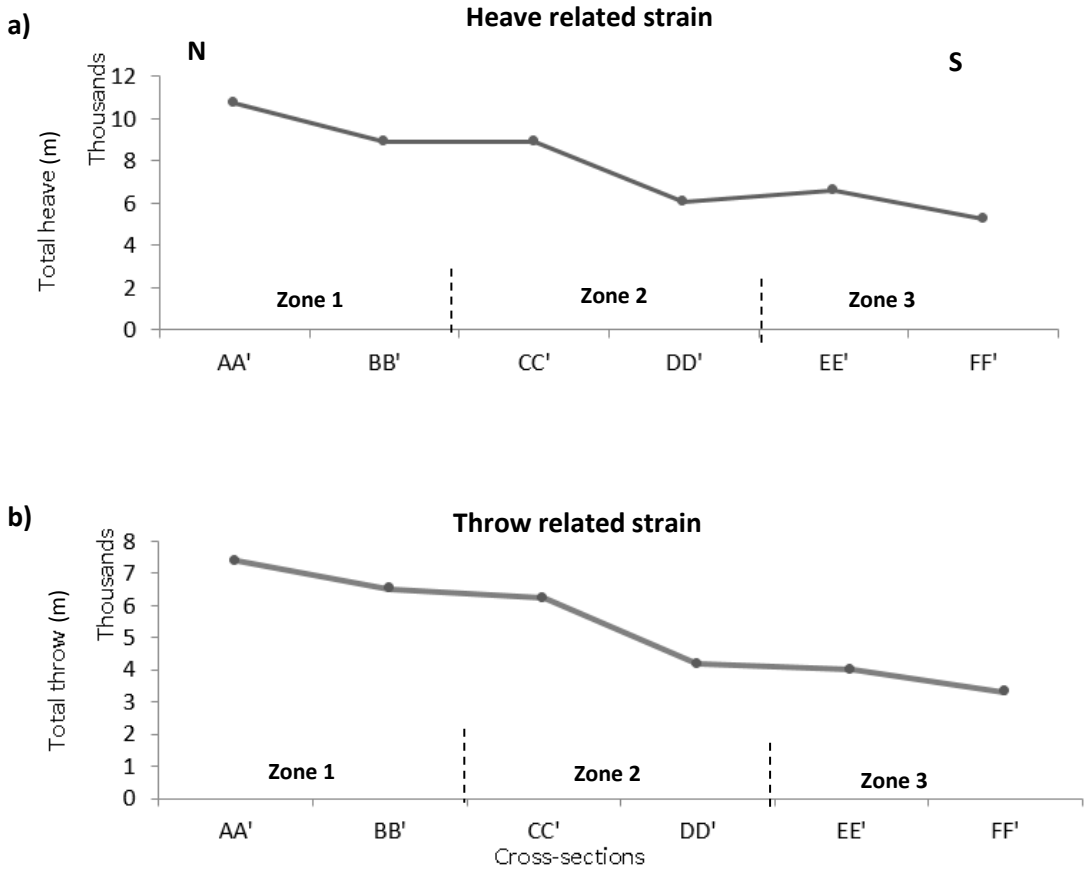

Figure 3.10. Strain estimations from summing heaves and throws across six transects in study area (see Figure **3.4** for the cross-sections locations.)

Table 3.1 shows that the ß-factor for the pairs of cross-sections in each zone is consistent. The largest extensional strains (ß-factor) manifested in cross-section DD` (ß=1.16) and that is because this cross-section passes through the largest number of faults within the Rift, and the original length of the cross-section itself is shorter compare to the other cross-section. The length of cross-section were defined by measuring the distance between the first and the last fault found across the selected location. The heave related strain profiles (Figure 3.10a) exhibit that cross-section AA` in the northernmost part of the Rift accommodates 34% of the total strain along this part of the Rift, cross-section BB` in zone 1 and CC` that passes across relatively large number of faults and accommodate comparable extensional strain of 20% each of the total strain. On the other hand, cross-section FF` in the southernmost part of the Rift zone also crosses through relatively large number of faults but still has the least extensional strain of 6%, and that is because faults in zone 3 are relatively smaller in size as indicated by heave and throw estimates (Table 3.1). It is worth mentioning that, the extrusion of extensive basaltic lava flows in northern Kenya that was reported by Ebinger (1989b) may have filled in the Rift basins and decreasing the apparent offset along individual faults, therefore, these estimated values for extension strain are considered minima. This method of estimating extensional strain (Figure 3.10) showed that zone 1 (where n=149) accommodates the largest amount of strain, followed by zone 2 (n=295) then zone 3 (n=177), the trend of these estimations suggest that the strain increase from zone 3 in the south through zone 2 in the centre up to zone 1 in the north. These observations support the hypothesis that a northward increase of total strain exist in the study area (see section 1.2).

3.6.2 Spatial heterogeneity of extensional strain and fault frequency

The spatial distribution of brittle strain that is accommodated by different structures such as faults in the upper crust is heterogeneously distributed (Dawers et al., 1993). Although scaling relationships are useful for estimating the total strain in a region, they do not provide any information on the spatial distribution of structures and strain. The Kuiper model (see section 2.1.4.4) has been used in order to quantifying the spatial heterogeneity of extensional strain and faulting across the fault network. Therefore, heterogeneity of brittle strain depends on two attributes; the spatial distribution of the extensional structures (faults in the current study) and the amount of horizontal separation (heave) on each of these structures (Putz-Perrier and Sanderson, 2008a). In other words, this model provides a measure of spatial heterogeneity based on both the position and displacement of individual faults /fractures. strain is described as homogenous when it is accommodated across a large number of evenly spaced faults whereas, when more strain is accommodated by few large faults then the distribution of strain can be characterised as heterogeneous (Nixon et al., 2014). Therefore, the purpose of this analysis is to investigate the spatial distribution of faults (the degree to which faults are clustered) along the study area and the lateral variability of brittle deformation in order to better understand growth and evolution of fault system. This method was also used by Putz-Perrier and Sanderson (2008a), Putz-Perrier and Sanderson (2008b) and Nixon et al. (2014).

The spatial heterogeneity of strain was quantified along the central Kenya Rift in accordance to Kuiper model, where the cumulative distributions of faulting and extensional strain were compared against a uniform distribution

Figure 3.11 for the six transects shown in Figure 3.4 to calculate values of heterogeneity of faulting (Vf) and extensional strain (Vs) (Table 3.2). Fault heave populations were acquired by measuring fault heaves for successive fault scarps that intersect with the one dimensional scanlines drawn perpendicular to the average fault strike along the Rift. Values of spatial heterogeneity have been calculated for all cross-sections made in the study area (Table 3.2).

Table 3.2. Values of heterogeneity of fault frequency (Vf) and extensional strain (Vs) in the three zones.

		Vs	Vf
Zone 1	AA'	0.43	0.35
	BB'	0.62	0.34
	Average	0.52	0.34
Zone 2	CC'	0.36	0.48
	DD'	0.35	0.19
	Average	0.36	0.33
Zone 3	EE'	0.31	0.25
	FF'	0.46	0.51
	Average	0.38	0.38

Graphs of cumulative distributions of fault frequency and extensional strain for cross-section AA` & BB` in zone 1 (Figure 3.11) in the north display relatively large stair-like distribution, which indicates heterogeneity and localized deformation for both extensional strain Vs and faulting Vf, because the majority of strain is localized onto fewer but larger longest border faults at the flanks of the Rift, and therefore this zone represents a localized faulting deformation. The two cross-sections showed average values of heterogeneity of Vs = 0.52 for extensional strain and Vf = 0.34 for faulting frequency Vf (Table 3.2).

Graphs of spatial heterogeneity of extensional strain in zone 2 in the centre of the Rift (Figure 3.11) show that the central segment of cross-section CC` and most of cross-section DD` exhibit relatively uniform steps and less variant gradients dominating the middle part of the profile, which represents less heterogeneity due to strain and displacement being distributed across a large number of relatively small faults segments that contribute to the strain accommodation. The average values of spatial heterogeneity for cross-sections CC` & DD` showed Vs of 0.52 and Vf of 0.34 (Table 3.2), which suggests a more distributed deformation in zone 2 as opposed to cross-sections AA` &BB`.

Graphs of heterogeneity of extensional strain Vs and fault frequency Vf for cross- sections EE`& FF` (Figure 3.11) in zone 3 show that deformation is not largely distributed, yet there is still some individual large fault segments represented by large steps in the graph that take up fairly large amount of strain. The average values of extensional strain heterogeneity (Table 3.2) suggest that the deformation in zone 3 appear to be less heterogeneous than

zone 1 but more heterogeneous that zone 2, this observation is also evident in (Figure 3.12a) that show along strike variations of heterogeneity of extensional strain Vs. therefore, the domain of deformation in zone 3 can be considered as rather distributed.

Therefore, these graphs of spatial heterogeneity (Figure 3.11) show that there is a rather distributed domain of deformation in the southernmost zone (zone 3 n= 177) exemplified in cross-section EE`& FF`, a distributed domains of deformation in zone 2 (n= 295) in the centre shown by cross-section CC`& DD`, where deformation becomes more distributed and less heterogeneous as it contains more faults contributing to the strain accommodation, whereas cross-section AA`& BB` in zone 1 (n= 149) crosses through a region with less faulting where the strain is localized on fewer faults at Rift borders forming a domain of localized deformation in the north of the this part of the central Kenya Rift. Therefore, fault populations with localized deformation are significantly more heterogeneous (Nixon et al., 2014), this observation is illustrated in (Figure 3.12a) when values of the extensional strain heterogeneity Vs (total heaves) were plotted against locations of transects to assess the along strike variations of heterogeneity.

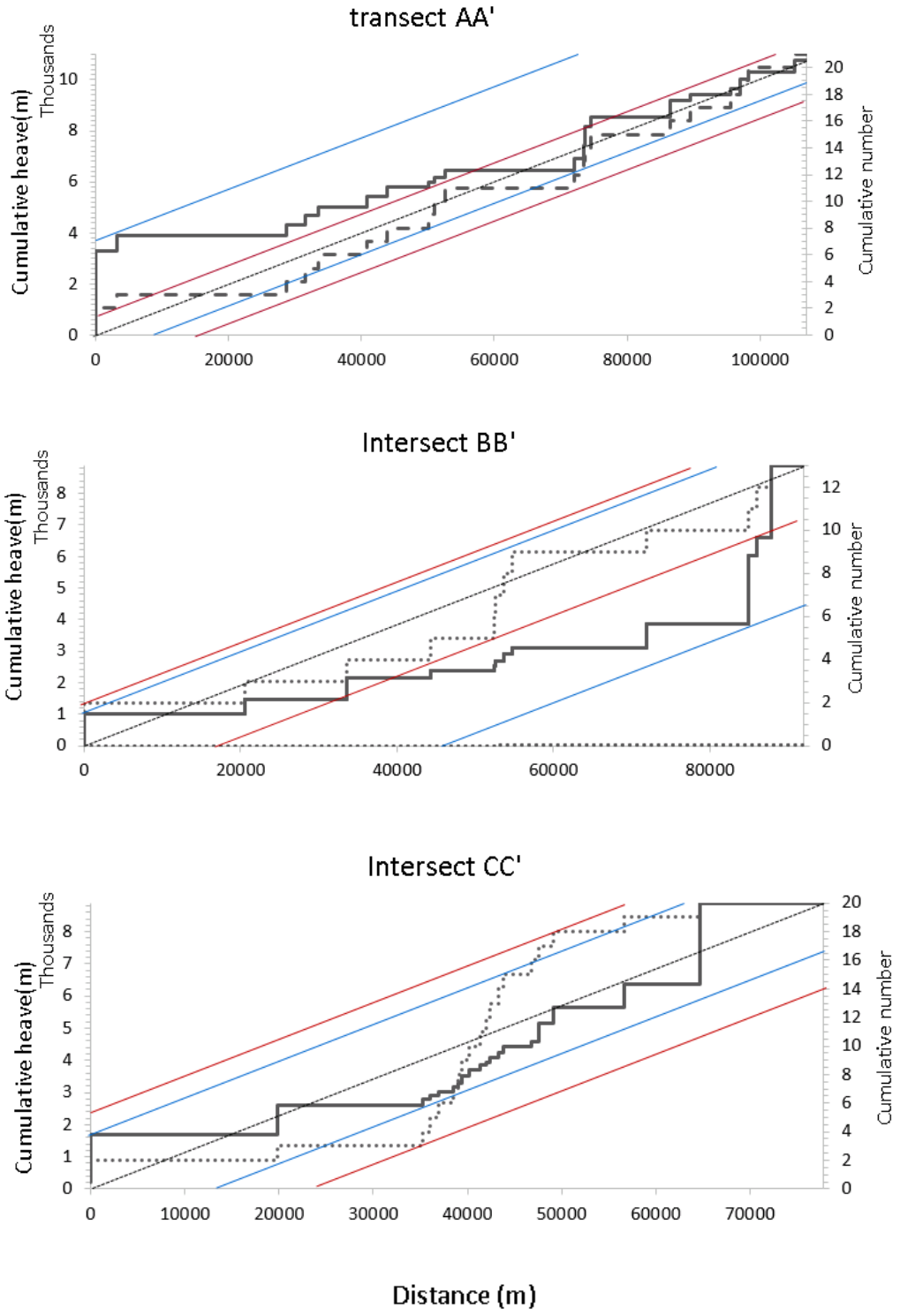

Figure 3.11 Cumulative plots for transects AA`(zone 1), DD` (zone 2) and EE` (zone 3) showing the spatial distribution of extensional strain Vs (solid line) and fault numbers Vf (dotted line). Blue lines are Max & Min deviation from uniform distribution (diagonal dashed line) for Vs, red lines are Max & Min deviation from uniform distribution for Vf.

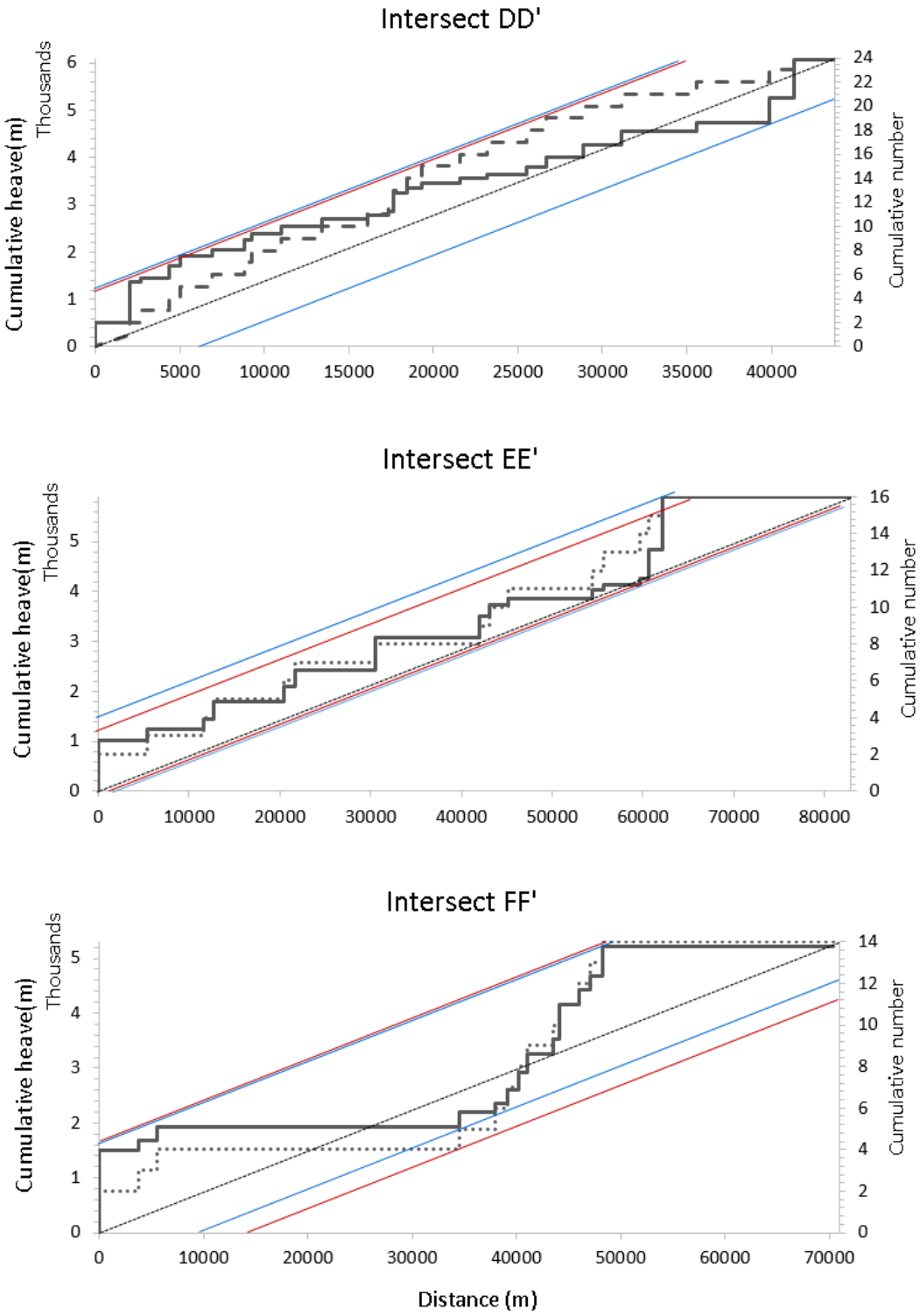

Figure 3.11 (continued).

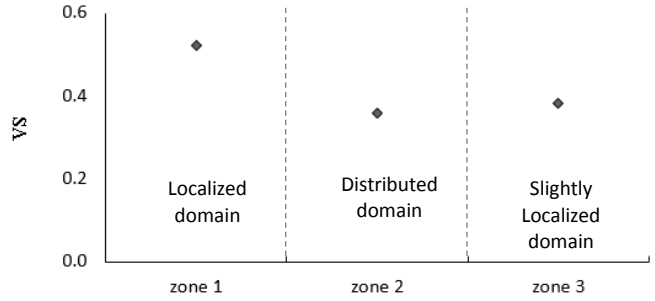

Figure 3.12. Along strike variations of averages of extensional strain heterogeneity (VS) in each zone.

Moreover, the effect of total extension estimated at each cross-section on the amount of heterogeneity was also examined by plotting values of heterogeneity of fault frequency Vf and extensional strain Vs against estimated total extension (Figure 3.13), the result showed that there is no correlation between the total fault extension and variations in Vf and Vs, which indicates that the heterogeneity within the network is independent of bulk extension, this lack of correlation has also been observed in similar investigations as shown in Moriya et al., (2005) and Putz-Perrier and Sanderson, (2008b).

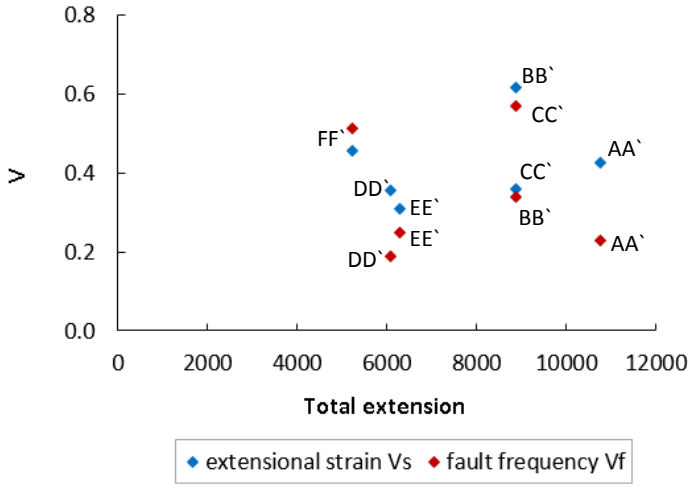

Figure 3.13. Heterogeneity measures compared with the overall extension accommodated by each transect line along the Rift.

3.7 Fault analysis

The following sections the characteristics of sub-sets of fault populations are categorized in terms of the average of their strike (section 3.5.1). The key purpose is to establish the scaling properties of fault size distributions and to examine the extent to which these can be related to the evolution of the normal fault system in this part of the central Kenya Rift.

3.7.1 Data validation and calibration

The 620 normal faults were identified and mapped in this Rift segment in the same way described in the methodology in chapter 2 (section 2.2.2). In validation of the fault interpretation from DEM, the mapped fault data were plotted along with published displacement-length data collected from outcrops from different tectonic settings with different rheological properties around the world for 13347 fault as shown Gillespie et al. (1992), Bailey et al. (2005). The mapped faults fit reasonably well within the range for normal faults from published data set. This validation is very important as it suggests that dataset is reliable to curry out further analysis (Figure 3.14).

The best fit linear trend line for the dataset (white trend line) (Figure 3.14) returned an exponent slope of 0.1, which is lower than that of the global data set (black trend line) with exponent slope of 1.98. This difference could be due to underrepresentation of the maximum throw as well as a systematic underestimation of the maximum fault lengths due to geological and resolution effects. (Bailey et al., 2005)

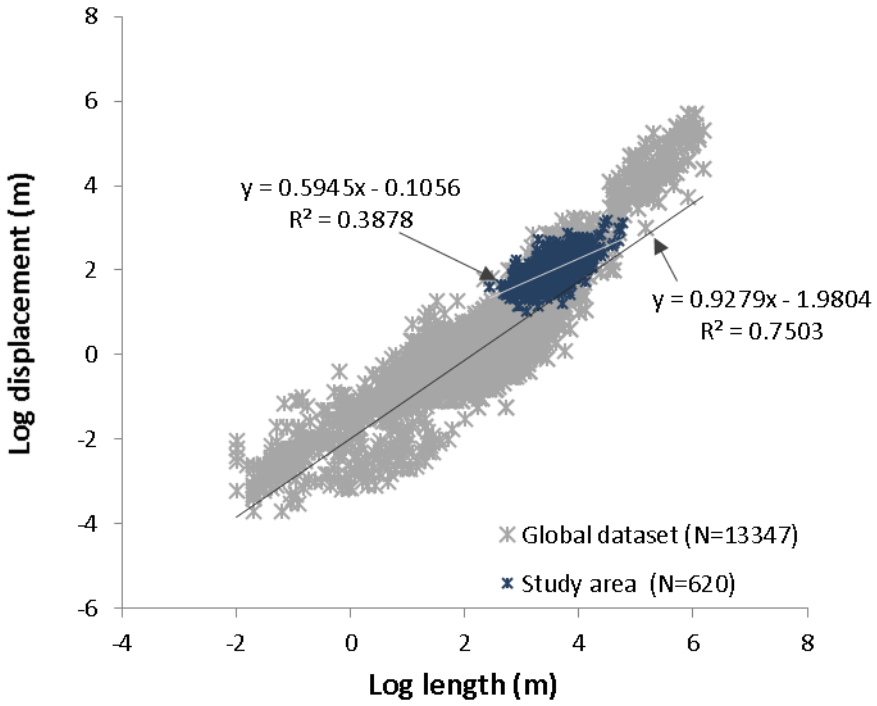

Figure 3.14. Log-log Plot of minimum displacement (D)\ fault length (L) for faults from the study area along with published data set **(Bailey et al., 2005)**.

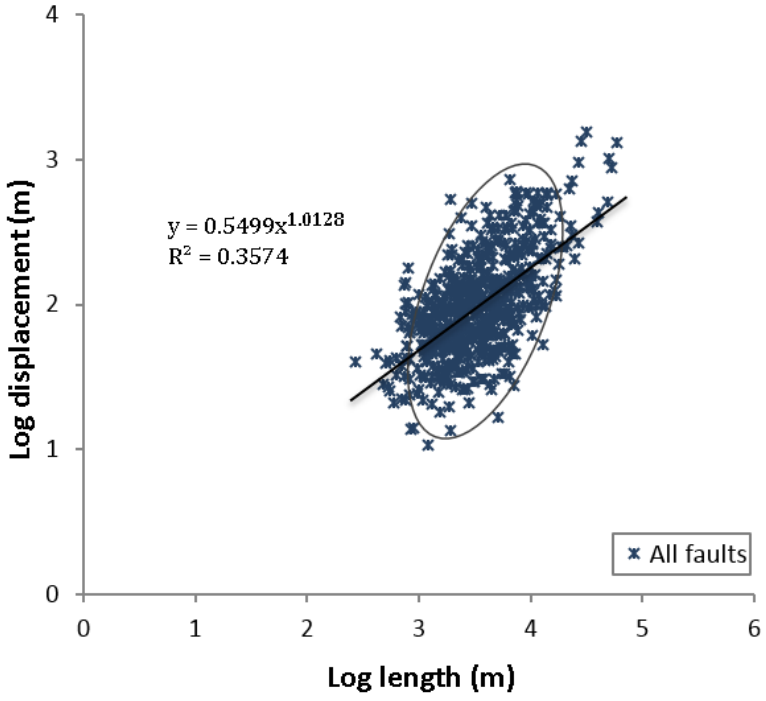

Figure 3.15. Log-log plot for D vs L for all faults (isolated and linked) mapped in the three zones, the ellipse shows the upward increase of D\L ratio

3.7.2 Fault trace length and throw relationship

Fault trace-length and their throw are the most measured components of faults. The relationship between fault lengths versus displacements is the most studied scaling relations. Scaling relations describe the statistics of the frequency-size distribution of fault size population, such as trace-lengths and throws, the relation between the fault trace-lengths and throw and the spatial distribution of faults (e.g. Cowie, 1998b).

It has been generally assumed that there is proportional relationship between fault throw (D) and fault length (L) (section 2.1.3.1), and their parameters were plotted in log-log plots (Figure 3.15). It is noted that there is general upward trend of increasing Throw/Length ratio. The data also showed a large scatter that spans about two orders of magnitude in both variables (Figure 3.15). This scattering has been known as a common feature in fault studies and has been attributed to: combining data sets from different lithology and material properties (e.g. Cartwright et al., 1995, Peacock and Sanderson, 1991, Peacock, 2002, Cowie and Scholz, 1992a), fault growth and segment linkage (Cartwright et al., 1995, Schlische et al., 1996, Cartwright et al., 1996, Mansfield and Cartwright, 2001), sampling effects and inaccurate measurement of fault displacement/throw and length.

3.7.3 Isolated faults

Investigations of scaling relations of isolated faults (show bell-shaped displacement) provide a basis for tracing fault evolution. Isolated faults are not common in this study area, there are 2 faults in zone 1, 12 faults in zone 2 and 11 in zone 3. Isolated faults (identified from DEM and google map images) appear as simple pattern of displacement (bell-shaped escarpment), which increase from zero at the tips to a maximum value usually near the centre of the fault trace as indicated in Dawers et al. (1993). In this section the D\L relationship for isolated faults in the study area have been analysed in order to assess patterns of fault growth either as scale-invariant (self-similar) or scale-dependent behaviour of growth between fault length and fault displacement. Isolated faults in zone 1 are not included in the analysis as there are only two isolated faults identified in this zone.

It has been noted from the log-log plot (Figure 3.16 a, b & c) showing isolated faults as yellow dots in the three zones that isolated faults in zone 2 and zone3 reveal slightly different distribution (discussed later in section 3.8.2). Fault throw profiles (Figure 3.17a &b) of these isolated faults show that faults in zone2 appear to be smaller in throw compared to those of zone3, where the largest isolated fault in zone2 is about 104 m in throw while the isolated faults in zone3 show a range of throw between about 50m and 220m, which may indicates that isolated faults in zone2 are less mature in development than isolated faults in zone 3. It has been noted that the majority of these isolated faulted in zone 2 are found in the Rift valley, whereas most isolated faulted in zone 3 are located near the margins of the border faults.

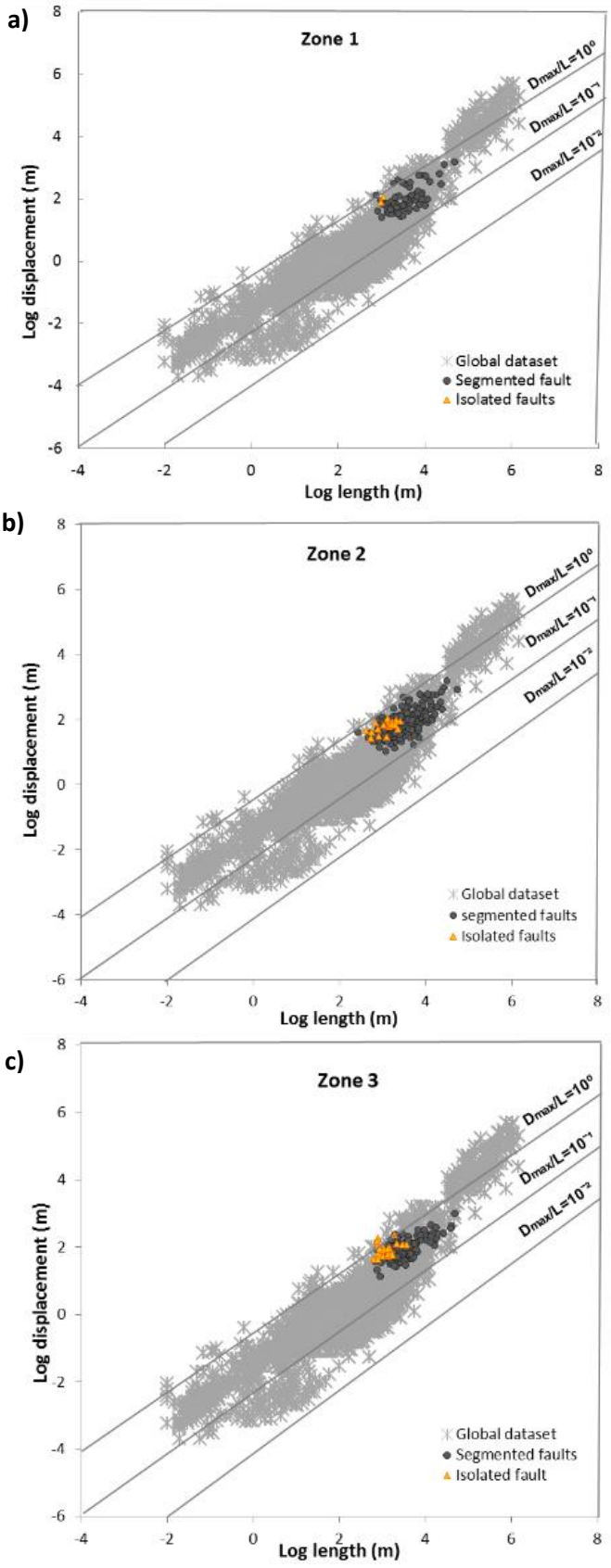

Figure 3.16: Log-log Plot of length vs displacement for the three zones showing isolated faults and segmented faults

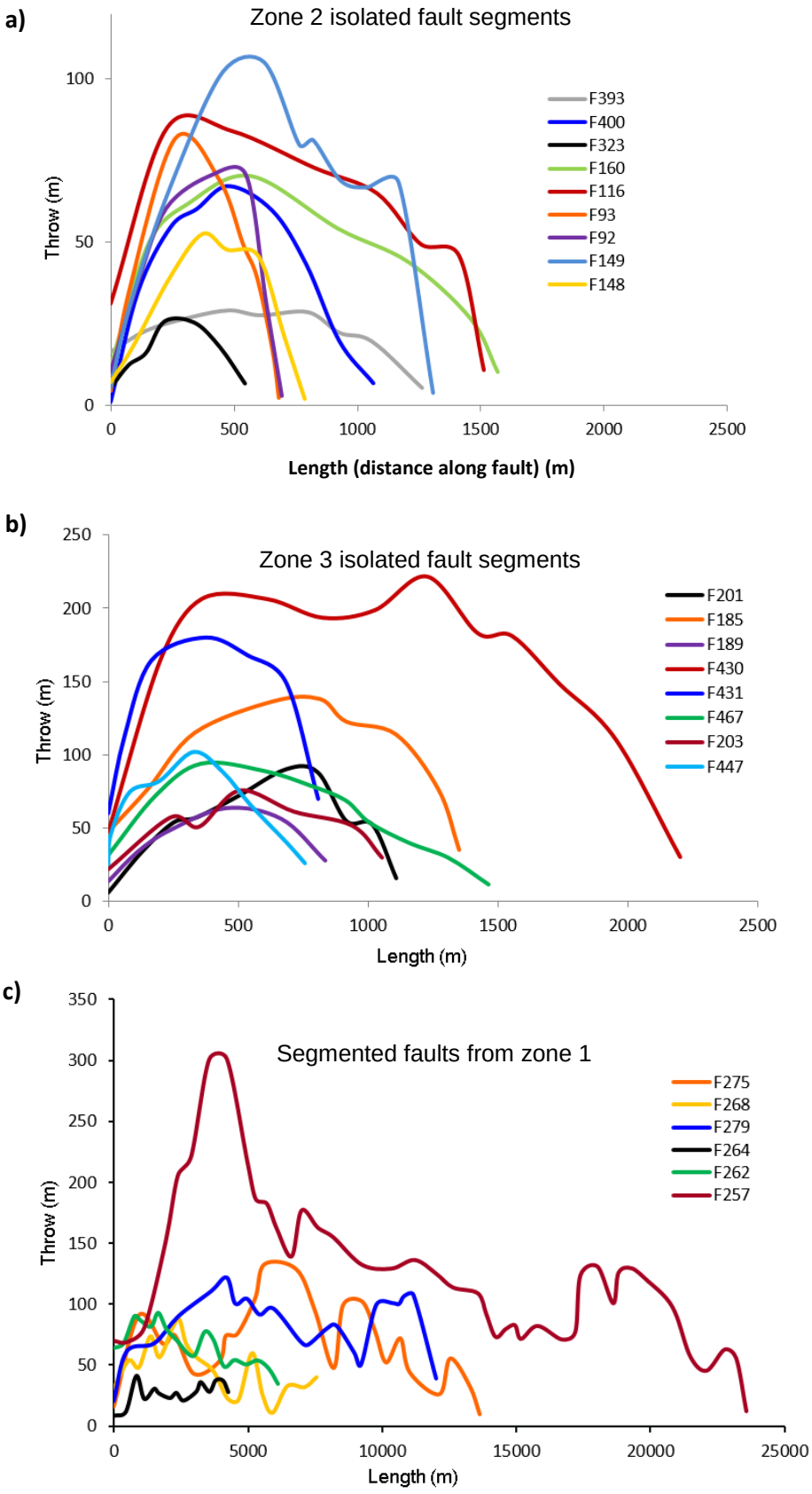

Figure 3.17: fault displacement profile showing a) dominant peaked pattern for isolated faults shown in zone2, b) dominant plateaued profile observed in zone3, C) distributions of linked Fault segments.

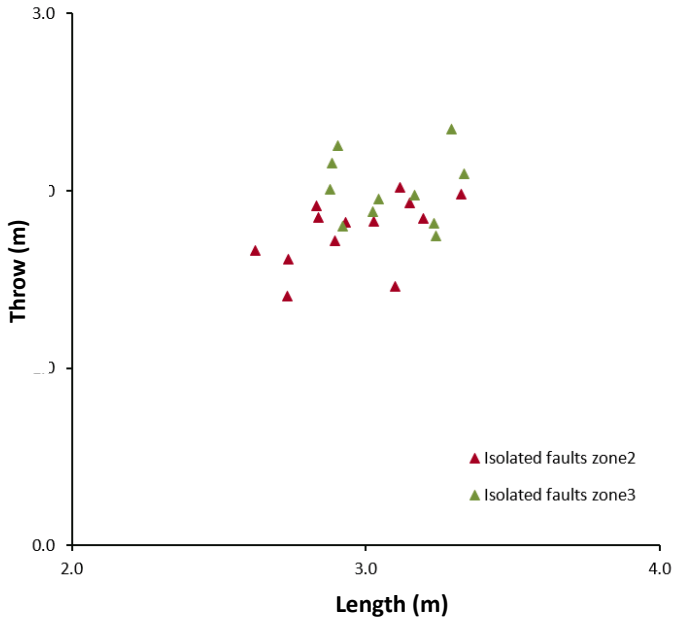

Figure 3.18: Log-log plot for D vs L of isolated faults in zones 2 &3

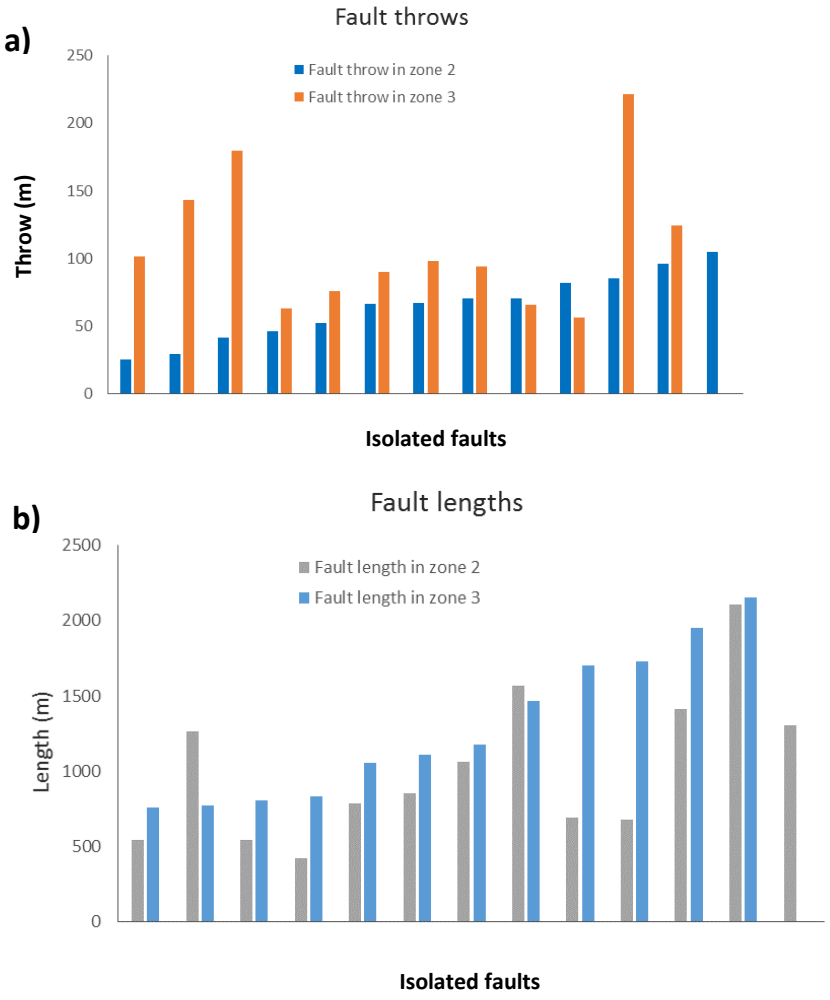

Figure 3.19. Chart showing differences in a) fault trace length, b) fault throw for isolated faults in zone 2 and 3

3.7.4 Segmented faults

Segmented faults are found where fault segments are linked either by soft linkage where isolated faults can propagate towards each other and interact and evolve without obvious connection, or hard linkage where fault segments link by breaching the relay zone. This linkage mechanism has been proposed in several studies as a model for fault growth in Peacock and Sanderson (1991), Cartwright et al. (1995), and Walsh et al. (2001). The pattern of fault growth for segmented fault arrays in the three zones is hard to be traced as they exhibit similar patterns of fault throw profiles as shown in (Figure 3.20).

Segmented faults in the three zones show similar distribution trend involving scattering (Figure 3.20). This scattering is similar to that found by several previous studies of normal faults conducted elsewhere such as (Peacock and Sanderson, 1991, Cowie and Scholz, 1992a, Cartwright et al., 1995, Peacock, 2002), where faults were mainly identified by field work. Those studies attributed large scatter in the D\L plot to combining data sets from different lithology and material properties. Several other studies (e.g. Cartwright et al., 1995, Cartwright et al., 1996, Schlische et al., 1996, Mansfield and Cartwright, 2001) referred to the scattering in the D\L plot to fault growth and segment linkage and precluded measurement error, sampling problems, and variations in the mechanical properties and lithology of the rock units to cause such scatter in the data.

According to the geological map of Kenya (Ministry of energy of Kenya 1987), it has been noted that the study area where the faults exist is covered by Quaternary and Tertiary volcanic sediments that could be relatively uniform in lithology. Therefore, according to studies mentioned above, it could be argued

that scattering shown by dataset used in this study (Figure 3.20) for segmented faults could be related to several other source other than the rock lithology.

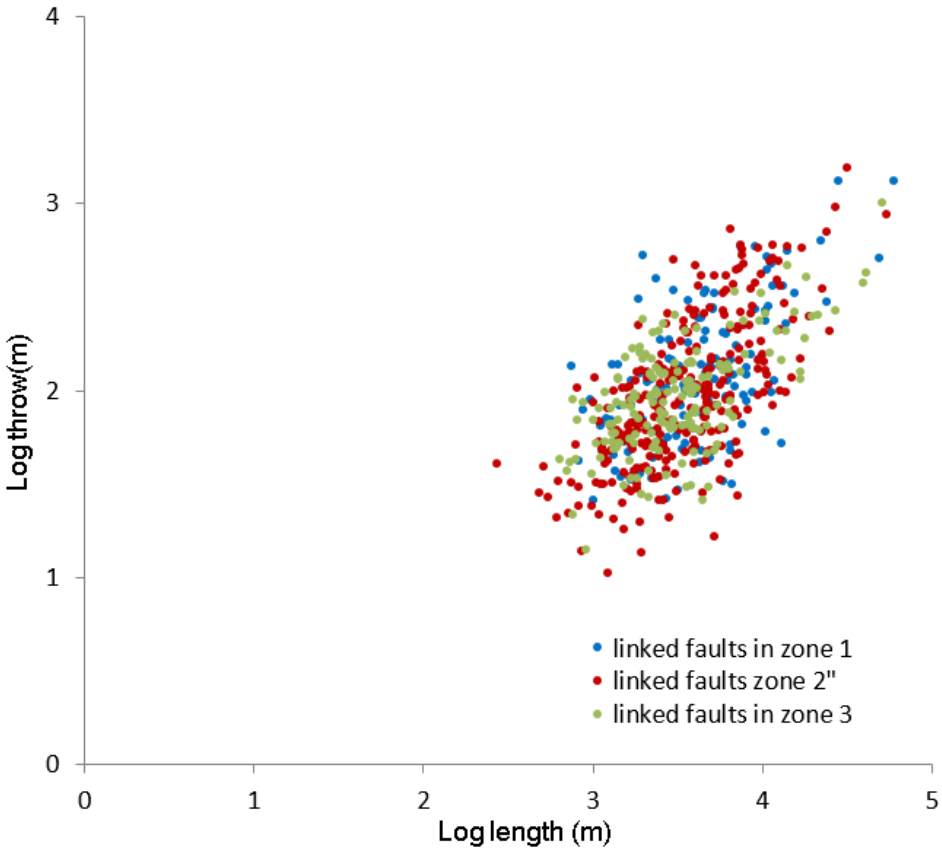

Figure 3.20: Log-log plot for D vs L for Segmented faults in the three zones show scattering distribution.

3.7.5 Fault size populations

The scaling properties of fault systems are studied in order to inform our understanding about the mechanism of fault growth and evolution (e.g. Cowie, 1998b). Cumulative frequency distribution function (CDF) is the most common way to describe attributes of fault populations (e.g. length, throw) (e.g. Childs et al., 1990, Walsh et al., 1991, Jackson and Sanderson, 1992, Cladouhos and Marrett, 1996, Bonnet et al., 2001). The wide range of fault size populations in this study; lengths (272 m – 50477 m, average 4788m) and throw (27 – 1561 m, average 137 m) permits detailed quantitative assessment of the scaling properties of faults and fault related strain.

3.7.6 Fault throw populations

The fault throw data (including isolated and segmented faults) for the three zones were analysed by fault cumulative frequency in a log-log plot, and three statistical models including power law, lognormal and exponential laws have been used to examine the best fit the fault throw populations (Figure 3.21, Figure 3.23 &Figure 3.22). Generally power law frequency distribution is found to be the best fitting model for the fault throw data based upon value of coefficient of determination R^2 (Table 3.3). However, log-normal exhibited the best statistical model for fault throw data in zone 3. Furthermore, It is generally recognized that resolution and finite size effects on a power law population can also result in distributions that appear to be exponential or lognormal (Bonnet et al., 2001). Therefore, with the rise of scaling concepts in Earth sciences power law distributions have been favoured over lognormal distributions because of their greater physical significance (Barton and Zoback, 1992).

Power-law distribution is defined by a straight line segment with fractal dimension D, which is the exponent of the slop equation (Figure 3.21). Knowledge of the power-law exponent (fractal dimension) allows assessment to be made about the amount of deformation in a given region (Marrett and Allmendinger, 1991, Meyer et al., 2002, Bailey et al., 2005). The power-law exponent provides a measure of the relative importance of large and small objects. The larger the exponent (steeper distribution) for a given population, the more small objects there are for every large object. (Yielding et al., 1996). Therefore, variations in fractal dimension reflect the contribution of different fault size to the strain accommodation. The higher the exponent of population slopes D (fractal dimension), the higher the contribution of small size faults to strain accommodation (Marrett and Allmendinger, 1991).

In this investigation, the fault throw data from the three zones combined were also tested against the same scaling laws and power law scaling found to fit the best (Figure 3.24 & Table 3.3). The exponent of the power-law distributions of fault throw data for zone1, zone2 and zone3 was found to be1.0, 1.1 &1.4 respectively (Figure 3.21), and 1.2 for the three zones combined (Figure 3.24). These distributions were corrected for truncation and censoring effects (see section 3.7.8)

Table 3.3 Results of functions fit to throw data

Rift zone	R^2 for Function fits		
	Power-law	Exponential	Log-normal
zone 1	0.96	0.81	0.90
zone 2	0.93	0.82	0.90
zone 3	0.90	0.85	0.92
All zones	093	0.83	0.90

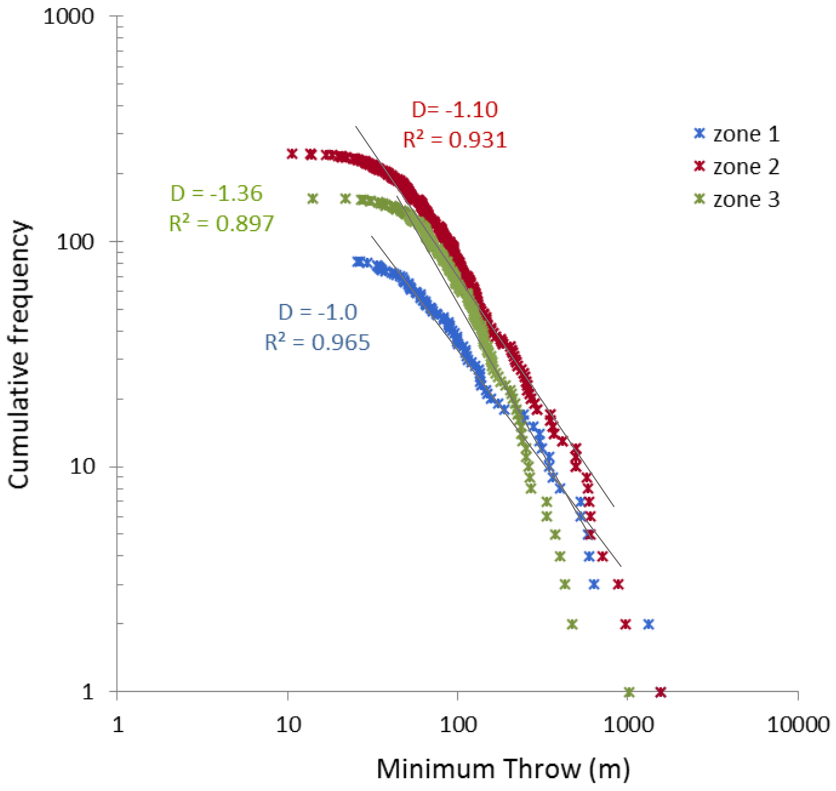

Figure 3.21: Log-Log plot of fault throw against cumulative frequency for the three zones showing power-law function fit

.

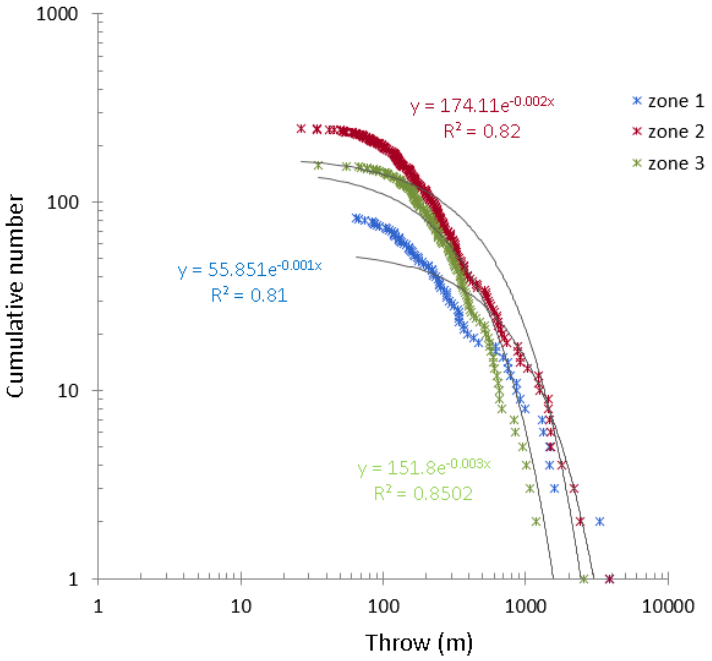

Figure 3.23 Log-Log plot of fault throw vs. cumulative frequency for the three zones showing exponential function fit

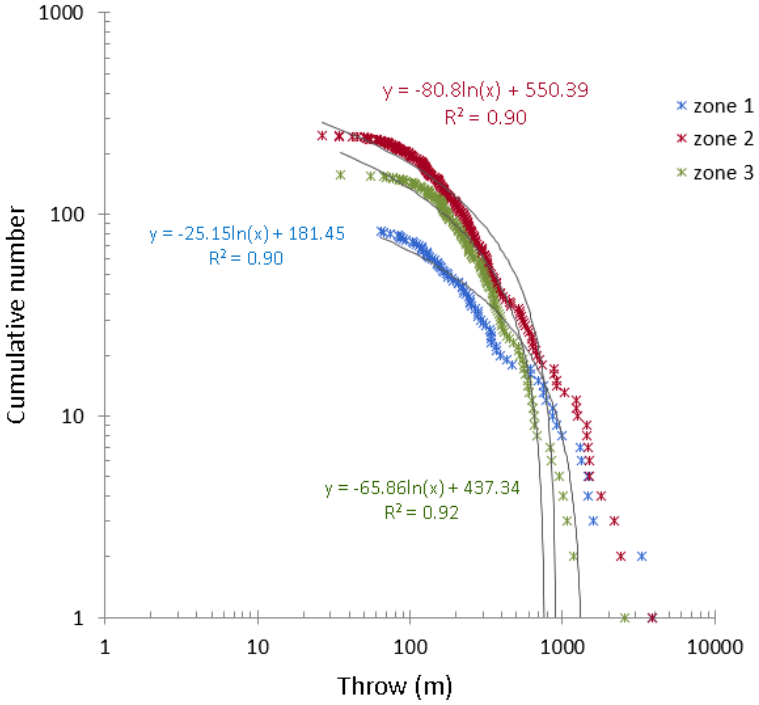

Figure 3.22 Log-Log plot of fault throw vs. cumulative frequency for the three zones showing log-normal function fit

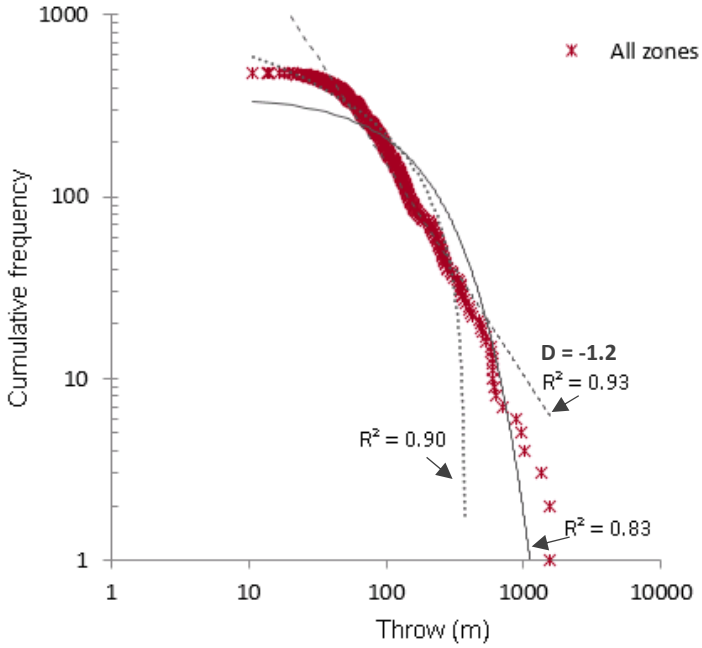

Figure 3.24. Log-Log plot of fault throw against cumulative frequency for the three zones combined.

3.7.7 Fault length populations

In the same way as for fault throw data, fault length data for the three zones were analysed by fault cumulative frequency in a log-log plot, and three frequency distributions including power, exponential and lognormal laws have been used to fit the data (Figure 3.25, Figure 3.26& Figure 3.27) respectively. Table 3.4 shows value of least square coefficient R^2 that indicate goodness of fit of the statistical models applied to the fault length data. Log-normal appear to be the best fit model (Figure 3.27) followed by power aw (Figure 3.25).

However, as mentioned above in section 3.7.6, the rise of log-normal distribution are often mistaken for power-law distributions (Mitzenmacher, 2004) and in geoscience can be attributed to degradation of underline power law distribution due to resolution and finite size effects (Bonnet et al., 2001).

Moreover, it has been shown in the literature that, should these competing laws (power law and Log-normal) arise, the power law is favoured over lognormal because of their greater physical significance (Barton and Zoback, 1992, Bonnet et al., 2001) where analysis of fractal dimension can provide a better description of the data than other plausible alternative distribution (Bonnet et al., 2001). Additionally, there has been a strong correlation between throws D and fault lengths L as indicated in several studies Walsh and Watterson (1988), Peacock and Sanderson (1991), Cowie and Scholz (1992a), Gillespie et al. (1993), Cartwright et al. (1995), Cowie (1998b) and Kim and Sanderson (2005) that suggests that the distribution of fault length should follow similar scaling functions as fault throw (Cladouhos and Marrett, 1996). Therefore, for these reasons, the power law distribution of fault length data has also been preferred over the long-normal distribution for analysis in this study.

The fault length data from the three zones combined were also tested against the same scaling laws and power law scaling found to fit the best (Figure 3.25 & Table 3.4). The general trend of the power law distribution of fault length population (Figure 3.25) show shallower slope to that of the fault throw population (Figure 3.21) , and that is because the magnitude of fault lengths are much greater than the magnitude of fault throw. The power-law distribution of fault trace length displayed fractal dimension (the exponent D) of (~1.0) for each individual zone (Figure 3.25) and for the three zones combined (Figure 3.28). These power-law distribution distributions (Figure 3.25) were corrected for truncation and censoring effects (see section 3.7.83.7.10)

Table 3.4 Results of functions fit to the fault trace-length data

Rift zone	R^2 for Function fits		
	Power-law	Exponential	Log-normal
zone 1	0.80	0.67	0.90
zone 2	0.84	0.82	0.95
zone 3	0.87	0.67	0.88
All zones	0.91	0.87	0.88

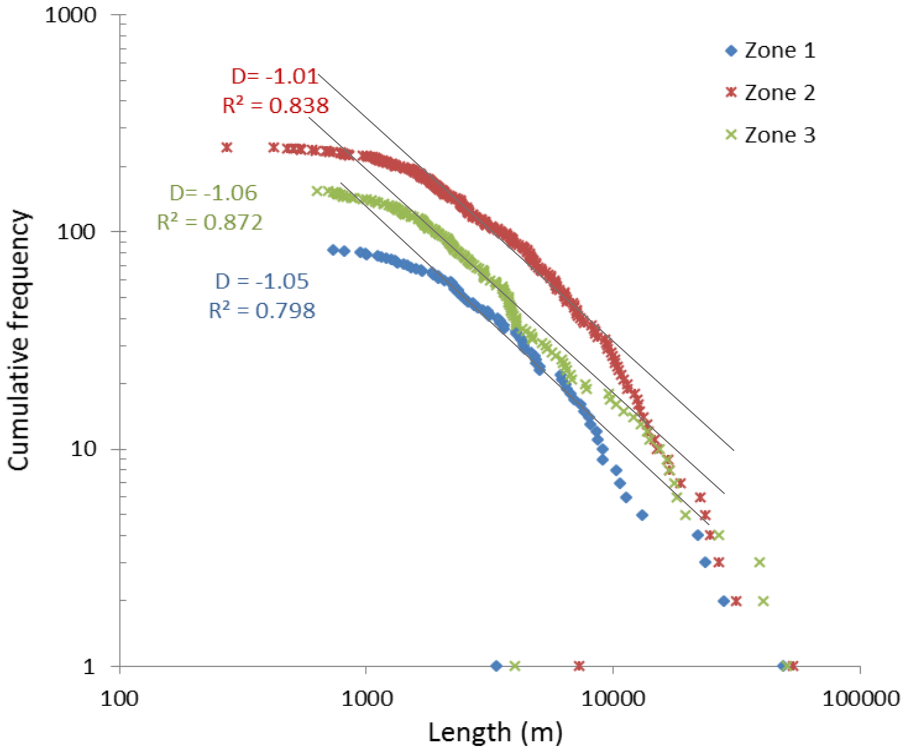

Figure 3.25: Log-Log plot of fault trace length vs cumulative frequency for the three zones.

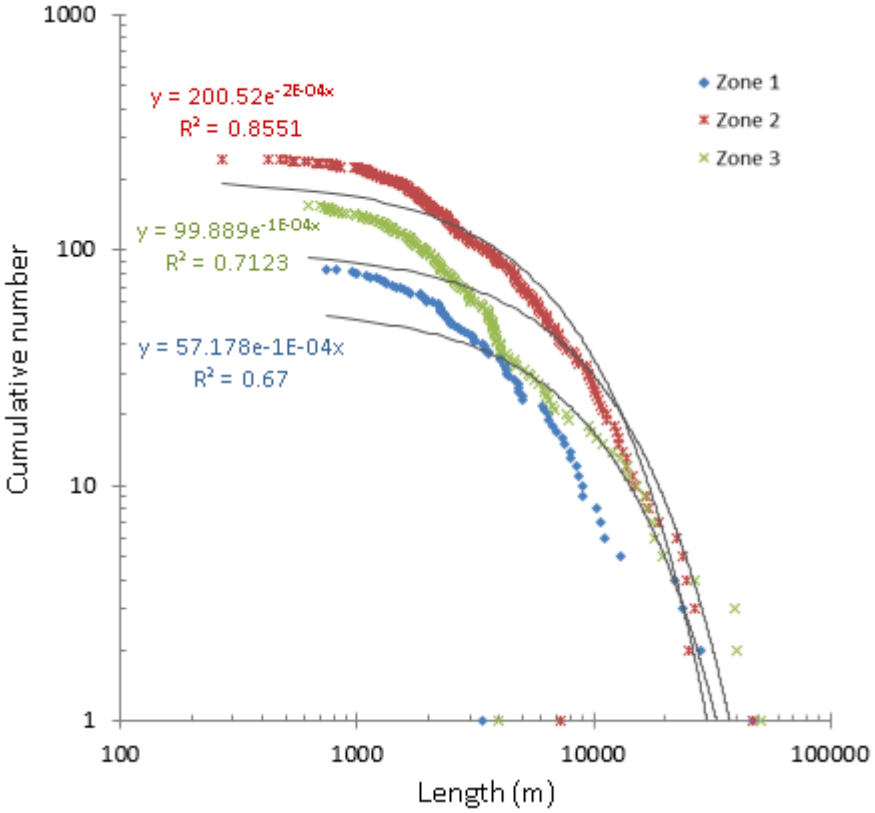

Figure 3.26 Log-Log plot of fault trace length vs. cumulative frequency for the three zones showing exponential function fit

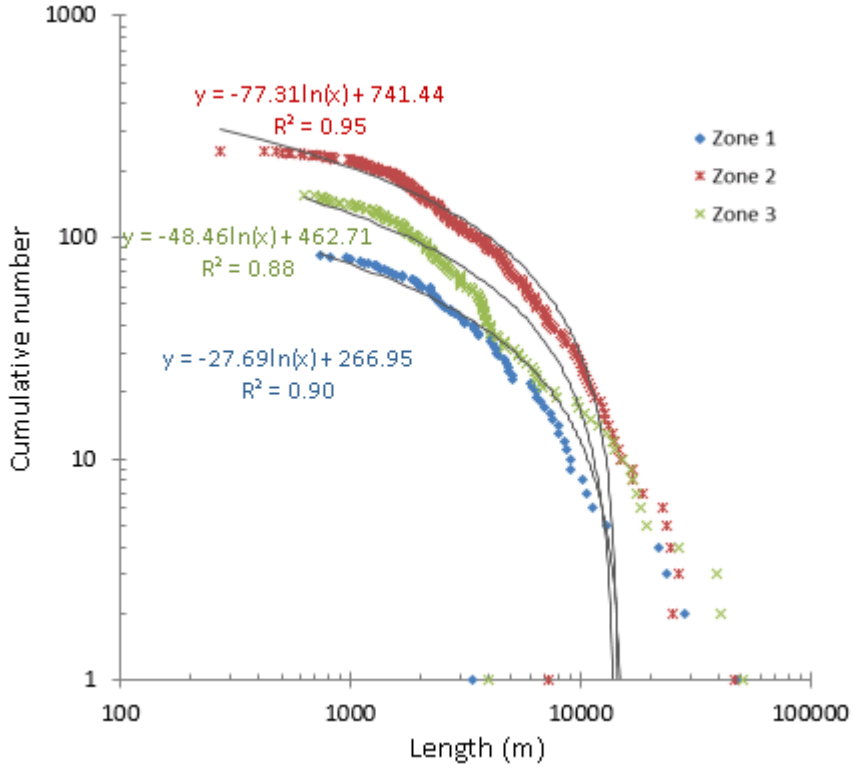

Figure 3.27 Log-Log plot of fault trace length vs. cumulative frequency for the three zones showing log-normal function fit

The power law scaling exponent for fault trace-length data plotted on a cumulative distribution plot can also be used to quantify and distinguishing between interacting normal faults from non-interacting faults (Vallianatos and Sammonds, 2011). Therefore, applying equation 2 of Vallianatos & Sammonds (2011) (see section 2.1.3.2) to the power law exponent of fault trace length population in the central Kenya Rift shows that fault system population in the study area returns a q factor of 1.95, 1.99 and 1.94 for zones 1, 2 & 3 respectively. The highest value (~2) of q factor calculated for zone 2 indicates high interaction and linkage activity, which can be observed by the fault geometry in this zone (Figure 3.7a, b, c & d).

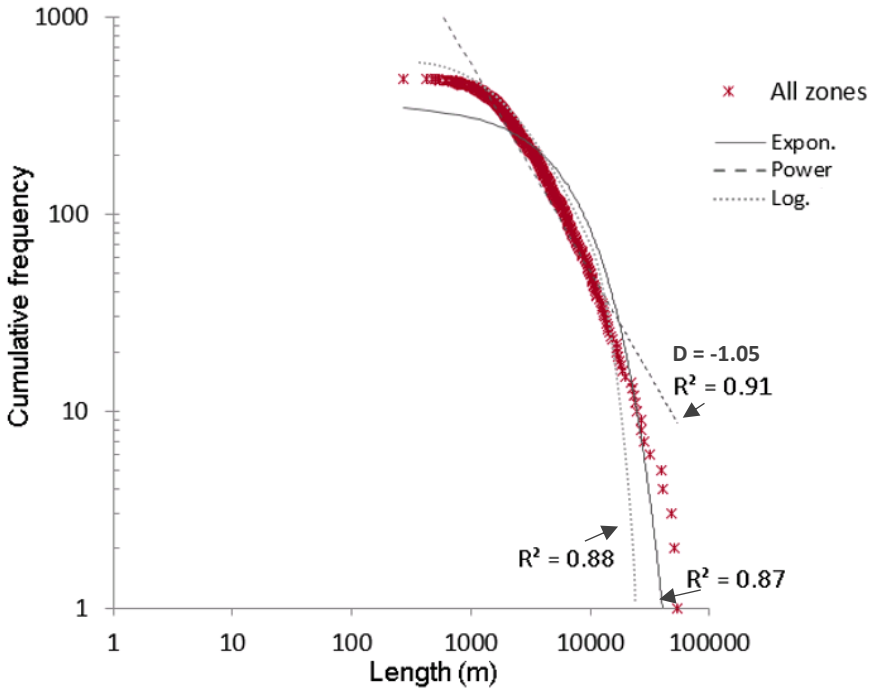

Figure 3.28. Log-Log plot of fault trace length vs cumulative frequency for all faults in the three zones.

3.7.8 Correction of resolution errors

Fault populations displaying a power-law distribution derived from maps or topographic surfaces are subject to scale limitations of the data and can appear as non-linear, even when the sample is ideally power law. Cumulative distribution of fault size populations that show a power-law distribution fits to a line as a straight segment, the slop of this straight segment has an exponent known as fractal dimension of slope (D), sampling bias make the straight segments curve from upper and lower ends (Figure 3.29 & Figure 3.30).

Commonly recognised sampling biases affecting power-law distribution are truncation and censoring (Pickering et al., 1995, Zhang and Einstein, 2000). Truncation bias refers to effects caused by a systematic underrepresentation of smaller faults and fractures in a sample due to limitations in data resolution (Pickering et al., 1995, Bonnet et al., 2001). The effect of this under-representation is reflected as a gradual decrease in power-law slope and exhibits the convex upward shape that is commonly presents in the cumulative distribution. Censoring bias refers to partial sampling of large faults that extend beyond the sample area and therefore are incompletely characterized. Sampling biases associated with the largest faults can potentially lead to a shallowing of power law distribution and increasing power-law exponents as a result (Pickering et al., 1995, Bonnet et al., 2001). Censoring is not of great significance unless the sample area is small relative to the full lengths of most of the fault traces (Heffer and Bevan, 1990).

Some previous studies (e.g. Pickering et al., 1995, Ackermann and Schlische, 1997) suggested that data that deviate from a straight line of power law distribution are not representative of the distribution and therefore they should

be excluded from the analysis, by setting a lower threshold below which small faults are thought to be undetected. It was also suggested that the biased data should be corrected to match closely the average exponents measured in natural and synthetic fault maps at the same scales (Pickering et al., 1995, Manzocchi et al., 2009).

As discussed in chapter 2 (section 2.2.3.2), when DEM data is used to trace a fault, there are relative errors associated with the horizontal and vertical resolution of the mapping technique, below which the fault length and throw cannot be detected, that is in addition to two other possible errors caused jointly by digitizing technique and the interpretation of the geological features that involves the human eye. Therefore, the overall error in the fault throw and length caused by the those factors combined (see chapter 2 section 3.7.8) was quantified from the cumulative throw distribution diagram for the corrected data (Figure 3.29) by projecting a line from the upper cut-off of the power law throw population down to the throw axis. It was estimated to be about ± 70 m, which include the 20 meter of the vertical resolution of DEM plus 50 m that could be attributed to digitizing and human errors (Figure 3.29). As for the fault trace-lengths, the overall error is found to be about 1km (Figure 3.30), which means faults <1 km long cannot be identified. If each fault tip is underestimated by I km, the measurement errors are then up to +2 km for fault with two tips. Furthermore, the effect of these errors on the medium to large scale fault populations mapped for this study (lengths between 272m to 50477m, with an average of 4788m and throw from 22 to 1.561m, average 137m) is marginal, which would not affect the overall outcomes of this research.

3.7.9 Correction for throw cumulative distribution

In this study, the distribution of the fault throw populations (section 3.7.6) was corrected for the effect of truncation and censoring to exponents of 0.99, 1.23 and 1.33 for zones 1, 2 and 3 respectively, these exponents are comparable to those defined from a number of tectonic, fault systems that range from 1.0 to 1.5 (Scholz and Cowie, 1990, Marrett and Allmendinger, 1992, Watterson et al., 1996). The distribution was corrected by eliminating biased values (the extreme values that deviate from the straight line that represent power-law distribution) (Figure 3.29). Interestingly, the difference in power-law exponent of biased and unbiased data was barely noticeable, biased data show exponents of 1.0, 1.10 and 1.36 for zone1, zone2 and zone3 respectively, whereas, unbiased data exhibit power-law exponents of 0.99, 1.23 and 1.33 for zone1, zone2 and zone3 respectively. Thus, it is noted that there is a decrease of the D value from the southern zone (zone3) to the northern zone (zone1) with the increase in extensional strain, as estimated in section 3.6.1.

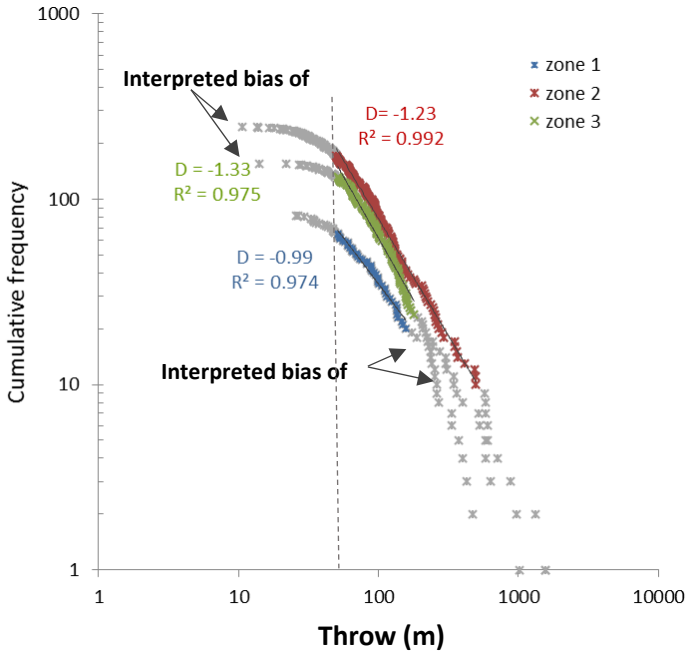

Figure 3.29: Cumulative throw distributions of the fault population in the study area showing unbiased data (coloured stars) and excluded Biased data (grey stars).

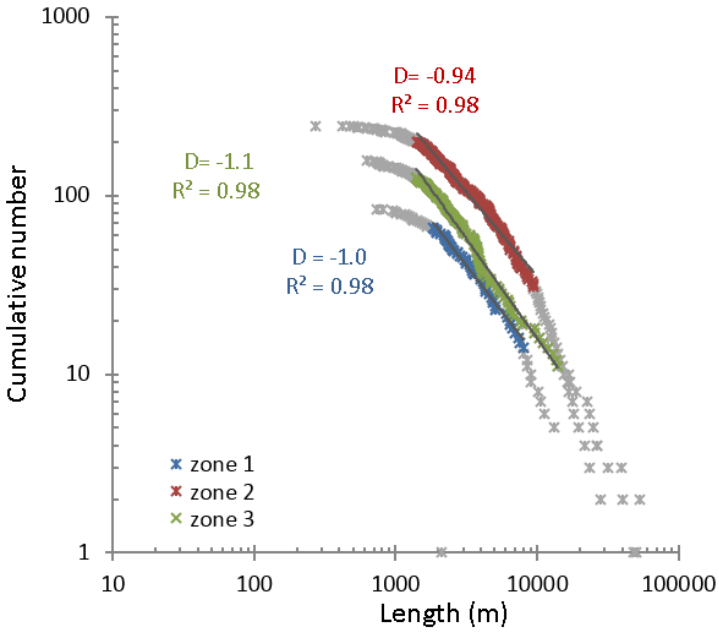

Figure 3.30. Cumulative length distributions of the fault population in the study area showing unbiased data (coloured stars) and excluded Biased data (grey stars).

3.7.10 Correction for trace length cumulative distribution

As mentioned earlier, data resolution and burial of fault tips may mask the true positions of fault tips and therefore underestimate fault lengths. However, having 620 faults with a fault trace-length population ranging from 272 m to 50477 m, with an average of 4788 m, make such trace-length data appropriate for fractal analysis. The effects of truncation are relatively more significant on smaller faults populations (Walsh et al., 1996, Watterson et al., 1996, Yielding et al., 1996). Moreover, the cumulative distribution for fault trace population was also corrected for truncation and censoring effects and yet again with no remarkable difference between corrected and uncorrected data. The power law exponent (D) for the length population for the three zones was found to be about (1.0), which is consistent with the range of 1.0 to 1.7 of previously published fault length populations observed in natural fault systems (Gauthier and Lake, 1993, Scholz et al., 1993, Watterson et al., 1996). This implies that few faults extend outside the defined zones as can be observed from Figure 3.4. Therefore, the data used in this study appear to be reliable to curry out analysis of scaling relations for fault populations.

It was observed in this investigation that the fractal dimension D for the fault trace length populations stays constant across the three zones in spite of different strain accommodation estimated for these zones (section 3.6.1), which contrasts with most fault linkage models that would suggest that, the value of D should decrease systematically with increasing fault strain (Cartwright et al., 1995, Cladouhos and Marrett, 1996). This consistency in D values may suggest that the fault length population is independent of strain.

3.7.11 Correction for missing displacement

As discussed earlier, the displacement values measured in this study are maximum values of the apparent throw for each fault, measured perpendicularly to the fault strike on DEM surface. The extent of displacement into the subsurface was not constrained due to lack of seismic data over this region of EARS. However, the only image of a seismic line I came across in the literature was found in (Morley and Ngenoh, 1999c) and shot by the National Oil Corporation of Kenya (NOCK) in 1990 over the study area at the southern end of Kerio Rift between Elgeyo escarpment and Kamasia horst (Figure 3.3). This seismic line (Figure 3.31 b) was processed and interpreted by Pope (1992) and Ngenoh (1993), and they found no significant structures in the processed line, however, the seismic data does show a large boundary fault, the Elgayo Fault (Figure 3.31 c), which marks the western boundary of the Rift. The DEM image show the continuation of the Elgayo escarpment on the surface (Figure 3.31 a).

This area of the northern central Kenya Rift is characterized by extensive basaltic lava flows as indicated in Ebinger (1989b). This area also has relatively similar compositions and lithology (Stoyan and Gloaguen, 2011). The brittle crust is predominantly composed by post-Miocene lavas, the thickness of volcano-sedimentary infill is 4.5-5 km (Hautot et al., 2000). The average seismic velocity for basaltic lavas is about 3500 m/s, and the seismic line shows that the Elgayo Fault extends down more than 2.5 sec (TWT), therefore the extent of fault displacement into the subsurface is about 5 km, which is about 2.5 times of the apparent throw observed at the surface. For that reason, in an attempt to account for the underestimated displacement in the study area, it is assumed that all mapped faults extend under the surface by the same factor of 2.5.

Subsequently, Multiplying all fault throw data in the three zones by 2.5 and adding the estimated surface throw for all faults has shown no significant change in displacement/ length relationship (Figure 3.32a) and cumulative distribution (Figure 3.32c) compared to the original plots (section 3.7.6 & Figure 3.21) other than shifting the distribution of the data to a higher displacement position within the graphs. Plotting the new (assumed) maximum displacement vs. length plot (dark blue points in Figure 3.32b) behind the published dataset shows that, some faults are plotted outside the range of published dataset which suggests that not all mapped faults have maximum throw of about 2.5 times the apparent throw originally defined from the DEM surface. The cumulative distribution of estimated maximum fault displacement attributes still exhibit a power-low distribution and maintain the same values of fractal dimension D as those obtained from apparent throw (Figure 3.21) in the three zones.

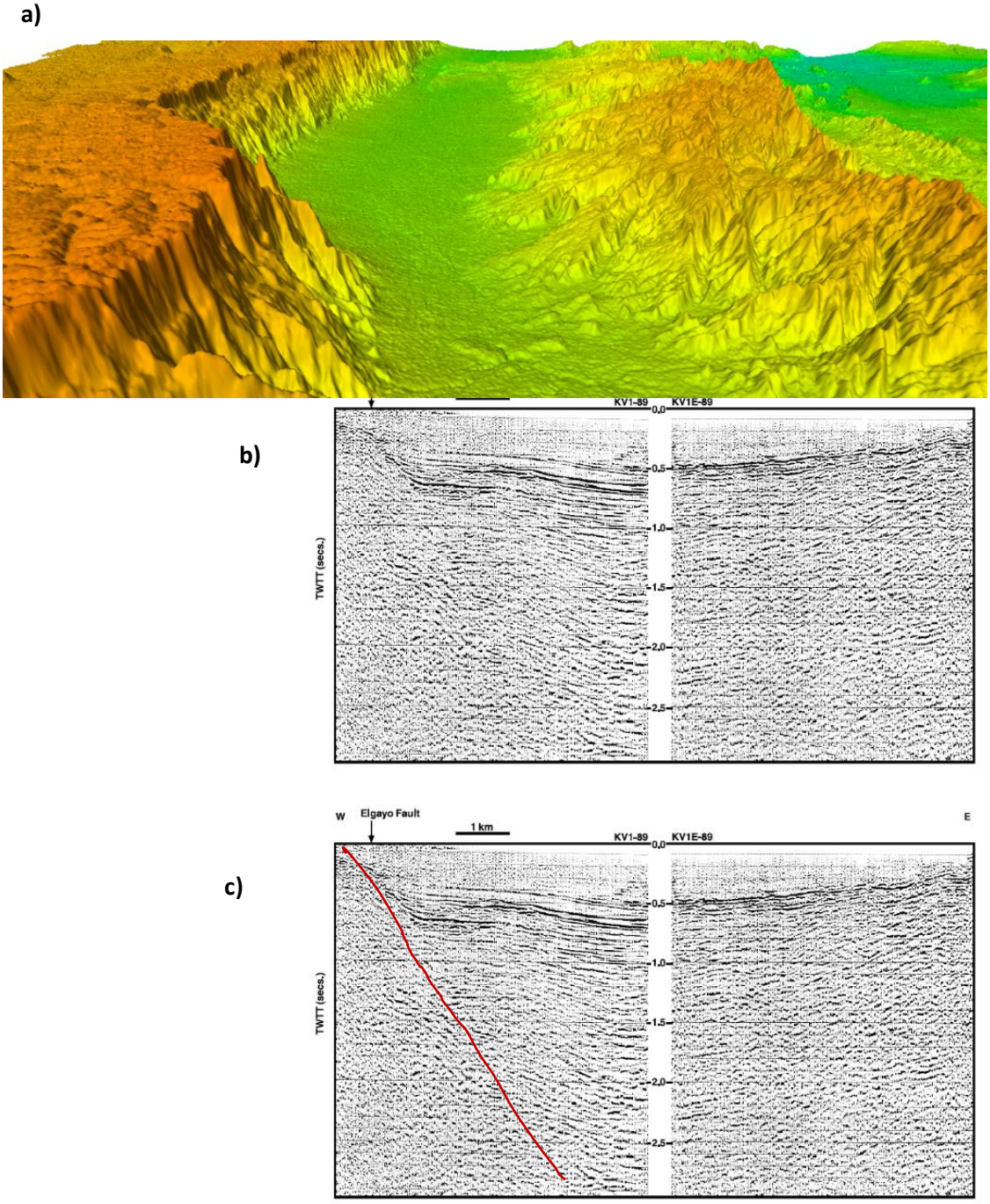

Figure 3.31. a) DEM surface showing Elgayo fault escarpment, b) seismic line in Kerio Rift, see Figure **3.3** for location c) interpretation of the Elgayo fault.

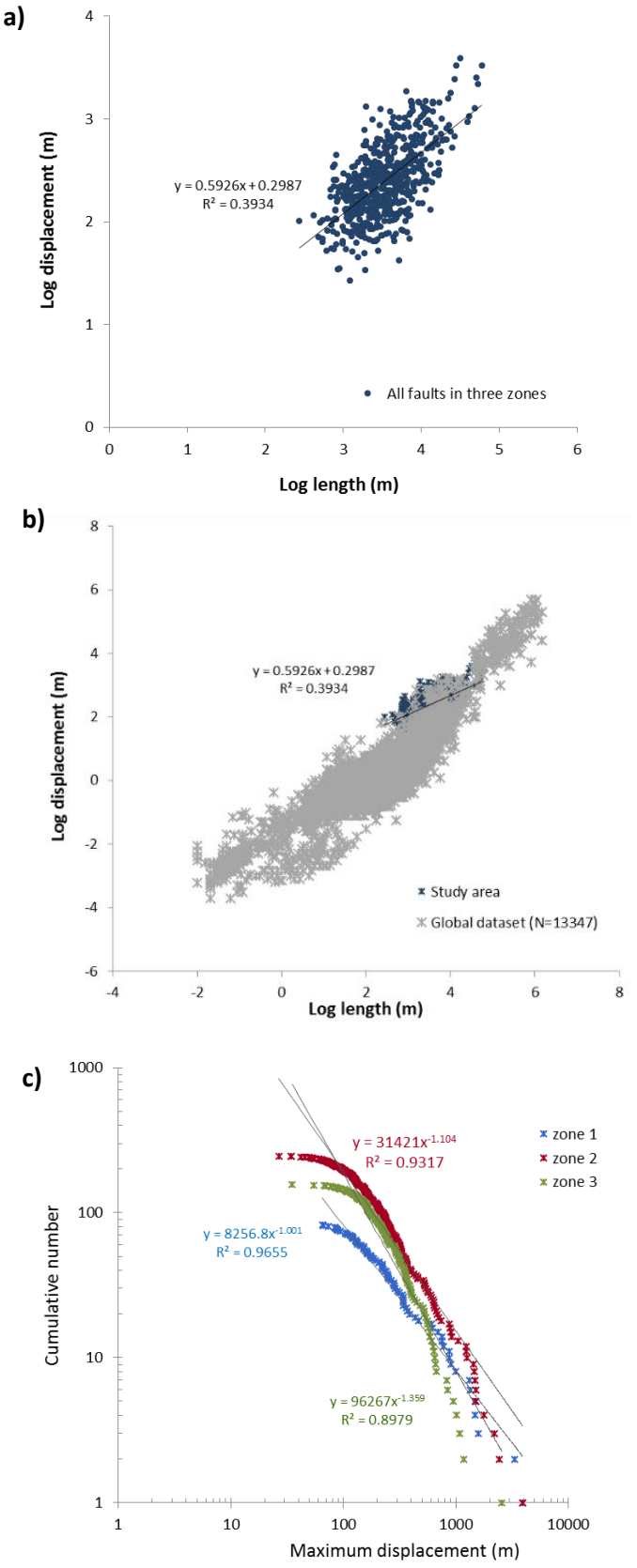

Figure 3.32. a) Log-log Plot the assumed max D vs L for faults from the study area along with published data set (Gillespie et al., 1992) b) Log-log plot for assumed max D vs L for relationship for all faults in the three zones c) Log-Log plot of fault maximum displacement against cumulative frequency for the three zones.

To sum up, the observations below show that the dataset used in the current study seem to be robust enough and the potential sampling and resolution errors seem to be insignificant, and that was indicated by:

- A reasonable match with major faults from published geological map.
- The general trend of segmented faults shows scattering, which is roughly equivalent to those of previous studies by (Peacock and Sanderson, 1991, Cowie and Scholz, 1992a, Cartwright et al., 1995, Peacock, 2002).
- Fractal dimension D values for fault throw populations are consistent with those defined from previous studies, which range from 1.0 to 1.5 (Scholz and Cowie, 1990, Marrett and Allmendinger, 1992, Watterson et al., 1996).
- The exponent (slop D) of power law distribution for the length population for the three zones is (1.0), which is comparable to the range of previously published fault length populations datasets, from different fault systems (the common range is 1.0 to 1.7) (Gauthier and Lake, 1993, Scholz et al., 1993, Watterson et al., 1996).

3.8 Discussion

3.8.1 Spatial distribution of strain

The spatial heterogeneity of strain was analysed through a model of Kuiper (1960) along the three Rift zones defined within the central Kenya Rift in order to characterize the pattern of deformation for each individual fault zone (section 3.6.2). graphs of spatial heterogeneity (Figure 3.11) have shown that cross-sections AA` & BB` in zone 1 (n= 149) in the northern part of the central Kenya Rift crosses through a region with less faulting where the strain is localized on large but fewer border faults. Cross-section CC` & DD` in zone 2 in the centre goes through an area with the largest number of faults (n= 295) that contribute to the overall strain accommodation, and therefore the deformation becomes more distributed and less heterogeneous, whereas cross-section EE` & FF` in the southernmost zone (zone 3 n= 177) show a slightly more localized domain of deformation as opposed to zone 2. The spatial strain heterogeneity of brittle deformation along this part of the central Kenya Rift suggests that there is a rather localized domain of deformation in the southernmost zone (zone 3), distributed domains of deformation in zone 2 in centre and a domain of localized deformation towards the north at zone 1.

Unlike zone 1 in the north and zone 3 in the south where deformation is concentrated on the Rift margins, zone 2 in the central part of the Rift near Bogoria Lake, the Rift valley exhibits dense and closely spaced en-echelon pattern of faulting, these characteristics are in contrast to the typical characteristics of an early continental, where the largest part of deformation is being accommodated by boundary faults with almost an absence of internal faults (e.g. Corti, 2009, Agostini et al., 2011b). Moreover, the fault geometry in

this zone also exhibits patterns of high fault interaction and linkage and associated relay structures (Figure 3.7) (see section3.7.7) that result from the strain being transferred between adjacent faults as indicated by Trudgill and Cartwright (1994), (2001), Walsh et al. (2003b), and Hus et al. (2005), these observations of increasing fault interactivity and linkage in zone 2 are also supported by analysis of power law scaling exponent for fault trace-length (section 3.7.7) by using the model of Vallianatos and Sammonds (2011) where, the q factor returns a value of ~2 that indicates a highly interactive and linkage fault system, however, zone 1 and 3 display Parallel or sub parallel fault geometries with less interaction (Figure 3.7e & f). In addition, as discussed above, zone 2 is characterized as a distributed domain of deformation whereas the spatial distribution of strain in zone 1 and 3 is generally localized. These contrasting characteristics observed in zone2 may suggest that they could be related to a different geological event rather than the same Rifting that involves zones 1 & 3.

3.8.2 Isolated faults and their implications for fault growth model

Unlike throw profiles of most isolated faults in zone2 that exhibit relatively large throw gradients with fairly peaked distributions (Figure 3.17a), throw profiles of most isolated faults in zone3 show a gentler throw gradients with a rather plateaued distribution (Figure 3.17b). Moreover, the plot for D\L relationship for isolated faults of zones 2 &3 Figure 3.18 and Figure 3.19a again, generally show that isolated faults in zone 3 are larger in throw compared to those of zone2. However, it is worth noting that even though some isolated faults in zone2 generally appear to be smaller in throw, their fault trace length appear to be to comparable with fault trace length of isolated faults in zone 3, which show much bigger throw (Figure 3.19b). This apparent under-displacement of isolated faults in zone2 could be as a result of establishing fault length at an early stage of evolution of the fault, and cumulative displacement is added later according to the models by Poulimenos (2000), Meyer et al. (2002), Walsh et al. (2002a) and Vétel et al. (2005). Therefore, if the smaller isolated faults in zone 2 have a comparable fault length as the bigger ones in zone 3, this may again suggest that these faults may grow in accordance to the constant length fault growth model, where near full fault length is established in early stage of growth.

Flat-topped (plateaued) isolated faults similar to those in zone 3, were interpreted by Soliva and Benedicto (2005) in their study as vertically restricted faults that accommodate less relative strain than unrestricted faults. However, the observed vertical growth trend for isolated faults in zone3 (Figure 3.18a) could be as a consequence of minimal lateral propagation and increase of throw, this observations again favour the near-constant fault length model (the alternative growth model) of Walsh et al. (2002a). This deviation from a fault growth model by self-similarity has also been observed in the Turkana Rift, North Kenya (Vétel et al., 2005). It has also suggested by Morley (1999b) that Rift bounding faults show no evidence of lateral propagation throughout the evolution of east African Rift system.

3.8.3 Cumulative distributions and their implications for fault growth and Rift evolution

Table 3.5. Averages of fault lengths and fault throws in the three **zones**

	Length (m)			Throw (m)		
	Min	Max	Average	Min	Max	Average
Zone1 (n = 149)	737	59608	5812	32	1336	171
Zone2 (n = 295)	272	53515	4775	27	1561	142
Zone3 (n = 177)	629	50477	4610	30	1020	117

The exponent value of the equation of the throw/Length trend line (Figure 3.15) may suggest that the fault system in the central Kenya Rift evolve in accordance to isolated fault model (see section 2.1.3.5), however, the correlation of coefficient (R^2) is very low, consequently, this exponent cannot be used to represent any fault growth model. Therefore, Patterns of fault growth can be deduced from fractal dimension of cumulative distribution of fault size populations (Poulimenos, 2000). The cumulative distributions of fault throw populations for the three zones (Figure 3.21) best fit to a power law distribution. The key parameter in describing a power law distribution is the exponent, or slope of the line. Differences in the exponent of power law scaling distributions of fault size population distribution is used to assess the contribution of different fault size to the strain accommodation. The higher the exponent of population slopes D (fractal dimension), the higher the contribution of small faults to strain accommodation (Marrett and Allmendinger, 1991), and

this reflects fault system development. Previous studies (e.g. Cartwright et al., 1995, Cladouhos and Marrett, 1996) and experimental models (e.g. Sornette et al., 1993) indicate that in all fault linkage models, the value of D (the exponent of slope of throw population curves) decreases systematically with increasing fault strain. This decrease indicates that the deformation is increasingly localised onto large faults as the fault system evolves to establish a more localized fault system (Marrett and Allmendinger, 1992, Cartwright et al., 1995, Cowie et al., 1995, Cladouhos and Marrett, 1996, Ackermann et al., 2001, Walsh et al., 2001, Walsh et al., 2003b, Moriya et al., 2005). This fact is evidenced in the current study for the examined fault throw attributes, where in zone3 in the south accommodates the least strain estimations (Figure 3.10 & Table 3.1) and has the highest fractal dimension of D=1.33 (Figure 3.21) but the smallest average fault length (Table 3.5), and this implies that zone 3 encompasses a larger number of small faults contributing to the strain accommodation more than Zone2 and zone1. As we move to zone2 in the centre that contains the largest number of faults, the power law exponent decreases to (D= 1.23) with the increasing strain (Figure 3.10 & Table 3.1), where the average fault throw is greater (Table 3.5). Further decrease in power-law exponents in zone 1 in the north to (0.99) where the highest strain was estimated, the number of faults is the least and the average fault trace-

length and fault throw is the greatest (Table 3.5) in this zone, this indicates that the strain is increasingly localised onto large border faults as the fault system evolves to establish a more localized fault system and more mature in terms of development. The mechanism of strain localization in continental Rifts has been attributed to crustal rheology, heat fluxes or changes in regional strain rates (Cowie et al., 2005).

This observed decrease of the power law exponent in the cumulative throw distributions for the three zones could be regarded as an indication of different stages of spatial and temporal fault evolution within this part of Kenya Rift. Therefore, this analysis may indicate that faults in zone3 in the south are in a less mature stage of growth than zone2 faults in the centre, and zone2 fault population is in a less developed phase of growth than faults in zone1 in the northern part of the study area. This phenomenon of northward increase in continental Rift evolution was also observed in the North Ethiopian Rift–Afar transition area (Soliva and Schultz, 2008) and the Main Ethiopian Rifts (Agostini et al., 2011b).

Graph of fault trace length populations exhibited that the power law exponents (D) for the length population in each individual zone is about (~1.0) (section 3.7.10), which stays almost constant in the three zone despite increasing strain, Given that, in all of the linkage models, the value of D

decreases systematically with fault strain (e.g. Cartwright et al., 1995, Cladouhos and Marrett, 1996), this consistency in D values may suggest that the fault length population is independent of strain, that is in contrast to fractal dimensions of fault throw population that decreased with increasing strain. Therefore, this would mean that the increasing strain correlates with increasing fault throws and nearly constant fault length, which leads to an increasing of D\L ratio, these observations are in line with results of Gupta and Scholz (2000) and Poulimenos (2000) for fault growth. If that is the case, this would explain the upward trend in the D\L ratio observed in Figure 3.15, (section 3.7.2). These observations favour the near-constant fault length model (the alternative growth model) by (Walsh et al., 2002a, Walsh et al., 2003a, Childs et al., 2009). This departure from a fault growth by self-similarity has also been observed further north in the Turkana Rift, north Kenya by Vétel et al. (2005).

Fitting to a power law distribution for fault length populations in the three zones is compatible with the low-strain settings of early continental Rifting (Gupta and Scholz, 2000a, Vétel et al., 2005). That is in contrast to a high strain settings where Rifts are more evolved and exponential scaling function appears in the cumulative distribution for fault lengths as observed in some studies (Anupma Gupta, 2000b, Ackermann et al., 2001).

3.9 Summary and Conclusions

Fault scaling relations within the central Kenya Rift have been examined for fault populations defined from ASTER DEM data in order to characterize any patterns of fault growth and distribution of strain accommodation along this part of the Rift. Three fault population zones (zone1, zone2& zone3) displayed distinct fault orientations; (NNE), (NNE to NNW) and (NNW) respectively. The relationship between fault length (L) and minimum throw (D) for the 620 picked faults fit reasonably to a power-law distribution and displayed a good fit within the spread of published global data set. Analysis of scaling properties of fault populations in the central Kenya Rift revealed that:

- Estimations of extensional strain revealed a progressive increase of strain from south to north.
- Interaction and linkage geometry observed in zone 2 indicate fault grow by segment linkage.
- Isolated faults in zone 3 are larger in throw compared to those of zone2, while the fault trace length appear to be to some extent comparable in the two zones. These inferences may imply that fault grow by establishing near maximum length in early stage and accumulating displacement later on in accordance to constant length fault growth model.
- The cumulative distributions of fault throw populations showed a decrease in the exponents (D) of power law distributions from the south (zone3) through the centre (zone2) to north (zone1), which indicates increasing strain. This decrease indicates that the strain is increasingly localised onto larger faults as the fault system evolves. Increasing fault throw population

with increasing strain while fault length population remains nearly constant, again agrees with the constant length coherent fault growth model.

- This decrease of power law exponent for fault throw could indicate different stages of spatial and temporal fault evolution within this part of Kenya Rift, which may suggest that faults in zone3 in the south are in a less mature stage of growth than zone2 faults in the centre, and zone2 fault population is in a less developed phase of growth than faults in zone1 in the northern part of the study area.
- Analysis of spatial distribution and heterogeneity of strain exhibits three domains of deformation in the three zones; a rather localized domain of deformation in the southernmost zone (zone 3), distributed domains of deformation in zone 2 in centre and a domain of localized deformation towards the north at zone 1. The observed increasing of the amount of strain and increasing fault maturity from the south to the north confirms the hypothesis that the amount of strain progressively increases and localizes onto few large faults as the fault system becomes more evolved as we move from the south to the north. These observations are in accordance with previous studies conducted within the Main Ethiopian and Afar Rifts.
- Results of this study showed that this part of Kenya Rift displays a range of variations not only in fault orientation, but also in strain accommodation, the amount of strain and fault growth along the valley of the Rift. Results of the current study also imply that the processes of progressive fault system maturity and strain localization onto large faults could happen even at relatively small scale of fault populations within the Rift system.

Chapte 4. Examining scaling properties of fault populations in the northern and central main Ethiopian rifts

4.1 Introduction

For the purpose of investigating the evolution of continental rifting along the EARS, the central Kenya rift has been investigated in chapter 3 as an example of the early stage of rifting in which continental rifting is characterized with large border faults that accommodate a significant amount of deformation (Cowie and Scholz, 1992a, Cowie and Scholz, 1992b, Cowie et al., 1995, Nicol et al., 1997, Meyer et al., 2002, Walsh et al., 2003b, Corti, 2009). Chapter 4 will investigate the brittle deformation in the central main Ethiopia rift (CMER) and the northern main Ethiopia rift (NMER) segments that respectively represent intermediate and late evolutionary stages of continental rifting. In the intermediate stage, the process of continental rifting involves an incipient migration of deformation from rift border faults to the rift axis where some internal faults start to emerge (Hayward and Ebinger, 1996, Agostini et al., 2011b) whereas the late stage involves localization of deformation within the rift axis, which gives rise to volcano-tectonic segments, and deformation being distributed across a large number of small-offset normal faults that occupy the weakened lithosphere within the rift axis (Hayward and Ebinger, 1996, Keir et al., 2006, Corti, 2009, Agostini et al., 2011b). 1509 fault traces (1041 for the NMER and 468 for the CMER) have been identified from DEM surface and manually mapped using the methodology described in section (2.2.2), and therefore, a new dataset (see appendix A) of the present day fault geometry

has been created for the sake of conducting a quantitative and statistical analysis on fault populations of these two rift segments (NMER & CMER) in order to characterize the pattern of fault growth and quantifying the strain distribution in these two regions, and hence inform our understanding about the evolution of continental rifting. Moreover, this chapter also tests the hypothesis that have been stated in chapter 1 (section 1.2) that; 1) the extensional strain increases from south to north, and 2) the average fault trace length in the late stage of continental rifting exemplified by the NMER is larger than that of the transitional stage represented in the CMER segment.

4.1.1 Study area

The second study area for this research encompasses a more evolved phase of continental rifting within the east African rift system (EARS) , namely in the main Ethiopian rift (Figure 4.1), two rift segments where investigated within this rift; the first rift being the central MER (CMER) that extends from Lake Ziway in the north up to Lake Awasa region in the south (Bonini et al., 2005) (Figure 4.2), and the axis of the rift trends ~N30°–40°E (Agostini et al., 2011b), to the south of the CMER is the southern MER (SMER) covers the area to the south of Lake Awasa up to the borders with the Kenya rifts through the wide area known as broadly rifted zone (Ebinger et al., 2000). The central MER (CMER) represent an intermediate evolutionary stage of rift evolution, with significant Quaternary activity of marginal deformation represented by boundary faults and subordinate axial faulting (Agostini et al., 2011a, Agostini et al., 2011b, Molin and Corti, 2015), these boundary escarpments are likely to

have formed during the first extension phase that affected the area during the early Miocene (20–21 Ma) in relation to the northern propagation of the Kenya rift (Molin and Corti, 2015).

The second rift segment is, the Northern MER (NMER) that trends ~N50°–55°E- (Agostini et al., 2011b) and extends from the Afar depression southwards to the Lake Koka area (Bonini et al., 2005) (Figure 4.2). The NMER is characterized by tectono-magmatic deformation localized at the rift axis (Hayward and Ebinger, 1996, e.g. Boccaletti, 1998, Ebinger and Casey, 2001, Keir et al., 2006, Corti, 2009, Agostini et al., 2011a, Keir et al., 2013), where further extension is accommodated by small-offset normal faults controlled by magma injection at depth (Corti, 2009, Keir et al., 2006). The marginal escarpments at this stage of rifting are inactive and undergo erosion (Keir et al., 2013, Agostini et al., 2011a, Corti, 2009, Hayward and Ebinger, 1996), that is in contrast to the central Kenya rift (discussed in chapter 3), a typical initial stage with deformation localized mostly along boundary faults (e.g. Baker and Wohlenberg, 1971, Morley et al., 1992, Hautot et al., 2000). The boundaries between the NMER and CMER (Figure 4.2) were defined in accordance to the division by Hayward and Ebinger (1996) that were also used by Keranen and Klemperer (2008), Corti (2009) and Agostini et al. (2011b).

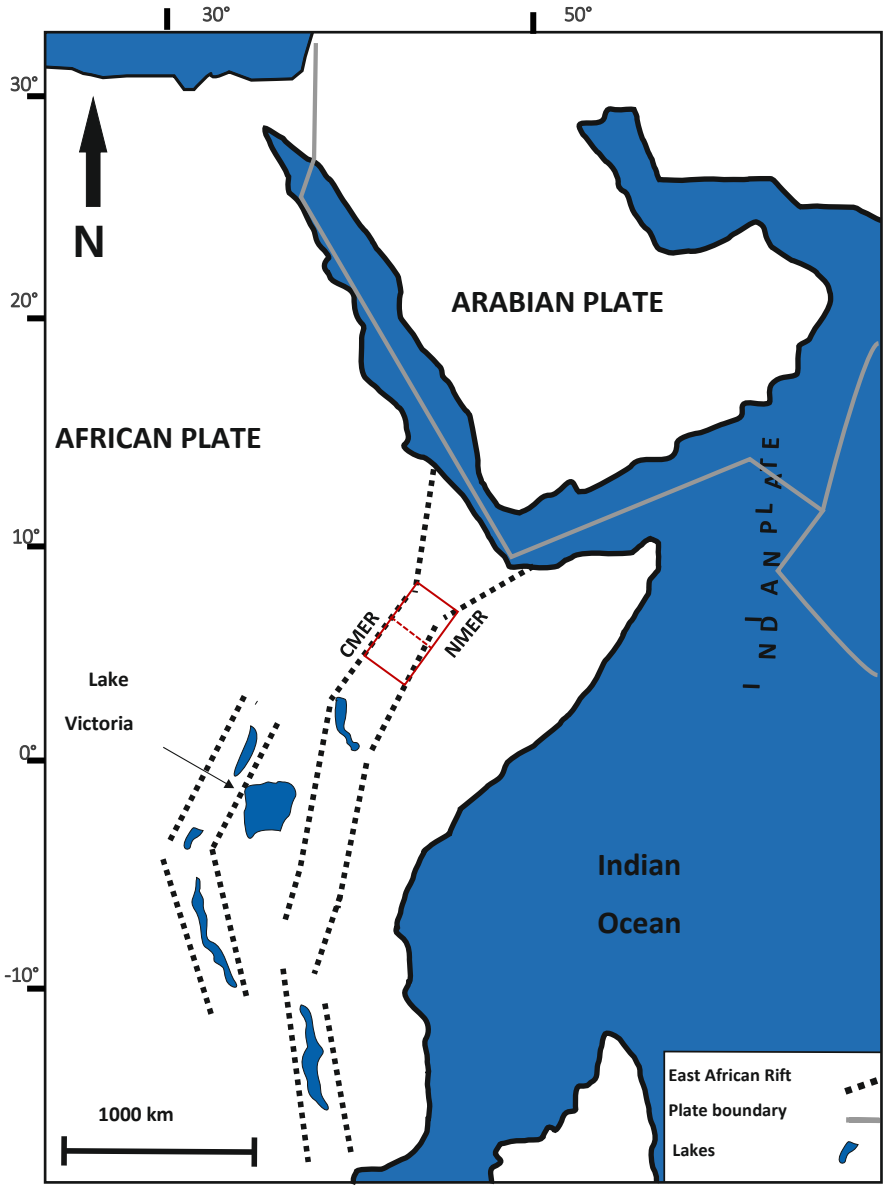

Figure 4.1 Location of study area the within the main Ethiopian Rift MER)

4.1.2 Geological background

The Main Ethiopian Rift (MER) (Figure 4.1) is a key rift zone in the East African Rift (EARS). The MER extends from the Afar depression in the north to Turkana depression in the Kenya Rift to the south (Corti, 2009, Ebinger, 2005, Chorowicz, 2005). The MER is considered to be an ideal location to investigate the evolution of continental rifting as it manifests all the different stages of continental rifting, from rift initiation to incipient oceanic spreading (Ebinger, 2005, Molin and Corti, 2015, Agostini et al., 2011a, Corti, 2009, Hayward and Ebinger, 1996). The depression of the MER divides the uplifted western (Ethiopian) and eastern (Somalian) plateaus. Structural and stratigraphic patterns within the northern Main Ethiopian Rift indicate that extensional strain has migrated from the border faults to a narrow (20 km) zone within the rift axis from 2.5 Ma to the present day (Maguire et al., 2006).

The rift valley in the Main Ethiopian Rift is ~80 km-wide and its maximum elevation is ~1700 m, whereas this elevation decreases gradually northward into the Afar depression (Corti, 2009). Local increases in the rift valley elevation are generally due to volcanic structures that overlie older sedimentary rocks, as in the northern MER where several volcanoes emerge from the flat rift axis (Corti 2009). The rift axis comprises of oblique intersecting en- echelon style fault zones known as Wonji Fault Belt, which formed as a result of an oblique extension stress in the Quaternary (Boccaletti 1998). Late Pliocene-Quaternary volcanism is also contained in the rift axis (Morton, Rex et al. 1979).

Volcanic activity in Ethiopia started about 30 Ma ago with uplift followed by eruption of large volumes of basalts, and oceanic crust evolution from Pliocene

to the present time (Mohr and Zanettin 1988, WoldeGabrial, Aronson et al. 1990). Baker (1987) and WoldeGabrial et al. (1990) found that faulting in the main Ethiopian rift has occurred in stages so that initial half grabens had produced a largely symmetrical graben structure by 3.5 Ma. They also found that the main Ethiopian rift witnessed six episodes of volcanic activity since the mid-Oligocene or before, all those episodes contained the eruption of transitional basalts, but no evidence was found of lateral migration of volcanism from flanks to the rift valley as observed in the Kenya rift. The Ethiopian flood basalts have been attributed to melting related to the activity of single or multiple mantle plumes (Afar plume and /or Kenyan plume) intruding the base of the continental lithosphere (Ebinger and Sleep 1998).

The MER has been traditionally divided into three main rift zones; 1) the Northern MER (NMER), 2) the Central MER (CMER), and 3) the Southern MER (SMER), based upon variations in crustal and lithospheric characteristics (e.g. Hayward and Ebinger, 1996), rift axis orientation, geometries of normal fault (e.g. trace length, vertical throw) and timing of faulting and magmatism (Corti, 2009, Agostini et al., 2011b). These three rift zone have been interpreted to represent different stages of the continental rifting process from early rifting in the Southern MER to more evolved stages in the Central and Northern MER (Hayward and Ebinger, 1996, Boccaletti, 1998, Bonini et al., 2005).

The Northern MER (NMER) trends ~N50°–55°E- (Agostini et al., 2011b) and extends from the Afar depression southwards to the Lake Koka area (Bonini et al., 2005) (Figure 4.2). The major border faults in this rift zone developed since ~10–11 Ma and display an orientation on average of $N50^0$ (Hayward and Ebinger, 1996, Kazmin et al., 1980, Wolfenden et al., 2004). The axis of the

central MER (CMER) trends ~N30°–40°E (Agostini et al., 2011b) and extends from the Lake Ziway in the north up to the Lake Awasa region in the sought (Bonini et al., 2005) (Figure 4.2). Major border faults in this rift zone are thought to have started to developed since ~8.3–9.7 Ma and display an orientation of an average of $N30^0$-35^0. The Southern MER (SMER), covers the area to the south of Lake Awasa (**Figure 4.2**) up to the borders with the Kenya rifts through the wide area known as broadly rifted zone (Ebinger et al., 2000). The trend of this rift zone ranges between ~N0° to 25°E. Boundary faults in this rift zone were well developed after about 18 Ma with an orientation of about N-S (Bonini et al., 2005).

4.1.3 Method and Data Collection

The methodology used in this study for data acquisition and data analysis is similar to that used in chapter 3 for the central Kenya rift, a detailed description of the DEM data and the method used to create the shaded relief surfaces for the study areas is described in chapter 2 (section 2.2.1). Capturing fault traces and measurements of fault lengths and throws from DEM surface was achieved by the approach described in chapter 2 (section 2.2.2). Hence, a dataset encompassing attributes of fault length, throws, aspect ratio (D\L) and fault orientaion has been acquired and analysed in the current chapter for 1041 and 468 faults from the NMER and the CMER segments respectively (see appendix A for full dataset).

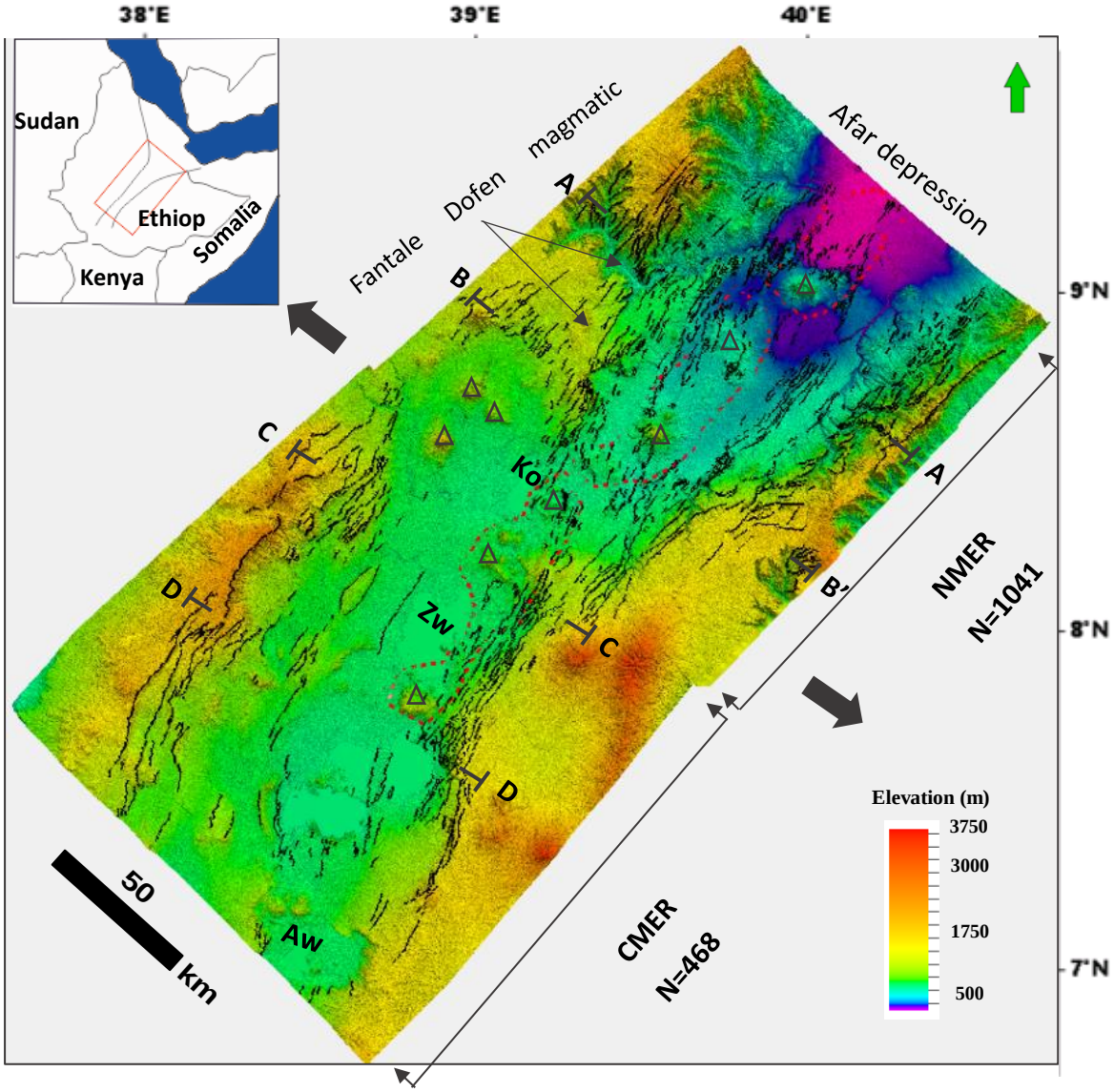

Figure 4.2. DEM surface showing mapped faults. Red dashed lines indicate Quaternary-Recent basaltic volcanism from Ebinger and Casey (2001). Red triangles are major volcanoes after **(Cornwell et al., 2006)**. Black arrows indicate extension direction. Ko: Lake Koka; Zw: Lake Ziway; Aw: Lake Awasa;

4.2 Analysis

Fault populations in a given tectonic setting exhibit systematic scaling properties which can be characterized statistically. Thus, a number of analysis have been used in this chapter in order to examine fault scaling relation of populations in the brittle crust of the NMER and the CMER segments, these analyses include the spatial pattern of faulting, the displacement, length and spacing size frequency distributions.

4.2.1 Strain accommodation

4.2.1.1 Strain estimations

The extensional strain of the fault networks for both the NMER and CMER rift zones was estimated by using two transect lines in each of these rift zone, in order to estimate how much strain is accommodated at each zone, these transects lines were defined perpendicular to the average trend of the fault population (see Figure 4.2 for location). The trend of transects AA`, BB` in the NMER rift zone is ~NW-SE for transect CC` DD` in the CMER rift and ~WNW-ESE.

The extensional strain was estimated in two ways that are; 1) Estimations of the horizontal separation (heave) through measuring the horizontal separation distance between the hanging-wall and footwall cut-offs, measured perpendicular to the trace of the fault on the map view for all faults along each cross-section. The extensional strain expressed by total fault heaves was then estimated by summing fault heaves across each cross-section. 2) Estimations of the vertical separation (throw) by measuring picks of hanging-wall and

footwall cut-offs for all faults at the point of intersection with the cross-sections, the extensional strain expressed by total fault throw was then calculated by summing fault throws across each cross-section. Estimating both total heaves and throws provide different ways of characterizing the strain distribution and are geometrically related to one another, Moreover, accumulation of erosional and/or depositional sediment reduces the apparent height of, which may introduce systematic error into throw measurements and strain estimations. Therefore, the rationale behind using both estimations is due to the lack of any other data (other than DEM data) that can be used to constrain estimations of fault displacements (heave and throw), consequently, estimations of the vertical separation (throw) was used as a validation to insure that the result is not biased by measurement errors in case only the horizontal separation (heave) is measured. Values of the total fault heaves and total fault throw were estimated along each cross-section and shown in (Table 4.1). However, all of these values for extension are considered minima, as later basalt flows may have filled in basins, decreasing the apparent offset along individual faults.

Plots of strain accommodation estimated from fault heaves and fault throws (Figure 4.3) show comparable trend in both graphs, where the strain values are fairly comparable at transects CC` and DD`, then a sharp increase in the strain is observed towards the north at transects BB` and AA`. Consequently, strain estimations in both methods revealed a dramatic increase of strain from the CMER in the south to the NMER in the north.

Table 4.1 Total fault heaves and throws obtained from each cross-section.

Zones	NMER		CMER	
Cross-sections	AA`	BB`	CC`	DD`
Total throws (m)	30834	19830	7941	8438
Total heaves (m)	17805	12393	6489	6327

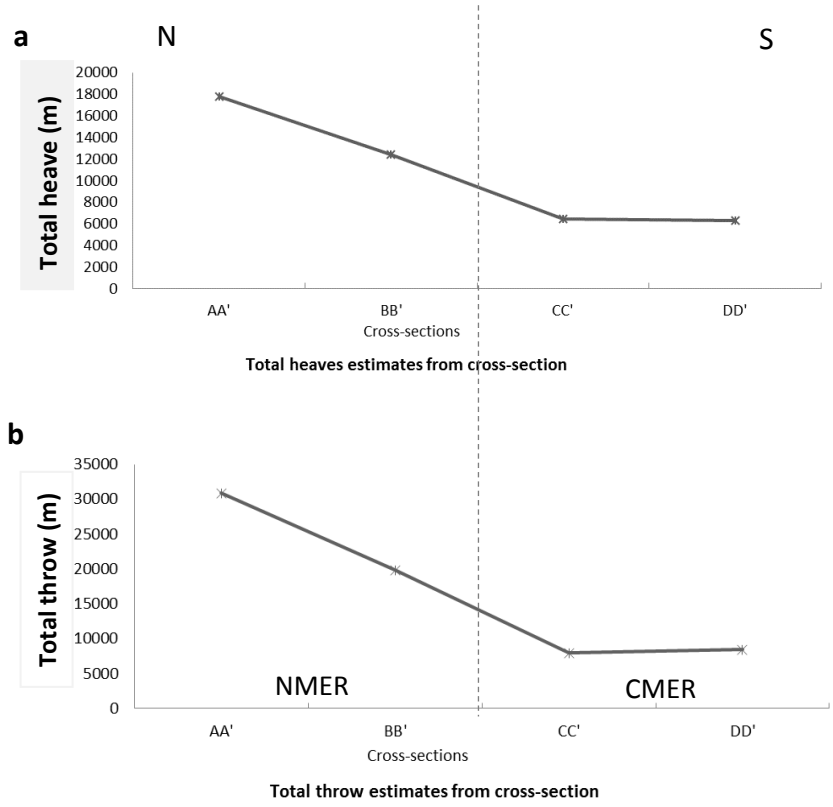

Figure 4.3**.** Strain estimations from summing fault heaves (a) and throws (b) across four transects in study area (see Figure **4.2** for the cross-sections locations)

4.2.1.2 Spatial heterogeneity of extensional strain and faulting

Spatial heterogeneity of strain was quantified along the NMER and CMER rift zones in the same way as presented in chapter 3, section 3.6.2 by using the model of Kuiper (1960) (see section 2.1.4.4). Table 4.2 displays values of heterogeneity of fault frequency (Vf) represented by fault spacing and heterogeneity of extensional strain (Vs) represented by fault heaves (see section 2.1.2.2 for details). Graphs of cumulative distributions of fault frequency and extensional strain (Figure 4.4) for transect AA`, BB` in the NMER rift zone and CC` DD` in the CMER rift zone indicate that the spatial heterogeneity of both fault spacing Vf and extensional strain Vs varies along strike of the fault network in the two rift zones, this is supported by the values of Vf and Vs in (Table 4.2).

The transect AA`, BB` in the NMER exhibited small gradients, which indicates homogeneous distribution of deformation for both fault spacing Vf and extensional strain Vs (Figure 4.4 a & b). Segments of low gradient represent lower extension, whilst steep slopes represent larger extension. As for plots of cumulative number of (Vf) versus distance (Figure 4.4 a & b dashed grey lines), segments of high gradient represent high frequencies of faulting, whereas segments of low gradients indicate low frequencies. However, transect CC`, DD` in the CMER zone show large steps and gradient changes, which indicates heterogeneity and localized deformation for both extensional strain Vs and fault frequency Vf, (solid line and dashed lines respectively , Figure 4.4 c & d). From these graphs it is noticeable that transects CC`, DD` in the CMER zone cross through a region with less faulting, evidenced with a significant portion in the graphs with no strain, where the strain is localized on fewer faults

at rift borders and near the borders towards the rift axis whilst the deformation becomes distributed across more faults for transect AA`, BB` in the NMER zone towards the north. Moreover, these cumulative distribution graphs show a localized domain of deformation to the south at the CMER zone and a distributed domain of deformation to the north at the NMER zone. The domain of localized deformation represented in CC` & DD` (Figure 4.4 c & d) shows higher heterogeneity of extensional strain Vs >= 0.47 and higher heterogeneity of fault frequency Vf >= 0.52 whereas cross-sections (AA` & BB`) (Figure 4.4 c & d) that representing the domain of distributed deformation appear to have much lower heterogeneity of Vs <= 0.37 and Vf <= 0.27 (Table 4.2).

Table 4.2. Values of heterogeneity of fault frequency Vf and extensional strain Vs.

	Vs	Vf
AA'	0.37	0.25
BB'	0.32	0.27
CC'	0.47	0.52
DD'	0.89	0.67

The along strike variations in the heterogeneity between localized faulting to distributed faulting is shown in (Figure 4.5), where values of heterogeneity both of faulting Vf (fault frequencies) and extensional strain Vs (total heaves) are plotted against locations of transects along strike. These graphs illustrate the decrease of spatial heterogeneity for Vs and Vf from the CMER rift zone to the NMER, and the dashed line in the graph marks the transition from

localized strain deformation in the CMER to more distributed strain in the NMER. Moreover, the effect of total extension estimated at each cross-section on the amount heterogeneity was also examined by plotting values of heterogeneity of fault frequency Vf and extensional strain Vs against estimated total extension (Figure 4.6), the result showed that there is no correlation between the total fault extension and variations in Vf and Vs, which indicates that the heterogeneity within the network is independent of bulk extension, this lack of correlation has also been observed in similar investigations as shown in Moriya et al. (2005) and Putz-Perrier and Sanderson (2008b).

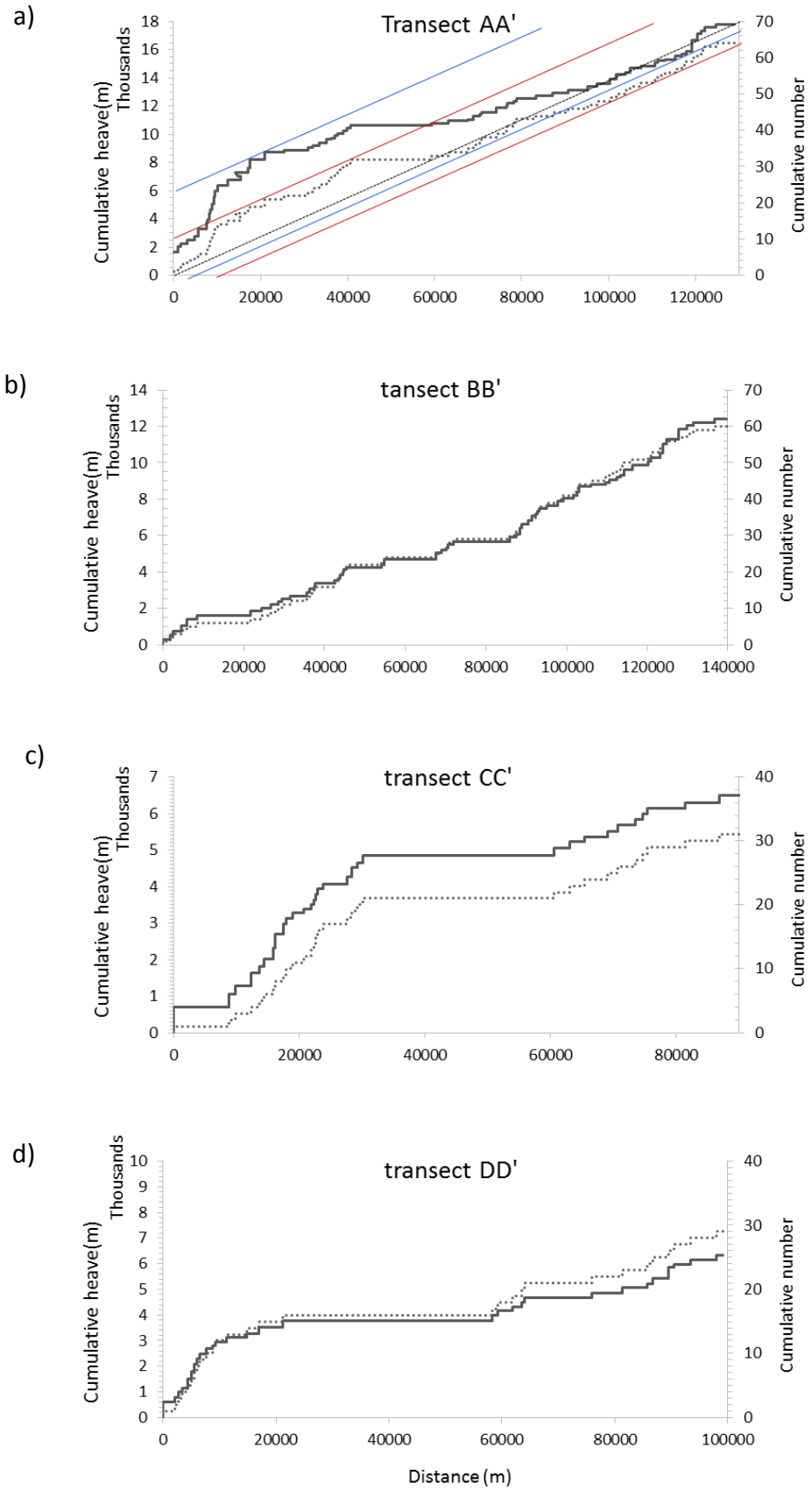

Figure 4.4. Cumulative plots for transects AA`& BB` (NMER), CC` & DD` (CMER) showing the spatial distribution of extensional strain Vs (solid line) and fault numbers Vf (dotted line). Blue lines are Max & Min deviation from uniform distribution (diagonal dashed line) for Vs, red lines are Max & Min deviation from uniform distribution for Vf.

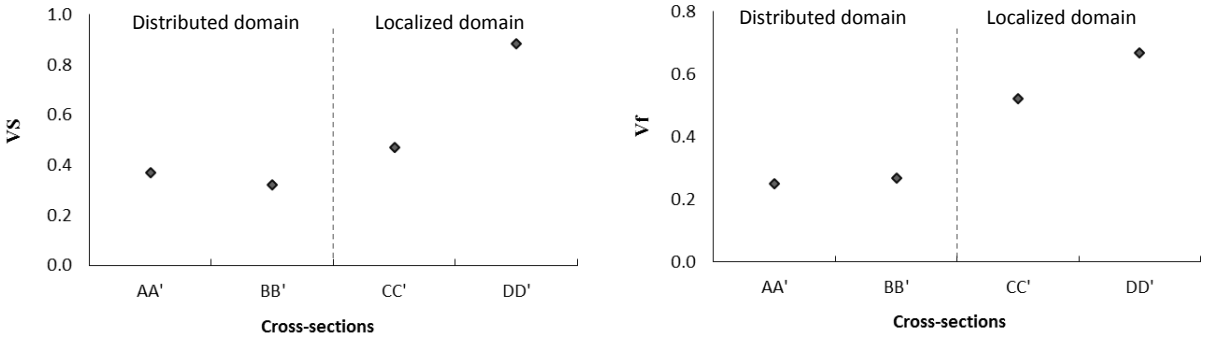

Figure 4.5. Along strike variations in the heterogeneity measures for Vs and Vf

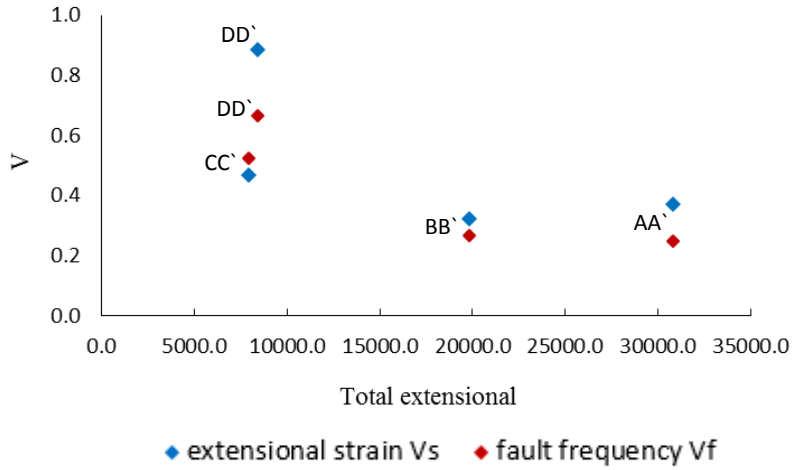

Figure 4.6. Heterogeneity measures compared with the overall extension accommodated by each transect line along the rift

4.2.2 Relationship between fault trace length and throw

As shown in the literature review (Section 2.1.3.1), it has generally been assumed that there is a proportional relationship between the fault length (L) and the throw/displacement (D). Therefore, displacement and length data for 1041 and 486 normal faults were identified and manually digitized from DEM surface of the northern main Ethiopian rift (NMER) and the central main Ethiopian rift (CMER) respectively (see section 2.2.1 and 2.2.2 for description of the DEM data and the way in which faults were picked). The fault interpretation was validated by plotting the displacement\ length data for faults of the northern NMER and the central MER along with published displacement-length data collected from outcrops of different tectonic settings with different rheological properties around the world for 13347 fault as shown in (Gillespie et al., 1992, Bailey et al., 2005) (Figure 4.7). The mapped faults from both NMER and CMER rift zones fit reasonably well within the range of normal faults of published data set, this calibration is crucial as it insures that further analysis can be carried out on the dataset. What can be considered as another validation is that, plotting the length/ throw dataset on logarithmic scale (Figure 4.8) showed a general trend towards increasing throw (D) with length (L), but with a large scatter of similar trend for both rift zones that spans about two orders of magnitude in both variables, in the same way as shown by the dataset of central Kenya rift (chapter 3). This scattering has been known as a common feature in fault studies and has been attributed to: combining data sets from different lithology and material properties (e.g. Cartwright et al., 1995, Peacock and Sanderson, 1991, Peacock, 2002, Cowie and Scholz, 1992a), fault growth and segment linkage (Cartwright et al., 1995, Schlische et al., 1996, Cartwright et al., 1996, Mansfield and Cartwright, 2001), sampling effects and inaccurate

measurement of fault displacement and length. The current data used in this research in the three study areas (The central Kenya rift, the central and northern MERs) are characterised by relatively homogeneous lithology of volcanic sediments of post Miocene lava (Stoyan and Gloaguen, 2011), which could rule out the cause of the large scatter to different lithology.

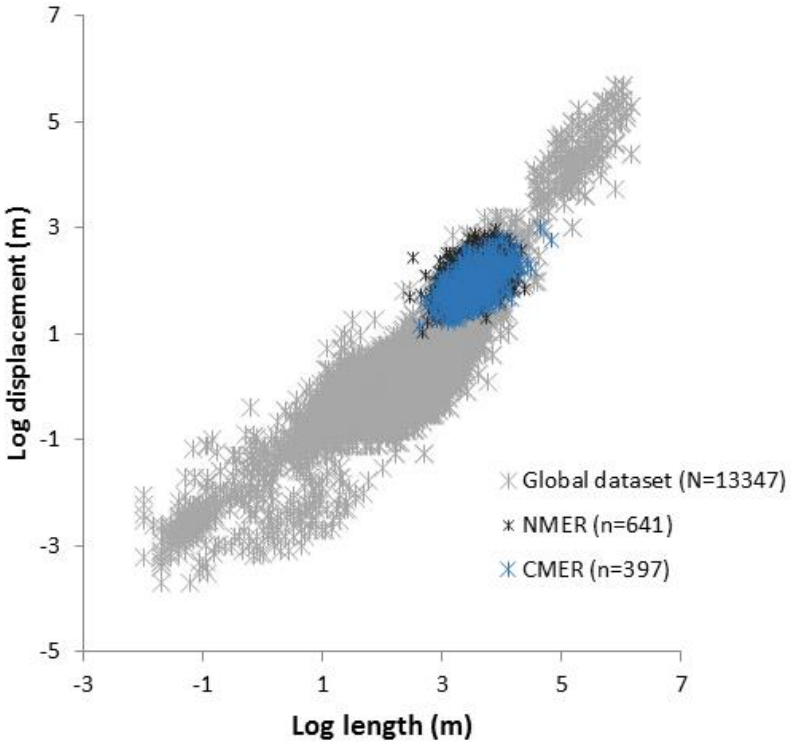

Figure 4.7. Log-log Plot of fault length vs minimum throw faults in NMER and CMER plotted along published data set (Bailey et al., 2005).

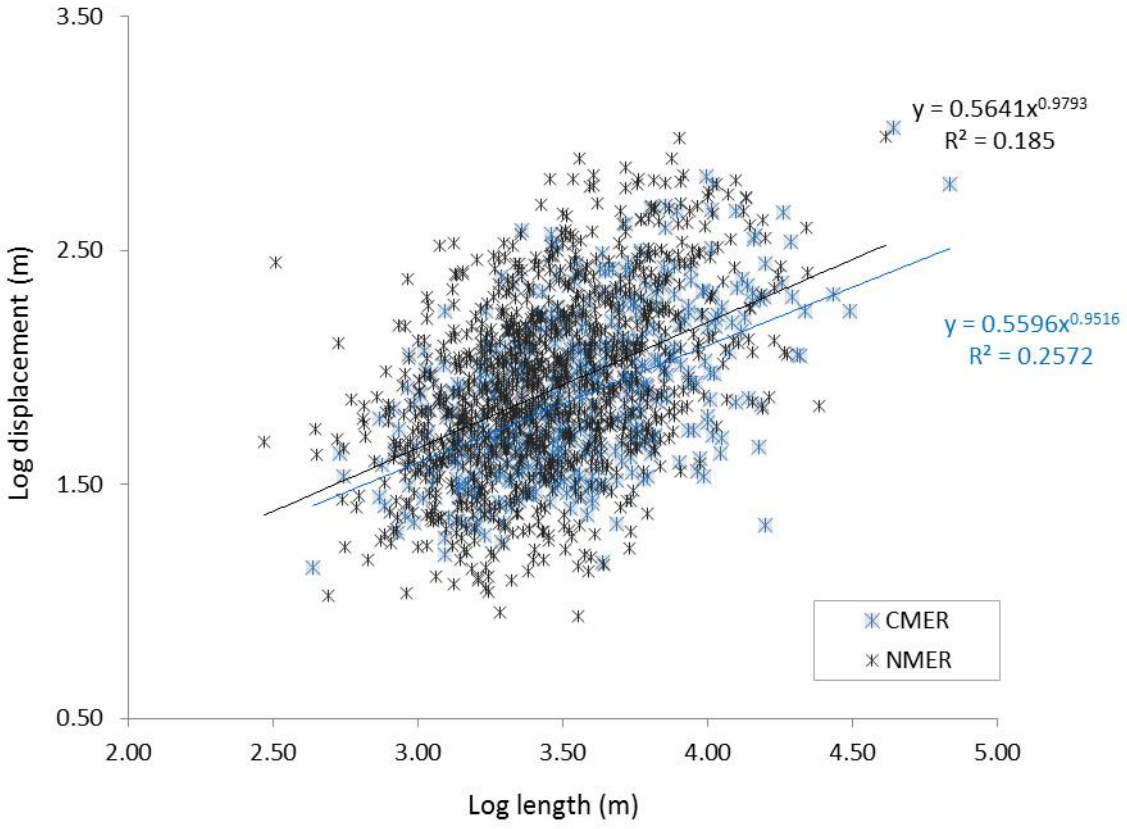

Figure 4.8. Log-log Plot of fault length vs minimum throw faults in NMER and CMER.

4.2.3 Analysis of fault scaling populations

A number of analytical techniques have been applied to the fault size attributes in the northern main Ethiopian rift (NMER) and the central main Ethiopian rift (CMER), in the same way as in chapter 3, including the quantitative characterization of trace length, throw and spacing, in addition to strain estimations and spatial heterogeneity of strain and faulting. Results of these analysis were then used to infer the nature of normal fault evolution, and consequently the evolution of the NMER and CMER rift segments, these results were also compared with those from the central Kenya rift (study area1 chapter 3) in the discussion chapter (chapter 7).

4.2.3.1 Fault throw populations

Cumulative frequency distribution function (CDF) is the most common way to describe attributes of fault populations (e.g. spacing, length, displacement) (Childs et al., 1990, Walsh et al., 1991, Jackson and Sanderson, 1992, Cladouhos and Marrett, 1996, Bonnet et al., 2001). Therefore, a fault throw population dataset measured in 2D method for the rift zones NMER and CMER were plotted by ranking the attribute data in a descending order and then plotting fault length attribute against the cumulative frequency, where both the x-axis and the y-axis are plotted in a logarithmic scale (Figure 4.9 a& b).

Standard statistical function that contain power law, lognormal and exponential laws have been used to examine the best fit for the fault length data (Figure 4.9 a & b) through the least squares estimation or coefficient of determination (R^2) method. This standard statistical function has been widely

used in geological studies (e.g. Pickering et al., 1995, Pickering et al., 1996, Poulimenos, 2000, Peacock, 2002, McCaffrey et al., 2003b, Bailey et al., 2005, Soliva and Benedicto, 2005, Soliva et al., 2006, Soliva and Schultz, 2008).

Unlike fault throw data from the central Kenya rift (chapter 3) that was generally described by power law distribution, fault throw population for the NMER and CMER best fit to both log-normal and an exponential distributions based upon value of R^2 (Table 4.3). However, the power-law distribution also fit the data with lesser degree of (Table 4.3). The extreme large and small values that are not considered as representative for the population and yet bias the distribution have been removed from the distribution, which further confirmed the best fit to be exponential and log-normal for the throw data in both the NMER and CMER (Figure 4.10 a& b).

Table 4.3. Results of functions fit to the fault throw data.

Rift zone	Function fit	R^2 (all data)
NMER	Log-normal	0.97
	Exponential	0.98
	Power-law	0.86
CMER	Log-normal	0.96
	Exponential	0.95
	Power-law	0.90

Moreover, to examine if the observed exponential and log-normal distributions are real, more rigorous methods were applied on the fault throw population to assess the degree of fit between the data and underlying statistical model (e.g. power law, exponential or log normal). These methods are: 1) Maximum

Likelihood Estimation (MLE) process, which is a type of goodness of fit algorithm which iteratively minimizes the error of goodness of fit. 2) A Kolmogorov-Smirnov (KS) statistic test, which is a further goodness of fit measure that measures the distance between the data and hypothesized function fit. These two methods are contained within the MatLab code developed by Healy et al. (2017), which was used in the analysis for this section. The cumulative distribution and histogram plots (Figure 4.14 & Figure 4.15) of fault trace length populations for both the NMER and the CMER zones best fit to log-normal distributions. The probabilities of the analysed throws to be Log-normal were 85% and 71.5% for the NMER and CMER zones respectively.

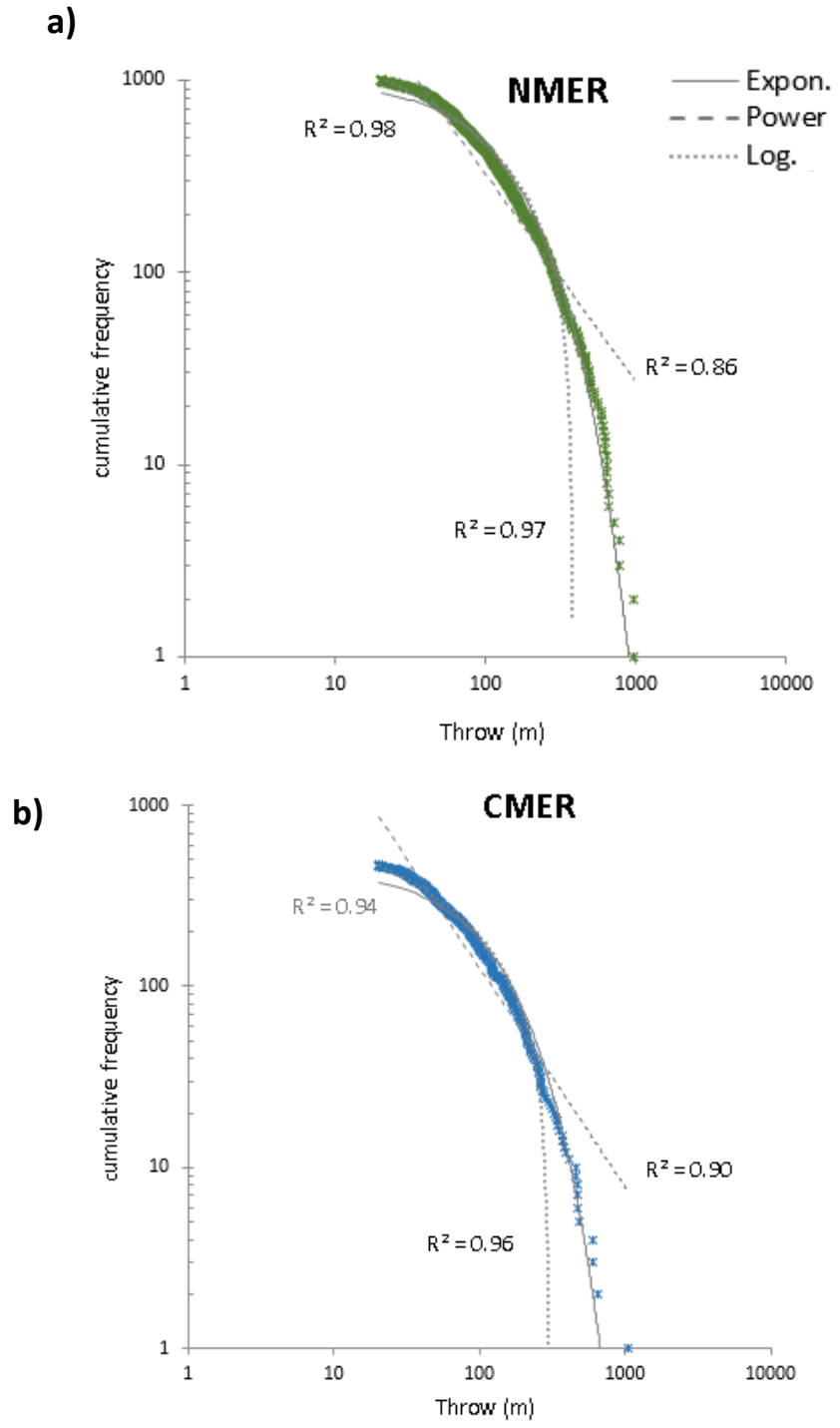

Figure 4.9. Log-Log plot of fault throw vs cumulative frequency from 2D data for a) the NMER and b)the CMER, showing power, exponential and log-normal laws (see Table **4.3**)

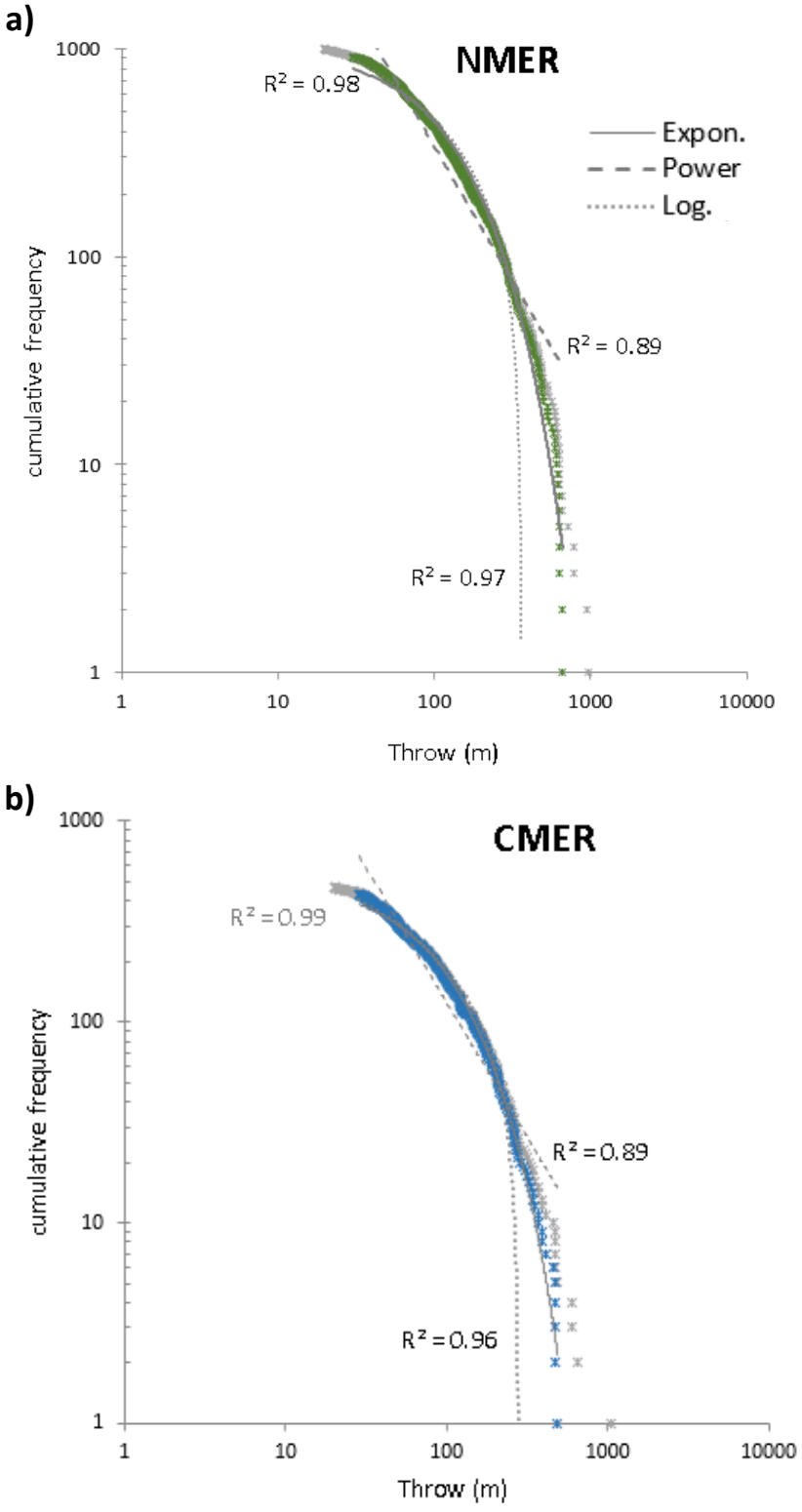

Figure 4.10 Cumulative throw distributions of the fault population in NMER and CMER showing the best fit of statistical distributions after eliminating the extreme value from the data (grey stars)a.

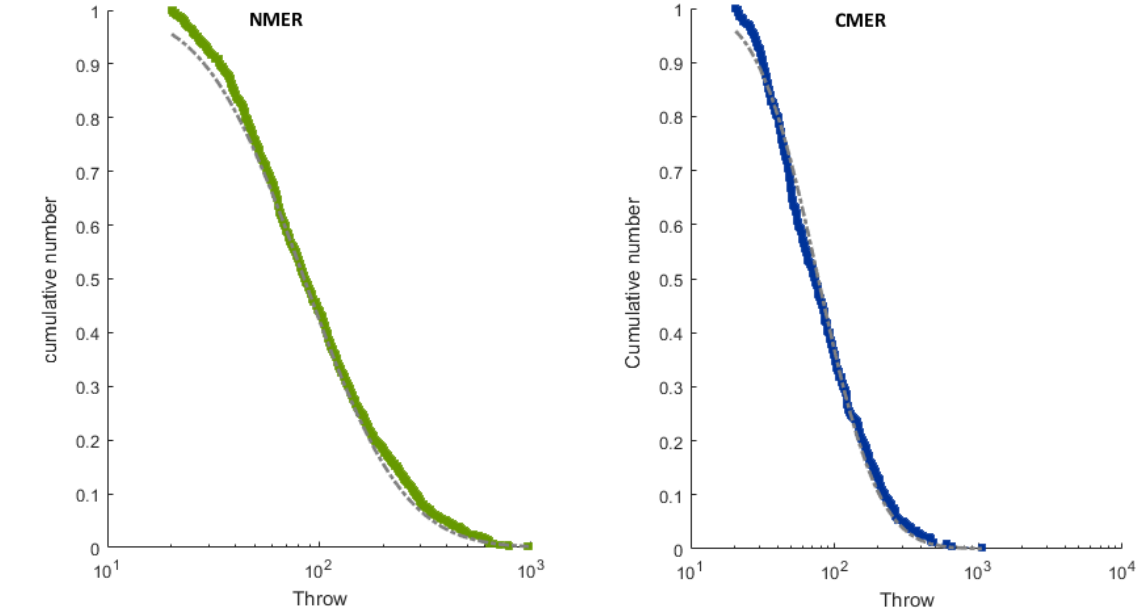

Figure 4.11. Log-Log plot showing log-normal distribution of fault throw vs cumulative from 2D data for the NMER (left) and the CMER (right)

4.2.3.2 Fault length populations

Fault length population data measured in 2-dimensions (see section 2.2.2) for the rift zones NMER and CMER were plotted as fault length values versus cumulative frequency when both the x-axis and the y-axis are plotted in a logarithmic scale.

Power law, lognormal and exponential functions have been applied to the cumulative distribution of fault trace length (**Figure 4.12**), and the goodness of fit was examined by coefficient of determination (R^2). **Table 4.4** shows that the log-normal and exponential models are generally the best fit for fault length data in both the NMER and CMER. Power-law model also fit the data with lower degree in both rift segments. The extreme values at the upper and lower ends of the curve have been removed from the distribution, because they are either too small or too big to the majority of the data, which may bias the distribution. Eliminating the data that are not representative for the population further improved the best fit for exponential and log-normal for the length data for both the NMER and CMER, and increased the gap with power-law model (Figure 4.13 a& b).

Results of cumulative frequency distribution that show that attributes of fault throw and fault length in both the NMER and CMER fit to the same statistical distribution are in line with the view that has been indicated in several studies (e.g. Walsh and Watterson, 1988, Peacock and Sanderson, 1991, Gillespie et al., 1992, Cowie and Scholz, 1992a, Cartwright et al., 1995, Cowie, 1998a, Kim and Sanderson, 2005) that there is a strong correlation between displacements D and fault lengths L, where the distribution of fault length follows similar scaling functions as fault displacement/throw.

The curve of the exponential distribution for the NMER zone appears to be steeper than that of the CMER (Figure 4.12). This steep slope represents relatively more small faults and relatively fewer large faults in the data set, this observation agrees with the fault length statistics shown in Table 4.5 & Table 4.6, where the average fault length in the NMER is smaller than that of the CMER, it is also noted that the negative slope of the exponential trend increases in the CMER compared to the NMER, which according to Cowie (1998a), Ackermann et al. (2001), Soliva and Benedicto, 2005 and Soliva et al. (2006) may indicate that a larger proportion of large faults related to a power law distribution. Figure 4.12 a& b show that the curve of the distributions are bounded at low value in the upper end as a result of truncation artefacts, and at the lower end as a result of censoring effect (see section 2.2.3.2). The low frequency of data at lower end reflects fewer large faults dataset as opposed to relatively smaller ones. According to Ackermann et al. (2001), Soliva et al. (2006) and Soliva and Schultz (2008), the development of the fault trace-length distribution towards exponential scaling suggests inhibition of fault interactions with increasing strain.

Table 4.4. Results of functions fit to the fault trace-length data.

Rift zone	Function fit	R^2 (fault length)
NMER	Log-normal	0.95
	Exponential	0.95
	Power-law	0.86
CMER	Log-normal	0.95
	Exponential	0.88
	Power-law	0.85

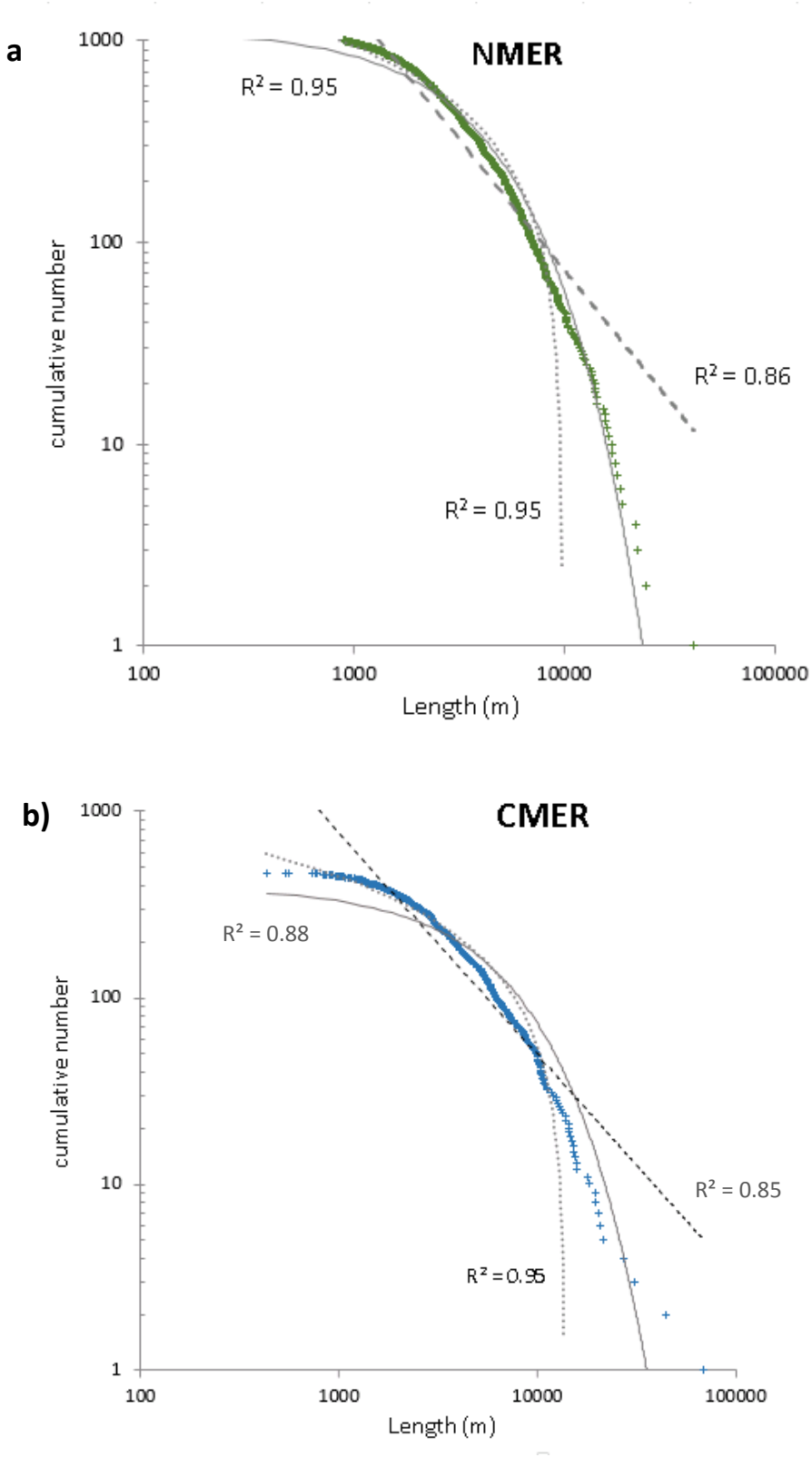

Figure 4.12. Log-Log plot of fault trace length vs cumulative number for a) the NMER from and b) the CMER, showing power, exponential and log-normal laws (see Table 4.4).

The majority of data sets reported in the literature for fault length distributions are best described by a power-law distribution e.g. Pickering et al. (1995), Pickering et al. (1996), Watterson et al. (1996), Ackermann and Schlische (1997), Poulimenos (2000), Gillespie et al. (2001), Peacock (2002), Bailey et al. (2005), Soliva and Benedicto (2005), and Soliva and Schultz (2008). However, other distributions such as exponential e.g. Soliva and Benedicto (2005), Soliva et al. (2006), and Soliva and Schultz (2008) and log-normal e.g. Castaing et al. (1996), Odling et al. (1999), and Gillespie et al. (2001) were also reported. Sampling errors of fault geometries could lead to under-estimation of truncation and censoring effects, which in turn leads to degradation of the underlying power-law distribution and give rise to apparent exponential/log-normal distributions instead (Castaing et al., 1996, Ouillon et al., 1996, Bonnet et al., 2001).

In the same way as discussed in the previous section (4.2.3.1) for fault throw population, the distribution of the length attributes data were further tested against the Maximum Likelihood Estimation (MLE) process and a Kolmogorov-Smirnov (KS) using the model by Healy et al. (2017) to examine if the observed exponential and log-normal distributions are real and not resulting from degradation of an underlying power-law distribution due to censoring and truncation effects. Again, similar to the fault throw, the cumulative distribution plots (Figure 4.15) for fault length populations for both the NMER and the CMER zones also best fit to log-normal distributions.

The probabilities of the analysed lengths to be log-normal were 95.5% and 97% for the NMER and CMER zones respectively.

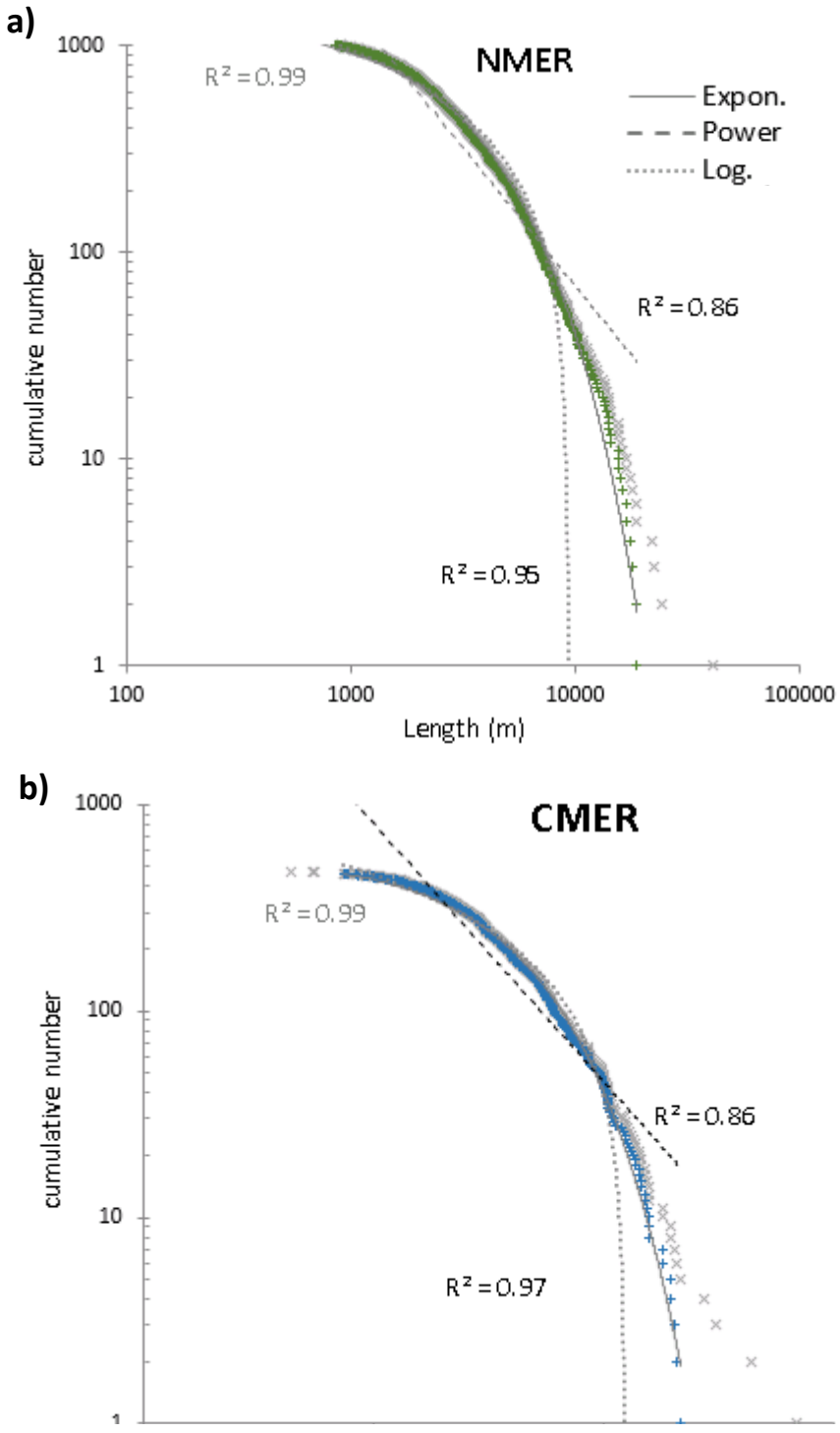

Figure 4.13 Cumulative lengt distributions of the fault population in NMER and CMER showing the best fit of statistical distributions after eliminating the extreme value from the data (grey stars)a.

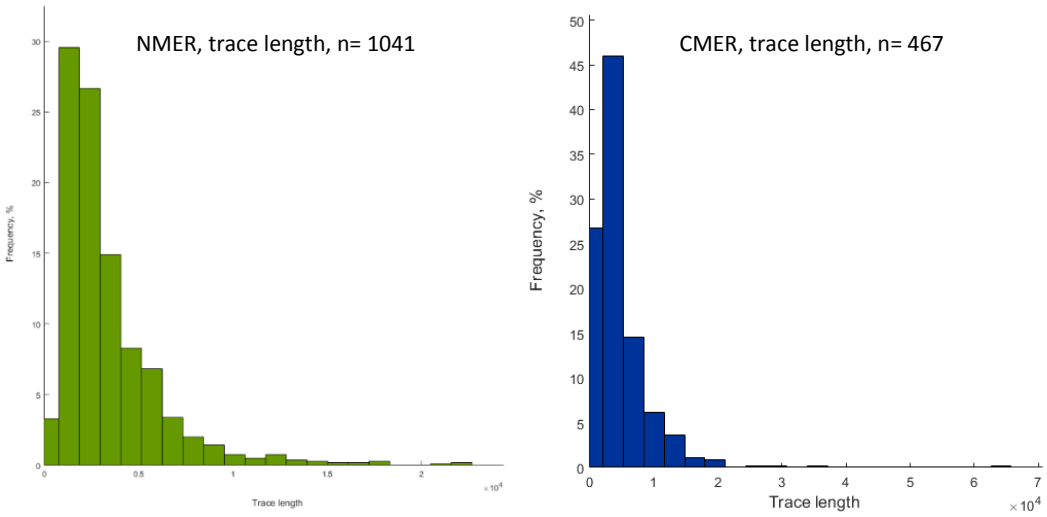

Figure 4.14. Histogram of fault trace length in NMER and CMER.

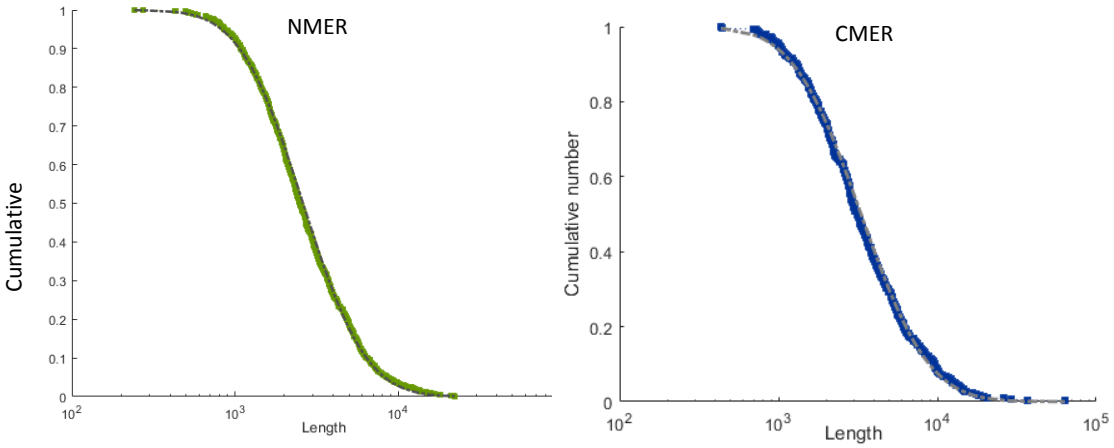

Figure 4.15. Log-Log plot of fault Trace length vs cumulative number for the NMER from 2D data.

It is noted from Table 4.5 that the average fault length in the NMER is less than that of the CMER whereas, the average fault throw in the NMER is larger than that of the CMER. This observation is shown for the average of all faults in each rift zone (NMER & CMER) (Table 4.5) as well as the average of internal faults (found at rift valley) and border faults (forming shoulders or flanks of the rift) separately in each rift zone (Table 4.6). These observations of the southward increase in fault length concur with similar observations by Hayward and Ebinger (1996) and (Ebinger, 2005), who observed a general south to north decrease in the length scale of border faults along the MER - Afar rift segments where the crust is thinner due to decreasing lithospheric strength.

Table 4.5. Descriptive statistics of fault parameters populations.

Rift zone	Length (m)					Throw (m)				Ave. D/L
	N	Min	Max	Average	StDev	Min	Max	Average	StDev	
NMER	1041	294	41210	3604	3207	30	974	123	126	0.04
CMER	468	432	68615	4823	5316	30	1054	106	105	0.03

Table 4.6. Averages of fault parameters for internal and border faults within the rift zones

Rift zone	Internal faults		Ave. D/L	Border faults		Ave. D/L
	Ave. Length	Ave. Throw		Ave. Length	Ave. Throw	
NMER	3409	89	0.03	4367	182	0.04
CMER	3792	83	0.02	5897	154	0.03

4.2.3.3 Fault spacing populations

In order to provide a reasonable explanation for the state of deformation in the central MER and the northern MER, the pattern and distribution of fault spacing data that were collected from a one dimensional line transect have been analysed in this section in two ways that are; cumulative frequency plots, coefficient of variation.

4.2.3.3.1 Cumulative frequency of fault spacing

Fault spacing populations have been examined by measuring the distance between successive intersections of faults along 1-dimensional transects perpendicular to the average fault strike in order to assess changes in fault spacing and degree of clustering along the one-dimensional line sample. Therefore, four 1-dimensional line transects have been made in the study area with orientation of NW-SE in the Northern MER zone (transects AA` and BB`) and WNW-ESE in the Central MER zone (for transects CC` and DD`), (see Figure 4.2 for location of transects). To examine the degree of clustering along the one-dimensional line transect; values of fault spacing are plotted in a descending order against cumulative frequency when the x axis was plot in normal scale and the y axis in logarithmic scale (Figure 4.16 & Figure 4.17). The majority of the spacing data sets reported in the literature are best-fitted by either exponential (e.g. Cowie et al., 1995, Ackermann et al., 2001) or log-normal distributions (e.g. Gillespie et al., 1993, Gillespie et al., 2001). For this study, fault spacing attributes in all transects are best fit to an exponential distribution with least squares (R^2) of 0.99, 0.98, 0.097 and 0.96 for transects AA` and BB` in the NMER, (Figure 4.16 a) and CC` and DD` in the CMER respectively (Figure 4.17 a).

For a better representation of the data, fault spacing attributes for the two cross-sections in each rift zone (AA` and BB` for the NMER, and CC` and DD` for the CMER) were combined. The combined cross-sections were also best described by an exponential distribution with least square of 0.96 for the NMER (Figure 4.16 b) and 0.98 for the CMER (Figure 4.17 b) when two to three highest values that plot far off from the rest of the datasets were excluded. According to the literature, the exponential distribution suggest that the fault spacing data are randomly distributed (e.g. Putz-Perrier and Sanderson, 2008a, Putz-Perrier and Sanderson, 2008b), which indicates that the fault system has not yet reached a saturation stage that is characterized by regular fault spacing where fault spacing stops evolving and remains nearly constant as the strain continues to increase (Wu and Pollard, 1995).

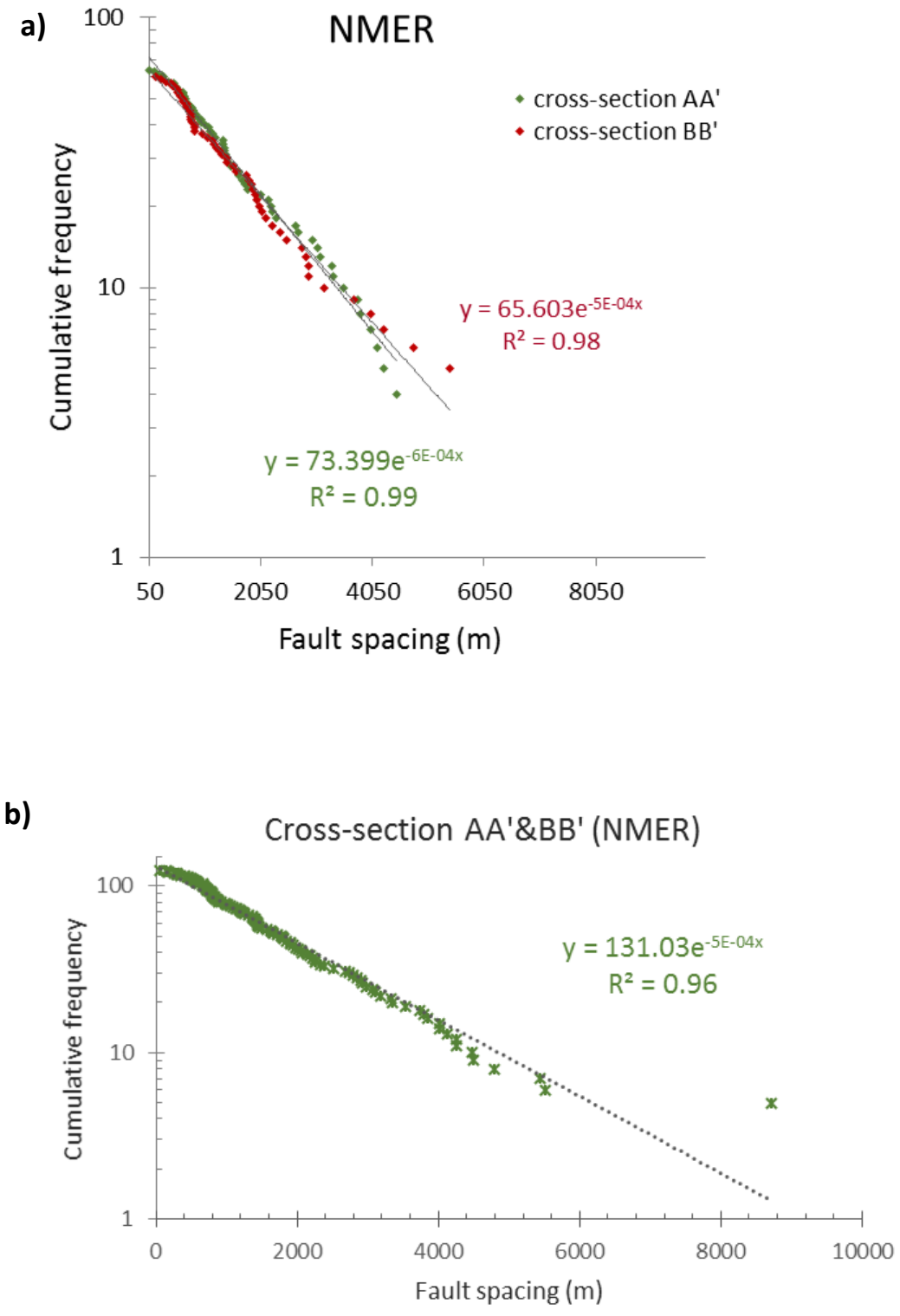

Figure 4.16. Log- linear plots of fault spacing vs cumulative number for a) two transects in the NMER from 1D data, b) the two transects combined.

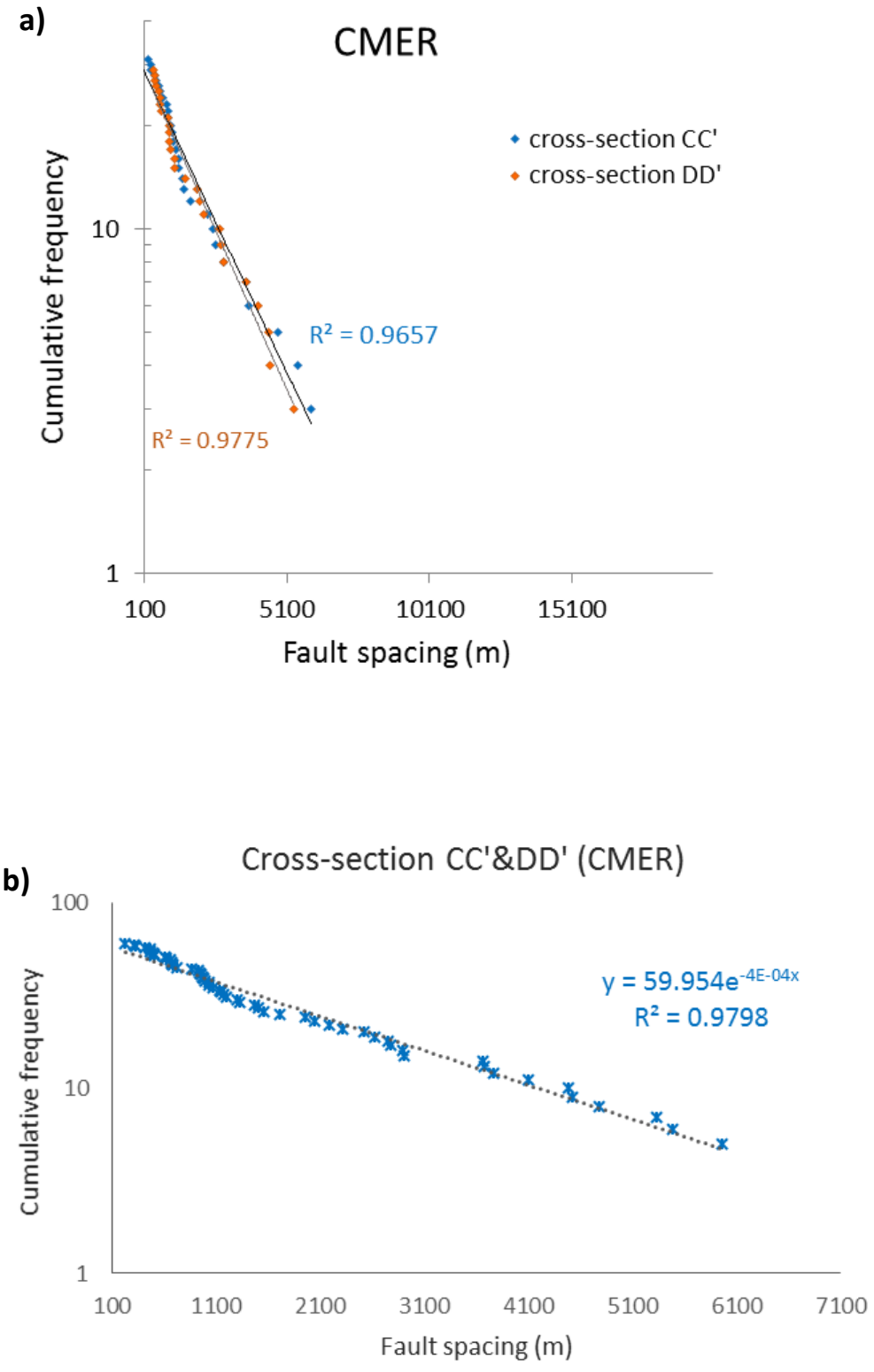

Figure 4.17. Log- linear plots of fault spacing vs cumulative number for a) two transects in the CMER from 1D data, b) the two transects combined.

4.2.3.3.2 Coefficient of variation Cv

The most common method for characterizing the spacing of fracture and fault populations is the determination of the coefficient of variation Cv, which is defined in statistics as the relationship between the standard deviation (s) and the mean (m) of spacing attribute (see section 2.1.4.3). The Cv values (Table 4.7) were found to be 1.2 and 1.3 for individual transects AA` & BB` respectively and 1.2 for them combined. The values of coefficient of variation for transects AA` & BB` individually and AA` & BB` combined is Cv ~1, which indicates that faults in the NMER rift are spaced in a random manner (see section 2.1.4.3). According to the literature, fault spacing data fitting to exponential function would be randomly distributed **(e.g. Putz-Perrier and Sanderson, 2008a, Putz-Perrier and Sanderson, 2008b)**, therefore, these results are consistent with the observed exponential distribution of spacing attributes for transects AA` & BB (Figure 4.16 a). As for the CMER, the Cv values (Table 4.7) for transects CC` and DD` were 1.9 and 2 respectively, and 1.9 for them collectively, which suggest highly clustered faults (see section 2.1.4.3). Nevertheless, a fault spacing that is best described by a clustered pattern is likely to have power-law distribution **(Ackermann et al., 2001, Sleight, 2001)**, but that is not the case for transects CC` and DD` that best fit to an exponential distribution. This lack of correlation between the Cv and the statistical distribution may indicate that fault spacing is not strictly clustered but may include some degree of randomness.

Table 4.7. Statistics of fault spacing data and coefficient of variation.

Transect	Standard deviation(s)	Mean (m)	coefficient of variation (Cv)
AA`	2488	2046	1.2
BB`	2948	2327	1.3
AA` & BB`	2710	2166	1.2
CC`	5401	2865	1.9
DD`	6883	3417	2
CC` & DD`	6141	3179	1.9

4.3 Synthesis and discussion of fault scaling properties.

This section discusses and synthesis results and information obtained from analysis of fault scaling relations that characterize fault populations formed in the brittle crust of the NMER and the CMER segments, in order to get an insight into how these relationships may be indicative of the underlying physical mechanisms of crustal deformation, and therefore can inform our understanding about the evolution of normal faults in continental rifting.

4.3.1 Throw

The Northern MER is also characterized by a relatively thin crust (28-35 km) (e.g. Maguire et al., 2006, Keranen and Klemperer, 2008) and a strong magma rising, where deformation is accommodated by a combination of intrusion, dyking and normal faulting (e.g. Kendall et al., 2005, Keir et al., 2006). It has been observed in the current study that there has been a slight increase in the average of fault throw in the NMER comparing to the CMER (Table 4.6). In this rift segment as beneath the Fantale–Dofen magmatic segment (Figure 4.2) where the majority of faulting is occurring; Keranen and Klemperer (2008) observed that the crust is thicker than the surroundings and correspond to the highest velocity anomaly, which suggests that magmatic processes may have locally thickened the crust with respect to the rest of the Northern MER. This observation by Keranen and Klemperer, (2008) could explain the observed higher average of the apparent fault throw measured from DEM surface of the NMER in this study. This higher fault throw in the NMER compared to the that in the CMER could also be explained in the same way as suggested by

Poulimenos (2000) and Gupta and Scholz (2000a) that in a later stage of evolution, and once fault saturation is achieved, stress shadows of nearby faults inhibit fault nucleation and restrict tip propagation while the displacement increase for some faults to accommodate increasing strain, which leads to higher displacement\ length ratios.

Another explanation for the observed higher average fault throw in the NMER (Table 4.5 & Table 4.6) is that, the higher extension strain estimated in the NMER as shown in Table 4.1 may have led to a large footwall uplift and large hanging wall subsidence, resulting in faults having a bigger throw or scarp height as referred to by some workers (e.g.Gross et al., 1997, Wilkins and Gross, 2002, Torabi and Berg, 2011) in the NMER comparing to the CMER, this observation is evidenced in topographical profiles (Figure 4.18), where the topographical profile in the NMER appear to be more ridged and rough (Figure 4.18 a) as opposed to the CMER (Figure 4.18 b), this difference in surface roughness that indicates differences in scarp heights is also evident in topographical profiles shown in Wolfenden et al. (2004) for NMER and in Abebe et al. (2005) for the CMER.

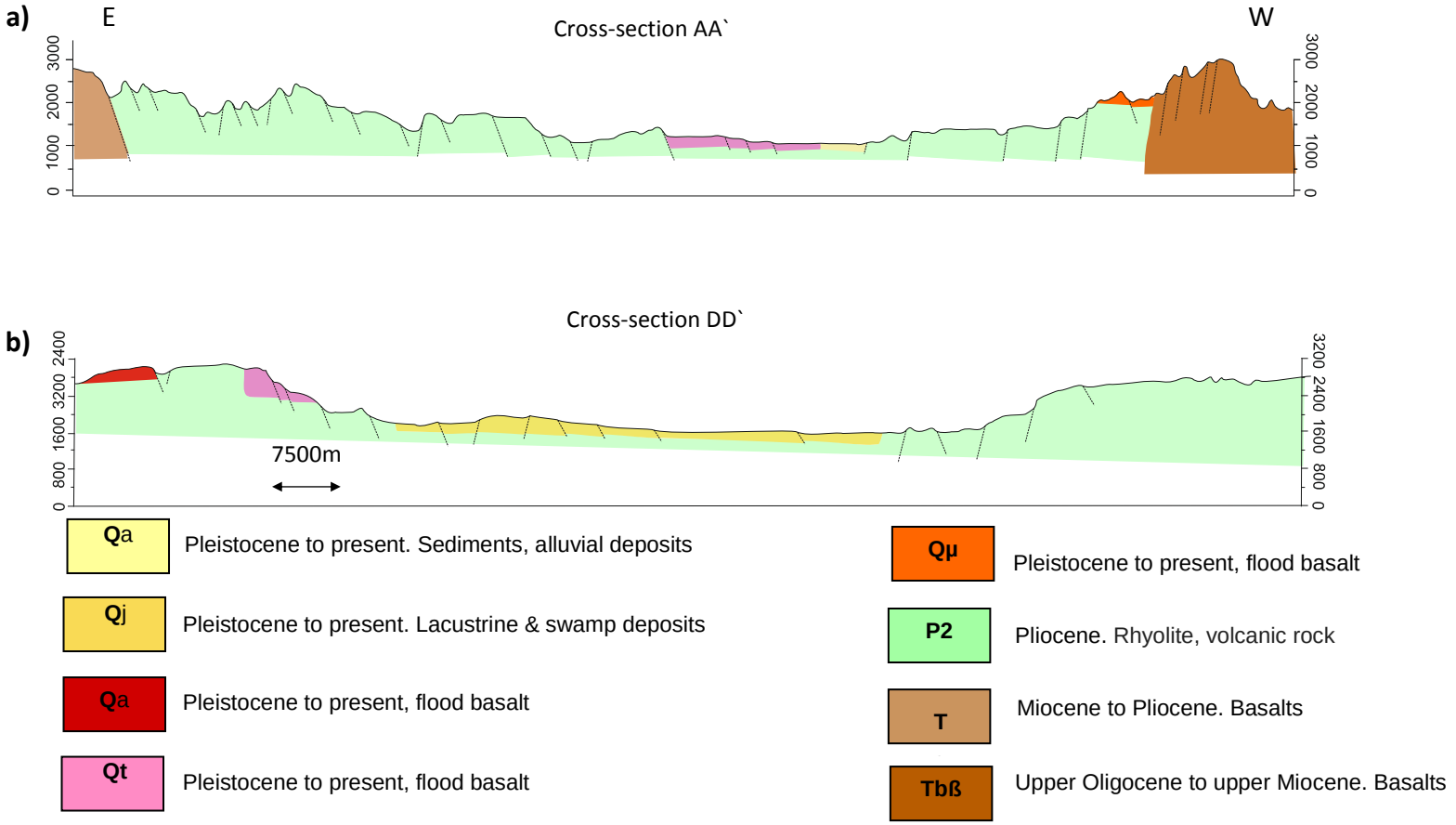

Figure 4.18. Cross-rift showing topographic profiles in a) the northern MER, b) the central MER. Faults projected in the subsurface; vertical exaggeration x 5. see Figure 4.2 for cross-section locations, geological units from geological map of Ethiopia and Somalia 1973.

4.3.2 Length

It has been shown in section (4.2.3.1) that fault length attributes for both rift zones (NMER and CMER) are best fit to both log normal and exponential distributions (Table 4.4) based on cumulative frequency plots (Figure 4.12) when the least squared regression analysis was used. The same data fit only to a log-normal distribution (Figure 4.15) when the maximum likelihood estimation (MLE) method was used to assess the degree of fit between the data and underlying statistical model (e.g. power law, exponential or log normal). Similarly, fitting fault attributes to two different distributions was also reported in (Harris et al., 1991) who observed an exponential distribution fitting to fault spacing data in a standard statistical function, and a log-normal distribution when Kolmogorov (K-S test) analysis was used.

Exponential or log normal distributions are statistically close (section 2.1.3.2), and that could be one reason why a dataset can fit two different statistical distributions by the same or different models for testing goodness of fit to the data. Moreover, both log-normal and exponential are also scale-dependent laws (Soliva and Schultz, 2008) and can be caused by the same tectonic and stratigraphic condition, therefore, combining additional information from other analysis is very important in order to infer the nature of fault evolution.

It has been commonly recognized that resolution and finite size effects on a power law population can also result in distributions that appear to be either exponential or log-normal (Einstein and Baecher, 1983, Castaing et al., 1996, Bonnet et al., 2001). Therefore, this section discusses factors affecting these statistical distributions including:

4.3.2.1 Effect of data quantity

Insufficient number of data involved in analysis can produce either an exponential or log-normal distribution for fault trace lengths, whereby the data set is not large enough to be representative of the population, and therefore cause the statistical distribution to be biased. Therefore, it has been suggested by Bonnet (2001) that a minimum of 200 fractures (including faults) should be sampled to adequately characterize distribution of fault length. Therefore, data sets analysed in the current study contain 1041 and 468 faults for the NMER zone and the CMER zone respectively. The data sets used in this study are large enough to be representative of the fault system and to provide realistic analysis and estimates for fault length population.

4.3.2.2 Effect of geological errors

Geological processes such as accumulation of erosional and depositional sediments at the fault hanging wall cause a partial exposure of fault scarps, which may introduce systematic error into throw and length measurements, this effect may effect internal faults more than border faults as volcanic, sediment and erosional deposits accumulate more in the rift axis. These effects may cause misrepresentation of what was originally power-law distributions of fault length data set to appear either as log normal or exponential distribution. Therefore, fault throw and fault length attributes for internal faults and border faults from the NMER and the CMER were plotted separately (Figure 4.19 & Figure 4.20) in order to examine whether the observed exponential/log normal distribution of fault length and throw populations are true representation of the dataset, or whether these distributions are affected by sampling errors that lead to degradation of the underline power-law distribution that appear as

exponential distribution instead (e.g. Castaing et al., 1996, Ouillon et al., 1996, Bonnet et al., 2001). Results of this analysis (Figure 4.19 & Figure 4.20) show that fault size attributes (length and throw) in rift axis and rift border in the NMER and the CMER fit to both exponential and log normal distribution and no power-law distribution was observed. These results are similar to that of fault attributes (throw and lengt) from rift axis and rift border combined for each rift segment (see section 4.2.3.1 and 4.2.3.2, Figure 4.12 and (Figure 4.12). These results to some extend could rule out the assumption that the observed exponential/log normal distribution may be caused by geological effects (accumulation of volcanic, sediment and erosional deposits).

4.3.2.3 Effect of Resolution

The fault dataset used in the analysis might be incomplete due to missing and unmapped faults that fell under the resolution of observation. To further test the robustness of the results and their sensitiveness to missing data and resolution effect, a dataset of fault length of the Main Ethiopian rift collected from field studies by Agostini (2011) and available online at (http://www.mna.it/MER/utilities.htm) was used in this study to generate cumulative frequency distributions (not generated previously by Agostini (2011)) for fault length in the NMER and the CMER to examine how they compare to cumulative distributions of data captured from DEM surfaces in this current study (Figure 4.12 & Figure 4.15). The distribution of these field data by Agostini (2011) were also best described by an exponential distribution with R^2 of 88 for NMER and R^2 of 96 for CMER and also fit to log-normal

distributions (Figure 4.21) by the two different methods for testing the goodness of fit. This would indicate that the effect of sampling in the collected dataset (from DEM) is not significant, and that would also indicate that the observed exponential and log-normal distributions for the data used in this study are real and representative of the fault length distribution, and not caused by resolution effects that would cause degradation of an underlying power-law distribution to appear either as exponential or log-normal distributions (e.g. Castaing et al., 1996, Ouillon et al., 1996, Bonnet et al., 2001). However, it is worth mentioning that number of faults used in the current study for the NMER and CMER is 1041 and 468 respectively comparing to 983 and 1870 from Agostini (2011), The difference in the number of faults in the NMER is fairly comparable whereas in the CMER is about four times larger for Agostini (2011) data, which may makes such comparison invalid.

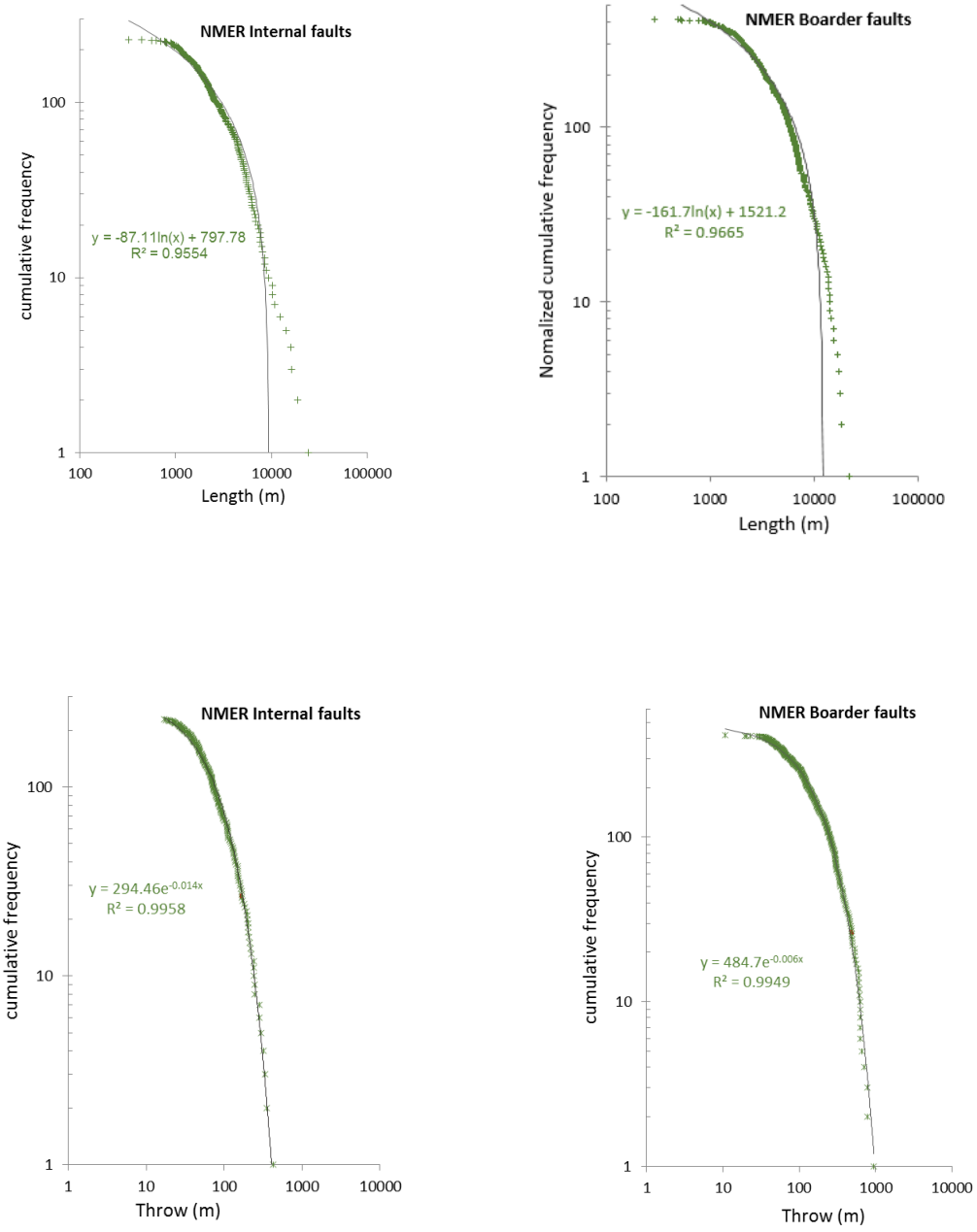

Figure 4.19. Log-Log plots showing exponential distribution of fault throw and fault length attributes for internal faults and border faults separately from the NMER.

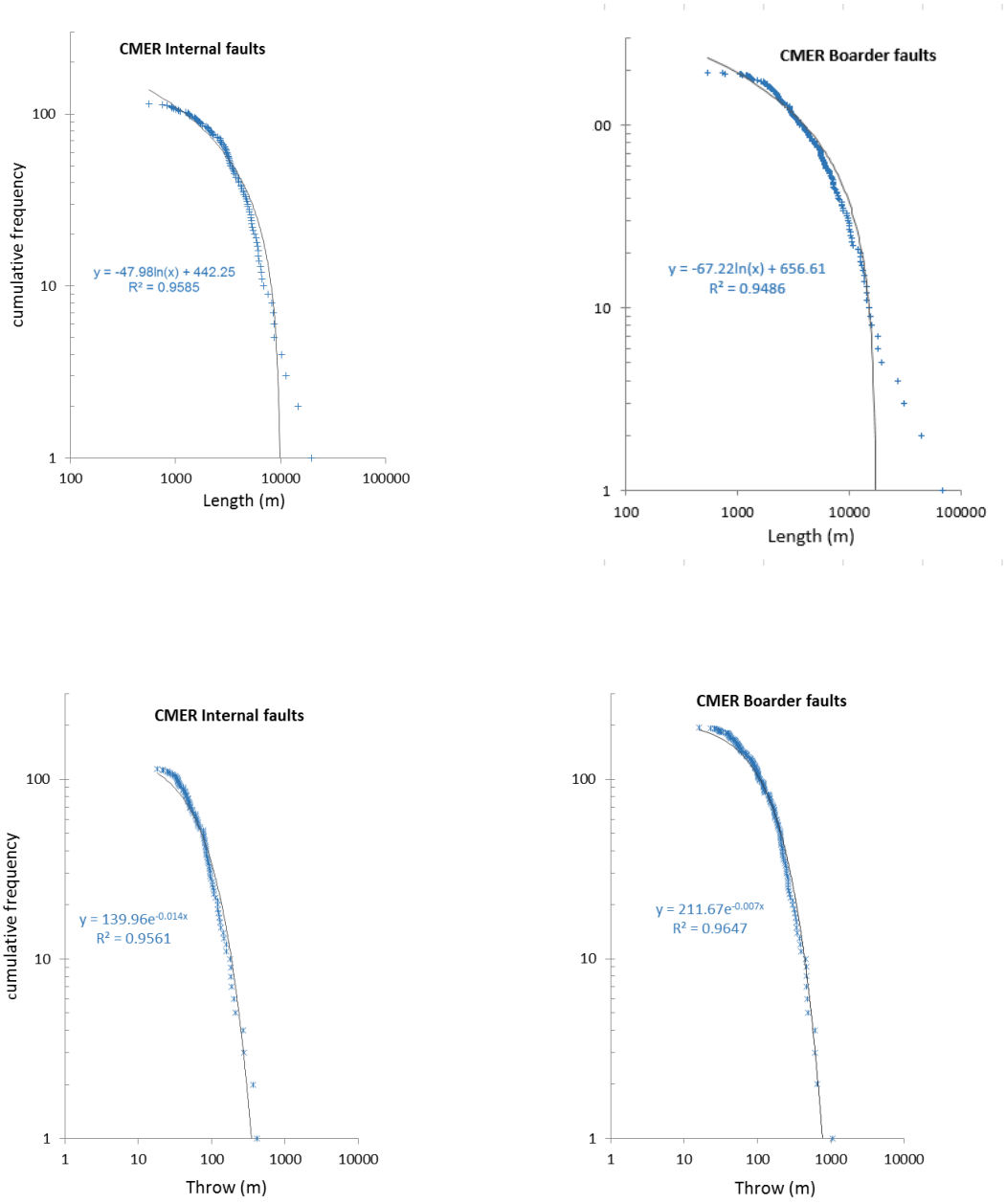

Figure 4.20. Log-Log plots showing exponential distribution of fault throw and fault length attributes for internal faults and border faults separately from the CMER.

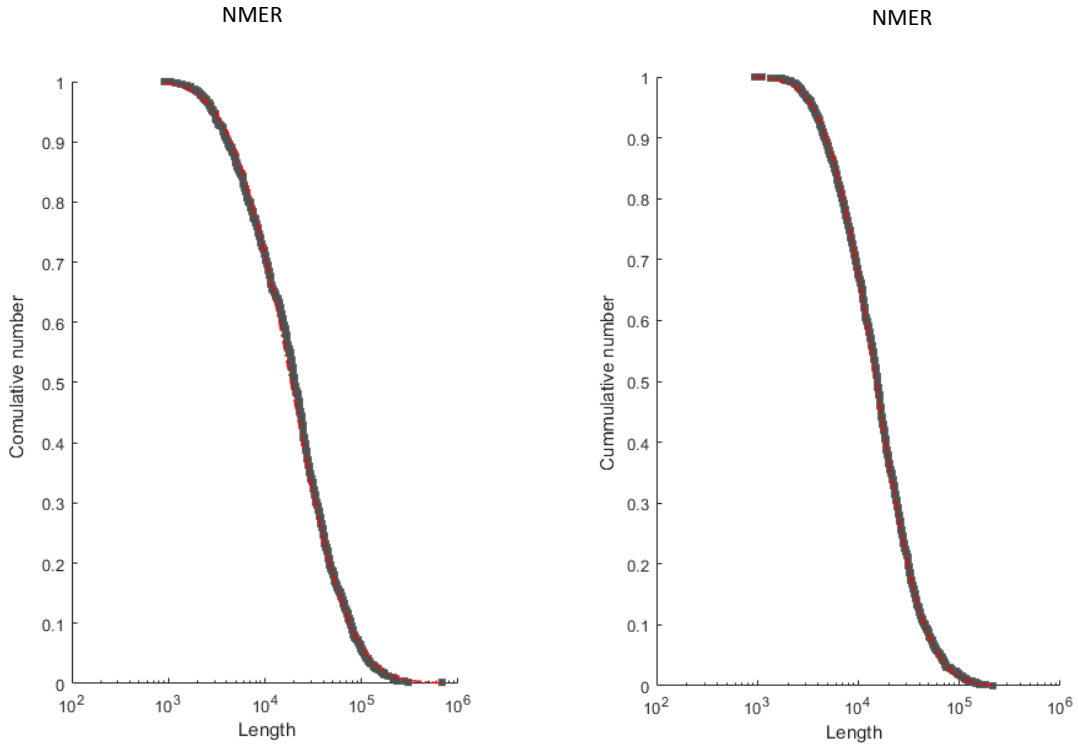

Figure 4.21. Log- Log cumulative plots of fault length data measured from field data collected by Agostini (2011) in both NMER and CMER

4.3.2.4 Effect of layer thickness

Exponential or log normal distributions are both scale-dependent laws, dependent on brittle layer thicknesses (Soliva and Schultz, 2008). Furthermore, the literature shows that layering plays an important role in restricting fracture (including faults) growth, in other words, the vertical restriction of faults is suggested as being a possible process occurring for faulting at a crustal-scale, in a brittle mechanical layers (Wilkins and Gross, 2002), or where the ductile crust of inelastic behaviour can mechanically suppress brittle faulting represented by fault displacement (e.g. Jackson and White, 1989, Scholz and Contreras, 1998). Moreover, fault vertical restriction inherently related to the mechanical layer results in modifications of the fault scaling relation between maximum displacement and fault length (Gross et al., 1997, Wilkins and Gross, 2002), and therefore, the thickness of the brittle crustal layer control the fault growth process. The vertical restriction applies to fault systems confined to different scales of mechanical layers with thicknesses ranging from sedimentary bed to the whole crust (e.g. Nicol et al., 1996, Ackermann and Schlische, 1997, Cowie, 1998a, Odling et al., 1999, Ackermann et al., 2001, Soliva and Benedicto, 2005, Soliva et al., 2006).

Reches (1986) also suggest that the transition from a power law distribution to a log-normal that may be related to the finite size of the mechanical layer of the experiment, where Log-normal distribution is most appropriate for fractures/faults confined to a finite layer thickness and a power law is appropriate for fractures/faults in more massive rocks (Odling et al., 1999). Other studies indicate that normal fault populations that grow in confined brittle layers of finite thickness are characterized by faults growing in length with

restricted fault displacement, due to limited layers thickness acting as mechanical barriers, leading to a horizontally distributed fault system (e.g.Nicol et al., 1996, Ackermann et al., 2001, Soliva and Benedicto, 2005, Soliva et al., 2006).

Consequently, based upon the thinning of crustal layers observed along the rift axis of the MER and Afar region (Figure 2.2) and development of Exponential or log-normal distributions for fault length and fault throw populations in both the NMER and the CMER, I would suggest for this study that fault system in these two rift segments could be confined to a brittle mechanical layer. The motive for such a suggestion is that, the area adjacent to the NMER from the north, in the southern Afar, at the MER-Afar transition area also exhibited an exponential size distribution and was therefore inferred by Soliva and Schultz (2008) to be confined to brittle mechanical layers.

4.3.3 Characterization of pattern of deformation.

Fault spacing attributes collected from one dimensional line transect have been analysed by different approaches including cumulative frequency plots, coefficient of variation and step-plots of spacing heterogeneity, to make a better conclusion for the fault spacing distribution and pattern. The majority of the spacing data sets reported in the literature are best-fitted by either exponential (e.g. Odling et al., 1999) or log-normal distributions (e.g. Gillespie et al., 2001).

For the current study, the cumulative frequency analysis of fault spacing showed that spacing data from the NMER (cross-sections AA` & BB`) conform to an exponential distribution, which suggests that the fault spacing data are randomly distributed (e.g. Putz-Perrier and Sanderson, 2008a, Putz-Perrier and Sanderson, 2008b) and that is supported by values of Cv being ~1, which is in agreement with results of Gillespie et al. (2001). Furthermore, Step plots of fault spacing that have been used to examine the spatial heterogeneity of fault frequency/spacing in section 4.2.1.2 (Figure 4.4) can also be used to identify areas of high strain and low strain as well as areas of distributed and localized strain (Putz-Perrier and Sanderson, 2008b; Nixon et al., 2014).

The stepping pattern shown in transects AA` and BB in the northern MER (Figure 4.4a & b) indicate partitioning of faulting into areas of dense faulting represented by segments of steep slope and narrow spacing in the graph, the wider the spacing of the fault the fewer faults per unit area and vice versa (Nixon et al., 2014). Therefore, the wide range of relatively narrow-spaced small and uniform steps shown in transects AA` and BB` (Figure 4.4 a& b) suggest relatively low heterogeneity supported by values of heterogeneity

shown in (Table 4.2), and also indicate that the strain is distributed across a large number of relatively small fault segments that contribute to the strain accommodation and forms a distributed domain of faulting deformation according to Kuiper's model. This nature of distributed deformation observed in transects AA` & BB` in the NMER are also qualitatively visible on map view of the DEM surface of the NMER segments (Figure 4.2), where the mapped faults appear to have spread across wider range between the rift flanks, which implies more distributed deformation of faulting, all these observations obtained from analysis of data collected from 1D and 2D confirm that the NMER represents a domain of distributed deformation.

As for the CMER, fault spacing data from this rift segment (cross-sections CC` & DD`) also fit to an exponential distribution, which again indicate to a random distribution. On the other hand, graphs of spatial heterogeneity of fault frequency in the central MER (transects CC` and DD` Figure 4.4 c & d) generally show wider spacing segments and larger steps distribution as opposed to that of transects AA` and BB` (Table 4.7) which generally indicates a rather higher heterogeneity and more localized deformation as suggested by Nixon et al. (2014), and that is supported by values of heterogeneity shown in Table 4.2.

Furthermore, the visual inspection of the DEM surface of the CMER rift segments (Figure 4.2) suggest a fairly localized deformation showing concentration of faulting around the rift flanks in this rift segment, this observation was reinforced by analysis of step-plots of spatial heterogeneity of fault spacing (Figure 4.4 c & d) that show relatively high spatial heterogeneity of fault spacing (Table 4.2), and analysis of the coefficient of variation (CV),

where CV = .2, which is associated with a clustering pattern of faulting Gillespie et al. (2001), all these observations indicate to a localized deformation, which that therefore should give rise to a power-law distribution as suggested by Ackermann et al. (2001) and Sleight (2001) instead of exponential distribution as shown by the cumulative frequency distributions of fault spacing (section 4.2.3.3.1), this inconsistency might be due to the distribution of strain is relatively diffused and localization is not strong enough to produce a power-law distribution for fault size attributes (fault length, fault throw and spacing) in the CMER. Nevertheless, the deviation from power-law distribution could be a good indicator of the concept that this rift segment of the CMER is in a transitional or intermediate stage of continental rifting according to Hayward and Ebinger (1996), Agostini et al. (2011a), Agostini et al. (2011b) and Molin and Corti (2015) (section 4.1 & 4.1.1), where faulting deformation is transferring from rift borders to the rift axis. Thus, lack of strong localization of deformation represented by the cumulative frequency distributions could be due to the system is emerging from localized faulting regime to a more distributed faulting regime, this findings present a new quantitative observations that advocate the concept that the deformation in CMER is in incipient transition from border faults into rift valley, this concept has not been well documented in previous studies. Therefore this findings make a distinction from several previous studies (e.g.Hayward and Ebinger, 1996, Agostini et al., 2011b, Agostini et al., 2011a, Molin and Corti, 2015) that, even though they suggest that the CMER represents an intermediate evolutionary stage of continental rifting with significant Quaternary activity of the boundary faults and some secondary internal faults, without a particular emphasis on migration of

deformation from rift bounded faults to rift axis, yet these studies suggest that deformation is still focused at the rift margins as the SMER.

4.3.4 Implications on fault growth model

In Figure 4.8, the exponent value (~1) of the equation of displacement/Length trend lines for the central MER and the northern MER may suggest that fault system in these rift segments evolve in accordance to isolated fault model (see section 2.1.3.5), however, the correlation of coefficient (R^2) of displacement/Length trend line were as low as 0.257 and 0.185 for the central MER and the northern MER respectively and therefore, this exponent cannot be used as an indication to any fault growth model.

However, in the absence of seismic data that could show the sedimentary strata, comparing scaling properties of different fault populations is the only approach to infer the fault growth and evolution in the study area. Therefore, results of the analysis in this chapter have shown that the average fault lengths decreased from CMER to NMER, whereas, the average fault throws and aspect ratio (D/L) increased, section (4.2.3.1) (Table 4.5 & Table 4.6). If what has been observed happened after reaching the maximum fault length at an early stage of development in the NMER, thus that would be in line with the constant length fault model (coherent fault growth model) by (Walsh et al., 2003a, Childs et al., 2009), which suggests that as stress is applied to the volume of rock, faults would initiate with low displacements but with lengths at or near maximum, this length would then remain almost fixed as displacement takes over accommodation of strain to start accruing the majority of the strain onto a few large displacement faults in the volume. Thus this could explain the

observed increase of displacement in the NMER. This model requires faults to have higher Displacement/Length ratios than the isolated fault model as fault displacement will grow more rapidly than fault length, this increase of Displacement/Length ratio is also observed within statistics of the NMER faults (Table 4.5 & Table 4.6) as opposed to that of CMER, where the strain was estimated higher than in the CMNR (Figure 4.3). These results are in consonance with results of Poulimenos (2000) and Gupta and Scholz (2000) who estimated higher displacement\length ratios in the high-strain zone, and Polit (2009) who observed a decrease in fault length ratio in vertically restricted fault system, these results are also similar to that of Nicol et al. (1997) and Poulimenos (2000) who suggest that when saturation is achieved that is, when fault spacing stops evolving, faults grow by displacement rather than length to accommodate increasing strain, causing the displacement rates to increase.

Furthermore, the exponential distribution observed for both the NMER and the CMER could further indicate that the fault system in these two rift segments evolve in accordance to the constant length fault growth model, where normal faults establish their near maximum length in early phase of evolution according to Walsh et al. (2003a) and Childs et al. (2009), this rapid growth of fault length at an early evolutionary stage in extensional settings could also be triggered by reactivation of inherited basement fabric (Walsh et al., 2002a, Meyer et al., 2002). The effect of the pre-existing structure on the development of surface faults has been discussed in next chapter (chapter 5).

Hayward and Ebinger (1996), observed a generic decrease in length and scarp height of Quaternary border faults from south to north in the MER and Afar rift system, according to them, in an advance stage of continental rifting, like the

area under scrutiny of the NMER, the decrease in the length of active faults accompanied with massive basaltic magmatism as shown in Figure 4.2 (dashed red irregular polygons) is due to decreasing of lithospheric strength, which will result in rift segmentation dominated by basaltic volcanic ranges with a narrow zone of small faults along the rift axis. Therefore, the observed decrease of fault trace length in the current study add to that of Hayward and Ebinger (1996) by pinpointing and quantifying the decrease in length of border fault populations northward between the CMER and the NMER rift segments (Table 4.6).

In addition, according to models of Forsyth (1992) and Ackermann and Schlische (1997) the observed decrease of average fault length could also be caused by increasing extension to a sufficient degree capable of exceeding the shear strength of the volume and lead to formation of a new set of smaller grabens. Similar observations of relatively small grabens can be noticed on map view of the DEM surface of the NMER segments (Figure 4.2), and smaller and shorter fault system in the weakened lithosphere within the rift depression (see section 4.3.1), as evidenced by smaller average of fault length and throw of internal faults as opposed to those of border faults in the NMER (Table 4.6), which thought to have been deactivated during the Pleistocene (Keir et al., 2006, Casey et al., 2006, Wolfenden et al., 2004), as indicated by the lack of significant seismicity as reported by (Keir et al., 2006) and highly eroded escarpments as suggested by morphostructural indication (Wolfenden et al., 2004). This mechanism marks how deformation is localized in the rift valley through time during progressive extension as the lithospheric thins and extensively modified by magmatic processes. The decrease of average fault

length estimated in this study for the NMER contrast with the hypothesis set in chapter 1 (section 1.2) that expected an increase of average fault length in such late stage of continental rifting.

4.4 Conclusions

Detailed analyses of fault size parameters, collected within the Northern MER and the Central MER have been used to quantitatively describe and document the development and evolution of the fault system geometry. hence, results of various analysis carried out in this study were used in conjunction with each other so as to assess the upper crust brittle deformation in the CMER and the NMER segments. The main results of this study are summarized as follow:

- Faulting deformation in the NMER has been identified as distributed and less heterogeneous than the CMER, where the strain was estimated to be higher due to large number of faults contributing to the strain accommodation across the rift. Whereas the strain in the CMER is accommodated by fewer faults at and near the rift borders, which indicates a rather localized domain of deformation. The increase of strain estimated in the NMER is in line with the hypothesis that suggested a northward increase of strain in the MER.

- Fault length and throw attributes in both rift zones have best been described by exponential and log-normal distributions, which could be attributed to the thinning of the brittle crust layer (shown in the literature) that limited the thickness of the crust layer and restricted faults to grow more in length than displacement.

- Synthesis of scaling relations of fault size attributes offered a new statistical observations that may imply the incipient shifting of deformation from border faults into rift valley in the CMER, this pattern of deformation in the CMNR is poorly understood and has not been well addressed in previous studies e.g. Hayward and Ebinger (1996), Agostini et al. (2011b), Agostini et al. (2011a) and Molin and Corti (2015), (see section 4.3.3).

- Hayward and Ebinger (1996) and (Ebinger, 2005) generally identified a decrease in length and scarp height of Quaternary border faults along the MER up to Afar depression. The current study adds to those remarks by pinpointing and quantifying the decrease in length of border fault between the CMER and NMER segments (see section 4.3.4).

- The observed increase of average fault throws and D/L ratio from the NMER to the CMER may have occurred after reaching the maximum fault length at an early stage of development, and that would be in line with the constant length fault model.

- Previous studies (e.g. Mohr, 1983, WoldeGabrial et al., 1990, Hayward and Ebinger, 1996, Bonini et al., 2005, Keranen and Klemperer, 2008) have referred variation of brittle deformation along the MER to different lithospheric characteristics such as thinning of crust layer and decreasing lithospheric strength. This study suggests that fault systems within the NMER and the CMER segments could be confined to a brittle mechanical layer supported by the development of exponential size distribution, which is a function of fault size distributions (length and throw growing in a confined thickness of mechanical layer (see section 4.3.2.4).

Chapter 5. Assessment of the influence of pre-existing structure on fault orientation in the central Kenya rift, the central and northern main Ethiopian rifts: comparison with experimental models

5.1 Introduction

The process of continental rifting forms as inevitable consequence of divergent plate motions on a sphere (Dewey, 1975). Rifting in East Africa has been attributed to the eastward movement of the Somalia plate (or the Tanzanian craton) away from the Nubia plate (Corti et al., 2007) (Table 5.1). Continental basement commonly contains pre-existing structures (e.g. faults or fabrics) many of which are likely to be reactivated under certain extension direction caused by far field stress of plate tectonic (Dewey et al., 1998).

The evolution of rifting in the MER is strictly related to the long-term kinematics of the major Nubia and Somalia plates, that happened with a rotation pole that gave rise to a roughly ESE–WNW-directed extension at the latitude of the MER, with rates of ~6–7 mm/yr (Fig. 8), supported by GPS data (Fernandes et al., 2004) and local geodetic observations across the rift valley (e.g. Bendick et al., 2006).

Development of the Kenya rift is related to the occurrence of extension along three different microplates (Lwandle, Rovuma, Victoria) between the two major plates (Nubia and Somalia) (Table 5.1),south of latitude ~5°N (Corti, 2009). Extension is suggested to occur in an approximately E-W direction, as supported in nature by geological data (Daly et al., 1989, Morley, 1988),

current seismicity (Fairhead and Stuart, 1982, Foster and Jackson, 1998) and GPS analysis (Calais et al., 2006). Moreover, rate of extension is ~2 mm/yr (e.g. Corti et al., 2007) supported by analysis of the Nubia-Somalia motion based on plate kinematics (e.g. Jestin et al., 1994), GPS data (Fernandes et al., 2004), and current seismicity (e.g. Foster and Jackson, 1998). the extensional strain across the Kenyan Rift is very small, in contrast to the Red Sea and Gulf of Aden, and eastern Afar that was determined from geodetic studies to be 21 mm/yr in the NE-SW direction (Ruegg et al., 1993).

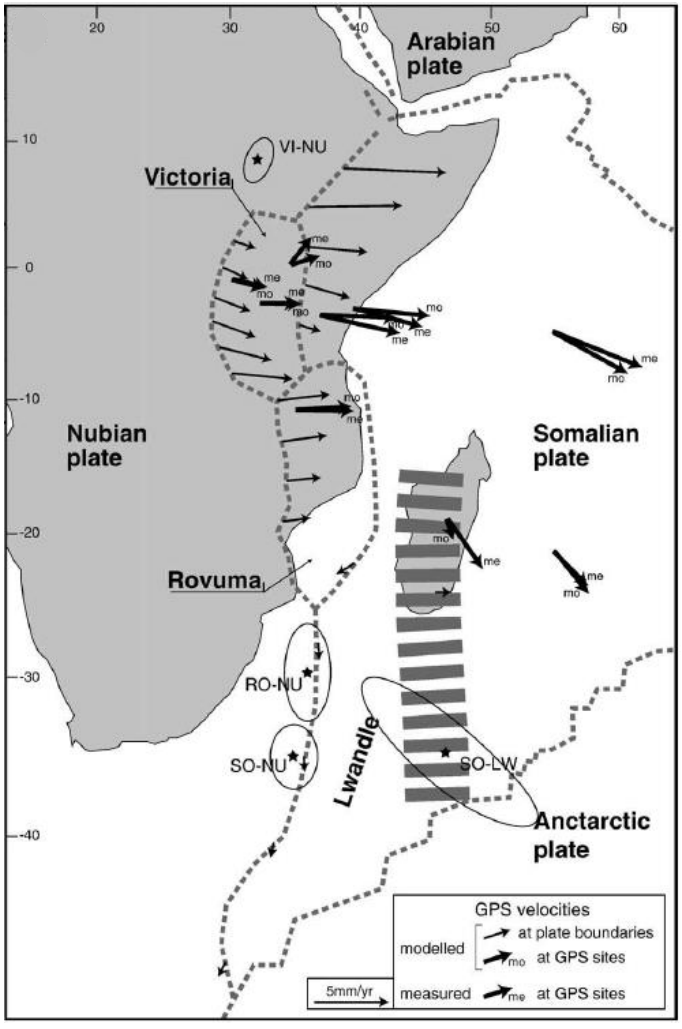

Figure 5.1 Seismotectonic setting of the East African Rift from (Corti, 2009). Thin black arrows indicate modelled velocities along plate or block boundaries; thick black arrows indicate motions at GPS sites.

It has been demonstrated that continental rifts including the EARS are not randomly distributed but tend to follow the trend of pre-existing weakness zones, hence rift zones are found in areas of previous intense deformation (such as many Precambrian and Palaeozoic belts) and are focussed between the cratons in mobile zones avoiding stronger regions (Versfelt and Rosendahl, 1989, Morley, 1999 a, Petit and Ebinger, 2000, Corti et al., 2003, Ziegler and Cloetingh, 2004). Therefore, extensional reactivation of inherited shear zones has contributed significantly to the evolution of many rift systems and in the geometry of their fault patterns e.g. East African rift system (Rosendahl 1987, Morley 1999 a, Ebinger, Yemane et al. 2000), East Brazil Rift system (e.g. Hung Kiang, Kowsmann et al. 1992), Cenozoic rift system of Europe (e.g. Ziegler 1994). Tthe development of narrow rift zones can also be attributed to basement structure reactivation (Buck, 1991).

The question as to whether pre-existing discontinuities in the basement affect the evolution of a normal fault at the Earth's surface remains not fully understood. Chapters 3 and 4 have investigated the evolution of normal faults and their implications on the evolution of continental rifting in the three study areas (central Kenya rift, central MER and norther MER), hence, the analysis that has been carried out in this chapter is an attempt to test the hypothesis that the local fault orientations of fault populations are influenced by the underlying basement structures at depth. Therefore, to achieve this aim, the full range of faults mapped from DEM data in the central Kenya rift (chapter 3) and the rift segments of the central MER and the northern MER (chapter 4) are used in the methodology described in section (5.3) that allowed to establish a qualitative and quantitative assessment of the possible influence of the underlying Precambrian crust/ lithospheric basement structures on later

Cenozoic brittle fault orientation on the surface, in relation to the local extension direction.

Nevertheless, for the EARS the influence of pre-existing structure is relatively simple due to few competing fabrics of different orientation along the rift (Morley, 1999d). Underling basement fabric structures such as faults (e.g. Bellahsen and Daniel, 2005, Giba et al., 2012) , shear zones (e.g. Corti, 2008, Agostini et al., 2011b, Corti, 2012) or foliations (Hetzel and Strecker, 1994) can influence the orientation of normal faults during their initiation and evolution.

Normal faults are formed in response to the extension caused by stress forces (thinning of the crust), generating new faults require higher stress levels than reactivating pre-existing ones (Krantz, 1991) as pre-existing structures are generally weaker zones than the surrounding rock volume (White et al., 1986). Where the influence of pre-existing structure is present, faulting deformation is geometrically and kinematically controlled by the angle between extension direction and deformation zone (or pre-existing structure) (e.g. Bellahsen and Daniel, 2005, Agostini et al., 2009, Henza et al., 2010, Chattopadhyay and Chakra, 2013), where extension is orthogonal to the deformation zone, fault patterns are relatively simply, conforming to Andersonian, plane strain fault models Anderson (1951). In oblique extension, the regional extension direction is oblique to the trend of the deformation zone, and the angle between the rift trend and the direction of extension (α) is inversely related to the degree of obliquity, therefore highly oblique rifts have low values of α (Withjack and Jamison, 1986) producing fault patterns that may significantly differ from the rather simple Andersonian fault patterns.

Analog modelling has been widely used in previous studies to understand the influence of pre-existing structure on rift structures (e.g. Bellahsen and Daniel, 2005, Corti et al., 2007, Agostini et al., 2009, Henza et al., 2010, Agostini et al., 2011b, Chattopadhyay and Chakra, 2013). Comparisons with sandbox models of Bellahsen and Daniel (2005) and Agostini et al. (2009) have been used in this study to provide a means to assess the role of pre-existing structures with varying orientations to extension direction. However, due to complexity of basement structure.

5.2 Geological setting

5.2.1 Basement structure of the central Kenya rift.

Sinistral NW–SE-trending upright shear zones represent a first order framework of basement structures in east and northeastern Africa (Smith and Mosley, 1993). The evolution of Kenya rift is thought to be influenced by the Precambrian basement structure, this rift system developed on a strongly heterogeneous basement, exhibiting a series of Late Proterozoic, regional-scale NW-SE and NS trending ductile/brittle shear zones, which exist in the lithosphere beneath the Kenya Rift, and these pre-existing faults and shear zones represent a mechanical weakness both at upper and lower crustal levels (Mosley, 1993, Maurin and Guiraud, 1993, Daly et al., 1989). These shear zones are thought to have been created as a result of the Cambrian–Ordovician collisional event (530–430 Ma) (Mosley, 1993, Braile et al., 2006). The rift structure follows the general north–south trend of the Mozambique Mobile Belt, and its location governed by the boundary between two contrasting types of lithosphere; the Archean Tanzanian craton and the Proterozoic Mozambique belt (Hetzel and Strecker, 1994, Smith and Mosley, 1993). These features and their apparent ability to cut both Archean crust and Proterozoic mobile belt without any deviation of trend indicates that they are steep to vertical structures probably of lithospheric extent (Smith and Mosley, 1993).

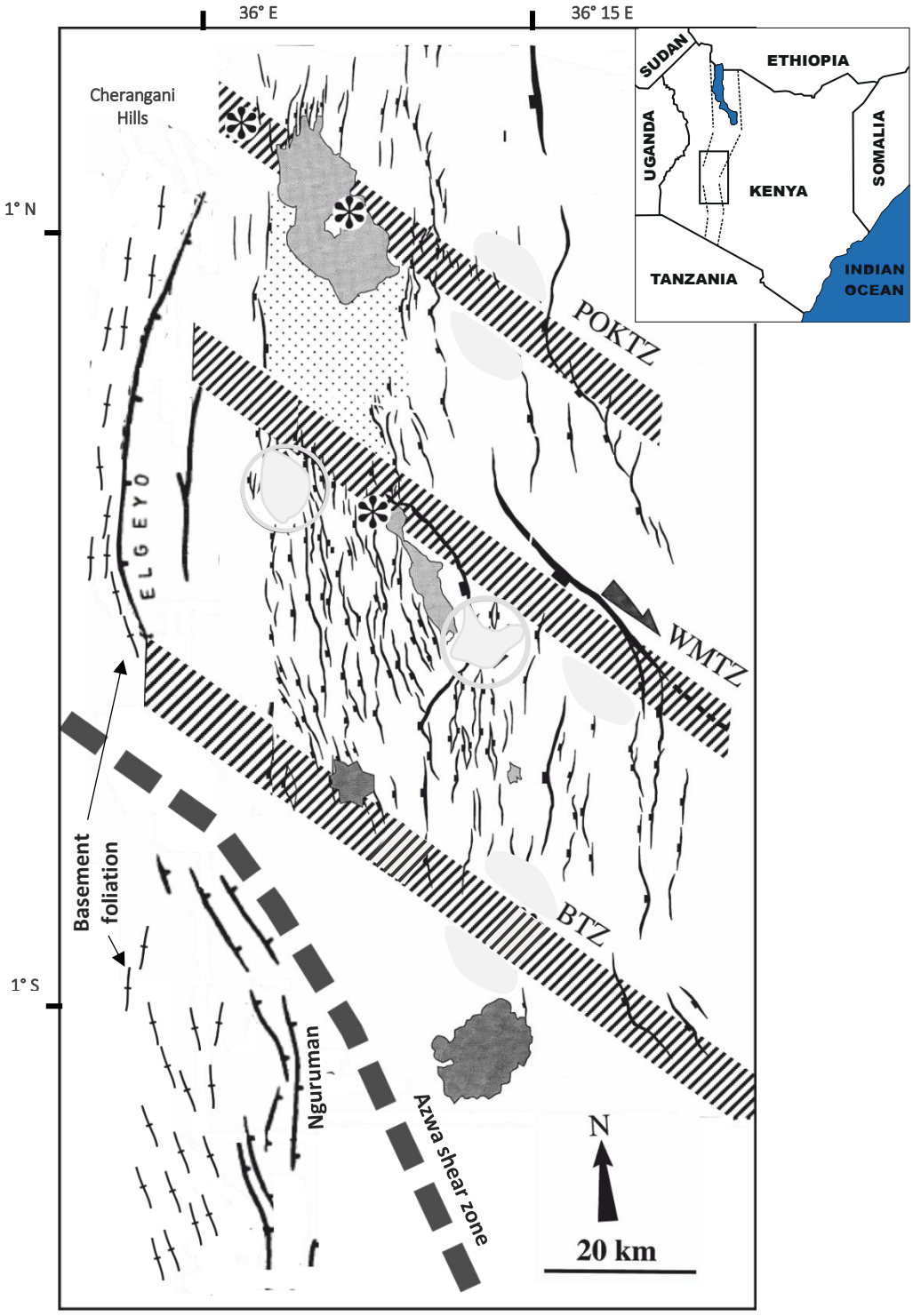

Figure 5.2. Simplified structural map (modified from (Le Turdu et al. (1999) and Hetzel and Strecker (1994)) for the central Kenya rift with basement structures showing three parallel shear zones: POKTZ (Porumbonyanza-Ol Kokwe Transverse Zone); WMTZ (Wasages-Marmanet Transverse Zone); (BTZ =Bahati Transverse Zone) interpreted by Le Turdu et al. (1999), and foliation within the basement along the Elgeyo and Nguruman Escarpments observed by Hetzel and Strecker (1994), and Aswa zone after (Katumwehe et al., 2016, Foster and Jackson, 1998).

The Precambrian basement is not evident within the rift axis, but well exposed outside it. However, several studies have suggested that the Precambrian fabrics continue underneath the rift and have influenced rift basin geometries; Mosley (1993), and Smith and Mosley (1993) pointed out that a network of a major NW and N trending Proterozoic shear zones such as the Aswa shear zone exist below the rift and affects the magma plumbing. Furthermore, the Aswa shear zone is an important Precambrian lithospheric structure in eastern Africa, which is 50 km in width and extends in a NW–SE direction from southern Kenya through Uganda and ending up in the southern part of south Sudan boarder (Katumwehe et al., 2016).

Hetzel and Strecker (1994) in their study observed from field observations two ductile shear zones within the Precambrian basement in the form of steeply E-dipping basement foliation along the western shoulder of the central Kenya rift. The reactivation of these foliations during the Miocene gave rise to the formation of asymmetric rift basin bounded by E-dipping normal faults marked by the Elgeyo and Nguruman escarpments. The Elgeyo escarpment in the north (Figure 5.2) mimics the N to NNE trend of the basement foliation, whereas, the Nguruman escarpment in the south is parallel to the N-NNW foliation (Hetzel and Strecker, 1994). The Elgeyo, Mau, and Nguruman escarpments bound the western flank of the Kenya rift (Zielke and Strecker, 2009). Le Turdu et al. (1999) also inferred three parallel oblique substratum heterogeneities, two of which according to the author, show nearly the same trend as the northwest striking brittle fault zones within the Precambrian basement that were inferred by Hetzel and Strecker (1994). These shear zones strike NW and produced from Neogene lava flows which cover the crystalline Precambrian basement in the axial graben of the central Kenya rift,

these discontinuities within the crust led to formation of atypical fault geometry (z and s shaped faults) within the axial graben of Baringo-Bogoria and Magadi areas, this atypical fault geometry was attributed to deformation of the oblique substratum heterogeneities under the regional extensional stress of east-west in the Kenya rift during early Pliocene (Le Turdu et al., 1999). Moreover, these major Proterozoic NW–SE shear zones were also mapped by Robertson et al. (2015) at both flanks of the rift in northern Kenya rift, at the Cherangani Hills (Figure 5.2), and in southern Kenya, near the Loita Hills, further south of the study area at the border with Tanzania.

The regional stress field in the central Kenya rift is demonstrated to be east-west during Miocene time (Bosworth and Strecker, 1997, Grimaud et al., 1994, Strecker et al., 1990, Ebinger, 1989a, Morley, 1988). The extension direction has rotated in clockwise motion in the northeast Africa during upper Pliocene-lower Pleistocene from E-W orientation to NW-SE orientation (Bosworth and Strecker, 1997, Strecker and Blisniuk, 1992, Strecker and Bosworth, 1991, Strecker et al., 1990, Young, 1989, Maguire et al., 1988), which was verified by analysis of fault kinematic and borehole-breakout data from the north eastern rift shoulder of Kenya rift ,about lat 2°N, long 37°E, where the lease compressive stress direction (*S*hmin) of 140° was calculated by Bosworth (1989), this rotation of extension direction is a regional phenomenon as it was also observed for example in the Malawi Rift (Mortimer et al., 2007). However, Hetzel and Strecker (1994) in their study suggested that this part of the Kenya rift does not seem to be affected by the new extension direction of NW-SE, they attributed the formation of sigmoidal fault geometry in some places of the central Kenya rift to reactivation of NW shear zones beneath the central Kenya rift under E-W stress direction.

5.2.2 Basement structure of the central and northern Main Ethiopian Rift.

The main rifting phases that existed along the Main Ethiopian Rift (MER) during the Mio-Pliocene time and within the Mozambique Belt are thought to be triggered and controlled by the reactivation of the Pre-Cambrian foliation at a lithospheric-scale, and influenced by E-W extension direction, and led to the creation of an oblique rifting (Boccaletti, 1998, Corti, 2009). Fault geometry, interaction and propagation at a local scale are thought to be controlled by the Tertiary extensional reactivation of inherited lithospheric structures, where the observed Tertiary structures are parallel to the existing foliation (Kazmin et al., 1980). There are two main prominent basement structure in the Ethiopian rift that have been recognised and described in (Mohr, 1987, Abbate and Sagri, 1980, Wolde, 1989, Abebe et al., 1998), these basement features are named, the Yerer-Tullu Wellel Volcanotectonic Lineament (YTVL) and Goba–Bonga lineaments (Figure 5.3), and thought to be associated with the development of the MER (Keranen & Klemperer 2008). They broadly trend E-W and consist of normal faults and major shield volcanoes (Abebe et al., 1998, Bonini et al., 2005, Keranen and Klemperer, 2008, Corti, 2009, Abebe et al., 2010). The YTVL (Figure 5.3) is a trend of volcanoes and fracture systems trending broadly east-west between ~8.5–9 N, intersecting the MER at the NMER–CMER boundary (Keranen and Klemperer, 2008).

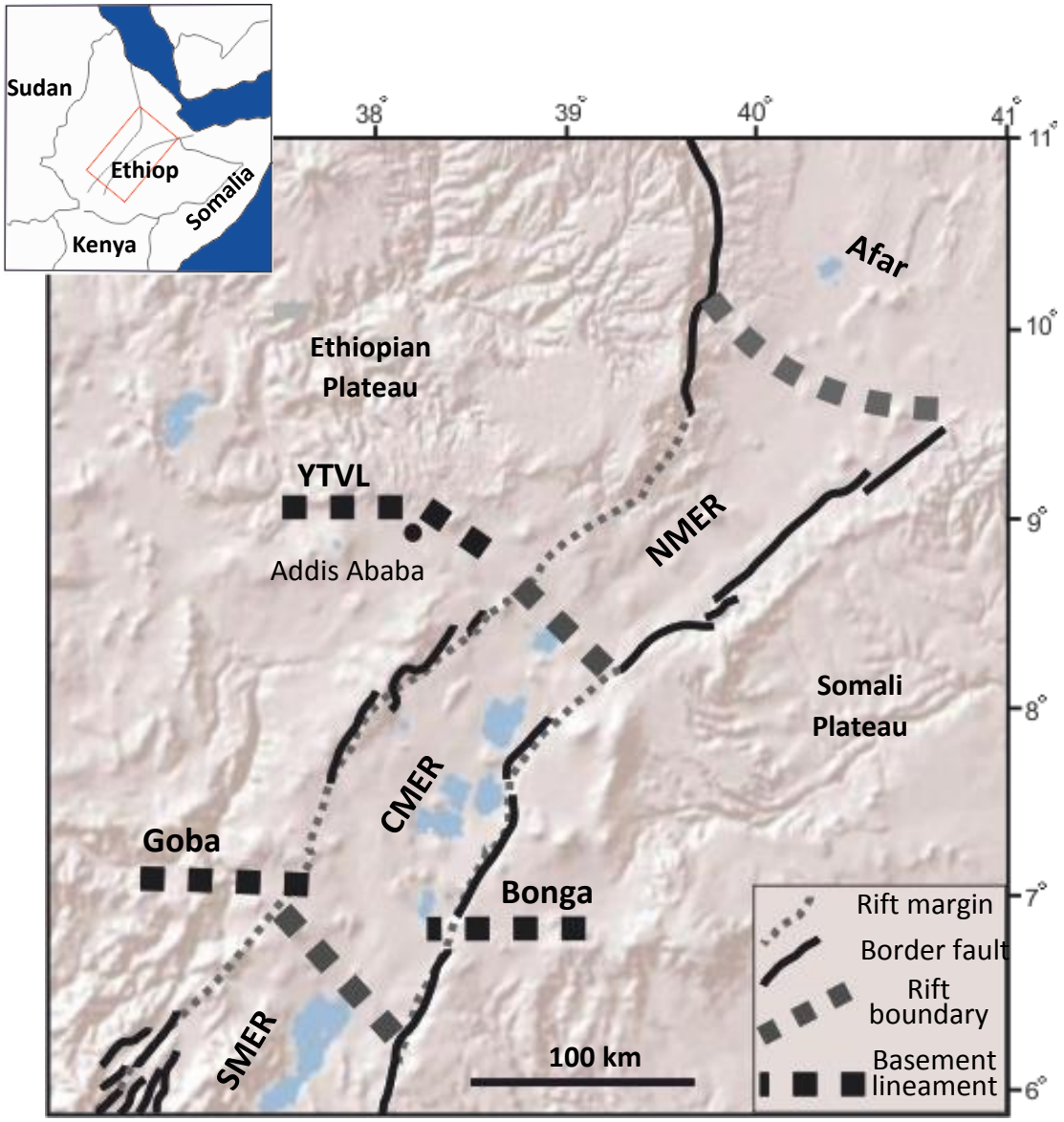

Figure 5.3. Location of the Main Ethiopian Rift MER. (NMER) the Northern MER, (CMER) the Central MER, and (SMER) the Southern MER. (YTVL) The Yerer–Tullu Wellel Volcanotectonic Lineament, and Goba-Bonga are from (Bonini et al., 2005) . segment boundaries are from Hayward and Ebinger (1996).

The YTVL is 80km in breadth and extends for about 700 km westward from the western border of the MER to extend to the Sudan border (Abebe et al., 1998). There has been an on-going debate as whether the YTVL (Figure 5.3) is related to the evolution of the Main Ethiopian Rift, e.g. Keranen and Klemperer (2008) has interpreted that the YTVL has a direct effect on the structural evolution of the Main Ethiopian Rift, whereas e.g. Abebe et al. (1998) and Abbate and Sagri (1980) speculated its relationships to the development of the MER, yet they associated the trends of these tectonomagmatic systems with the trend of the Gulf of Aden fracture system. The Goba–Bonga lineament extends across the central MER and terminated at the Ethiopian Plateau to the west of the western boarder of the central MER and formed Gojeb graben (Boccaletti, 1998). The Goba–Bonga lineament acts as a barrier that constrains the southward propagation of rift related deformation from Central MER to the Southern MER and vice versa (Bonini et al., 2005). Moreover, The YTVL and Goba–Bong alinements (Figure 5.3) have been widely adopted in recent geological and geophysical studies in the main Ethiopian rift including; e.g. Abebe et al. (1998), Abebe, Mazzarini et al. (1998), M Bonini et al. (2005), corti et al. 2009, Abebe, Balestrieri et al. (2010) as the main basement feature effecting the rift evolution.

5.3 **Method**

Analysis that have been carried out in this chapter required a combination of different geological and geophysical data (when available) in order to assess the influence of basement structure on fault evolution. All fault traces interpreted from DEM surfaces in the central Kenya rift, the central MER and the northern MER (chapter 3 & 4) were incorporated into ESRI GIS software, ArcMap 10.4.1. Underlying pre-existing structures (see section 5.4) were digitized from structural maps found in previously published studies on the Kenya rift (Figure 5.4) and MER (Figure 5.6), a simplified geological map and magnetic data (only for the central Kenya rift) were also included in the ArcGIS™ environment that allow all different data to be geospatially located in a consistent coordinate system (in this study all the data were assigned WGS 84 UTM Zone 37N). The spatial analysis was then carried out by first, using the overlay technique in 2D to qualitatively correlate between different fault trends on the surface and the pre-existing structures and other geological and geophysical datasets (Figure 5.4 for Kenya rift and Figure 5.6 for the MER). This ability to overlay various datasets within GIS has allowed spatial correspondences to be identified between pre-existing structures and later fault patterns.

The qualitative assessment was then quantitatively tested using the second spatial analysis that involved construction of rose diagrams (Figure 5.5 & Figure 5.7) that encompass orientations of fault populations in each rift segment. The present day stress orientations (local extension direction) based upon the least compressive stress, and orientation of pre-existing structures were plotted as azimuths and superimposed on the rose diagram, subsequent

angle between stress direction (σ3) and the azimuth of pre-existing fabric are displayed in (Table 5.1 &Table *5.2*).

The obtained results were then compared to the existing sandbox models to assess the role of pre-existing structures with varying orientations to extension direction on the geometry and orientation of surface faults, two sandbox models by Bellahsen and Daniel (2005) and Agostini et al. (2009) were used for this comparison in attempt to contribute to the overall understanding of the influence of pre-existing structural heterogeneities in the basement rocks upon surface fault geometry. These analogue models by Bellahsen and Daniel (2005) and Agostini et al. (2009) have been created to understand the influence of pre-existing anisotropy on the evolution of rifting. These experiments show how the orientation of pre-existing discontinuities with respect to the extension direction can control the geometry and evolution of a younger fault network. They have generated detailed information on the surface fault patterns and demonstrated that variations in the obliquity angle α (i.e. the angle between the pre-existing weakness and the extension direction) is the key factor in controlling rift kinematics. More details about the model set-up, experimental method, materials used and deformation conditions are extensively described in their related papers.

5.4 Results

5.4.1 Results of the central Kenya rift

As it has been previously discussed (chapter 3), fault populations in the central Kenya rift were divided into three subzones based upon their observed range of orientation. All the 620 faults mapped from DEM data in the central Kenya rift were overlaid Precambrian basement features (Figure 5.4) that include:

1) multiple NW shear zones; Nyangere Shear zone, Athi Shear zone and the NS trending Barsaloi Shear zone, and Aswa shear zone, and several inferred NW Shear zones shown in (Mosley, 1993). The Aswa shear zone trends NW (N 140°) (Katumwehe et al., 2016).

2) NW (N130°-140°) obliquely trending shear zones, these lineaments have been interpreted from gravity and aeromagnetic data as deep basement-controlled features, namely the Porumbonyanza- Ol Kokwe transverse zone (POKTZ) (Le Turdu et al., 1999), which was also interpreted as Kerio-Bogoria-Marmanet transfer zone (KBM) (Smith and Mosley, 1993), the Wasages Marmanet transverse zone (WMTZ), and the Bahati transverse zone (BTZ), these NW (N130°-140°) obliquely trending shear zones do not seem to continue across the rift in this region (Le Turdu et al., 1999).

3) Basement foliation along Elgeyo and Nguruman Escarpments forming NW trending shear zones (Hetzel and Strecker, 1994) (Figure 5.4). All these shear zones were identified as faults.

The spatial variations in fault orientation on the surface in this study can then be correlated with the basement structures defined in the literature to assess the possible influence from the basement pre- fabrics in relation to the reginal stress direction.

The overlay of a simplified geological map of Kenya (Figure 5.4), digitized and modified from (Simonet et al., 2004) and based upon the geological map of Kenya, survey of Kenya, 1969, showed that the whole rift segment falls within Cenozoic volcanic sediments and the Precambrian basement is only exposed outside the rift as indicated in some previous studies (e.g. Smith and Mosley, 1993, Mosley, 1993). The Nyangere Shear zone trending NW is located NW to the northern left shoulder of the rift and the Athi Shear zone trending NW and located SE to the southern right shoulder of the rift, these shear zones seem spatially related and only the Cenozoic volcanic sediments within the rift seem to obscure their continuation (Figure 5.4). The gap between these two shear zones coincides with the Kerio-Bogoria-Marmanet transfer zone (KBM) (Smith and Mosley, 1993), and the POKTZ and WMTZ inferred shear zones by Le Turdu, Tiercelin (1999), the evidence of their link can be realized by comparing them with the Aswa shear zone that is well defined in previous studies e.g. Mosley (1993) and (Le Turdu, Tiercelin (1999), and described by Morley (1999) as the best known oblique trend in the EARS, the Aswa shear zone has similar trend and spatial distribution to the Nyangea Athi shear zones (Figure 5.4), and cut across both the Archean crust and the Proterozoic mobile belt without any deviation of trend as indicated by Smith and Mosely (1993).

The visual inspection suggests that all fault populations in the three zones appear to be spatially sitting within vicinities of the underlying foliations and shear zones in the basement, zone 1 in the north (Figure 5.4) is characterized by fewer faults (149) than zones 2 (295) and 3 (177), most fault populations in this zone 1 sit midway between Nyangere and Athi Shear zones, and partially overlay the POKTZ transverse zone, and the Elgeyo escarpments appear to be affected by the basement foliation with overall trends of N and NNE at the north-western part of the rift.

Fault populations in zone 2 in the centre of the rift (Figure 5.4) overlays the basement structure that was described by Smith and Mosley (1993) as a 100 km wide complex zone comprising ductile and brittle shear zones of the Nyangea Athi from the north-eastern boundary and includes the Aswa Shear zone from the southern boundary (Figure 5.4), therefore, the relatively wide range of fault orientations (NNE to NNW) within this zone could have been influenced by the presence of these pervasive fabrics, and that is according to some previous studies of e.g. Morley (1999 a), Morley (1999d) and Chattopadhyay and Chakra (2013) that suggested that pervasive fabrics are responsible for most large-scale changes in fault orientation within rift system.

As for zone 3 in the south (Figure 3.4), the general trend of NW of the rift axis and the NNW trend of fault populations in this southern region, all seem to be influenced by the N140° Aswa shear zone.

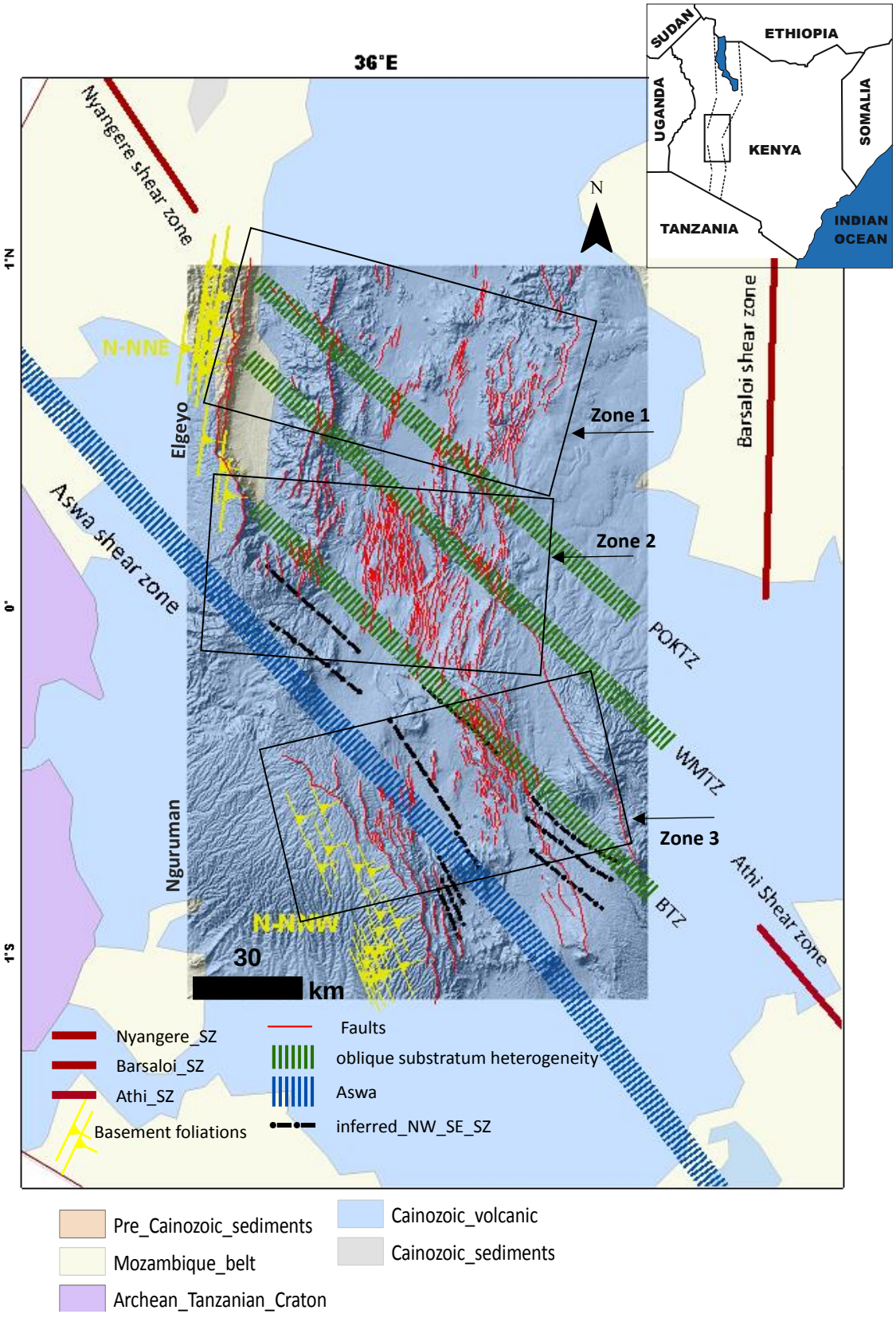

Figure 5.4 a simplified geological map superimposed on a shaded relief surface of the central Kenya rift showing the mapped surface faults (thin red lines), fault population zones (black rectangles) and pre-existing basement structures mapped from the literature

Table 5.1 Displays statistics of the rose diagrams

Zones	n	A	σ3	P1	α1	P2	α2
Zone 1	149	7°	277°	11°	88°	315°	38°
Zone 2	295	4°	274°	-	-	315°	41°
Zone 3	177	349°	259°	349°	90°	320	61

n: total number of faults

A: mean trend of fault population, also parallel to rift axis

σ3: least compressive stress perpendicular to mean segment orientation.

P1: trend of the basement foliations (yellow dashed line)

α1 angle between stress direction (σ3) and the basement foliations P1

P2: trend of the NW shear zones

α2 angle between stress direction (σ3) and the oblique NW shear zones P2

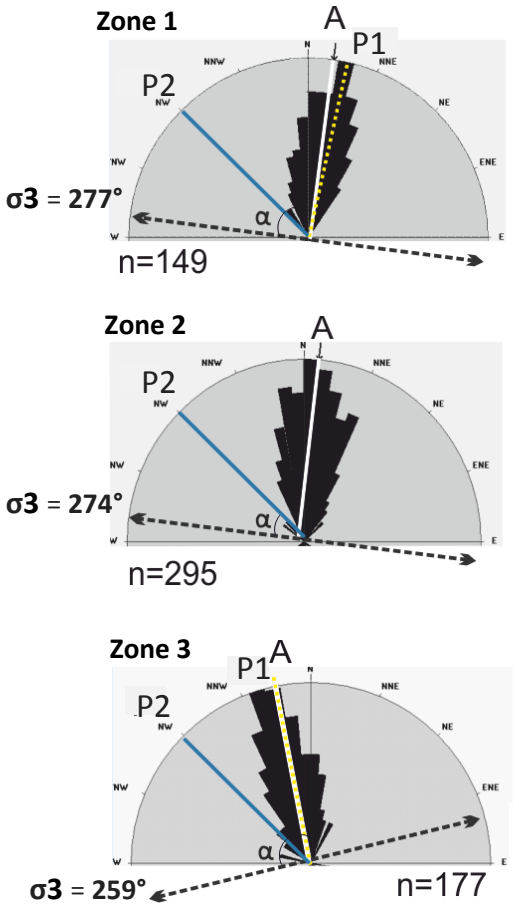

Figure 5.5. Rose diagrams showing fault orientations for each zone in the central Kenya rift, with regional stresses direction and pre-existing structures all plotted as azimuths, superimposed on the rose diagram.

5.4.2 Results of the central and northern main Ethiopian rift

As it has been presented in section (5.2.2), there are two EW prominent basement features that are believed to be related to the development of the MER, these features are the Yerer-Tullu Wellel (YTVL) volcanotectonic lineament and Goba-Bonga lineament (Abebe et al. 1998; Keranen & Klemperer 2008). These lineaments have been captured and incorporated into ArcGIS (Figure 5.6) and displayed along the mapped surface faults from DEM. The YTVL is 80 km wide between 9°05'N and 8°20'N (Abebe et al., 1998), which may suggest that it underlies a great deal of the northern MER and some of the northern part of the central MER. However, the NS extend (width) of the Goba-Bonga lineament has not been constrained in previous studies.

Therefore, to investigate the possible influence of these lineaments on the evolution of normal faults at the earth's surface in the northern and the central MER, the NW trend of the eastern part of the Yerer Tullu-Wellel linemeant has been extrapolated into the rift (Figure 5.17) in the same way as proposed by Mazzarini et al. (1999) and also adopted by Bonini et al. (2005), this extrapolation makes the central MER appear to be bounded by the boundary of the (YTVL) from the north and those of the Goba-Bonga lineament from the south. Moreover, for the sake of this investigation, in areas where some fault populations do not overlie the YTVL and the Goba-Bonga lineaments, we need to assume that more lineaments with similar trend exist underneath those fault populations, giving that the fault orientation is similar all over the area.

The rose diagrams (Figure 5.7) show orientations of fault populations, trend of basement structures, trend of stress direction as well as trend of rift axis,

values of theses orientations and subsequent angle between stress direction and the azimuth of pre-existing fabric are displayed in (Table *5.2*).

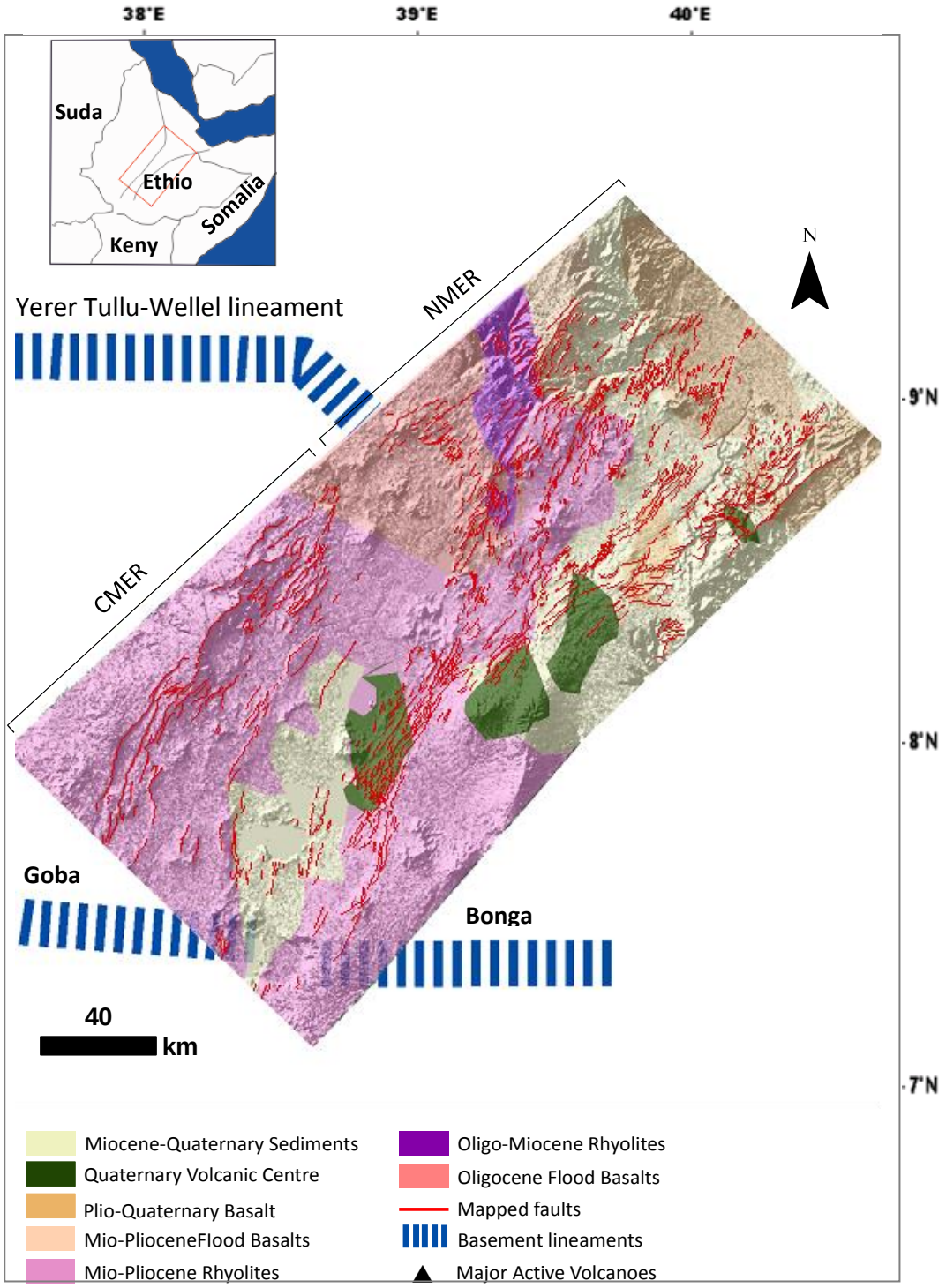

Figure 5.6. a simplified geological map superimposed on a shaded relief surface of the CMER and NMER showing the mapped surface faults (thin red lines) and pre-existing basement lineaments .

Table 5.2. Displays statistics of the rose diagrams (see Table 5.1 for abbreviations)

Zones	n	A	σ3	P	α
NMER	1041	32°	302°	315°	13°
CMER	468	28°	298°	270°	28°

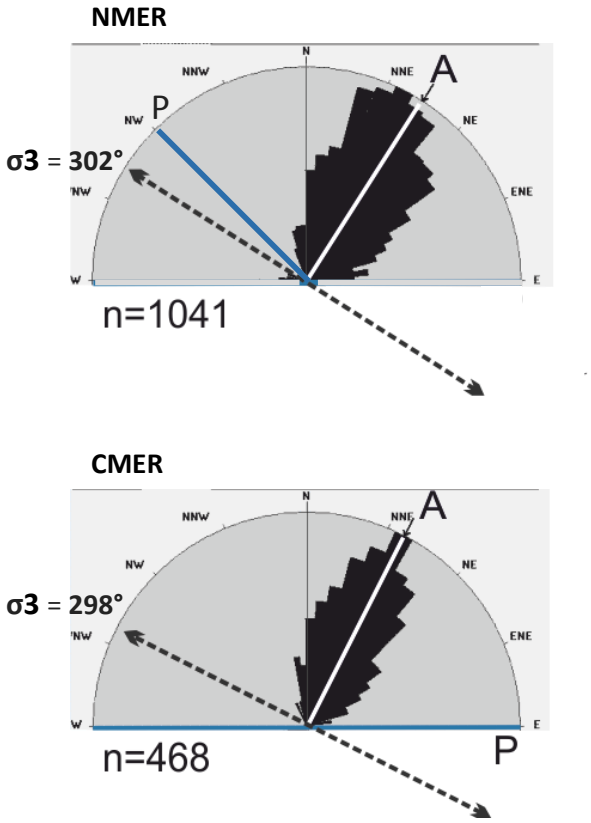

Figure 5.7. Rose diagrams showing azimuths of fault populations, local stresses direction and pre-existing structures for the northern MER and the central MER (see Table 5.1 for abbreviations).

5.5 Discussion: Interpretation of fault orientation and comparison with experimental models

The qualitative and quantitative analyses carried out above assume that the main factors that influence the geometry of normal faults (i.e. fault orientation) in the three study areas (The central Kenya rift, the central and northern MERs) are extension direction and pre-existing structures. It has been indicated in section 5.1 that the response of basement structures to the regional stress in active rifting is difficult to characterize, hence, to tackle this complexity, a number of assumptions have to be made (as shown in the following sections). Therefore, for this the purpose of this investigation, in areas where some fault populations do not directly overlay basement structures in the three study areas, it has been assumed that more inherited structures with similar trend as the defined ones (Figure 5.4 & Figure 5.6) exist underneath those fault populations, or the existent structures are wide enough to underlay those fault populations.

5.5.1 The central Kenya rift

Chapter 3 has discussed the variations of fault populations in terms of fault orientation, length and displacement in the three zones (zone 1, 2 & 3) of the central Kenya rift. These variation may suggest differences in the crust underlying these three zones or different influences by pre-existing structures. Consequently, to investigate this possibility further, it has been assumed that this study area undergo different local stresses imposed by the presence of pre-existing structure, as suggested in a number of studies (e.g.

Aleksandrowski et al., 1992, Teyssier and Tikoff, 1999) that regional stress distributions are likely to encounter perturbations due to interferences with pre-existing structures, leading to localised variations in stress/strain orientations that may depart considerably from regional stress trends. On the other hand, some other authors (e.g. Yale, 2003, De Guidi et al., 2013) found that the variation in local stress orientation is due to the presence of large scale faulting.

According to the theory of classification of tectonic stress by Anderson (1951), normal faults in a homogeneous rock type form perpendicular to the least compressive stress σ3, hence, it is worth noting that the three study areas (The central Kenya rift, the central and northern MERs) are characterised by relatively homogeneous lithology of volcanic sediments of post Miocene lava (Stoyan and Gloaguen, 2011). Anderson (1951) also pointed out that the least compressive stress is perpendicular to mean fault segment orientation and indicates to the local/regional extension direction. Therefore, the local stress orientation was estimated in this study based upon the average fault orientation in each zone using the rose diagram, assuming that all faults in their local zone are subject to the same local stress state, and therefore, the principal stresses should be the same for all faults. The mean fault orientation calculated by the rose diagram software was 7°N, 4°N and 349°N for zone 1, zone 2 and zone 3 respectively (Table 5.1). Subsequently, the calculated least compressive stress σ3 (representing stress direction) for zone 1, zone 2 and zone 3 are N277°, N274° and N259° respectively (Figure 5.5). It can be noticed that there are slight differences between these values of least compressive stress orientations and the east-west (N270°) regional extension direction during the Miocene in the central Kenya rift as reported in the

literature (e.g. Morley, 1988, Ebinger, 1989a, Strecker et al., 1990, Grimaud et al., 1994, Bosworth and Strecker, 1997). This consistency in the inferred extension direction indicates that these zones undergo a similar regional stress direction, however, the analysis in this chapter would still be based upon the local stress direction to accurately calculate the angle between the stress direction and the pre-existing structures.

. Therefore, the variations exhibited in the range of fault orientation in the three zones could be interpreted as follow:

5.5.1.1 Zone 1

The basement in zone 1 in the northern part of the study area (Figure 5.4), according to Key et al. (1989), connects the NW-SE and NNW-SSE Shear zones that include the Nyangere, Athi and POKTZ Shear zones with the N - S and to NNE-SSW trending shears, of these the Barsaloian Shear zone and the Elgeyo foliation zone (Figure 5.4). Therefore, the basement structure can be divided into two orders of pre-existing structure with the potential of reactivation.

The first order of pre-existing structure in this northern zone of the central Kenya rift is the N to NNE basement foliation that was observed by Hetzel and Strecker (1994) beneath the left shoulder of the northern part of the rift at the Elgeyo fault escarpment (Figure 5.4). This fault escarpment is parallel to the rift axis but perpendicular the local stress direction, reactivation of this N-NNE trending basement foliation under this stress orientation could have led to the formation of the Elgayo escarpment, as indicated by Hetzel and Strecker (1994) that the overall trend of the Elgeyo fault follows the N-S trend of

pervasive foliations in the Precambrian basement and the trend of Mozambique belt. The Elgeyo escarpment was formed in the Miocene due to E-W extensional reactivation of the steep E-dipping (sub vertical ~ 75- 80°) N-NNE foliations underneath Elgeyo, these E-dipping foliations were originally formed during the Barsaloian event, (580 Ma) by reactivation of the NW-trending brittle sinistral fault zones, crossing the present Elgeyo Escarpment (Hetzel and Strecker, 1994). This is the most common case for discrete fabrics to be oblique to the main foliation trend rather than parallel (Morley, 1999d). Therefore, that should also be the case for surface faults influenced by older faults in the subsurface or by foliations in the basement. Therefore, the orientation of other faults striking N and NNE in zone 1 such as that forming the Kamasia horst (Figure 3.2) and those faults in the rift floor and the eastern flank of the rift, may have been influenced by the reactivation of the NW sinistral shear zones of the Nyangere, Athi, POKTZ and WMTZS within zone1, this has been discussed further in the following analysis.

The least compressive stress (σ3), which is comparable to the regional extension orientation according to Anderson (1951), was calculated from the rose diagram to be 97° (or N277°) (Table 5.1), this orientation corresponds to approximately east west stress direction with a shift of 7° to the south from the east. This stress direction is perpendicular to the average orientation of fault population and the rift axis in zone 1 (Figure 5.5). The N to NNE basement foliation that represent the first order pre-existing structure is at an angle of α 1 = 88° to the stress direction if it is assumed that the trend of this foliation is P1 = ~11° (average between N and NNE (0 to 22.5)) (Table 5.1), this very high angle (88°) made this foliation nearly perpendicular to the local extension

direction with a miner obliquity of 2°, which explains why the Eglyeo escarpment is parallel to the underling foliation (Figure 5.9a). This observation is comparable to that of sand box model of Agostini et al. (2009) (Figure 5.9b), where the angle of obliquity (α) in this model defined as the angle between the orientation of a line of weakness within the basement and the regional extension applied to the box, this angle is measured from the sand box as the angle between a line orthogonal to the pre-existing weakness and the extension direction, this angle corresponds to the angle of obliquity (α) measured from rose diagrams in this study (Figure 5.5 & Figure 5.7) between local stress direction (σ3) and pre-existing structure. In the Agostini et al. (2009) model, surface faults followed the same trend as pre-existing fabrics at miner or no obliquity. Moreover, such a case of development of boundary fault segments perpendicular to the extension direction due to local reactivation of weakness zones, has also been observed along the entire length of both the rift model of (Corti et al., 2007) and in the western branch of the EARS (Ebinger, 1989b, Morley, 1999d)

On the other hand, the NW (N 315°) (Table 5.1) shear zones that represent the second order of the pre-existing structure (P2) in this region (zone 1) is orientated at α 2 = 38° (Table 5.1) to the extension direction, and therefore a high obliquity is created due to this low angle. The resultant N to NNE surface traces of fault population in zone 1 compare reasonably to those formed in experimental model of oblique rifting of Agostini et al. (2009) (Figure 5.10a), who observed that for models with α > 0°, the trend of internal faults rift does not coincide with the underlying weak zone, moreover, when the oblique trending pre-existing faults in the model oriented at a moderate angle of 45°

to the extension direction, reactivation of the pre-existing structures at such degree to the extension direction led the newly formed fault at the surface to deviate away from the trend of the pre-existing structure by ~ 90° (perpendicular) and slightly higher to the stress direction (Figure 5.10a & a1). Likewise, in zone 1 the surface traces of fault population striking N to NNE along the rift floor and the eastern boundaries ignored the NW trend of the inferred traverse shear zones in the basement and oriented ~45° to ~ 60° to these pre-existing weak zone and~ 90° to the stress direction (Figure 5.10b). This strong correlation between the experimental model and orientation of the fault population in zone 1 with regard to the basement structure suggests a possible basement influence in those surface faults.

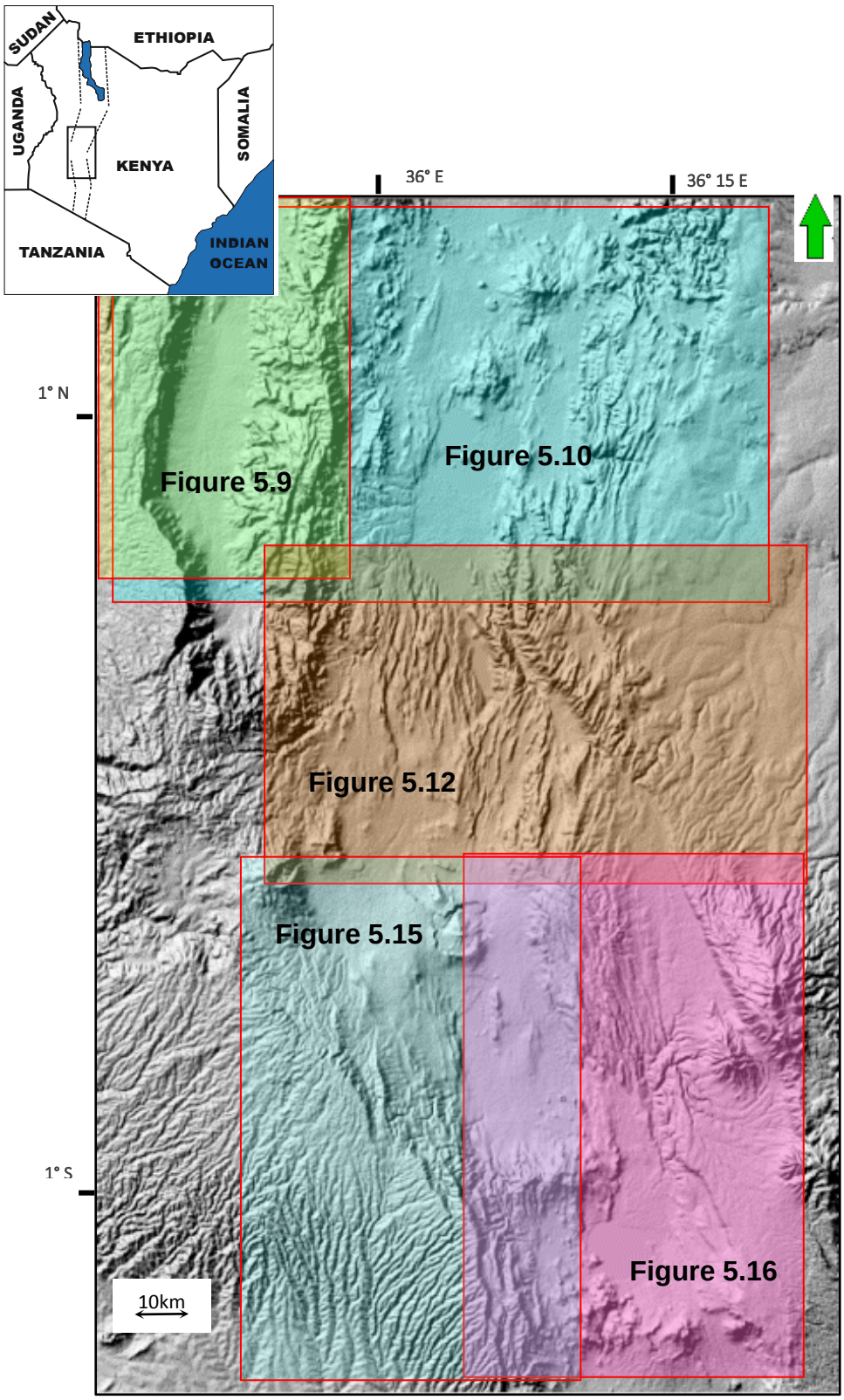

Figure 5.8 Location of figures used in section 5.5.1

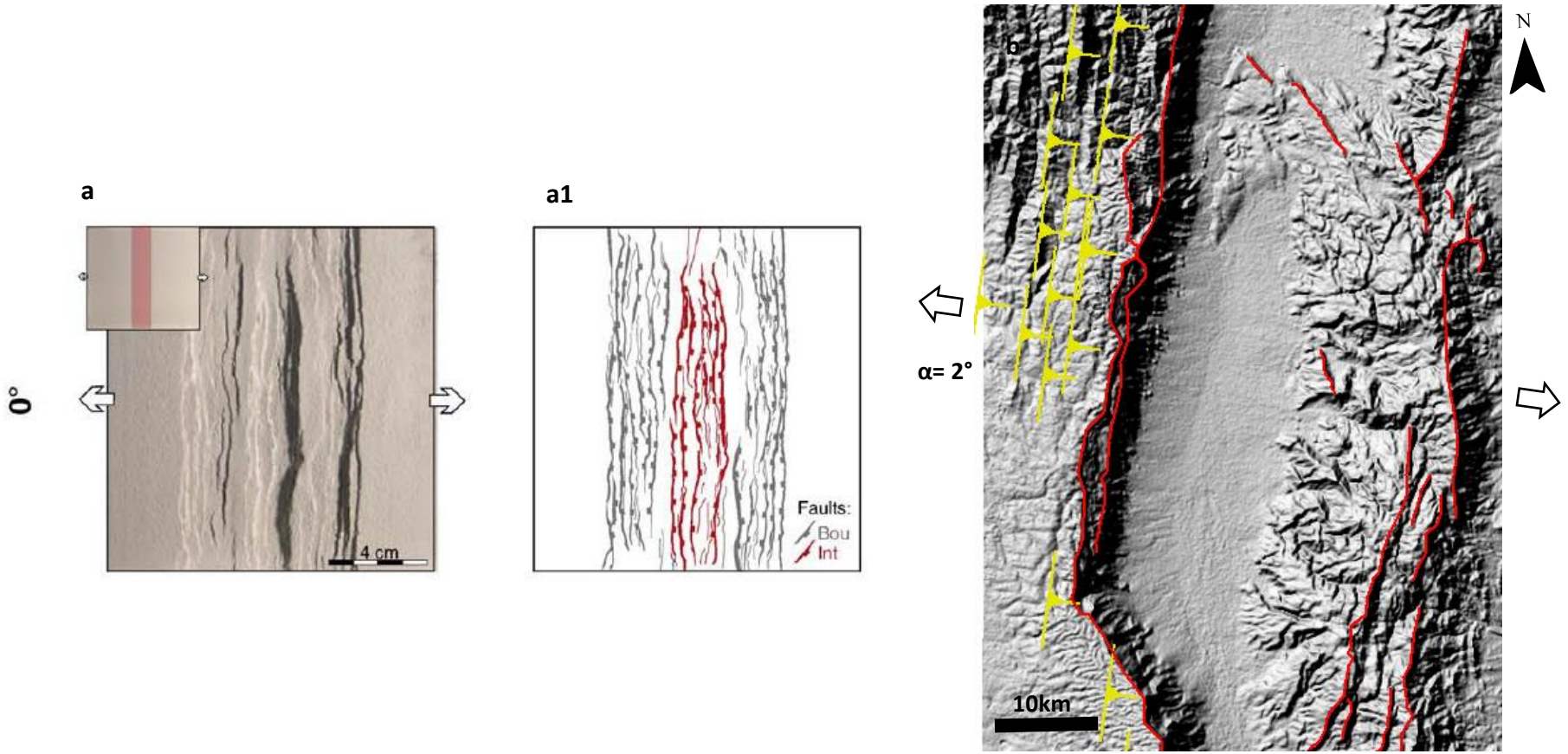

Figure 5.9 Comparing results of sandbox models of Agostini et al. (2009) (a and a1), where orthogonal model exhibiting surface faults perfectly coincide with the underlying weak zone at α=0°. The small inset image displays the orientation of pre-existing structure and extension direction. Figure 5.9b shows fault traces mapped in this research in zone 1, where high angle of 88° between the extension direction and the NNE basement foliation (yellow symbols) under Eglyeo escarpment produced a very low obliquity angle of 2° (see section 5.5.1.1 for details and Figure 5.8 for location).

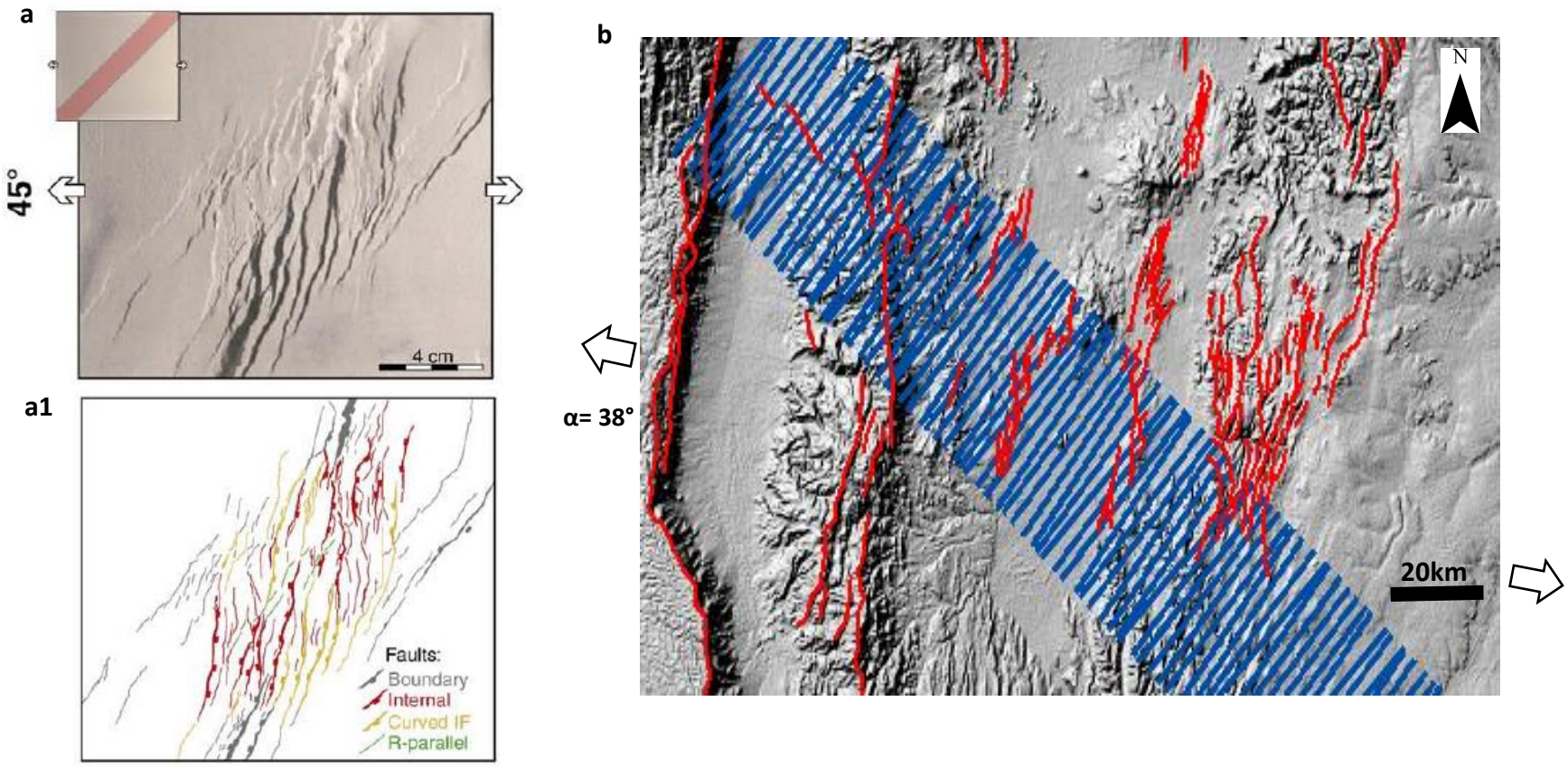

Figure 5.10 Comparing results of sandbox models of Agostini et al. (2009) Figure 5.10 a & a1 show an obliquity model exhibiting surface faults deviated upright to the underlying weak zone at α=45°. Figure 5.10 b shows the extension direction trends α=38° to the NW oblique shear zones (blue dashed lines) affecting rift floor and eastern rift boarder (see section 5.5.1.1 for details and Figure 5.8 for location).

5.5.1.2 Zone 2

The local extension orientation that was defined perpendicular to the average orientation of fault population and deformation zone of the rift axis for this central zone (zone 2) (Figure 5.5) is again in the region of approximately E-W direction, shifting slightly to the south of east, corresponds to least compressive stress (σ3) of 94° (or N274°), and trending at moderate angle of α2= 41° to the NW (315°N) transverse fabric (P2) (Table *5.2*) of WMTZ and BTZ

Fault populations in zone 2 in the centre of the rift (Figure 5.4) overlays the basement structure that was described by Smith and Mosley (1993) as a 100 km wide complex zone comprising ductile and brittle shear zones of the Nyangea Athi from the north-eastern boundary and includes the Aswa Shear zone from the southern boundary (Figure 5.4). This type of regional discontinuity in the Precambrian basement are referred to as pervasive fabrics (e.g. Morley, 1999 a, Morley, 1999d, Chattopadhyay and Chakra, 2013), and according to them, the pervasive fabrics are responsible for most large-scale changes in fault orientation within the rift system.

The central Kenya rift is typified by en echelon arrangements of normal faults (Morley et al., 1992, Baker and Wohlenberg, 1971). Moreover, en echelon arrangements of faulting results when the regional stretching direction is oblique to the deformation zone (Corti, 2012, Agostini et al., 2009, Corti, 2008, Dauteuil and Brun, 1996, Withjack and Jamison, 1986). Therefore, the en-echelon pattern of normal faults trending NNW to NNE observed at the surface in this zone (Figure 5.12) could have resulted from reactivation of that major pervasive NW (315°) trending Proterozoic basement fabrics (P2) under

approximately E-W extension direction at an angle of α= 41, which could have offered an oblique component of motion for such en-echelon to form. These inferences are similar to the sandbox models of Bellahsen and Daniel (2005), where pre-existing faults trend 45° to the extension direction (Figure 5.11), which led older faults to be reactivated and form as linking structures with relay ramp caused by en echelon arrangements. Moreover, the presence of en echelon pattern and the subsequent relay structures that were observed in this zone (figure 3.7, section 3.5.2) could also be an indication of reactivation of the basement structure, as suggested by Giba et al. (2012) that large pre-existing structure at depth can rupture through subsequent cover, resulting in en echelon segments at the surface, which are characterized by relay structures in the zones of fault overlap (Figure 5.11). Moreover, the development of such linking fault system observed in zone 2 (figure 3.7, section 3.5.2) suggest that the pervasive fabrics underlying this part of the central Kenya rift could have been active at the time of deformation, this inference was based upon the concept that active pre-existing fabrics act as through-going structure that has a uniform sense of shear that behave effectively as a through-going strike-slip zone that give rise to a linked fault system on the surface (Morley, 1999 a, Grimaud et al., 1994).

On the other hand, the relatively wide spread of fault orientation manifested in zone 2 around Bogoria lake, could also be due to accommodation of the abrupt change in rift orientation from N-S to ~NW (N150°) (Smith and Mosley, 1993) as a result of interference with the N140° Aswa Fault Zone (Le Turdu et al., 1999), which leads to development of complex fault patterns such as box ramp structures (Griffiths, 1980), and zigzag patterns and sigmoidal-shaped structures (Le Turdu et al., 1999). Another interpretation of the relatively wide

spread of fault orientation in zone 2 is the location of this area being at the junction showing significant variations in crustal thickness between the thick Tanzanian craton and the thin Mozambique mobile belt along the length of the Kenya rift as reported in (Smith and Mosley, 1993, Henry et al., 1990).

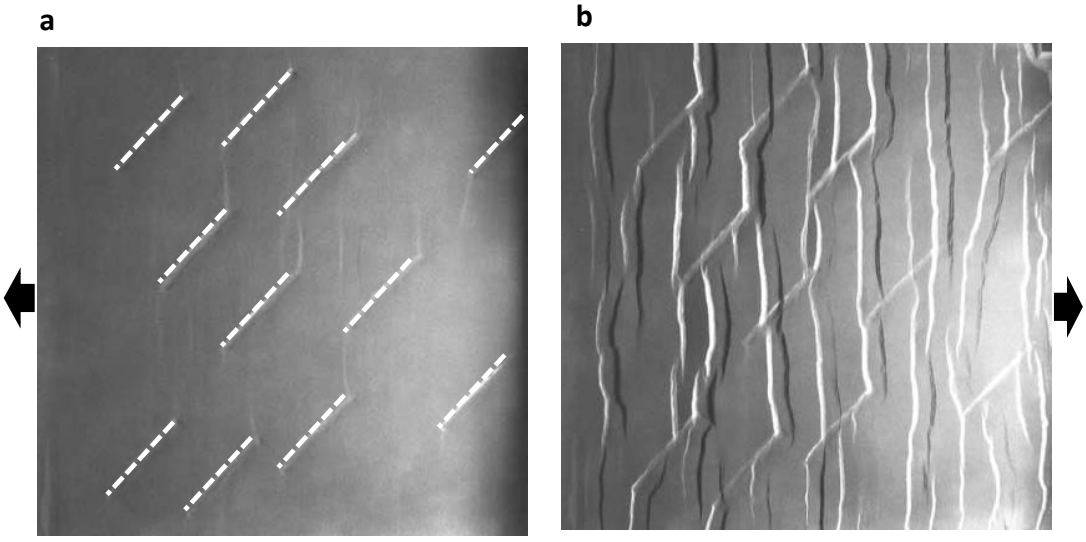

Figure 5.11. a) The pre-existing faults (dashed white lines) are at 45° to the extension direction , b) the faults are reactivated but are used as relay faults, modified from (Bellahsen and Daniel, 2005).

Furthermore, additional element worth noting that may indicate to different crustal characteristics, is offered by magnetic data over the study area (Figure 5.13), what can be noticed from this magnetic data is that, fault population in zone 2 coloured white overlay an E-W oriented magnetic low, while fault populations in zone 1 (north) and zone 3 (south) coloured red sit on a high magnetic anomaly (Figure 5.13). This law anomaly has a width of about 40km in average within vicinity of zone 2 (Bogoria basin) (Figure 5.14), and seem to extend for about 500km across the magnetic survey from east to west (dashed red line in Figure 5.14). This E-W low anomaly appear to separates

the N-S trending high amplitude magnetic anomalies along the rift axis even outside the study area to the north and to the south, and there are no other prominent E-W striking law anomalies with this size can be observed along the length of the rift within the survey. A traditional interpretation for such magnetic low within areas of magmatic activity, would suggest a magmatic or dike intrusion at depth. However, the observed large lateral extend of this anomaly (~500 km) may not favour this interpretation.

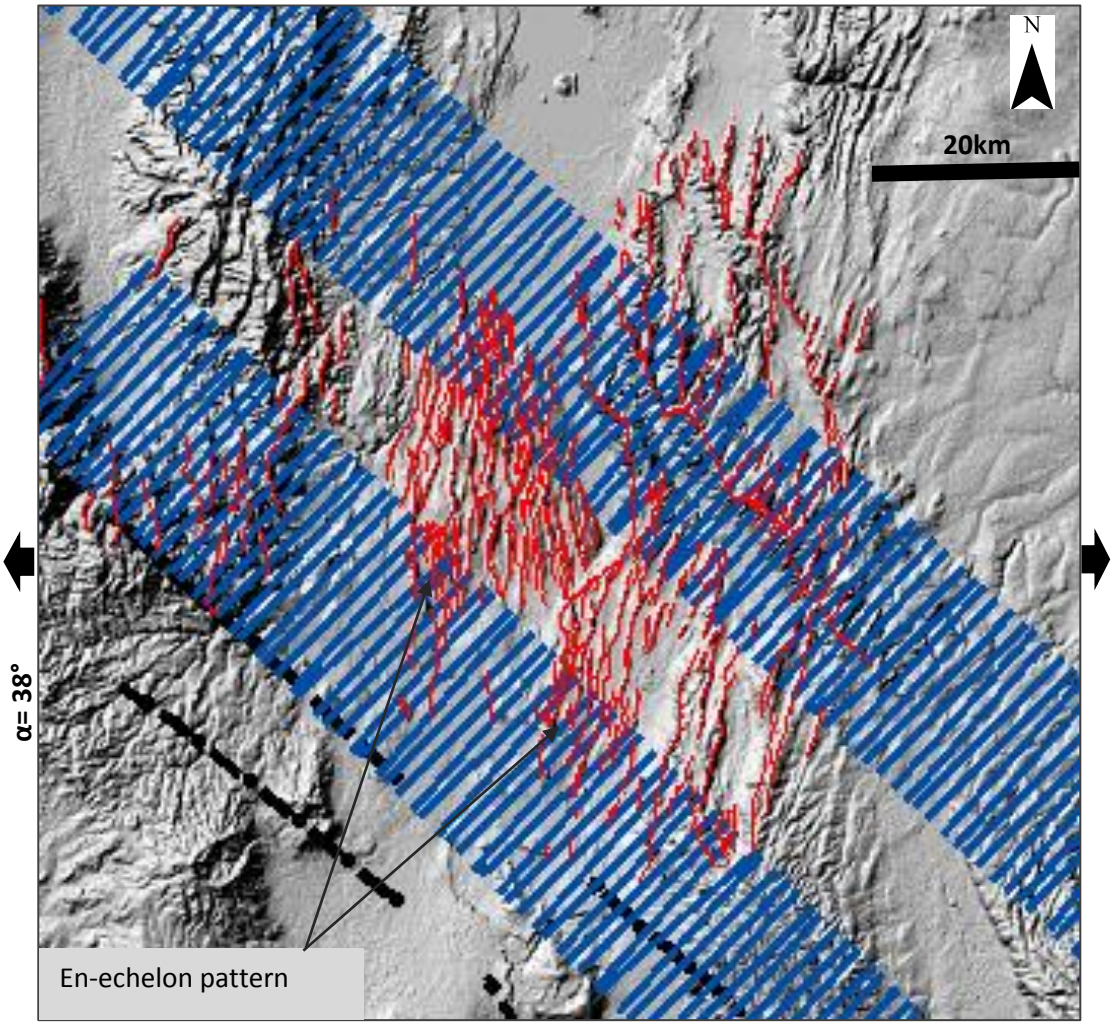

Figure 5.12. Fault trace population in zone 2 within the vicinity of underlying the NW oblique shear zones (blue dashed lines) and showing en echelon fault arrangements. Black bold arrows indicate to extension direction. See Figure 5.8 for location.

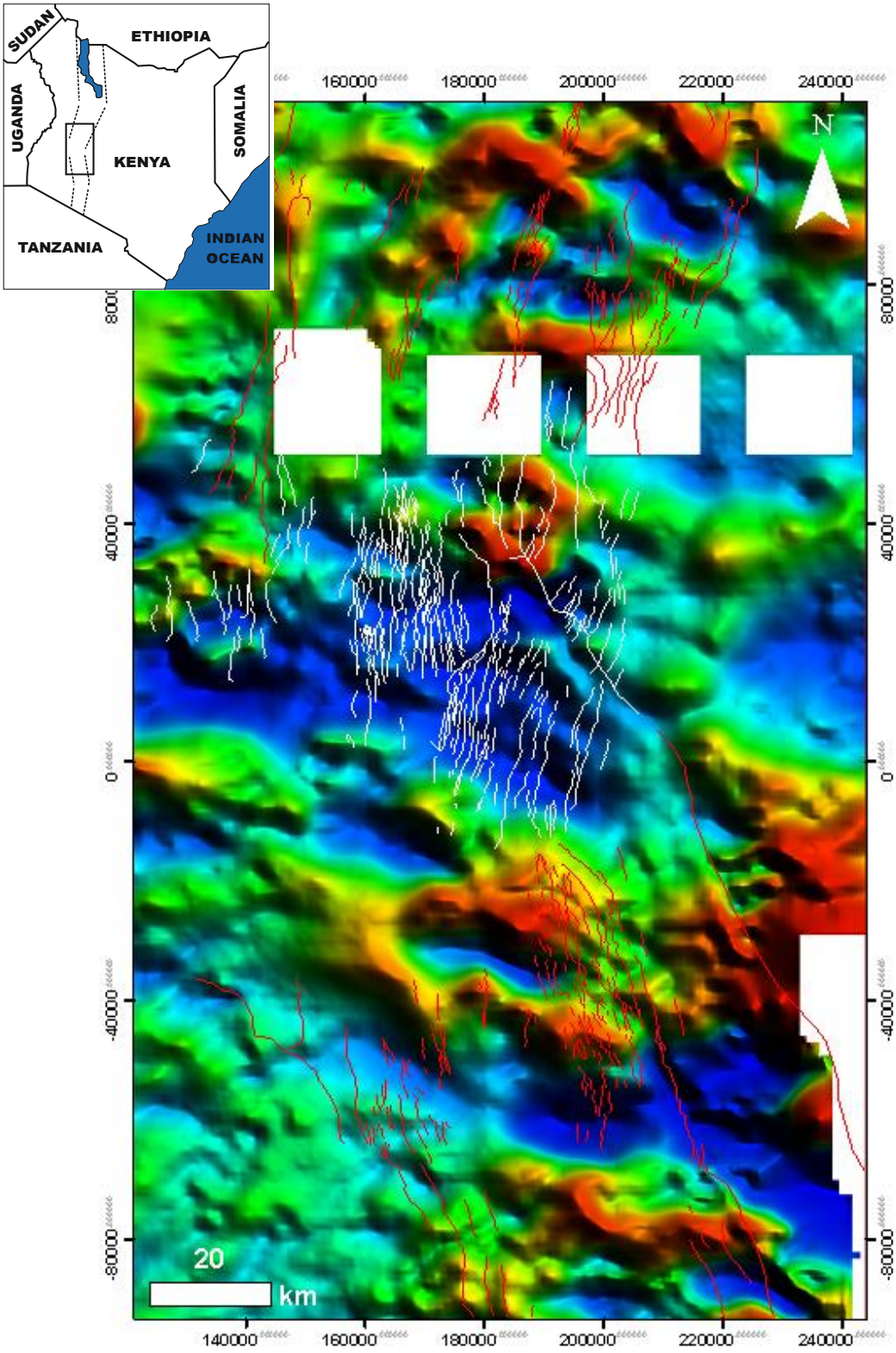

Figure 5.13. Magnetic anomaly map of the central Kenya rift. Fault population in zone 2 coloured white overlaying a low magnetic anomaly, while zone 1 (north) and zone 3 (south) coloured red sit on high anomaly, white boxes are areas with no survey.

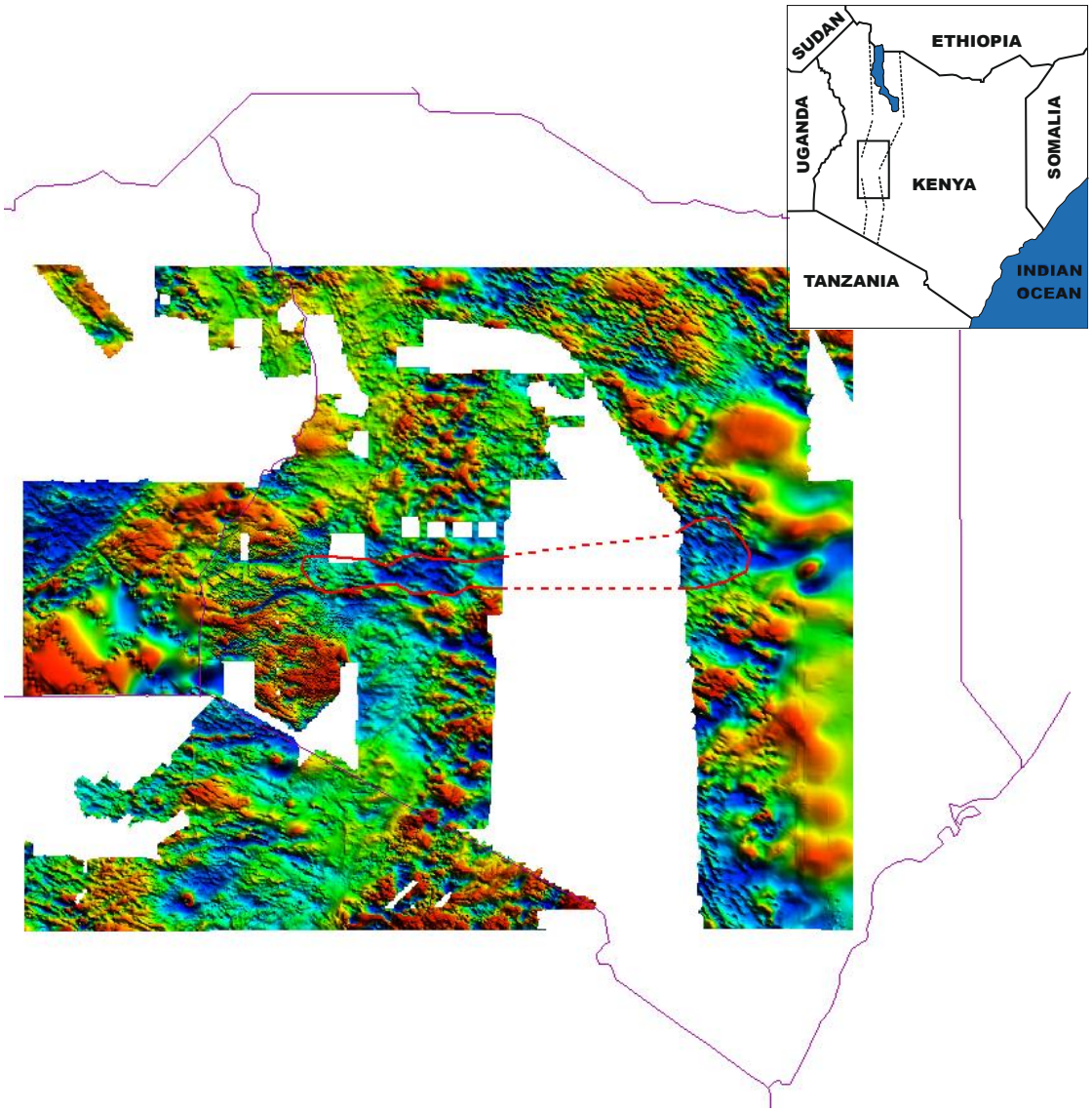

Figure 5.14. Magnetic survey over most of Kenya state, the red polygon delineate the extend of the E -W trending low magnetic anomaly, which cuts across the N-S trending magnetic highs along the rift axis even outside the study area.

5.5.1.3 Zone 3

Visual inspection on zone 3 in the south of the study area (Figure 5.4) suggests that the general trend of NW of the rift axis and the NNW trend of fault populations, all appear to fall under the control of the NW (N140°) trending large Proterozoic isolated fabric of the Aswa shear zone in the basement. Unlike pervasive fabrics, which can influence a large scale of fault orientation within the rift system (e.g. Morley, 1999 a, Morley, 1999d, Chattopadhyay and Chakra, 2013), discrete or isolated fabrics such as the Aswa shear zone can exert a local influence on rift faults (Morley, 1999 a, e.g. Morley, 1999d). In addition, some previous studies (e.g. Grimaud et al., 1994, Morley, 1999d, Morley, 1999 a) pointed out that lack of linked fault system in the NW trending fault populations within the vicinity of the Aswa shear zone may suggest that this shear zone is essentially passive.

Moreover, the N to NNW trending escarpment of Nguruman at the left shoulder of the southern part of the rift (Figure 5.4), is thought to have ben related to the Barsaloian event (-580 Ma), and formed at the same time as the Elgeyo escarpment in the northern left shoulder during the Miocene due to E-W extensional reactivation of the sub vertical E-dipping, N-NNW basement foliations underneath Nguruman escarpment that was observed by Hetzel and Strecker (1994). Therefore, as was the case in zone 1, the basement structure in this zone (zone3) can also be divided into two orders of pre-existing structure with the possibility of reactivation. The first order pre-existing structure (P1) (Table 5.1) is the N to NNW basement foliation beneath the Nguruman escarpment, and the second order of the pre-existing structure (P2) (Table 5.1) is represented by the Aswa shear zone.

Figure 5.5 and Table 5.1 shows that the local extension direction represented by the least compressive stress calculated for this southern zone (zone 3) is σ3= 79° (or N259°), this local extension direction is again approximately comparable to the regional extension direction of E-W with slight shifting of (11°) up to the north of east (Figure 5.5). The N to NNW basement foliation that represent the first order pre-existing structure (P1) in zone 3 is at angle of α 1 = 90° (Table 5.1) to the local extension direction if it is assumed that the trend of this foliation is at ~N349° (average between NNW (N337.5°) and N (N360°), this very high angle (90°) created a zero degree of obliquity between pre-existing fabrics and extension direction, which made the N to NNW basement foliation below the Nguruman escarpment perpendicular to the extension direction and therefore causing the Nguruman escarpment to emerge parallel to this foliation (Figure 5.15b) . This inferences are again comparable to that observed in the analogue model of Agostini et al. (2009) (Figure 5.15a & a1) where fault system at the surface followed the same trend as the pre-existing structure, when the later oriented 90° from the extension direction. In addition, the trend of the Nguruman could also be to some extend influenced by the NW (N140°) trend of the isolated fabric of Aswa shear zone (Figure 5.16b)

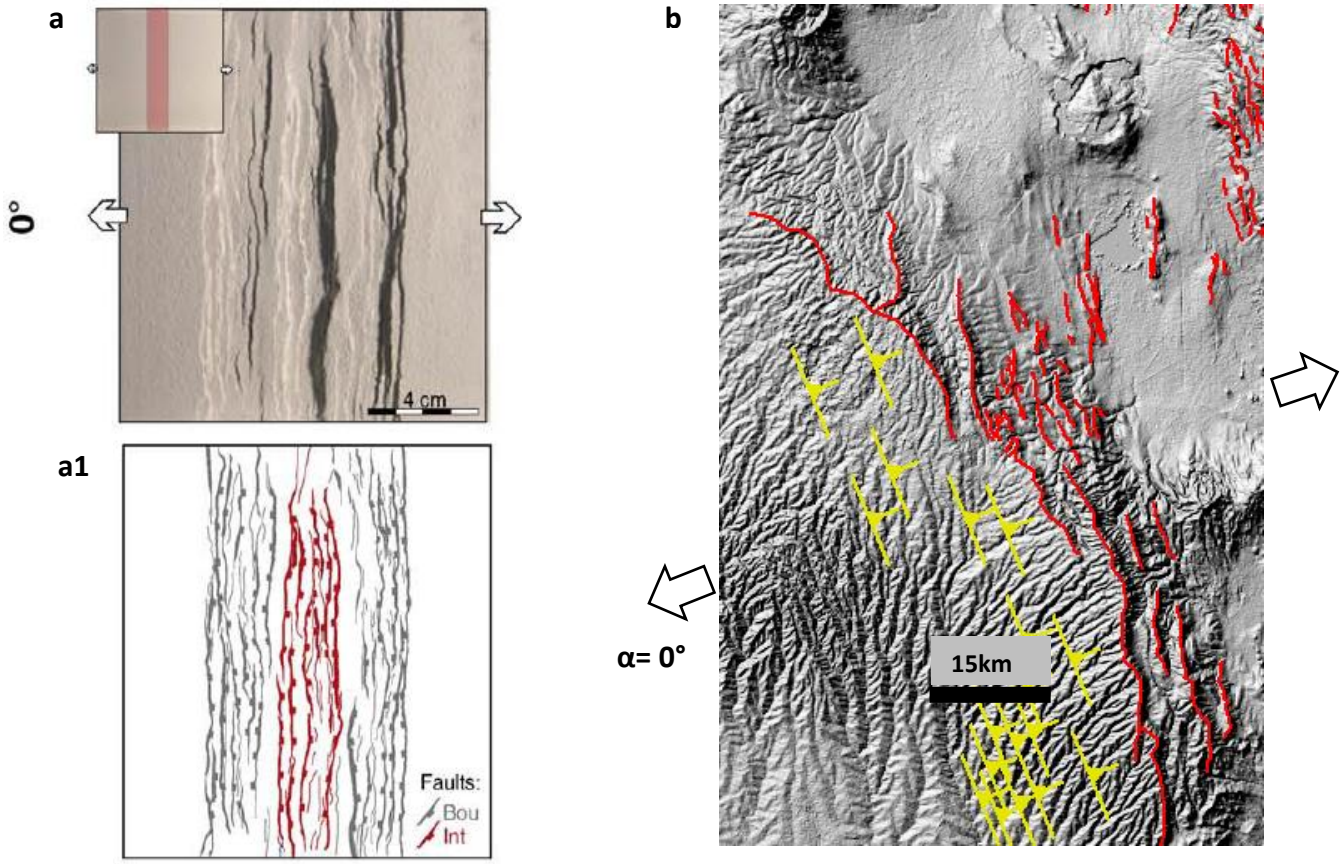

Figure 5.15 Comparing results of sandbox models of Agostini et al. (2009) (a and a1), where an Orthogonal model exhibiting surface faults perfectly coincide with the underlying weak zone at α=0°. Figure 5.15b shows fault traces and pre-existing structure in zone 3 of the study area, where the extension direction is at 90° (obliquity α= 0°) to NNW basement foliation (yellow symbols) under Nguruman escarpment (see section 5.5.1.3 for details ansd Figure 5.8 for location).

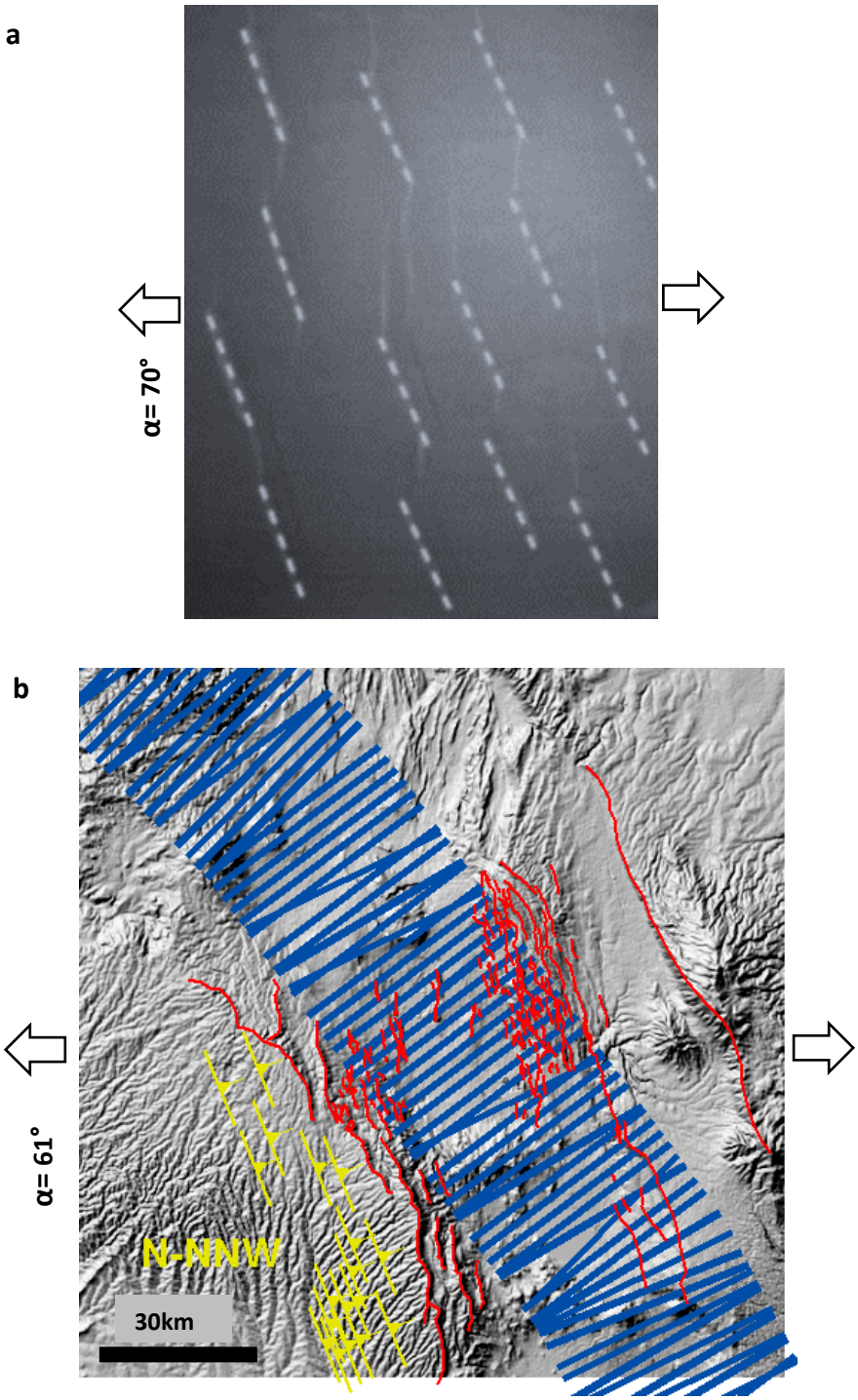

Figure 5.16 Comparing results of sandbox models of Bellahsen and Daniel (2005) (a), and fault traces in zone 3 of the study area (b). Figure 5.16a show newly formed fault at the surface of the model (grey lines) follow the same trend of the pre-existing fabric (Dashed white lines) when the latter oriented 70°to extension direction. Figure 5.16b shows the NW trending Aswa shear zone (blue dashed line) undergo extension at a high angle of α=61°, consequently, the surface faults also strike NW to NNW. See Figure 5.8 for location.

On the other hand, as for the second order pre-existing structure (P2) in zone 3, it has been suggested in Katumwehe et al. (2016) that the Aswa shear extends up to 50km in width. Therefore, I assumed that the Aswa shear zone could be bounding all faults in the rift floor and the eastern flank in the same way as exhibited in Figure 5.16. Hence, for the second order pre-existing structure (P2) in zone 3, the high angle of (α2= 61°) between the pre-existing structures of Aswa (N320°) to and the extension direction of 79° (or N 259°) (Table 5.1) exerted relatively low obliquity motion between these two components. In the sandbox models of Bellahsen and Daniel (2005) (Figure 5.16a), when the pre-existing faults in the model oriented 70° to the extension direction, the pre-existing discontinuities were reactivated and propagate from their boundaries perpendicular to the extension direction, and therefore, led the newly formed fault at the surface of the model to inherent the same trend of the pre-existing fabric as a result of relatively law obliquity motion. Mirroring the same trend as pre-existing fabrics at low or no obliquity is also addressed in experimental model of oblique rifting by Agostini et al. (2009) (Figure 5.9) as mentioned earlier, the higher the obliquity the more the deviation from the trend of the pre-existing structure. Therefore, in this present investigation, the NNW orientation of fault population around the rift floor and the eastern shoulder of the rift in zone3 can be interpreted as a result of the local extension direction defined above for this southern zone that may have imposed minor obliquity on the large NW Aswa shear zone (P2) (Figure 5.16b), and as a result, fault population followed the same trend as the pre-existing structure due to low obliquity motion, which may have led to the formation of simple fault pattern in the rift floor and some en echelon patterns at the rift shoulders in this southern zone (zone3) (Figure 5.16b). Moreover, it

can be observed that faults at and close to rift flanks appears to be more influenced by the trend of Aswa zone than that at the rift floor. The surface traces of the NNW trending fault population in zone 3 (Figure 5.16b) compare reasonably well to those developed in sandbox models of Bellahsen and Daniel (2005) (Figure 5.16a).

The aforementioned results reveal that the different orientations of fault populations observed in the three zones (zone 1, 2 &3) in the central Kenya rift can be attributed to difference in local extension direction in relation to the local pre-existing fabric, which in turn agrees with the concept that rift structure and fault geometries are influenced by inherited fabrics. Complications of these results on the evolution of normal faults in the study area are discussed in chapter 7.

5.5.2 The central MER and the northern MER

The East African Rift system is characterised by few competing basement fabrics of different orientation along the rift that led to relatively uncomplicated influence on rift structure and fault geometry (Morley, 1999d). Unlike the central Kenya rift that involved several NW shear zones and N-NNE and N-NNW foliations (section 5.5.1), the constrained basement structure around the MER is limited to two major EW lineaments (the YTVL and Goba-Bonga lineament). Rose diagrams (Figure 5.7) show a comparable extension direction of 302° and 298° for the NMER and the CMER respectively (Table *5.2*) and point towards WNW- ESE direction, this extension direction was calculated from the rose diagram to be equivalent to the least compressive stress (σ3) that represent a local stress direction, which is in

agreement with the reginal WNW-ESE direction of extension recorded for the MER as shown in e.g. Hayward and Ebinger (1996).

No evidence has been shown in previous studies that may suggest that the YTVL lineament underlying the northern MER, yet this lineament starts from outside the western border of the northern MER and extends westward away from the rift (see section 5.2.2). However, the YTVL and Goba–Bong alinements have been widely adopted in recent geological and geophysical studies including e.g. Abebe et al. (1998), Abebe, Mazzarini et al. (1998), M Bonini et al. (2005), corti et al. 2009, Abebe, Balestrieri et al. (2010) in the main Ethiopian rift as a major basement feature that might be effecting the rift evolution.

To investigate the possible influence of the Yerer Tullu-Wellel linemeant on the evolution of a normal fault at the Earth's surface in the northern MER, the northwest trend of the Yerer Tullu-Wellel lineament located in the eastern part of this lineament has been extrapolated into the rift (Figure *5.17*) in the same way as proposed by Mazzarini et al. (1999) and also adopted by Bonini et al. (2005). In this case the trend of the YTVL lineament is NW (N315°) and the trend of the extension direction represented by the least compressive stress is 302° and therefore the angle between them is 13°, such a small angle provide high obliquity between inherited basement structures and the extension direction, which makes them subparallel to each other. Corti (2012) pointed out that structures parallel to the extension direction may be important in influencing rift architecture since they are able to block the propagation of rift segments and to control the location of transfer zones, similarly, the YTVL intersect the MER at the NMER–CMER boundary (Figure 5.17) as indicated

by Keranen and Klemperer (2008), and this area has been identified as a discrete accommodation zone separating the two rift segments (Bonini et al., 2005), it has also shown by crustal-scale analogue models of e.g. Serra and Nelson (1988), McClay et al. (2002) and Corti (2004) that the formation of transfer zones is highly constrained to the transverse pre-existing structures and effect the geometrical pattern of interacting rift segments. Therefore, the en-echelon arrangement overlaying the extrapolated YTVL (Figure 5.17) and implies a strike-slip component of motion (Bonini et al., 2005, Agostini et al., 2009) could have resulted from reactivation of YTVL basement structure under the WNW extention direction.

Consequently, the strong connection between the presence of transfer zone and the en-echelon pattern of faults coinciding with the underlying YTVL basement may mean that the NW trend of the YTVL that has been extrapolated into the rift for the purpose of this analysis could in fact be present there since the whole rift segment is covered with Cenozoic volcanic sediments and this basement structure is only exposed outside the rift. This inference may also mean that the YTVL is only effecting fault geometry at the surface in the transfer zone between the northern MER and the central MER. Nevertheless, it is not clear whether the orientation of fault swarms deforming the valley floor beyond the YTVL lineament towards the NE (Figure 5.17) are induced by this basement structure since experimental models did not show such fault orientation when inherited structure is parallel to the extension direction. Therefore, this may suggest that the trend of faults traces in the northern MER resulted from orthogonal opening of the upper curst layer due to orthogonal extension to the rift axis rather than resulting from reactivation of pre-existing structures at depth.

The Goba-Bonga lineament underlying part of the central MER (Figure 5.6), and the rose diagrams (Figure 5.7) show that this lineament exhibit a trend of EW (N270°), which makes it at an angle of α = 28° to the extension direction (298°) (Table *5.2*). This low to moderate obliquity angle of α = ~30° calculated in this study for the Central MER (Table *5.2*) (Figure 5.18a) was compared to 30° obliquity angle model of Agostini et al. (2009) (Figure 5.18b). results of this investigation showed that the trend of surface faults in this study area (CMER) do not quite match with fault trends in the α = 30° model (Figure 5.18b) of Agostini et al. (2009) where fault traces are slightly oblique (~15–20°) to the trend of pre-existing weakness for α=30°, whereas fault traces in this study area (CMER) trend about 45° or slightly higher to the basement fabric (Goba-Bonga lineament). Therefore, the deformation observed in the study area did not quite correspond to that in the Agostini et al. (2009) model. These inferences do not support the view that assumes that orientation of faults traces in the central MER were influenced by the pre-existing structures at depth.

These results obtained from analysis of the influence of YTVL and Goba-Bonga lineament within the central and the northern MER in the light of existing experimental models suggest that the effect of these pre-existing structures is not very obvious, which may indicate that these lineaments could have only partially affected the orientation of fault population on the surface.

To sum up, the above mentioned results demonstrated that the effect of the Precambrian inherited fabric in the basement on the orientation of the Cenozoic fault on the surface is more evident in the central Kenya rift than in both the central MER and the northern MER, this conclusion can be attributed

to the relative abundance of basement structures within the central Kenya rift as opposed to the central MER and the northern MER. Thus, the hypothesis stated in section (5.1) that the local fault orientations of fault populations are influenced by the underlying basement structures at depth is applicable to the central Kenya rift and partially applicable to both the central MER and the northern MER.

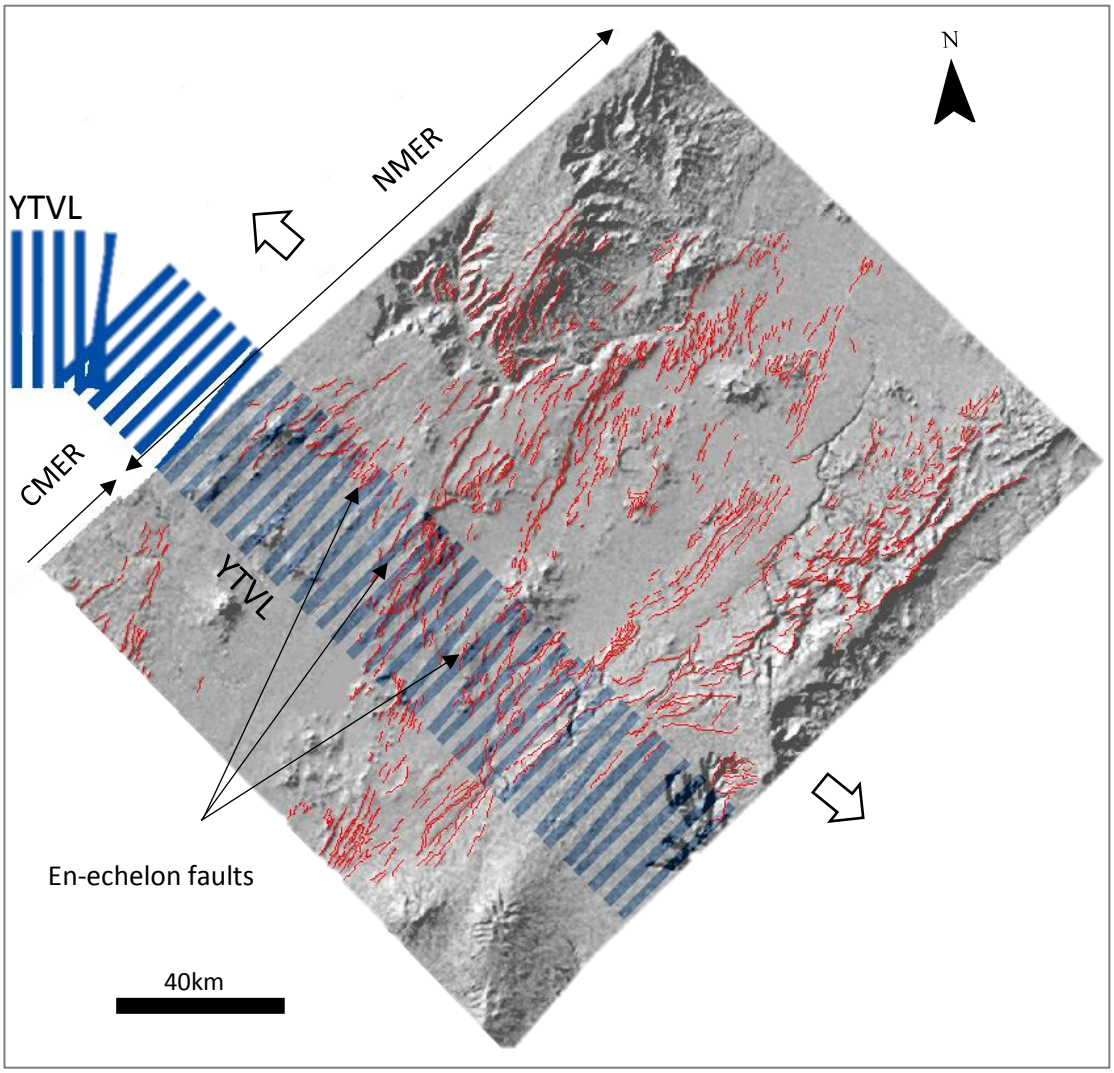

Figure 5.17. YTVL (the Yerer Tullu-Wellel lineament) extrapolated into the MER in the same way as proposed by Mazzarini et al. (1999) , and corresponding to the transfer zone between the NMER and CMER. See Figure 5.6 for location.

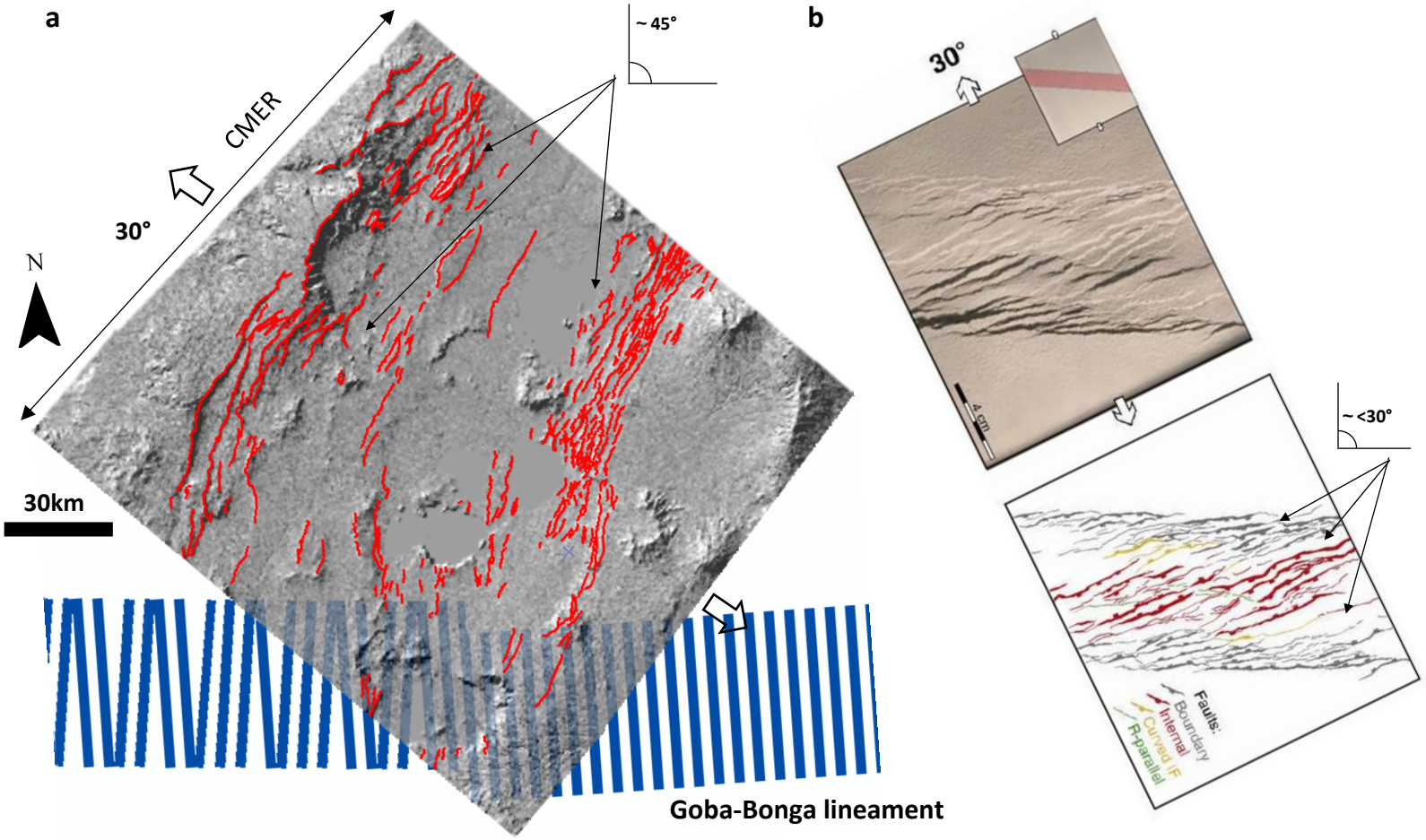

Figure 5.18. Comparing results of sandbox models of Agostini et al. (2009) (b) and fault traces in the CMER (a) (see section 5.5.2), the inset angle is fault trend relative to pre-existing zone. See Figure 5.6 for location.

5.6 **Conclusion**

The potential influence of basement structures on rift system evolution has been assessed through investigating the relationship between the orientation of surface fault, orientation of pre-existing basement structure captured from previous studies as well as local extension direction. Fault orientation of about 2130 surface fault traces mapped from DEM data for the central Kenya rift, the central MER and the northern MER were involved in a quantitative and qualitative analysis and compared to existing basement reactivation analogue models. Different trends of the basement fabrics relative to the local stress vector plays an important role in influencing fault orientation at the surface, extensional faults at the surface would obey the same trend of the pre-existing fabric when the latter trends at high angle ($\alpha>45$) to extension direction, for example, In the central Kenya rift, the Elgeyo escarpment and the Nguruman escarpment were parallel to the underlying basement foliation, when these foliation trended at 88° and 90° respectively to the extension direction, moreover, in the southern zone of the central Kenya rift (zone 3), the NNW trending fault population at the margins of the rift floor and at the eastern rift boarder appear to mimic the same trajectory as the large Aswa shear zone when the latter oriented at an angle of 61° to the extension vector. On the other hand, fault strike for the majority of surface fault in zone1 and zone 2 in the central Kenya rift departed away from that of the inherited basement structure when the angle between the latter and the extension direction was ($\alpha \leq 45$). These results showed a reasonable correlation between the sandbox models and fault orientations on the surface with respect to the extension direction relative to the orientation of pre-existing structures, which suggests

a possible influence of basement structures on Miocene faulting for the central Kenya rift.

The effect of the YTVL lineaments in the northern MER is only evident in the transfer zone between the two rift segments and could be responsible for the development of en-echelon pattern along the accommodation zone. However, the trend of fault populations within the rift valley did not match with the applied experimental models when inherited structure is subparallel to the extension direction, the Goba–Bong alinements also did not quite correspond with the sand box model, which may weaken the possibility of any effect from these basement fabrics.

Results of this study with regard to the presented experimental models used to assess the possible influence of pre-existing structures on fault orientation suggest that the effect from the basement does not seem to be as evident in the central MER and the northern MER as in the central Kenya rift due to lack of such basement structures in the former. I believe that this approach in part offers a means to gain an insight into the influence of basement structures, and can be applied to other neighbouring continental rift segments within the east African rift system.

Chapte 6. Landscape response to tectonic-erosion forces: analysis of stream networks

6.1 Introduction

In recent decades, the extraction of drainage networks or river systems has been made possible by remote sensing techniques and GIS modelling due to their increasing importance in geomorphological as well as structural geology studies. In tectonically active mountain regions, drainage networks reflect the continuous and complex interaction between exogenous processes (e.g. weathering and erosion) and endogenous tectonics that lead to the formation of folds and faults (Jackson and Leeder, 1994, Deffontaines and Chorowicz, 1991, Burbank and Anderson, 2011). The drainage network geometry is greatly affected by recent tectonics (Whipple, 2004, e.g. Burbank and Anderson, 2011, Kirby and Whipple, 2012, Molin and Corti, 2015). Therefore, studies of the tectonic geomorphology of erosional landscapes have been used to address structural geology and tectonic questions such as the spatial and temporal patterns of rock uplift and deformation of orogenic systems (e.g. Wobus et al., 2003, Schoenbohm et al., 2004). Analysis of the drainage pattern can help to elucidate the possible locations of structural features such as faulting (Abdullah et al., 2013).

Previous chapters presented in this thesis (Chapters 3, 4 & 5) have focused on the structural evolution and surface deformation of normal faults and their implications on continental rifting in the three study areas; the central Kenya rift, the central MER and the northern MER (figure 1.1) that represent three

different stages of continental rifting (section 2.1). This chapter is an attempt to propose a new idea for a preliminary method to reconstruct the possible original location of eroded footwalls of faults, and that this chapter lays the ground-work for future analysis. The proposed approach was used to qualitatively assess how good the initial estimations of extensional strain are in the study areas. This aim was achieved by extracting drainage network for the study areas (see section 6.2), and adopting a similar concept to that used in a wide range of studies (Grohmann et al., 2011, Mahmood et al., 2013, Slama et al., 2015, Amine and El Ouardi, 2017) to look for evidence of buried structures. Those studies utilized different stream orders of drainage network to describe the relationship between the relative position of stream segments in a drainage basin network and the topography, where streams of similar orders are connected together to represent a erosional-tectonic events (Golts and Rosenthal, 1993, Strahler, 1952). It has been concluded from those studies that the combination between the 2nd and 3rd order streams was always considered to provide the best visual representation of a smoothed and simplified surface map of the original topography that would show an inflexion in the fault line areas of fully eroded regions.

Therefore, In this investigation I used the 2nd and 3rd order streams of drainage network, in order to qualitatively identify and delineate the likely original position of fault planes (footwall blocks) of the Quaternary faults and compare the result to previously interpreted footwall cut-offs (see chapter 3 and chapter 4), this method has not been used before in active continental rifting.

6.2 Extraction of drainage network

Extraction of the drainage network of the study areas has been carried out on the same ASTER DEM used in previous chapters in the three rift zones. Drainage channels were semi-automatically extracted using hydrological feature of the spatial analyst tools available in ArcMap software, version 10.4. The hydrological toolset encompasses several functions (Figure 6.1) including: 1) Fill, to remove the sinks or depressions from DEM surface, the grids of no data (voids) and erroneous data are to be corrected by the fill function. 2) Flow direction, shows the direction water will flow out of each cell of a filled DEM based on cell elevation. 3) Flow accumulation, calculates for each cell the number of cells that will flow towards it and accumulate in it. 4) For defining the stream network, the flow accumulation grid was conditioned to take into account only pixels with flow accumulation values > 1000, which represents a drainage threshold for a stream to form, and all other grid cells are assigned a null value. A higher threshold value of flow accumulation will result in a less dense stream network than a lower threshold value. In this study, the river network was extracted by defining a threshold value of >1000 which appeared to provide a reasonable representation of stream network, sufficient for the purpose of this chapter. Stream ordering was then created in different colour scheme by ArcGIS according to Strahler (1952) method (section 2.1.4.5) and then transformed to vector layer for further analysis. Stream networks were generated to be equivalent in terms of number of stream order and value of flow accumulation (see section 6.2) for the three rift segments.

Result of generating the drainage networks are shown in Figure 6.2 for the central Kenya rift, Figure 6.3 and for the NMER and the CMER, the stream network are superimposed upon the shaded relief DEM surfaces for a better visualization and interpretation.

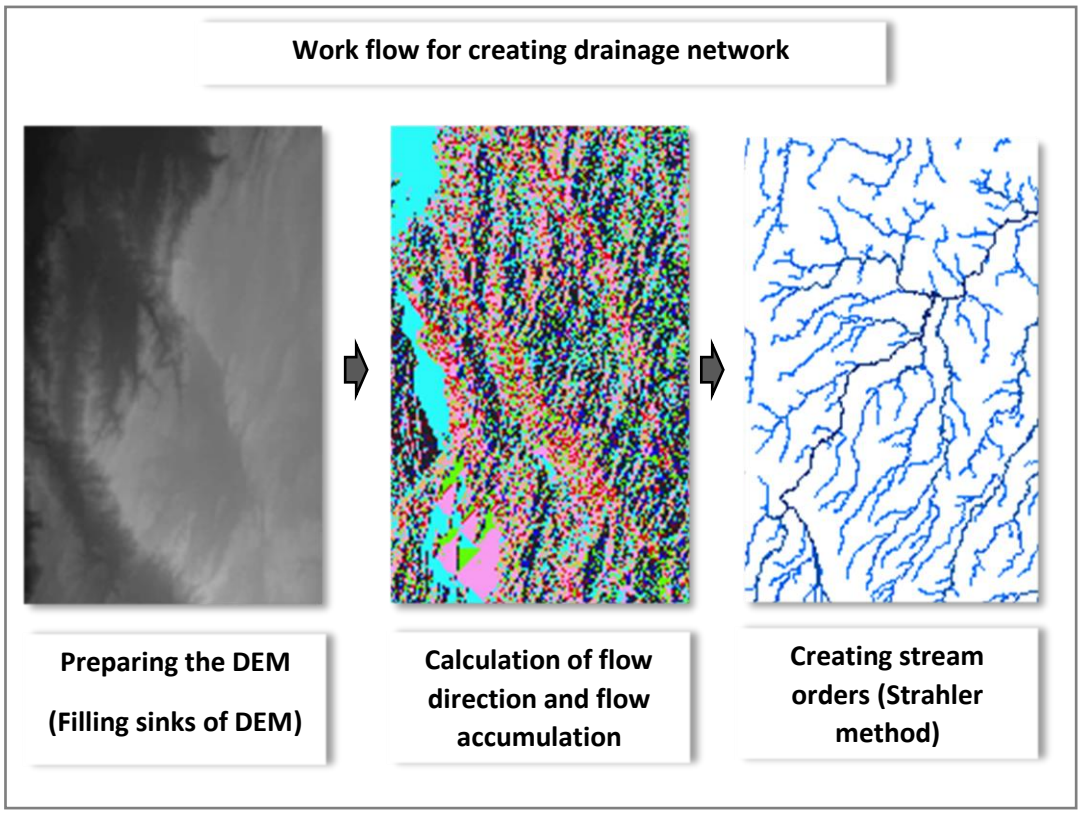

Figure 6.1 a summary of steps for extracting drainage network

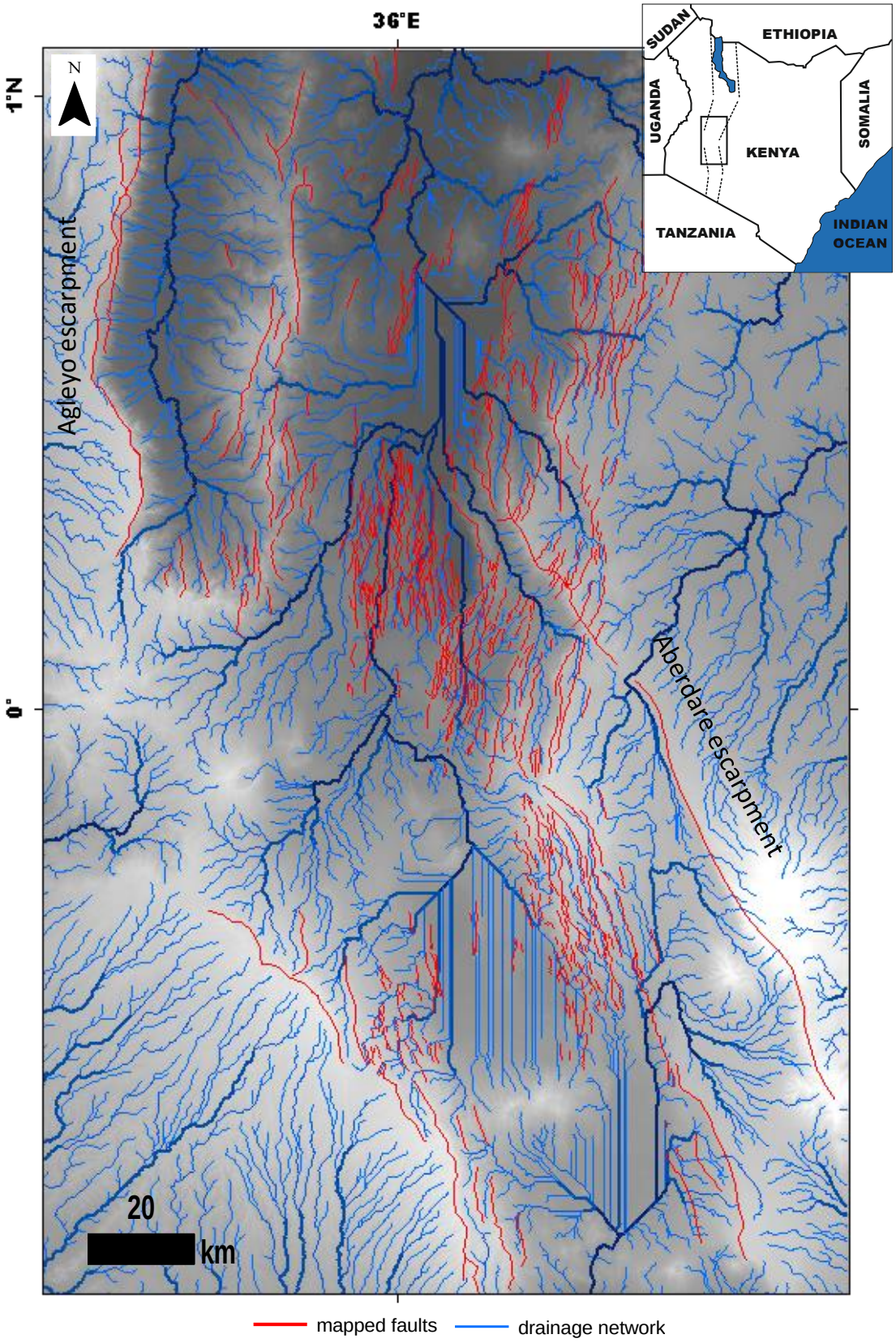

Figure 6.2. Map showing extracted drainage network draped over DEM surface of the central Kenya rift.

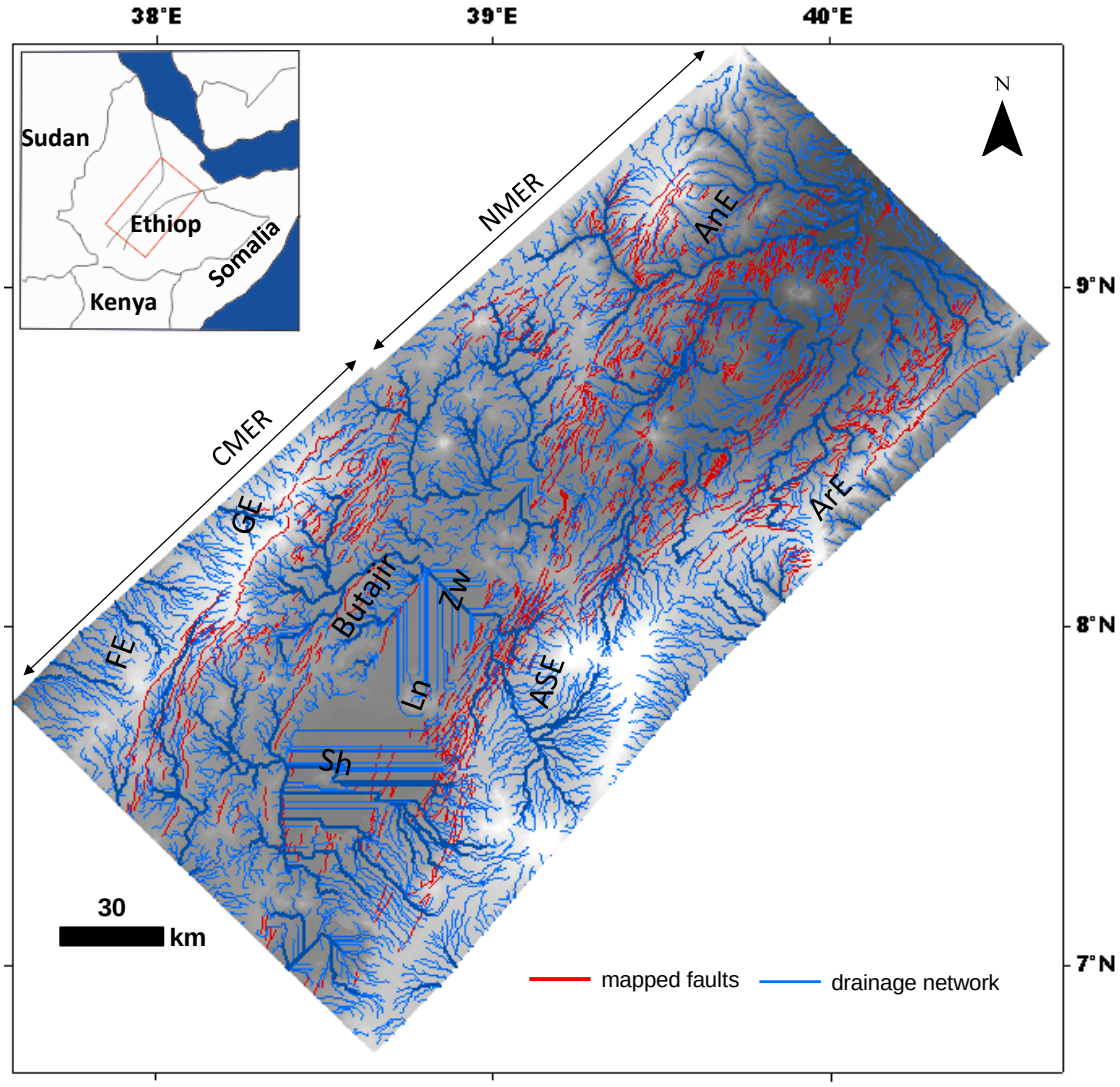

Figure 6.3. Map showing extracted drainage network draped over DEM surface of the central and northern MER. ASE: Asela escarpment; LAE: Langano escarpment; AnE: Ankobar escarpment; ArE: Arboye escarpment; GE: Guraghe escarpment; Ln: Lake Langano; Sh: Lake Shala; Zw: Lake Ziway

6.3 Description and implementation of the proposed method

A time span of about 10^5 yr would be sufficient to degrade a fresh fault scarp to a point where all remnants of the tectonic surface were removed (Stewart and Hancock, 1990). Hence, analysis of drainage system has been widely used in tectono-geomorphic studies (e.g. Golts and Rosenthal, 1993, Leverington et al., 2002, Grohmann et al., 2011, Mahmood et al., 2013, Slama et al., 2015, Jedlička et al., 2015, Amine and El Ouardi, 2017) in order to identifying areas that are likely to be locations of faulting or uplifting event in regions where the geological of structures are buried. Unlike those studies that have endeavoured to reconstruct the paleo topography in inactive and highly eroded areas, the current investigation has been carried out in a tectonically active area with homogeneous lithology (Stoyan and Gloaguen, 2011), where fault escarpments are the most prominent geological features.

a schematic diagram by Grohmann et al. (2011) for the geomorphological evolution of a normal fault scarp (Figure 6.4) shows the interaction between active tectonic and erosional processes where, the 1st-order streams formed as the fault scarp erodes, and hence the 1st order streams are always disregarded to eliminate the noise that could prevent the identification of fault scarps or other significant features of the topographic surface, the 3rd order streams appear to be slightly far off from the base of fault scarp (Figure 6.4c), whereas, the 2nd order streams crosses the fault scarp at the fault line (Figure 6.4c) that represent the original location of fault plane of the footwall blocks and the least affected by erosion. Therefore, the base of fault structures is an important reference point as it represents the last part of the surface to be removed.

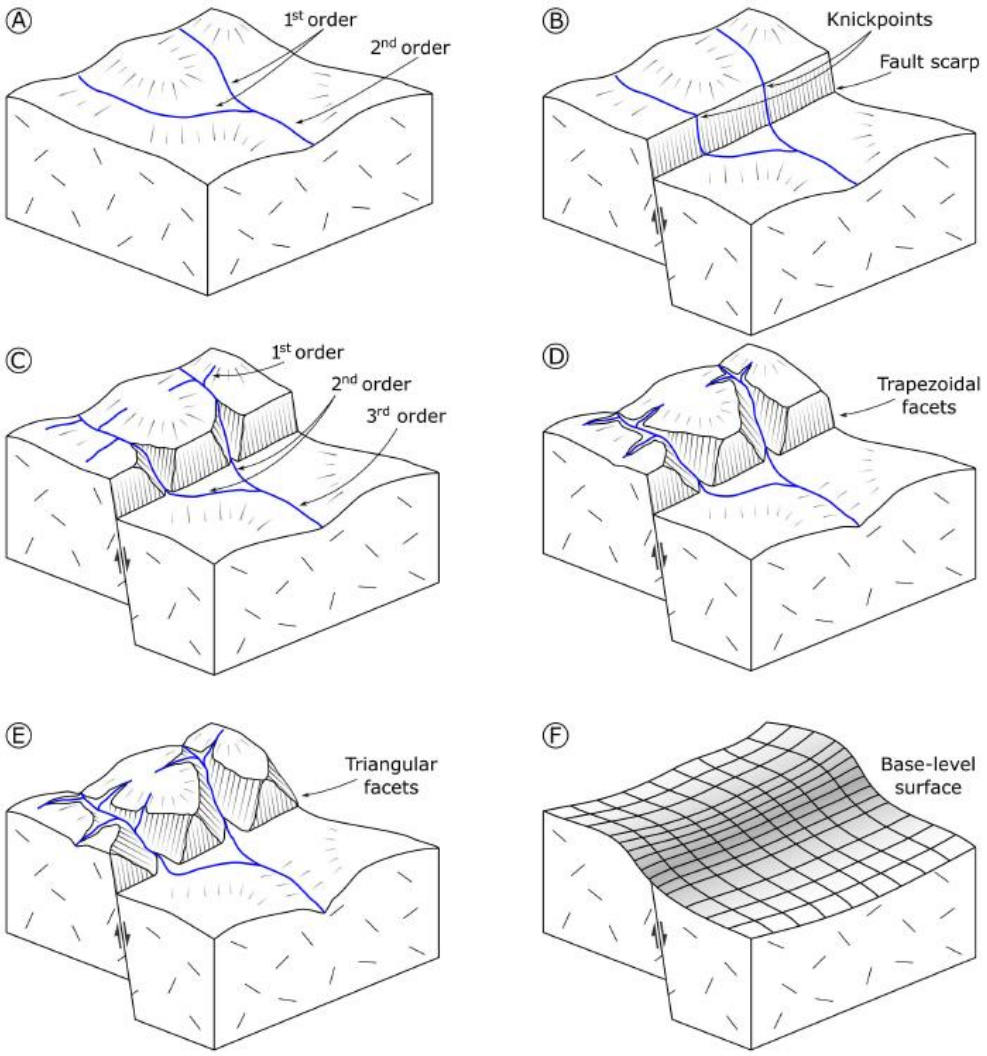

Figure 6.4 Schematic evolution of a normal fault scarp, with development of knickpoints and new 1st-order streams. The scarp will be segmented into a series of trapezoidal facets, which will became triangular and will be progressively eroded, until the original morphology cannot be recognized. A base-level map, constructed from the elevations of 2nd and 3rd order channels, shows an inflexion in the fault line area, from (Grohmann et al., 2011).

Another model for the geomorphological evolution of fault escarpment of the Montagna del Morrone ridge in central Apennines, shown in (Miccadei et al., 2004) (Figure 6.5) illustrates how stream network develops in different drainage basins based upon the degree of erosion, for instance, stream network flowing through ridges with relatively little erosion will only consists of 1st and 2nd order streams as is the case with drainage basins A,B & D in Figure 6.5, as erosion progresses, the drainage networks grows when new channels are created as a result, as is the case in drainage basins C,K & I with three orders of streams, and basin N with four orders (Figure 6.5).

The interaction between fault scarps and the drainage networks in the central Kenya rift (Figure 6.7) and the CMER (Figure 6.8) are similar to case presented in the model by Grohmann et al. (2011) (Figure 6.4), and also similar to the case of drainage basins A,B & D of the model by Miccadei et al. (2004) (Figure 6.5).

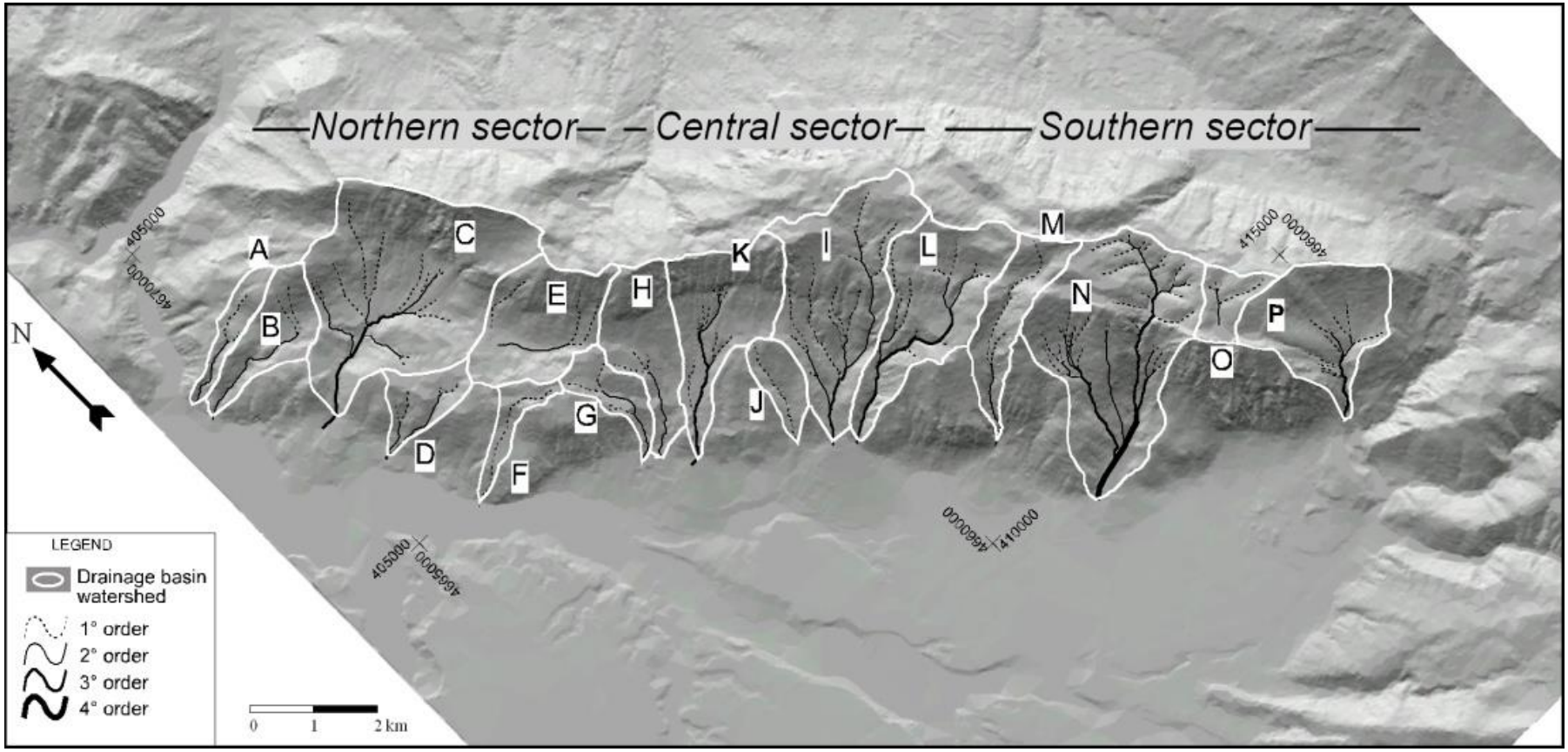

Figure 6.5 Drainage basins and streams (ordered according to Strahler, 1957), from (Miccadei and Piacentini, 2011), notice the number of stream orders forming in each basin based upon the degree of erosion.

Therefore, for the purpose of interpreting and mapping of the possible original location of eroded fault scarps in the central Kenya rift and the central MER, the 2nd order streams were draped on a shaded relief surfaces of the study areas using overlay technique available in ArcGIS in order to qualitatively delineate the original fault plane of the footwall blocks of the Cenozoic normal faults, by identifying segments of the 2nd order streams at the bottom of fault structures and manually drawing a line in a 2D view (map view) cutting across every second order stream found close to the bottom of the fault structure along the border faults, in the same way as shown (Figure 6.6a & b). Delineation and interpretation of the original location of fault scarps was only possible for the large border faults found at the rift flanks, whereas, for relatively smaller faults, there was no clear pattern of the 2nd order streams to follow.

The results of interpretation of the original location of fault scarps in the central Kenya rift (green lines) in Figure 6.7 was visually inspected and compared with the picked footwall cut-offs (red lines) in Figure 6.7 that meant to represent fault plane, the two lines exhibited a slight mismatch, which can be considered insignificant and that would also mean that the estimated extensional strain (section 3.6.1) for the central Kenya rift is appropriate.

The central MER appear to be more eroded, and it was only possible to interpret the original location of fault scarps for the two largest fault escarpment (Figure 6.8), namely the Fonko and Guraghe escarpment (Figure 6.8), and again the 2nd order streams was considered to be the best option for demarcating the possible original location of fault plane, and the results again showed that there is insignificant difference between the

interpreted possible original location of footwall block (green lines) and picked footwall cut-offs (red lines) (Figure 6.8).

a)

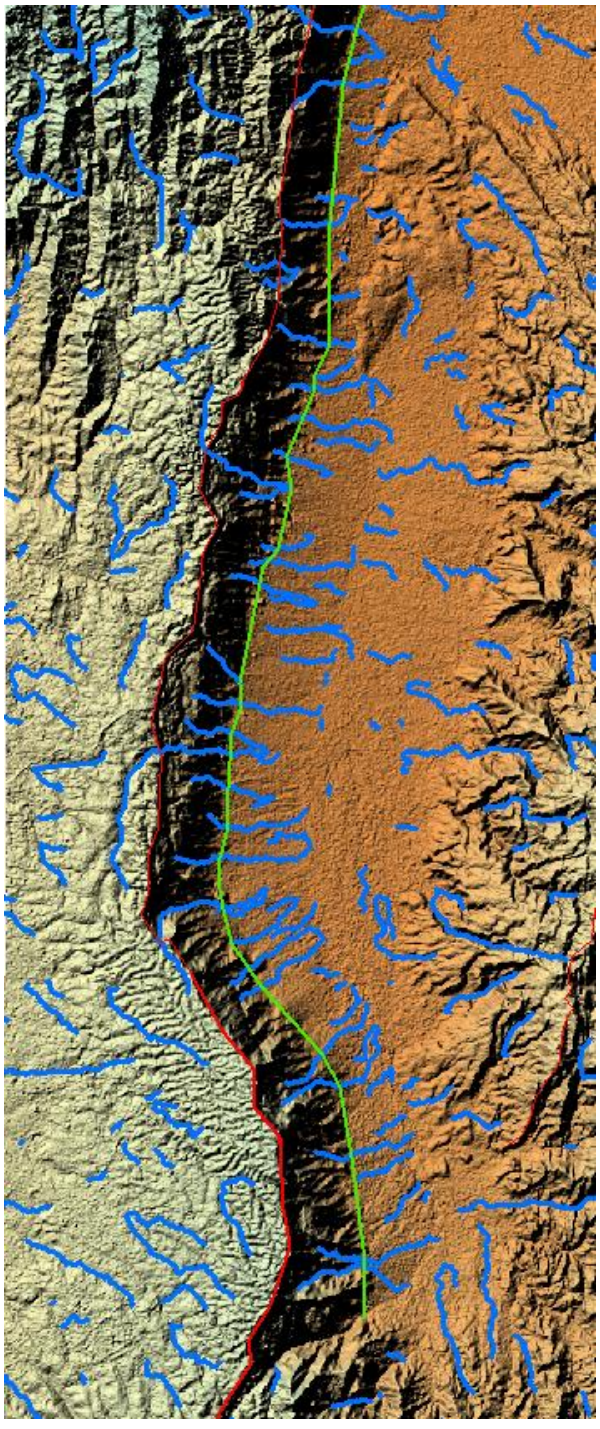

Figure 6.6a & b show examples of interpretation of the possible original location of footwall block by connecting all 2nd order streams at the bottom of fault scarps.

b)

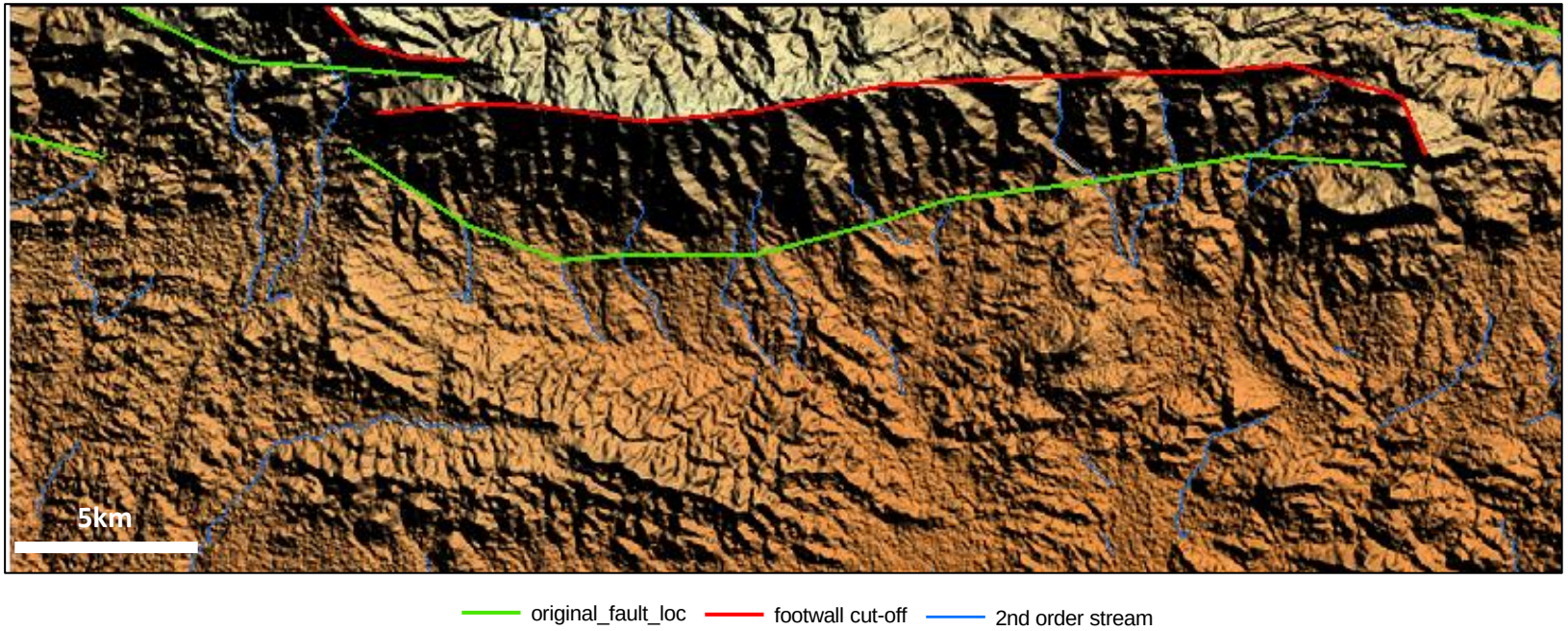

Figure 6.6 continued

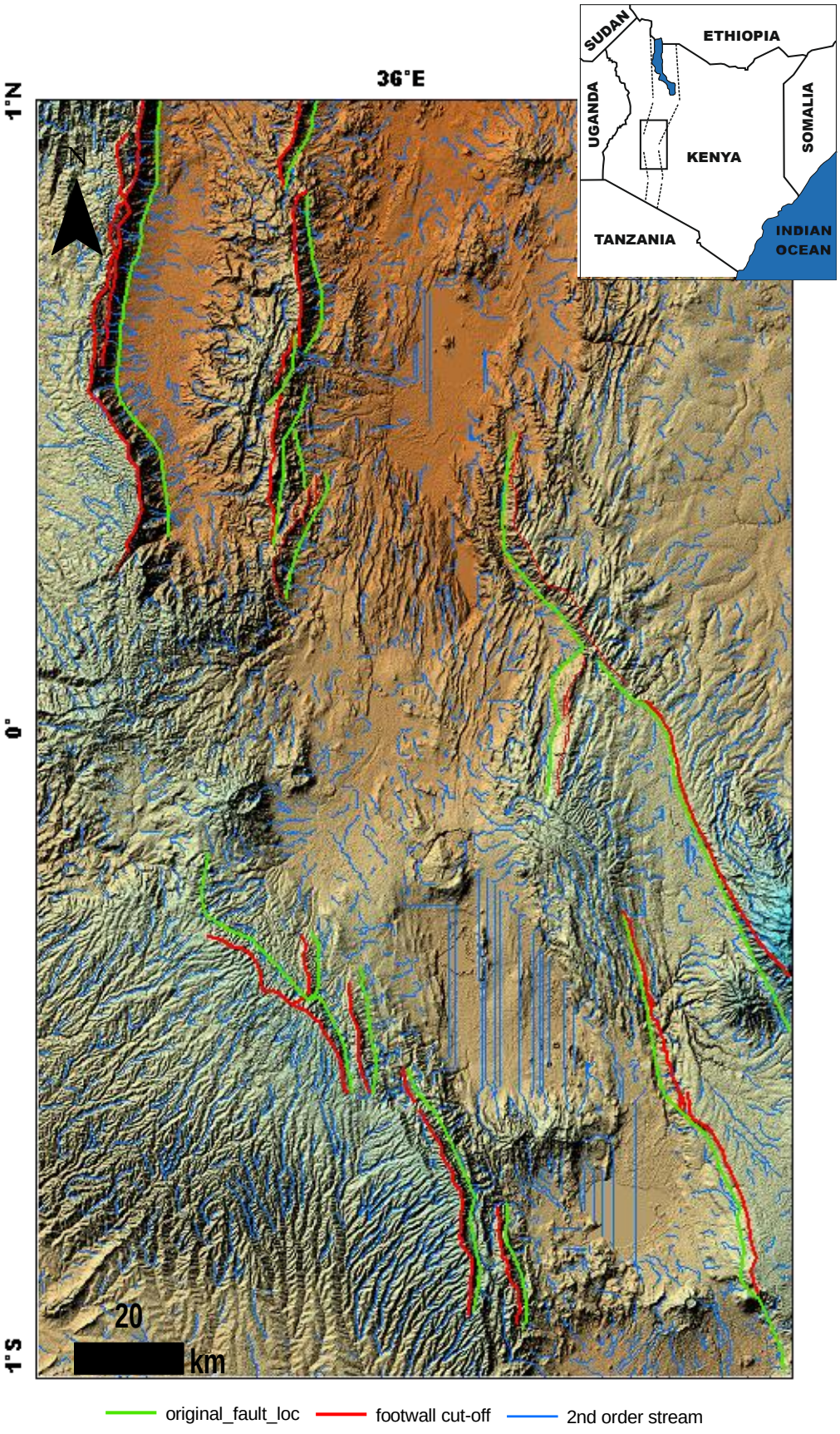

Figure 6.7. Shaded relief image with 2nd order streams, footwalls cut-offs and interpreted possible original location of fault planes in the central Kenya rift.

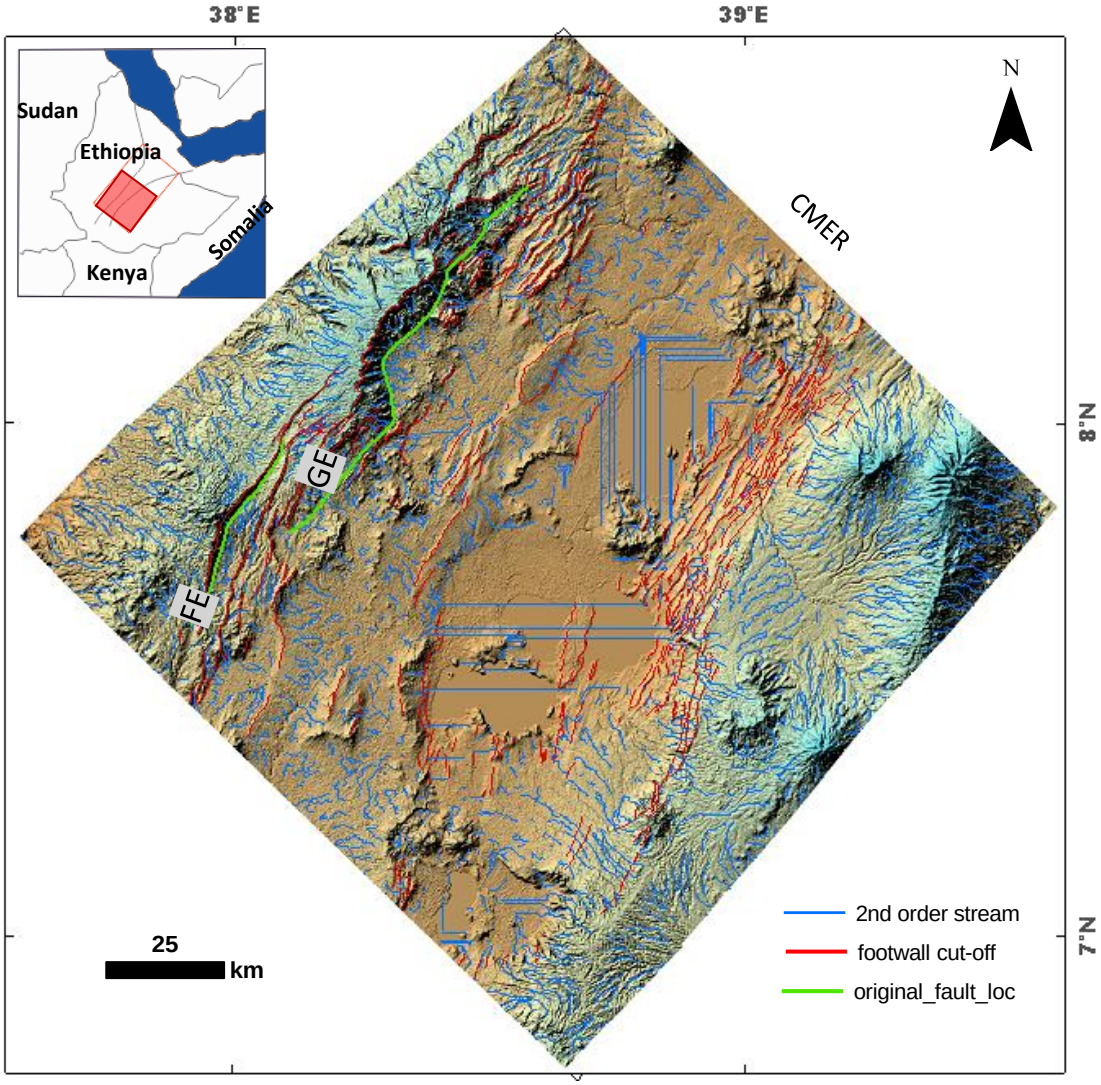

Figure 6.8 Shaded relief image with 2nd order streams, footwalls cut-offs and interpreted possible original location of fault planes in the central MER, see Figure 6.3 for abbreviations.

On the hand, in the present investigation, the interpretation of the likely original location of the footwall block in the NMER (Figure 6.9) has become even more difficult as this area appear to be highly eroded and the large border fault appear to be prominently degraded, as suggested by morphostructural evidence by Wolfenden et al. (2004), and consequently the interaction between fault scarps and the drainage networks in the NMER has become similar to the case of drainage basins C,K & I of the model by Miccadei et al. (2004) (Figure 6.5). Thus, the 2nd order stream was generally less helpful in identifying and marking the possible initial location of fault line, because the topographical evolution that occurred as a result of high erosion effect in this area, the 2nd order to form upstream of the river system in the same way as in basins C,K & I of the model by Miccadei et al. (2004) (Figure 6.5).

Therefore, for delineation of the original location of fault line of those border faults, the 3rd order stream channel cutting across the line of fault scarp was used for this purpose, the 3rd order stream has in fact replaced the 2nd order stream when new streams have been created in the river channel due to increasing erosion processes in a similar manner to that shown for basin C,K & I of Miccadei et al. (2004) model (Figure 6.5). Even with the 3rd order streams, it was not straight forward to interpret the initial position of the fault scarps due to high degree of erosion this area had experienced, thus some degree of subjectivity judgments was used to demarcate the likely old fault line (Figure 6.9) by drawing a line in a 2D view (map view) connecting all 3rd order stream found along both rift borders in the same way used in the central Kenya rift and the central MER for the 2nd order stream (Figure 6.6a & b). The results of interpretation of the original location of fault scarps in the northern MER

(green lines) in Figure 6.9, did not correspond to a single footwall cut-off as was the case for the central Kenya rift and CMER, yet it corresponded to multiple footwall cut-offs (red lines) (Figure 6.9) of what was previously mapped (Chapter 4) as individual fault scarps. If this interpretation holds, that would mean that those multiple fault scarps could in fact be ridges created by erosional processes and river incisions on what was originally large fault scarps at both flanks of the northernmost part of the northern MER, due to high degree of erosion this area had experienced. This interpretation may also indicate that estimations of extensional strain (section 4.2.1.1) in the northern MER could be overestimated.

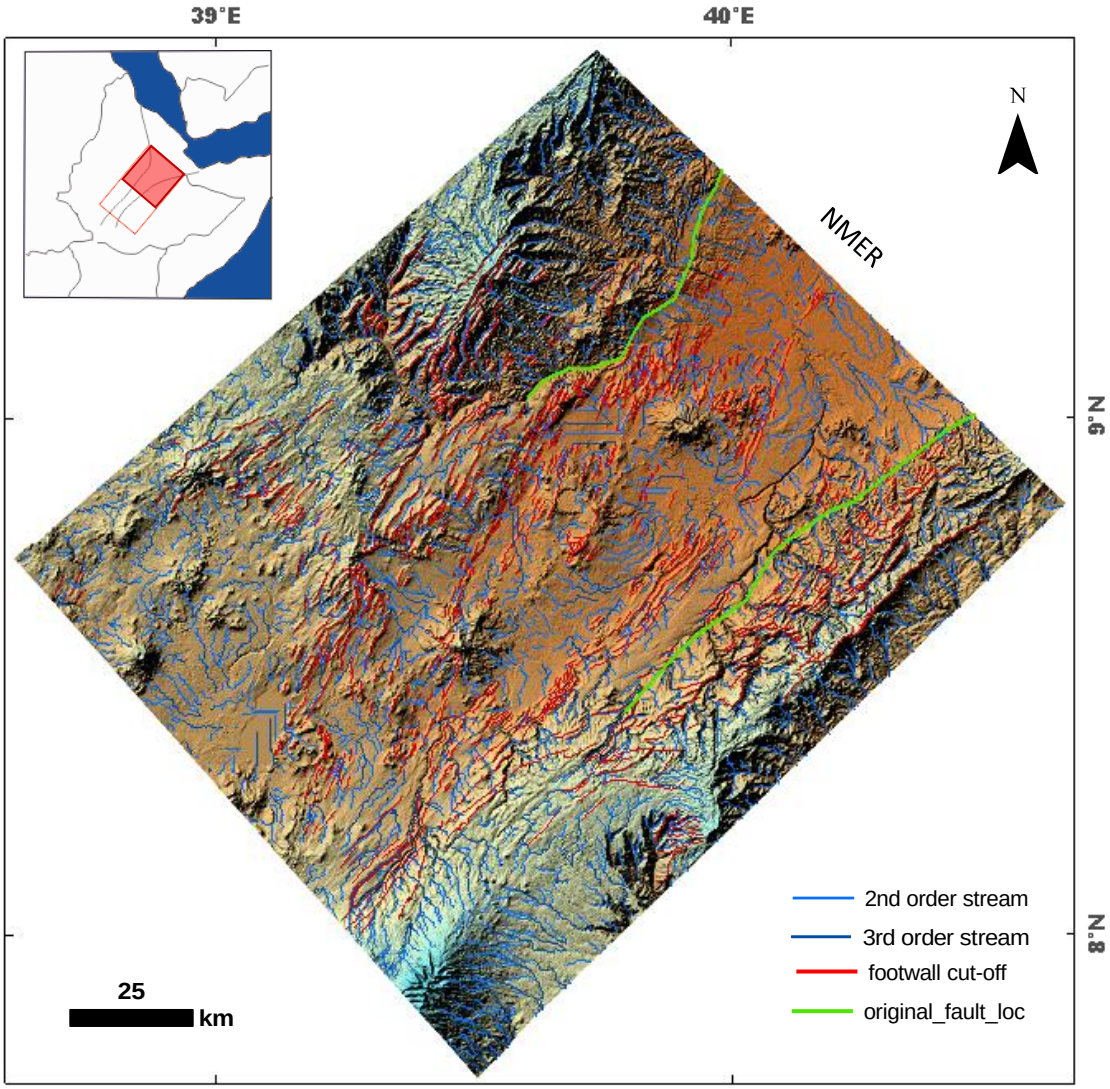

Figure 6.9. Shaded relief image with footwalls cut-offs and interpreted possible original location of fault planes based upon 3rd order streams in the northern MERs.

6.4 Conclusion

This chapter was an attempt to propose a preliminary method to interpret and define the likely original position of eroded footwall blocks of the Quaternary faults in continental rifting, and qualitatively assess how good the initial estimations of extensional strain are in the three study areas (the central Kenya rift, the CMER and the NMER). The approach implemented here has never been used before in active continental rifting, and was motivated by the methodology used to look for evidence of buried structures, by using order streams of drainage network to identify areas that are possible locations of faulting or uplifting events. The results showed that there is insignificant difference between the interpreted possible original location of footwall block and the picked footwall cut-offs in the central Kenya rift and the central MER, which suggests that estimations of extensional strain in these two rift zones were appropriate. The interpreted of initial position of the fault scarps in the northern MER corresponded to multiple footwall cut-offs that could have been created due to high degree of erosions and river incisions on what was originally a single large fault scarp. This inference may indicate that estimations of extensional strain in the northern MER could have been overestimated. Results obtained from this investigation are preliminary and the methodology introduced in this chapter lays the ground-work for future analysis.

Chapte 7. Discussions & Conclusions

7.1 Discussions: Comparison between the three Rifts segments

This section compares and contrasts results and information obtained from analysis of fault attributes (fault length, throw and spacing) that characterize fault populations formed in the brittle crust of the three Rift segments under investigation (Kenya Rift, the central main Ethiopian Rift and the northern main Ethiopian Rift). The best-fit statistical distributions for fault throw and length, spatial strain heterogeneity, fault growth model as well as implications of the influence of pre-existing structures are discussed. Throughout this research a variety of analysis techniques have been used to insure both consistency and reliability of the results. By using the same resolution of DEM data, 2130 normal faults were mapped from DEM surface of the three study areas, 620 faults for the central Kenya Rift, 468 faults for the CMER and 1041 faults for the NMER, these datasets are large enough in each Rift segment to make reliable assessments and observations of changes in geometry and behaviour of fault size attributes, which may shed light on the underlying physical mechanisms of crustal deformation

7.1.1 Fault size distributions

This section discusses the relationship between cumulative distributions of fault length and throw, thickness of brittle crust and accommodation of extensional strain. The cumulative distributions of fault throw and fault trace length from the three study areas (the central Kenya Rift, the CMER and the NMER) have been plotted together (Figure 7.2a & b) in their best fit as

discussed in chapter 3 & chapter 4, in order to compare the fault data sets in these three Rift segments. Figure 7.2a & b shows that distributions for the Kenya Rift fit a different statistical function to that of the central and northern MER. Moreover, as was demonstrated in chapter three, in the central Kenya Rift, the three defined fault population zones (zone 1, zone 2 and zone 3), either individually or combined have exhibited a power-law distribution for both fault length and throw attributes, whereas, it was shown in chapter four that, in the central MER and the northern MER, attributes of fault length and throw fit to both exponential and log-normal functions.

The steepness of these curves represent different fault sizes, the steeper the curve, the higher the contribution by small fault sizes (Marrett and Allmendinger, 1991), therefore, Figure 7.2a for throw attributes show that the curve for the central Kenya Rift that appear to be the least steep and therefore has the largest average of fault throws (Table 7.1), while the curve for the CMER seems to be the steepest and hence contains the smallest average of fault throws (Table 7.1).

These differences of fault size statistics for the three Rift segments are also evidenced in Table 7.1. Moreover, it can be noted from this variation that the central Kenya Rift exhibiting a power-law distribution has larger averages of fault length and throw whereas the relatively smaller average values of fault length and throw shown for the CMER and the NMER (Table 7.1) reflected exponential and log-normal distributions. These results are consistent with that of Soliva and Schultz (2008) who observed that where Rift bounding faults are well developed (length >50 km) the size distribution shows a predominantly power law trend, as was the case in the central Kenya Rift

(Table 7.1), however, the CMER contained a border fault of about 70 km in length but did not show a power law distribution (discussed in chapter 4 section 4.3.4.1).

Seismic refraction and regional reflection studies (e.g. Henry et al., 1990, KRISP, 1991) indicate significant variations in crustal thickness between the craton and the mobile belt along the length of the Kenya Rift, The major crustal thinning occurs along the axis of the Kenya Rift ranges from 35 to 40k in the south beneath the central part of Kenya, within the vicinity of Lake Naivasha to 18 -20 km in the north beneath lake Turkana. A velocity model along the Rift axis of the MER and Afar region shown in Keranen and Klemperer (2008) (figure 2.2), which has been reproduced here as Figure 7.1 shows that the crust thickness gradually thins to the north, from about 33–35 km at the central MER boundary to about 24–26 km in southern Afar. Therefore, these studies indicate that the lithosphere is not progressively thinning from south to north between the central Kenya Rift and the MER, yet the northward decrease in the thickness of brittle crust layer can be observed along individual Rift segments.

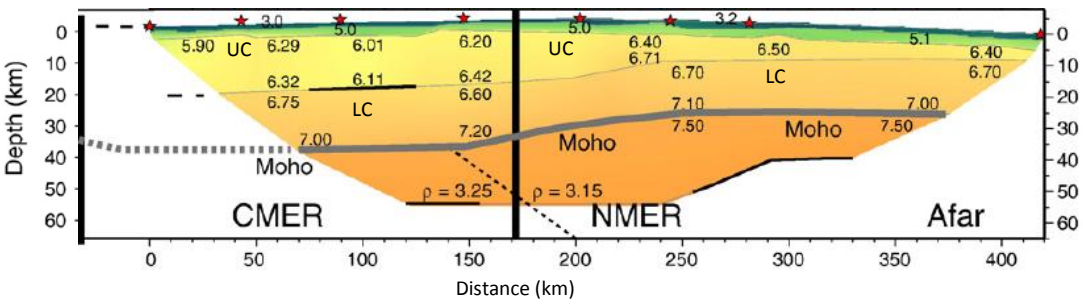

Figure 7.1 Cross-sections across Velocity model along the Rift depicting thinning of the crust layer northward, modified from (Keranen and Klemperer, 2008, Maguire et al., 2006)

Consequently, by taking the crustal thickness reported in those aforementioned studies into consideration as well as averages of estimates of strain accommodated in each Rift zone (Table 7.2), it can be suggested that fault populations studied in the current research in the three Rift segments belong to mechanical layers of different thicknesses . Moreover, for the statistical distributions produced in this research, it can also be suggested that the power law scaling is associated with the thick crust and low strain recorded for the central Kenya Rift (see Figure 7.4), which makes these interpretations in line with the concept that power law function arise from relatively low strain settings (Gupta and Scholz, 2000a, Vétel et al., 2005) and relatively thick crustal layers (Odling et al., 1999, Soliva and Schultz, 2008). Whereas, the exponential/log normal scaling is associated with higher average strain and a thinner crust in the CMER and the NMER segments (see Figure 7.4). These inferences are consistent with the view that the exponential distribution is associated with higher strain settings (Gupta and Scholz, 2000a, Vétel et al., 2005) and thinner crustal layers (Odling et al., 1999), which act as a mechanical barrier for faults to grow vertically and force faults to propagate laterally instead (Ackermann et al., 2001, Soliva and Benedicto, 2005, Soliva et al., 2006), and yield either the exponential or log-normal distribution. Therefore, the development of exponential, log-normal and power law size distributions in different fault populations can be attributed to variations in brittle crust heterogeneity (e.g. thickness and material properties), as suggested by Soliva and Schultz (2008), which has been reflected in this research through different patterns of surface deformation in the central Kenya Rift, the CMER and the NMER.

Table 7.1. Statistics of fault size attributes in the three Rift segments

	Length (m)					Throw (m)			
	N	Min	Max	Average	StDev	Min	Max	Average	StDev
NMER	1041	294	41210	3604	3207	25	953	123	126
CMER	468	432	68615	4823	5316	30	1054	106	104
Kenya	620	272	59608	5152	6607	30	1561	144	171

Table 7.2 Averages of strain estimates in the three Rift segments.

Rift segment	NMER	CMER	Kenya
extension strain (m)	15099	6408	7617

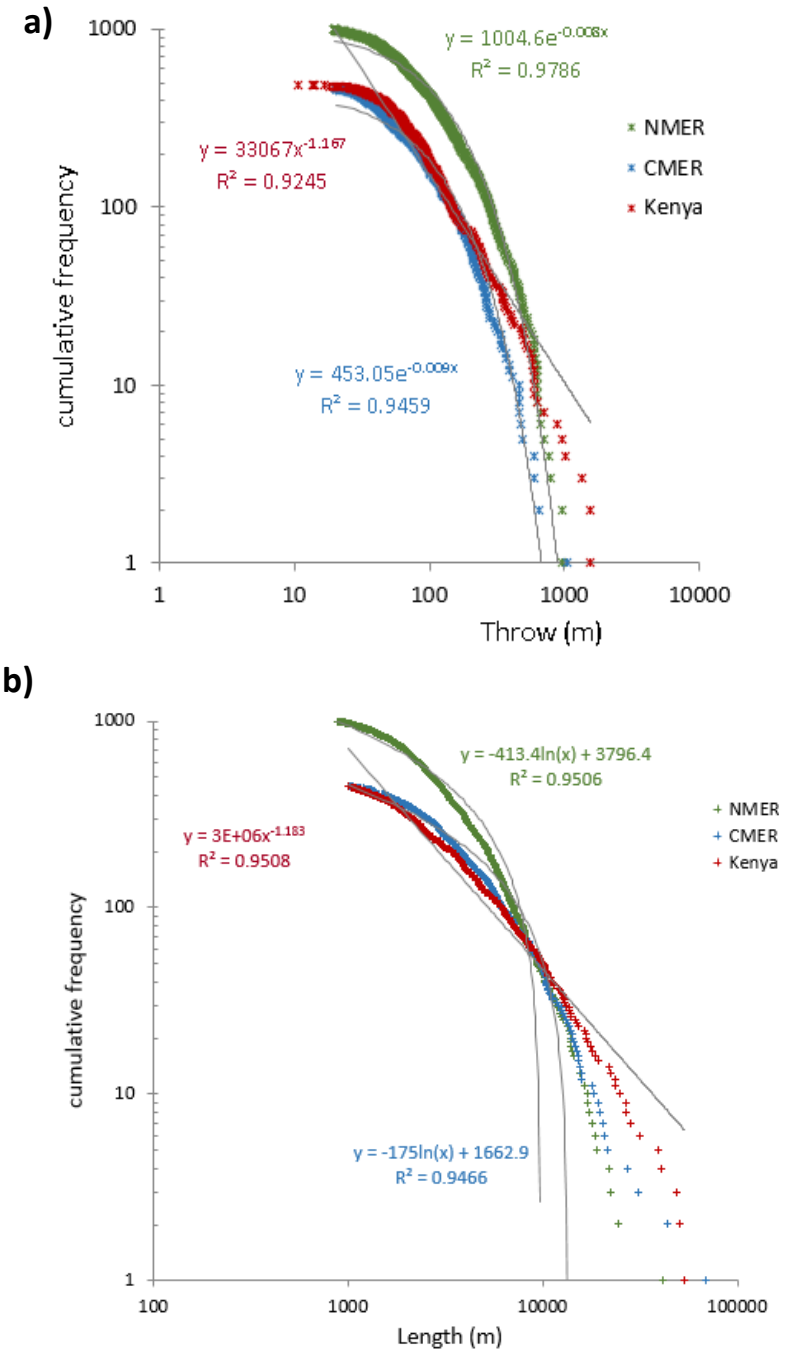

Figure 7.2. Log-Log plot for cumulative frequency vs. a) fault throws and b) for fault lengths in the three study areas.

7.1.1.1 Comparison with Weibull distribution

The statistical distributions of fault size attributes (length and throw) obtained in the current study and shown in Figure 7.2a & b for the central Kenya Rift, the CMER and the NMER can be compared to results of Stoyan and Gloaguen (2011) (Figure 7.3). They described and inferred the strength of the brittle crust through measures of fault length distribution using Weibull theory, which is a probability distribution that is used in statistics to provide the probabilities of occurrence of different possible outcomes. The Weibull distribution uses the Weibull modulus (m) which is a number similar to the fractal dimension of power-law, and used to describe variability in measured material strength of brittle materials (Afferrante et al., 2006). The strength of the brittle crust was regarded as the maximum amount of extensional stress that the crust can withstand without faulting. Stoyan and Gloaguen (2011) used DEMs derived from ASTER to automatically extract fault lengths from the Kenya, Ethiopia and Afar Rifts. They found that the modulus (m) increases from Kenya to AFAR (Figure 7.3) with decreasing crustal thickness and increasing thermal gradient, the increase of modulus (m) was attributed to increasing crustal strength from Kenya to Afar. Consequently, what is worth noting in this study is that the distribution of fault length for the Kenya Rift appear to be different to that of the MER and Afar Rifts (Figure 7.3). Similarly, in the current study, cumulative distributions of fault length and throws of the central Kenya Rift were predominantly described by power law distribution while those of the CMER and the NMER (Figure 7.2), were best expressed by exponential and log-normal distributions. These differences in the cumulative distributions in this study was also attributed to variations in thickness of brittle crust and

increasing strain along the three Rift segments being investigated (see above section 7.1.1).

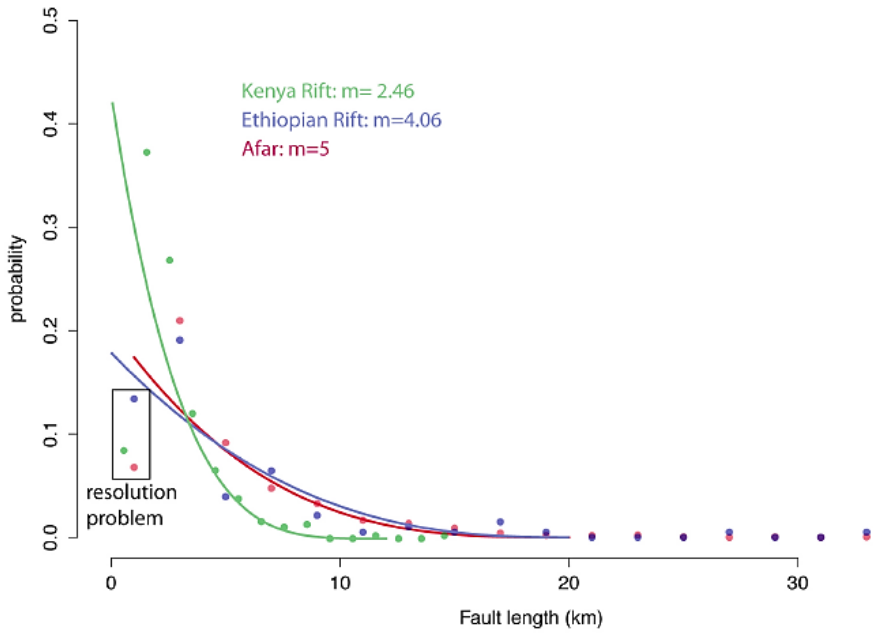

Figure 7.3 Estimation of the Weibull modulus for fault systems in the Magadi (green, m=3.47), the MER (blue, m=4.06) and Afar (red, m=5) (Stoyan & Gloaguen, 2011).

7.1.2 Distribution and localization of strain

The spatial distribution of strain heterogeneity has been qualitatively and quantitatively analysed through the model of Kuiper (1960) to characterize domains of deformation in the three Rift segments of interest that represent three different stages of continental Rifting. Two patterns of deformation (localized and distributed) have been recognized in the central Kenya Rift (Section 3.6.2) and between the central and northern MERs (Section 4.2.1.2).

What is worth noting in this investigation is that, the average of fault length populations can only be larger in areas of localized domain of deformation as opposed to areas of distributed deformation, this variation in fault length between localized and distributed faulting regimes can be explained by two different mechanisms in the central Kenya Rift and in the CMER and NMER segments. In the central Kenya Rift, zone 3 to the south that is recognised to have a fairly distributed deformation (section 3.6.2), and interpreted to be in a younger stage of fault evolution (section 3.8.2), that has a smaller average of fault length and throw (table 3.3) comparing to zone 1 (localized) in the north where border faults appear larger (table 3.3) and in a well-developed stage of linkage (see chapter 3 for more details), these observations are in consonance with existing models of early continental Rifting that invoke an initial phase of distributed, short normal faults, a phase of fault linkage, and ultimately linked faults forming Rift segments of large border faults (Cowie and Scholz, 1992a, Cowie and Scholz, 1992b). On the other hand, statistics of fault length distributions (Table 7.1) exhibited a decrease of the average of fault length along the three Rift segments as we move from south to north in a similar observations by Hayward and Ebinger (1996) and (Ebinger, 2005), who

observed a general south to north decrease in the length scale of boarder faults along the MER - Afar Rift segments. Moreover, the CMER in the south display a fairly localized deformation and larger average of fault length (Table 7.1) as opposed to the NMER in the north of the MER that exhibits distributed deformation. The observed decrease in average fault length in the NMER can be explained by models of Forsyth (1992) and Ackermann and Schlische (1997) that increasing extension to a sufficient degree capable of exceeding the shear strength of the volume and lead to formation of a new set of smaller grabens and smaller and shorter fault system in the weakened lithosphere within the Rift depression. By this stage, border faults are thought to be deactivated during the Pleistocene (Keir et al., 2006, Casey et al., 2006, Wolfenden et al., 2004) and highly eroded (Wolfenden et al., 2004). Therefore the jump from one domain of deformation to another indicates the transition from one Rift evolutionary stage to another.

The process of switching from distributed and localized deformation and from localized to distributed observed through fault populations in the study areas, has also been documented in previous field and theoretical studies, e.g. Gupta and Scholz (2000a) and Nixon et al. (2014) that observed a transition from localized faulting to distributed faulting. Whereas Ackermann et al. (2001), Soliva et al. (2006), Soliva and Schultz (2008) and Polit et al. (2009) observed a transition from distributed faulting to localized faulting. All these studies apart from Nixon et al. (2014) have discussed these two end members of deformation in terms of whether fault systems are restricted to a finite mechanical layer or have cut through a larger section of the crust, and suggested that fault systems in extensional settings are characterized by

either localized deformation associated with a power law size distribution or distributed faulting that follow an exponential size distribution.

Unlike these previous studies that recognized such shifting from distributed regime to localized regime or vice versa in experimental models or over relatively small areas, the large area size being investigated in the current study, allowed the observation and documentation of such spatial and temporal faulting domains over three Rift segments representing three different evolutionary stages, and suggest that deformation during Rifting alternates between distributed and localized faulting to allow the Rifting process to move forward.

Therefore, in reference to observations and theories of scaling properties of normal faults in relation to brittle crust and strain accommodation presented in previous studies (e.g. Ackermann et al., 2001, Soliva and Benedicto, 2005, Soliva et al., 2006, Soliva and Schultz, 2008, Nixon et al., 2014) and based upon the quantitative analyses of fault populations carried out in the current research, I would suggest a statistical component to be associated to the characteristics of the three stages of continental Rifting as follow: 1) the early stage of continental Rifting (i.e. the central Kenya Rift) occurring in a large crustal thickness and known by deformation being localized on few large border faults, can also be categorized by power law scaling for fault size distribution (length & throw). 2) The intermediate stage (i.e. the CMER) defined by incipient migration of faulting deformation from Rift borders to the Rift floor can be characterised by semi localized faulting (at Rift margins) conforming to exponential or/and log normal distribution. 3) The late stage of continental Rifting (i.e. the NMER) taking place in a relatively thin crustal thickness and

typified by deformation distributed across large number of rather small faults concentrated within the Rift floor and abandonment of border faults, can also be associated with exponential or/and log normal distribution (see Figure 7.4 for summary). I also believe that these statistical observations can be applied to similar stages of continental rifting elsewhere.

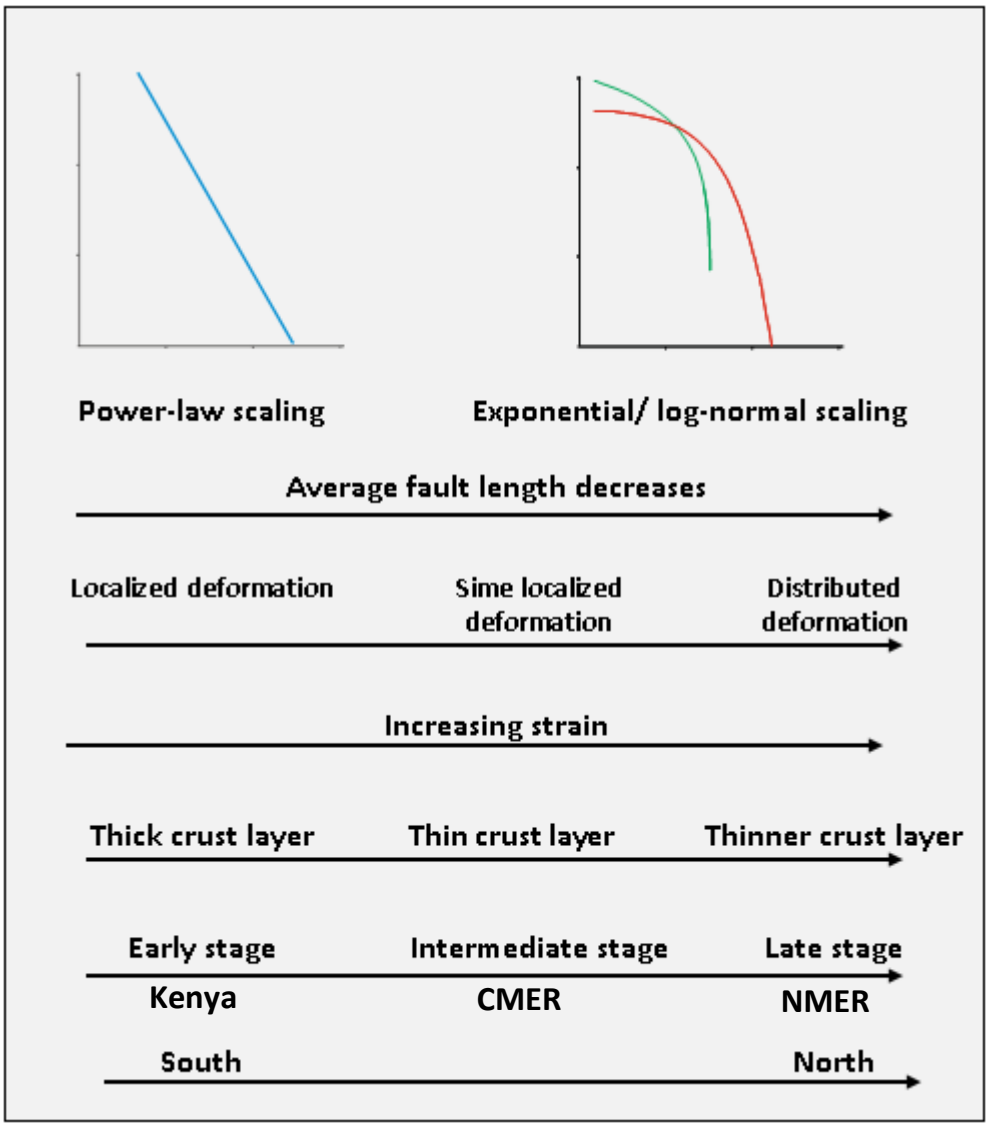

Figure 7.4 Summary of the observed properties in three different Rift segments (central Kenya Rift, CMER and NMER)

7.1.3 Implications for normal fault growth models

The fault datasets used in this research for the Kenya Rift (see chapter 3 section 3.8.2) and the CMER and the NMER (see chapter 4 section 4.3.4.2) appear to be consistent with the near constant length fault growth model (Figure 7.5) (the coherent fault growth model, chapter 2 section 2.1.3.5), in which faults grow by rapidly establishing their near maximum fault length in an early phase of deformation followed by accumulation of displacement with limited fault propagation (Walsh et al., 2002b, Walsh et al., 2003a, Childs et al., 2009, Giba et al., 2012) due to retardation of lateral propagation by interaction between fault tips (stress shadowing), resulting in a progressive increase in fault displacement to length ratios through time. This model has been inferred in current research through observations of different fault scaling relations of fault populations and their statistical distributions.

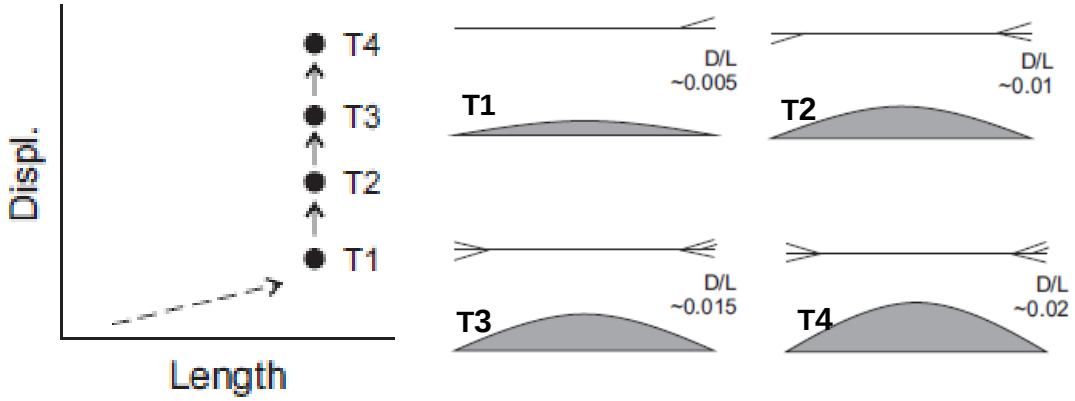

Figure 7.5 Schematic diagram illustrating constant length growth models, (T1–T4) increasing displacement profiles at four times. Modified from **(Nicol et al., 2016)**.

Moreover, in the central Kenya Rift, It has been discussed in (chapter 3 section 3.8.2) that, the fractal dimension of fault throw populations showed a decrease with increasing strain, while fractal dimension of fault length populations remained almost constant, moreover, the displacement vs length plot (chapter 3, section 3.7.1) also showed a general upward of increasing Displacement/Length ratio with a trend subparallel to the displacement axis, it was also observed that some isolated faults with small throw have comparable length as some bigger throw faults, these findings may imply that fault system in this central Kenya Rift segment may have established their near maximum length in early stage of evolution and accumulated displacement in a later stage in accordance to constant length fault growth model (Figure 7.5) or coherent fault model if the faults are kinematically and geometrically interrelated to a larger coherent underlying fault structure (see section 2.1.3.5).

As for the NMER and the CMER, it has been also discussed in section 4.3.4.2 that, as we move from CMER (south) to NMER (north), the NMER revealed a decrease of average fault lengths and an increasing of average fault throws and D/L ratio with increasing strain for all faults combined (table 4.4) and internal faults and bounding faults separately (table 4.5) as opposed to that of the CMER. The observed decrease of average fault length and increasing the ratio of displacement to length (D\L) may imply that the lateral propagation of the fault system has been retarded after reaching their near maximum fault length at their initiation, and then allowing the fault system to grow in displacement to accommodate the increasing strain in accordance to the coherent fault model presented in (Walsh et al., 2002b, Walsh et al., 2003a, Childs et al., 2009), this model which also suggests that if stress is applied to

the volume of rock, faults would initiate with low displacements but with lengths at or near maximum in an early stage of deformation.

Moreover, the coherent fault growth model is found to be a dominant configuration of normal fault growth in many extensional settings (e.g. Walsh et al., 2002a, Walsh et al., 2003a, Giba et al., 2012). In addition, It is thought that the constant length coherent fault growth model appear to be most relevant to fault systems that are reactivated and/or influenced by pre-existing structural (Walsh et al., 2002a, Giba et al., 2012, Lamarche et al., 2005, Meyer et al., 2002, Jackson and Rotevatn, 2013, Paton, 2006). However, the coherent fault growth model does not seem applicable in areas where fault reactivation and/or the influence of the inherited structural is not present (Jackson and Rotevatn, 2013). Moreover, Childs et al. (2017) pointed out that there is little doubt that pre-existing structure give rise to rapid fault length characterized in the coherent fault model.

In the current research, it has been demonstrated in chapter 5 (section 5.5.1) that the central Kenya overlay multiple Proterozoic basement fabrics, and the different orientations of fault populations observed in the three defined zones (zone 1, 2 &3) were attributed to variations in local extension direction in relation to the local pre-existing fabrics. Moreover, it has also been shown in section 5.5.2 that the pre-existing structures of Yerer-Tullu Wellel Volcanotectonic Lineament (YTVL) and Goba-Bonga lineaments within the CMER and the NMER could in part have influenced the orientation of fault population on the surface. However, the influence of the pre-existing structures in the CMER and the NMER segments is not evident due to scarcity of such basement structures as opposed to the central Kenya.

Therefore, the constant length fault model (Figure 7.5) appear to be the most plausible scenario for the mode of normal fault growth in the study areas. These inferences provide a description to the style of fault development during three phases of extension; in early continental Rifting (i.e. central Kenya Rift) in the presence of thick and strong mechanical layering, and in more advanced phases of continental Rifting (i.e. CMER & NMER) where the mechanical layering is thinner and weaker.

7.1.4 Limitations

Due to the limited nature of subsurface data sets in the region of EARS, measuring fault throw from DEM surface provides a minima representation of the actual throw and hence underestimation of the actual throw. Therefore, results obtained from minimal throw may not necessarily occur if the maximum throw is known. This limitations would introduce complications in identifying a simple D/L relationship. However, fault throw datasets used in this study provided supporting evidences and observations helped to make reasonable interpretations and reach realistic conclusions consistent with cases presented in the literature. Moreover, resolution limitations would also make it impossible to identify smaller discrete faults, which would lead to underestimation of the total strain accommodated in a given region.

7.2 Conclusions

Three different stages of continental Rifting within the EARS were investigated in this research by using DEM data and satellite images in order to understand the evolution of normal faults and their implications on propagation of continental Rifting from north to south. This aim was achieved by examining and comparing fault scaling relations between different fault populations in these three Rift segments. The three stages of continental Rifting are; an early continental Rifting phase represented in the central Kenya Rift, a transitional phase of continental Rifting exemplified in the central main Ethiopian Rift (CMER), and a late phase represented in the northern main Ethiopian Rift (NMER). A quantitative and statistical analysis have been applied to fault sizes datasets of 2130 normal faults captured from DEM surfaces of the three study areas. The implications of this work cover several key processes of continental Rifting, namely the evolution of fault populations, heterogeneity of strain accommodation, the potential influence of pre-existing fabrics on development of extensional faulting and the response the landscape to tectonic-erosional deformation. The main findings from the four result chapters reflecting the upper crust brittle deformation are synthesised in this conclusion chapter.

- Estimations of extensional strain obtained from the three studied Rift segments along the Rift revealed a general increase of strain from the south to the north, which agree with the hypothesis that has been set in the beginning of this research that there is a northward increase of total strain in Rift segments along the EARS (Hayward and Ebinger, 1996, Soliva and Schultz, 2008, Agostini et al., 2011b).

- The spatial temporal deformation domains (localized and distributed faulting) were observed and quantified over the three Rift segments representing three different evolutionary stages, and suggest that deformation during Rifting alternates between distributed and localized faulting to allow the Rifting process to move forward.

- The cumulative distributions of fault length and fault throw populations of the three Rift segments suggested that the power law scaling observed for the central Kenya Rift conforms to relatively thick crust and low strain setting of this region whereas, the exponential/log normal scaling is associated with a relatively thinner crust and high strain regime in the CMER and the NMER segments.

- Based upon the quantitative analyses of fault populations carried out in the current research with regard to theories and observations presented in the literature, I suggest a statistical component to be associated to the characteristics of the three stages of continental Rifting as follow; the early stage of continental Rifting (i.e. the central Kenya Rift) can also be categorized by power law scaling for fault size distribution (length & throw). The intermediate stage (i.e. the CMER) can be characterised as semi localized faulting following exponential or/and log normal distribution. The late stage of continental Rifting (i.e. the NMER) can also be associated with exponential or/and log normal distribution.

- With regard to the existing literature, it has been inferred through observations of different fault scaling relations and their statistical distributions that, the coherent fault model appear to be the most

relevant configuration for the mode of normal fault growth in the study areas.

- Results of examining the possible influence of basement structure on fault development in the light of experimental models have shown that such influence is more evident in the central Kenya Rift than in both the central MER and the northern MER, and that was referred to the relative abundance of basement structures within the central Kenya Rift as opposed to the central MER and the northern MER.
- The qualitative analysis of stream orders of drainage networks showed that interpreted possible original location of footwall block in the central Kenya Rift and the CMER appear to be fairly comparable to that initially mapped in this study, which suggests that estimations of extensional strain in these two Rift zones are appropriate, While in the NMER the interpreted original location corresponded to multiple footwall cut-offs, which may suggest that estimations of extensional strain in the NMER could be overestimated.
- Finding of this study show that this technique of fault picking using medium resolution of 30mx30m proves to be a useful alternative for collecting data in areas where seismic or high resolution data are not available, it is also useful in collecting a large number of faults than is feasible from field mapping alone with a satisfactory degree of precession. Therefore, the methodology applied here could be applicable for studying fault development and the consequent Rift evolution from structural topography in continental Rifts elsewhere.

7.2.1 Directions for future work

This study explored the scaling properties of normal fault population in the continental Rifting using DEM data. The conclusions drawn from this research have wide implications for the understanding of fault growth and their implications on the evolution of continental Rifting general. Therefore, recommendations for further work are as follow:

- The measured throw from the surface of DEM image is minima (apparent throw), which may not be representative for the maximum throw. The extent of displacement into the subsurface was not constrained due to lack of seismic data over this region of EARS Therefore, applicability of this research could be greatly improved with the investigation of 2D seismic datasets that would better constrain the maximum fault throw.

- The Rift floor within the central part of the Rift near Bogoria lake exhibits dense and closely spaced en-echelon pattern of faulting, these characteristics are in contrast to the typical characteristics of an early continental stage Rifting where the largest part of deformation being accommodated by boundary faults and almost absence of internal faults. These contrasting characteristics need further investigation as whether they relate to the same Rifting event or caused by a different geological event.

- In the CMER, the best-fitting statistical distributions for fault spacing data displayed exponential distribution indicative for random distribution. In contrast, coefficient of variation (Cv) values and step-plots of spatial heterogeneity of fault spacing suggest a clustering

distribution, the reason behind this discrepancy was interpreted in the present research as the clustering in fault spacing data was not strong enough. This relationship between these parameters needs to be investigated further to establish whether the exponential distributions can arise from fault spacing data that are moderately clustered for example.

- The influence of basement structure on evolution of normal faults on the surface in the three study areas need to be better constrained through analysis of different data (e.g. subsurface data).

- The preliminary methodology introduced in chapter6 for interpreting and defining the likely original position of eroded footwall blocks of the fault scarps, lays the ground-work for further investigation.

References

ABBATE, E. & SAGRI, M. 1980. Volcanites of Ethiopian and Somali Plateaus and major tectonic lines. *Atti Convegni Lincei,* 47**,** 219-227.

ABDULLAH, A., NASSR, S. & GHALEEB, A. 2013. Remote Sensing and Geographic Information System for Fault Segments Mapping a Study from Taiz Area, Yemen. *Journal of Geological Research,* 2013**,** 16.

ABEBE, T., BALESTRIERI, M. L. & BIGAZZI, G. 2010. The Central Main Ethiopian Rift is younger than 8 Ma: confirmation through apatite fission-track thermochronology. *Terra Nova,* 22**,** 470-476.

ABEBE, T., MAZZARINI, F., INNOCENTI, F. & MANETTI, P. 1998. The Yerer-Tullu Wellel volcanotectonic lineament: A transtensional structure in central Ethiopia and the associated magmatic activity. *Journal of African Earth Sciences,* 26**,** 135-150.

ACHAUER, U., MAGUIRE, P. K. H., MECHIE, J. & GREEN, W. V. 1992. Some remarks on the structure and geodynamics of the Kenya Rift. *Tectonophysics,* 213**,** 257-268.

ACKERMANN, R. V. & SCHLISCHE, R. W. 1997. Anticlustering of small normal faults around larger faults. *Geology,* 25**,** 1127-1130.

ACKERMANN, R. V., SCHLISCHE, R. W. & WITHJACK, M. O. 2001. The geometric and statistical evolution of normal fault systems: an experimental study of the effects of mechanical layer thickness on scaling laws. *Journal of Structural Geology,* 23**,** 1803-1819.

AGOSTINI, A., BONINI, M., CORTI, G., SANI, F. & MANETTI, P. 2011a. Distribution of Quaternary deformation in the central Main Ethiopian Rift, East Africa. *Tectonics,* 30**,** n/a-n/a.

AGOSTINI, A., BONINI, M., CORTI, G., SANI, F. & MAZZARINI, F. 2011b. Fault architecture in the Main Ethiopian Rift and comparison with experimental models: Implications for rift evolution and Nubia–Somalia kinematics. *Earth and Planetary Science Letters,* 301**,** 479-492.

AGOSTINI, A., CORTI, G., ZEOLI, A. & MULUGETA, G. 2009. Evolution, pattern, and partitioning of deformation during oblique continental rifting: Inferences from lithospheric-scale centrifuge models. *Geochemistry, Geophysics, Geosystems,* 10**,** Q11015.

ALEKSANDROWSKI, P., INDERHAUG, O. H. & KNAPSTAD, B. 1992. Tectonic structures and wellbore breakout orientation. *The 33th U.S. Symposium on Rock Mechanics (USRMS).* Santa Fe, New Mexico: American Rock Mechanics Association.

AMINE, A. & EL OUARDI, H. 2017. Active tectonics revealed by isobase surfaces analysis from South Rifian Ridges, Northern Morocco. *Geogaceta,* 61**,** 71-74.

ANDERSON, E. M. 1951. *The dynamics of faulting and dyke formation with applications to Britain*, Hafner Pub. Co.

ANUPMA GUPTA, C. H. S. 2000b. A model of normal fault interaction based on observations and theory. *Journal of Structural Geology*.

BAILEY, W. R., WALSH, J. J. & MANZOCCHI, T. 2005. Fault populations, strain distribution and basement fault reactivation in the East Pennines Coalfield, UK. *Journal of Structural Geology,* 27**,** 913-928.

BAKER, B. H., MOHR, P. A. & WILLIAMS, L. A. J. 1972. Geology of the Eastern Rift System of Africa. *Geological Society of America Special Papers,* 136**,** 1-68.

BAKER, B. H. & WOHLENBERG, J. 1971. Structure and Evolution of the Kenya Rift Valley. *Nature,* 229**,** 538-542.

BEGG, J. G. & MOUSLOPOULOU, V. 2010. Analysis of late Holocene faulting within an active rift using lidar, Taupo Rift, New Zealand. *Journal of Volcanology and Geothermal Research,* 190**,** 152-167.

BELLAHSEN, N. & DANIEL, J. M. 2005. Fault reactivation control on normal fault growth: an experimental study. *Journal of Structural Geology,* 27**,** 769-780.

BERGEN, K. J. & SHAW, J. H. 2010. Displacement profiles and displacement-length scaling relationships of thrust faults constrained by seismic-reflection data. *Geological Society of America Bulletin,* 122**,** 1209-1219.

BOCCALETTI, M. 1998. Quaternary oblique extensional tectonics in the Ethiopian Rift (Horn of Africa). *Tectonophysics,* 287.

BONINI, M., CORTI, G., INNOCENTI, F., MANETTI, P., MAZZARINI, F., ABEBE, T. & PECSKAY, Z. 2005. Evolution of the Main Ethiopian Rift in the frame of Afar and Kenya rifts propagation. *Tectonics,* 24**,** n/a-n/a.

BONNET, E., BOUR, O., ODLING, N. E., DAVY, P., MAIN, I., COWIE, P. & BERKOWITZ, B. 2001. Scaling of fracture systems in geological media. *Reviews of Geophysics,* 39**,** 347-383.

BOSWORTH, W. 1989. Basin and Range style tectonics in East Africa. *Journal of African Earth Sciences (and the Middle East),* 8**,** 191-201.

BOSWORTH, W. 1994. A MODEL FOR THE 3-DIMENSIONAL EVOLUTION OF CONTINENTAL RIFT BASINS, NORTHEAST AFRICA. *Geologische Rundschau,* 83**,** 671-688.

BOSWORTH, W., LAMBIASE, J. & KEISLER, R. 1986. A new look at Gregory's rift: the structural style of continental rifting. *Eos, Transactions American Geophysical Union,* 67**,** 577-583.

BOSWORTH, W. & STRECKER, M. R. 1997. Stress field changes in the Afro-Arabian rift system during the Miocene to Recent period. *Tectonophysics,* 278**,** 47-62.

BOTT, M. H. P. 1993. Modelling the plate-driving mechanism. *Journal of the Geological Society,* 150**,** 941-951.

BOTT, M. H. P. & KUSZNIR, N. J. 1979. Stress distributions associated with compensated plateau uplift structures with application to the continental splitting mechanism. *Geophysical Journal International,* 56**,** 451-459.

BRAILE, L., KELLER, G., WENDLANDT, R., MORGAN, P. & KHAN, M. 2006. The East African rift system. *Developments in Geotectonics,* 25**,** 213-III.

BRUN, J. 1999. Narrow rifts versus wide rifts: inferences for the mechanics of rifting from laboratory experiments. *PHILOSOPHICAL TRANSACTIONS-ROYAL SOCIETY OF LONDON SERIES A MATHEMATICAL PHYSICAL AND ENGINEERING SCIENCES*, 695-709.

BRUNE, S. 2014. Evolution of stress and fault patterns in oblique rift systems: 3-D numerical lithospheric-scale experiments from rift to breakup. *Geochemistry, Geophysics, Geosystems,* 15, 3392-3415.

BUCK, W. R. 1991. Modes of continental lithospheric extension. *Journal of Geophysical Research: Solid Earth,* 96, 20161-20178.

BUCK, W. R. 2004. Consequences of asthenospheric variability on continental rifting. *Rheology and deformation of the lithosphere at continental margins,* 62, 1-30.

BURBANK, D. W. & ANDERSON, R. S. 2011. *Tectonic geomorphology*, John Wiley & Sons.

CARTWRIGHT, J. A., MANSFIELD, C. & TRUDGILL, B. 1996. The growth of normal faults by segment linkage. *Geological Society, London, Special Publications,* 99, 163-177.

CARTWRIGHT, J. A., TRUDGILL, B. D. & MANSFIELD, C. S. 1995. Fault growth by segment linkage: an explanation for scatter in maximum displacement and trace length data from the Canyonlands Grabens of SE Utah. *Journal of Structural Geology,* 17, 1319-1326.

CASEY, M., EBINGER, C., KEIR, D., GLOAGUEN, R. & MOHAMED, F. 2006. Strain accommodation in transitional rifts: extension by magma intrusion and faulting in Ethiopian rift magmatic segments. *Geological Society, London, Special Publications,* 259, 143-163.

CASTAING, C., HALAWANI, M., GERVAIS, F., CHILÈS, J., GENTER, A., BOURGINE, B., OUILLON, G., BROSSE, J., MARTIN, P. & GENNA, A. 1996. Scaling relationships in intraplate fracture systems related to Red Sea rifting. *Tectonophysics,* 261, 291-314.

CHATTOPADHYAY, A. & CHAKRA, M. 2013. Influence of pre-existing pervasive fabrics on fault patterns during orthogonal and oblique rifting: An experimental approach. *Marine and Petroleum Geology,* 39, 74-91.

CHILDS, C., HOLDSWORTH, R. E., JACKSON, C. A.-L., MANZOCCHI, T., WALSH, J. J. & YIELDING, G. 2017. Introduction to the geometry and growth of normal faults. *Geological Society, London, Special Publications,* 439, 1-9.

CHILDS, C., MANZOCCHI, T., WALSH, J. J., BONSON, C. G., NICOL, A. & SCHÖPFER, M. P. J. 2009. A geometric model of fault zone and fault rock thickness variations. *Journal of Structural Geology,* 31, 117-127.

CHILDS, C., WALSH, J. J. & WATTERSON, J. 1990. A Method for Estimation of the Density of Fault Displacements below the Limits of Seismic Resolution in Reservoir Formations. *In:* BULLER, A. T., BERG, E., HJELMELAND, O., KLEPPE, J., TORSÆTER, O. & AASEN, J. O. (eds.) *North Sea Oil and Gas Reservoirs—II: Proceedings of the 2nd North Sea Oil and Gas Reservoirs Conference organized and hosted*

by the Norwegian Institute of Technology (NTH), Trondheim, Norway, May 8–11, 1989. Dordrecht: Springer Netherlands.

CHOROWICZ, J. 2005. The East African rift system. *Journal of African Earth Sciences,* 43**,** 379-410.

CHOROWICZ, J., COLLET, B., BONAVIA, F. F. & KORME, T. 1994. Northwest to north-northwest extension direction in the Ethiopian rift deduced from the orientation of extension structures and fault-slip analysis. *Geological Society of America Bulletin,* 106**,** 1560-1570.

CHOROWICZ, J., ICHOKU, C., RIAZANOFF, S., KIM, Y. J. & CERVELLE, B. 1992. A combined algorithm for automated drainage network extraction. *Water Resources Research,* 28**,** 1293-1302.

CLADOUHOS, T. T. & MARRETT, R. 1996. Are fault growth and linkage models consistent with power-law distributions of fault lengths? *Journal of Structural Geology,* 18**,** 281-293.

CORNWELL, D., MACKENZIE, G., ENGLAND, R., MAGUIRE, P., ASFAW, L. & OLUMA, B. 2006. Northern Main Ethiopian Rift crustal structure from new high-precision gravity data. *Geological Society, London, Special Publications,* 259**,** 307-321.

CORTI, G. 2004. Centrifuge modelling of the influence of crustal fabrics on the development of transfer zones: insights into the mechanics of continental rifting architecture. *Tectonophysics,* 384**,** 191-208.

CORTI, G. 2008. Control of rift obliquity on the evolution and segmentation of the main Ethiopian rift. *Nature Geoscience,* 1**,** 258-262.

CORTI, G. 2009. Continental rift evolution: From rift initiation to incipient break-up in the Main Ethiopian Rift, East Africa. *Earth-Science Reviews,* 96**,** 1-53.

CORTI, G. 2012. Evolution and characteristics of continental rifting: Analog modeling-inspired view and comparison with examples from the East African Rift System. Volumes 522–523**,** Pages 1–33.

CORTI, G. & MANETTI, P. 2006. Asymmetric rifts due to asymmetric Mohos: An experimental approach. *Earth and Planetary Science Letters,* 245**,** 315-329.

CORTI, G., VAN WIJK, J., BONINI, M., SOKOUTIS, D., CLOETINGH, S., INNOCENTI, F. & MANETTI, P. 2003. Transition from continental break-up to punctiform seafloor spreading: How fast, symmetric and magmatic. *Geophysical Research Letters,* 30**,** 1604.

CORTI, G., VAN WIJK, J., CLOETINGH, S. & MORLEY, C. K. 2007. Tectonic inheritance and continental rift architecture: Numerical and analogue models of the East African Rift system. *Tectonics,* 26.

COWIE, P. 1998a. Normal fault growth in three-dimensions in continental and oceanic crust.

COWIE, P. A. 1998b. A healing–reloading feedback control on the growth rate of seismogenic faults. *Journal of Structural Geology,* 20**,** 1075-1087.

COWIE, P. A., GUPTA, S. & DAWERS, N. H. 2000. Implications of fault array evolution for synrift depocentre development: insights from a numerical fault growth model. *Basin Research,* 12**,** 241-261.

COWIE, P. A., MALINVERNO, A., RYAN, W. B. F. & EDWARDS, M. H. 1994. Quantitative fault studies on the East Pacific Rise: A comparison of sonar imaging techniques. *Journal of Geophysical Research: Solid Earth,* 99**,** 15205-15218.

COWIE, P. A. & SCHOLZ, C. H. 1992a. Displacement-length scaling relationship for faults: data synthesis and discussion. *Journal of Structural Geology,* 14**,** 1149-1156.

COWIE, P. A. & SCHOLZ, C. H. 1992b. Growth of faults by accumulation of seismic slip. *Journal of Geophysical Research: Solid Earth,* 97**,** 11085-11095.

COWIE, P. A. & SCHOLZ, C. H. 1992c. Physical explanation for the displacement-length relationship of faults using a post-yield fracture mechanics model. *Journal of Structural Geology,* 14**,** 1133-1148.

COWIE, P. A., SORNETTE, D. & VANNESTE, C. 1995. Multifractal scaling properties of a growing fault population. *Geophysical Journal International,* 122**,** 457-469.

COWIE, P. A., UNDERHILL, J. R., BEHN, M. D., LIN, J. & GILL, C. E. 2005. Spatio-temporal evolution of strain accumulation derived from multi-scale observations of Late Jurassic rifting in the northern North Sea: A critical test of models for lithospheric extension. *Earth and Planetary Science Letters,* 234**,** 401-419.

DALY, M. C., CHOROWICZ, J. & FAIRHEAD, J. D. 1989. Rift basin evolution in Africa: the influence of reactivated steep basement shear zones. *Geological Society, London, Special Publications,* 44**,** 309-334.

DAUTEUIL, O. & BRUN, J. P. 1996. Deformation partitioning in a slow spreading ridge undergoing oblique extension: Mohns Ridge, Norwegian Sea. *Tectonics,* 15**,** 870-884.

DAWERS, N. H., ANDERS, M. H. & SCHOLZ, C. H. 1993. Growth of normal faults: Displacement-length scaling. *Geology,* 21**,** 1107-1110.

DE GUIDI, G., CAPUTO, R. & SCUDERO, S. 2013. Regional and local stress field orientation inferred from quantitative analyses of extension joints: Case study from southern Italy. *Tectonics,* 32**,** 239-251.

DEFFONTAINES, B. & CHOROWICZ, J. 1991. Principles of drainage basin analysis from multisource data: application to the structural analysis of the Zaire Basin. *Tectonophysics,* 194**,** 237-263.

DEWEY, J., HEMPTON, M., KIDD, W., SAROGLU, F. & ŞENGÖR, A. 1986. Shortening of continental lithosphere: the neotectonics of Eastern Anatolia—a young collision zone. *Geological Society, London, Special Publications,* 19**,** 1-36.

DIXON, T. H., STERN, R. J. & HUSSEIN, I. M. 1987. Control of Red Sea rift geometry by Precambrian structures. *Tectonics,* 6**,** 551-571.

EBINGER, C. 2005. Continental break-up: The East African perspective. *Astronomy & Geophysics,* 46**,** 2.16-2.21.

EBINGER, C. J. 1989a. Geometric and kinematic development of border faults and accommodation zones, Kivu-Rusizi Rift, Africa. *Tectonics,* 8**,** 117-133.

EBINGER, C. J. 1989b. Tectonic development of the western branch of the East African rift system. *Geological Society of America Bulletin,* 101**,** 885-903.

EBINGER, C. J. & CASEY, M. 2001. Continental breakup in magmatic provinces: An Ethiopian example. 29.

EBINGER, C. J. & SLEEP, N. H. 1998. Cenozoic magmatism throughout east Africa resulting from impact of a single plume. *Nature,* 395**,** 788-791.

EBINGER, C. J., YEMANE, T., HARDING, D. J., TESFAYE, S., KELLEY, S. & REX, D. C. 2000. Rift deflection, migration, and propagation: Linkage of the Ethiopian and Eastern rifts, Africa. *Geological Society of America Bulletin,* 112**,** 163-176.

EINSTEIN, H. H. & BAECHER, G. B. 1983. Probabilistic and statistical methods in engineering geology. *Rock Mechanics and Rock Engineering,* 16**,** 39-72.

ETHERIDGE, M. A. 1986. *On the Reactivation of Extensional Fault Systems*.

FAIRHEAD, J. D. & STUART, G. W. 1982. The Seismicity of the East African Rift System and Comparison with Other Continental Rifts. *Continental and Oceanic Rifts.* American Geophysical Union.

FAULKNER, D. R., JACKSON, C. A. L., LUNN, R. J., SCHLISCHE, R. W., SHIPTON, Z. K., WIBBERLEY, C. A. J. & WITHJACK, M. O. 2010. A review of recent developments concerning the structure, mechanics and fluid flow properties of fault zones. *Journal of Structural Geology,* 32**,** 1557-1575.

FINKBEINER, T., BARTON, C. A. & ZOBACK, M. D. 1997. Relationships among in-situ stress, fractures and faults, and fluid flow: Monterey Formation, Santa Maria Basin, California. *AAPG bulletin,* 81**,** 1975-1999.

FORSYTH, D. 1992. Finite extension and low-angle normal faulting. *Geology* (1992) 20 (1): 27-30.

FORSYTH, D. & UYEDA, S. 1975. On the Relative Importance of the Driving Forces of Plate Motion. *Geophysical Journal International,* 43**,** 163-200.

FOSSEN, H. & HESTHAMMER, J. 1997. Geometric analysis and scaling relations of deformation bands in porous sandstone. *Journal of Structural Geology,* 19**,** 1479-1493.

GAUTHIER, B. & LAKE, S. 1993. Probabilistic modeling of faults below the limit of seismic resolution in Pelican Field, North Sea, offshore United Kingdom. *AAPG Bulletin,* 77**,** 761-777.

GIBA, M., WALSH, J. J. & NICOL, A. 2012. Segmentation and growth of an obliquely reactivated normal fault. *Journal of Structural Geology,* 39**,** 253-267.

GILLESPIE, P. A., HOWARD, C. B., WALSH, J. J. & WATTERSON, J. 1993. Measurement and characterisation of spatial distributions of fractures. *Tectonophysics,* 226**,** 113-141.

GILLESPIE, P. A., WALSH, J. J. & WATTERSON, J. 1992. Limitations of dimension and displacement data from single faults and the consequences for data analysis and interpretation. *Journal of Structural Geology,* 14**,** 1157-1172.

GILLESPIE, P. A., WALSH, J. J., WATTERSON, J., BONSON, C. G. & MANZOCCHI, T. 2001. Scaling relationships of joint and vein arrays from The Burren, Co. Clare, Ireland. *Journal of Structural Geology,* 23**,** 183-201.

GOLTS, S. & ROSENTHAL, E. 1993. A morphotectonic map of the northern Arava in Israel, derived from isobase lines. *Geomorphology,* 7**,** 305-315.

GRIFFITHS, P. S. 1980. Box-fault systems and ramps: atypical associations of structures from the eastern shoulder of the Kenya Rift. *Geological Magazine,* 117**,** 579-586.

GRIMAUD, P., RICHERT, J. P., ROLET, J., TIERCELIN, J. J., XAVIER, J. P., MORLEY, C. K., COUSSEMENT, C., KARANJA, S. W., RENAUT, R. W., GUERIN, G., LETURDU, C. & MICHELNOEL, G. 1994. FAULT GEOMETRY AND EXTENSION MECHANISMS IN THE CENTRAL KENYA RIFT, EAST-AFRICA - A 3D REMOTE-SENSING APPROACH. *Bulletin des Centres de Recherches Exploration-Production Elf Aquitaine,* 18**,** 59-92.

GROHMANN, C. H., RICCOMINI, C. & CHAMANI, M. A. C. 2011. Regional scale analysis of landform configuration with base-level (isobase) maps. *Hydrol. Earth Syst. Sci.,* 15**,** 1493-1504.

GROSS, M. R., GUTIE´RREZ-ALONSO, G., BAI, T., WACKER, M. A., COLLINSWORTH, K. B. & BEHL, R. J. 1997. Influence of mechanical stratigraphy and kinematics on fault scaling relations. *Journal of Structural Geology,* 19**,** 171-183.

GUPTA, A. & SCHOLZ, C. H. 2000. A model of normal fault interaction based on observations and theory. *Journal of Structural Geology,* 22**,** 865-879.

GUPTA, A. & SCHOLZ, C. H. 2000a. Brittle strain regime transition in the Afar depression: Implications for fault growth and seafloor spreading. *Geology,* 28**,** 1087-1090.

HARRIS, C., FRANSSEN, R. & LOOSVELD, R. 1991. Fractal analysis of fractures in rocks: the Cantor's Dust method-comment. *Tectonophysics,* 198**,** 107-111.

HAUTOT, S., TARITS, P., WHALER, K., LE GALL, B., TIERCELIN, J.-J. & LE TURDU, C. 2000. Deep structure of the Baringo Rift Basin (central Kenya) from three-dimensional magnetotelluric imaging: Implications for rift evolution. *Journal of Geophysical Research: Solid Earth,* 105**,** 23493-23518.

HAYWARD, N. J. & EBINGER, C. J. 1996. Variations in the along-axis segmentation of the Afar Rift system. *Tectonics,* 15**,** 244-257.

HEFFER, K. & BEVAN, T. Scaling relationships in natural fractures: data, theory, and application. European Petroleum Conference, 1990. Society of Petroleum Engineers.

HENRY, W. J., MECHIE, J., MAGUIRE, P., KHAN, M., PRODEHL, C., KELLER, G. & PATEL, J. 1990. A seismic investigation of the Kenya Rift Valley. *Geophysical Journal International,* 100**,** 107-130.

HENZA, A. A., WITHJACK, M. O. & SCHLISCHE, R. W. 2010. Normal-fault development during two phases of non-coaxial extension: An experimental study. *Journal of Structural Geology,* 32**,** 1656-1667.

HENZA, A. A., WITHJACK, M. O. & SCHLISCHE, R. W. 2011. How do the properties of a pre-existing normal-fault population influence fault development during a subsequent phase of extension? *Journal of Structural Geology,* 33**,** 1312-1324.

HETZEL, R. & STRECKER, M. R. 1994. Late Mozambique Belt structures in western Kenya and their influence on the evolution of the Cenozoic Kenya Rift. *Journal of Structural Geology,* 16**,** 189-201.

HOLDSWORTH, R. E., BUTLER, C. A. & ROBERTS, A. M. 1997. The recognition of reactivation during continental deformation. *Journal of the Geological Society,* 154**,** 73-78.

HOSSEINZADEH, S. R. 2011. Drainage Network Analysis, Comparis of Digital Elevation Model(DEM) from ASTER with High Resolution Satellite Image and Areal Photographs. *International Journal of Environmental Science and Development,* 2**,** 194-198.

HUS, R., ACOCELLA, V., FUNICIELLO, R. & DE BATIST, M. 2005. Sandbox models of relay ramp structure and evolution. *Journal of Structural Geology,* 27**,** 459-473.

ILLIES, J. H. 1981. Mechanism of graben formation. *Tectonophysics,* 73**,** 249-266.

JACKSON, C. A.-L. & ROTEVATN, A. 2013. 3D seismic analysis of the structure and evolution of a salt-influenced normal fault zone: a test of competing fault growth models. *Journal of Structural Geology,* 54**,** 215-234.

JACKSON, J. & LEEDER, M. 1994. Drainage systems and the development of normal faults: an example from Pleasant Valley, Nevada. *Journal of Structural Geology,* 16**,** 1041-1059.

JACKSON, J. A. & WHITE, N. J. 1989. Normal faulting in the upper continental crust: observations from regions of active extension. *Journal of Structural Geology,* 11**,** 15-36.

JACKSON, P. & SANDERSON, D. J. 1992. Scaling of fault displacements from the Badajoz-Cordoba shear zone, SW Spain. *Tectonophysics,* 210**,** 179-190.

JANSSEN, M. E., STEPHENSON, R. A. & CLOETINGH, S. 1995. Temporal and spatial correlations between changes in plate motions and the

evolution of rifted basins in Africa. *Geological Society of America Bulletin,* 107**,** 1317-1332.

JEDLIČKA, K., SLÁDEK, J. & ŠILHAVÝ, J. 2015. Semiautomatic construction of isobase surfaces: A case study from the central Western Carpathians. *Computers & Geosciences,* 78**,** 73-80.

JONES, W. B. & LIPPARD, S. J. 1979. New age determinations and the geology of the Kenya Rift-Kavirondo Rift junction, W Kenya. *Journal of the Geological Society,* 136**,** 693-704.

KARSON, J. A. & CURTIS, P. C. 1989. Tectonic and magmatic processes in the Eastern Branch of the East African Rift and implications for magmatically active continental rifts. *Journal of African Earth Sciences (and the Middle East),* 8**,** 431-453.

KATUMWEHE, A. B., ABDELSALAM, M. G., ATEKWANA, E. A. & LAÓ-DÁVILA, D. A. 2016. Extent, kinematics and tectonic origin of the Precambrian Aswa Shear Zone in eastern Africa. *Gondwana Research,* 34**,** 241-253.

KAZMIN, V., SEIFE, M., NICOLETTI, M. & PETRUCCIANI, C. 1980. Evolution of the northern part of the Ethiopian Rift. *Atti Convegni Lincei,* 47**,** 275-292.

KEIR, D., BASTOW, I. D., PAGLI, C. & CHAMBERS, E. L. 2013. The development of extension and magmatism in the Red Sea rift of Afar. *Tectonophysics,* 607**,** 98-114.

KEIR, D., EBINGER, C. J., STUART, G. W., DALY, E. & AYELE, A. 2006. Strain accommodation by magmatism and faulting as rifting proceeds to breakup: Seismicity of the northern Ethiopian rift. *Journal of Geophysical Research: Solid Earth,* 111**,** n/a-n/a.

KENDALL, J. M., STUART, G. W., EBINGER, C. J., BASTOW, I. D. & KEIR, D. 2005. Magma-assisted rifting in Ethiopia. *Nature,* 433**,** 146-148.

KERANEN, K. & KLEMPERER, S. L. 2008. Discontinuous and diachronous evolution of the Main Ethiopian Rift: Implications for development of continental rifts. *Earth and Planetary Science Letters,* 265**,** 96-111.

KEY, R., CHARSLEY, T., HACKMAN, B., WILKINSON, A. T. & RUNDLE, C. 1989. Superimposed upper Proterozoic collision-controlled orogenies in the Mozambique orogenic belt of Kenya. *Precambrian Research,* 44**,** 197-225.

KIM, Y.-S. & SANDERSON, D. J. 2005. The relationship between displacement and length of faults: a review. *Earth-Science Reviews,* 68**,** 317-334.

KING, B. C. 1978. Structural and volcanic evolution of the Gregory Rift Valley. *Geological Society, London, Special Publications,* 6**,** 29-54.

KIRBY, E. & WHIPPLE, K. X. 2012. Expression of active tectonics in erosional landscapes. *Journal of Structural Geology,* 44**,** 54-75.

KOGAN, L., FISSEHA, S., BENDICK, R., REILINGER, R., MCCLUSKY, S., KING, R. & SOLOMON, T. 2012. Lithospheric strength and strain localization in continental extension from observations of the East

African Rift. *Journal of Geophysical Research: Solid Earth (1978–2012),* 117.

KRISP, W. G. 1991. Large-scale variation in lithospheric structure along and across the Kenya rift *Nature,* 354.

KUIPER, N. H. Tests concerning random points on a circle. Indagationes Mathematicae (Proceedings), 1960. Elsevier, 38-47.

LAMARCHE, G., PROUST, J.-N. & NODDER, S. D. 2005. Long-term slip rates and fault interactions under low contractional strain, Wanganui Basin, New Zealand. *Tectonics,* 24**,** n/a-n/a.

LE GALL, B., NONNOTTE, P., ROLET, J., BENOIT, M., GUILLOU, H., MOUSSEAU-NONNOTTE, M., ALBARIC, J. & DEVERCHÈRE, J. 2008. Rift propagation at craton margin.: Distribution of faulting and volcanism in the North Tanzanian Divergence (East Africa) during Neogene times. *Tectonophysics,* 448**,** 1-19.

LE TURDU, C., TIERCELIN, J., RICHERT, J., ROLET, J., XAVIER, J., RENAUT, R., LEZZAR, K. & COUSSEMENT, C. 1999. Influence of preexisting oblique discontinuities on the geometry and evolution of extensional fault patterns: evidence from the Kenya Rift using SPOT imagery. *Geoscience of Rift Systems–Evolution of East Africa,* 44**,** 173-91.

LEVERINGTON, D. W., TELLER, J. T. & MANN, J. D. 2002. A GIS method for reconstruction of late Quaternary landscapes from isobase data and modern topography. *Computers & Geosciences,* 28**,** 631-639.

LOGATCHEV, N. A., BELOUSSOV, V. V. & MILANOVSKY, E. E. 1972. East african rift development. *Tectonophysics,* 15**,** 71-81.

MACKENZIE, G., THYBO, H. & MAGUIRE, P. 2005. Crustal velocity structure across the Main Ethiopian Rift: results from two-dimensional wide-angle seismic modelling. *Geophysical Journal International,* 162**,** 994-1006.

MAGUIRE, P. K. H., KELLER, G. R., KLEMPERER, S. L., MACKENZIE, G. D., KERANEN, K., HARDER, S., O'REILLY, B., THYBO, H., ASFAW, L., KHAN, M. A. & AMHA, M. 2006. Crustal structure of the northern Main Ethiopian Rift from the EAGLE controlled-source survey; a snapshot of incipient lithospheric break-up. *Geological Society, London, Special Publications,* 259**,** 269-292.

MAGUIRE, P. K. H., SHAH, E. R., POINTING, A. J., COOKE, P. A. V., KHAN, M. A. & SWAIN, C. J. 1988. The seismicity of Kenya. *Journal of African Earth Sciences (and the Middle East),* 7**,** 915-923.

MAHMOOD, S. A., QURESHI, J., AHMAD, S. R., SAMI, J., MASOOD, A. & RAFIQUE, H. M. 2013. Identification of Neotectonics using DEM-based Local Base-level Approach in Pothowar Plateau.

MANSFIELD, C. & CARTWRIGHT, J. 2001. Fault growth by linkage: observations and implications from analogue models. *Journal of Structural Geology,* 23**,** 745-763.

MANZOCCHI, T., WALSH, J. J. & BAILEY, W. R. 2009. Population scaling biases in map samples of power-law fault systems. *Journal of Structural Geology,* 31**,** 1612-1626.

MARIITA, N. O. & KELLER, G. R. 2007. An integrated geophysical study of the northern Kenya rift. *Journal of African Earth Sciences,* 48**,** 80-94.

MARRETT, R. & ALLMENDINGER, R. W. 1991. Estimates of strain due to brittle faulting: sampling of fault populations. *Journal of Structural Geology,* 13**,** 735-738.

MARRETT, R. & ALLMENDINGER, R. W. 1992. Amount of extension on "small" faults: An example from the Viking graben. *Geology,* 20**,** 47-50.

MAURIN, J.-C. & GUIRAUD, R. 1993. Basement control in the development of the early cretaceous West and Central African rift system. *Tectonophysics,* 228**,** 81-95.

MAZZARINI, F., T. ABEBE, F. I., P. MANETTI, A. & PARESCHI, M. T. 1999. Geology of the Debre Zeyt area (Ethiopia) (with a geological map at scale 1:100.000). Acta Vulcanol., 11, 131 – 141.

MCCAFFREY, K. J. W., SLEIGHT, J. M., PUGLIESE, S. & HOLDSWORTH, R. E. 2003b. Fracture formation and evolution in crystalline rocks: Insights from attribute analysis. *Geological Society, London, Special Publications,* 214**,** 109-124.

MCCLAY, K. R., DOOLEY, T., WHITEHOUSE, P. & MILLS, M., 2002 2002. 4-D evolution of rift systems: Insights from scaled physical models. *American Association of Petroleum Geologists,* Bulletin 86, 935–959.

MCCONNELL, R. B. 1972. Geological Development of the Rift System of Eastern Africa. *Geological Society of America Bulletin,* 83**,** 2549-2572.

MEJÍA, A. I. & NIEMANN, J. D. 2008. Identification and characterization of dendritic, parallel, pinnate, rectangular, and trellis networks based on deviations from planform self-similarity. *Journal of Geophysical Research: Earth Surface,* 113**,** n/a-n/a.

MEYER, V., NICOL, A., CHILDS, C., WALSH, J. & WATTERSON, J. 2002. Progressive localisation of strain during the evolution of a normal fault population. *Journal of Structural Geology,* 24**,** 1215-1231.

MICCADEI, P, P. & T, P. 2004. The SW escarpment of Montagna del Morrone (Abruzzi, Centra Italy): geomorphology of a fault-generated mountain front.

MICCADEI, E. & PIACENTINI, T. 2011. *Two Tectonic Geomorphology Studies on the Landscape and Drainage Network of Chain and Piedmont Areas of the Abruzzi Region (Central Apennines, Italy)*.

MOHR, P. 1983. Ethiopian flood basalt province. *Nature,* 303**,** 577-584.

MOHR, P. 1987. Patterns of faulting in the Ethiopian Rift Valley. *Tectonophysics,* 143**,** 169-179.

MOHR, P. 1989. Nature of the crust under Afar: new igneous, not thinned continental. *Tectonophysics,* 167**,** 1-11.

MOLIN, P. & CORTI, G. 2015. Topography, river network and recent fault activity at the margins of the Central Main Ethiopian Rift (East Africa). *Tectonophysics,* 664**,** 67-82.

MORIYA, S., CHILDS, C., MANZOCCHI, T. & WALSH, J. J. 2005. Analysis of the relationships between strain, polarity and population slope for normal fault systems. *Journal of Structural Geology,* 27**,** 1113-1127.

MORLEY, C. 1988. Variable extension in lake Tanganyika. *Tectonics,* 7**,** 785-801.

MORLEY, C. 1999d. AAPG Studies in Geology# 44, Chapter 9: Influence of Preexisting Fabrics on Rift Structure.

MORLEY, C. & NGENOH, D. 1999c. AAPG Studies in Geology# 44, Chapter 1: Introduction to the East African Rift System.

MORLEY, C. K. 1990. Transfer Zones in the East African Rift System and Their Relevance to Hydrocarbon Exploration in Rifts

MORLEY, C. K. 1999 a. How successful are analogue models in addressing the influence of pre-existing fabrics on rift structure? *Journal of Structural Geology,* 21**,** 1267-1274.

MORLEY, C. K. 1999b. Patterns of displacement along large normal faults: implications for basin evolution and fault propagation, based on examples from east Africa. *AAPG bulletin,* 83**,** 613-634.

MORLEY, C. K., WESCOTT, W. A., STONE, D. M., HARPER, R. M., WIGGER, S. T. & KARANJA, F. M. 1992. Tectonic evolution of the northern Kenyan Rift. *Journal of the Geological Society,* 149**,** 333-348.

MORTIMER, E., PATON, D. A., SCHOLZ, C. A., STRECKER, M. R. & BLISNIUK, P. 2007. Orthogonal to oblique rifting: effect of rift basin orientation in the evolution of the North basin, Malawi Rift, East Africa. *Basin Research,* 19**,** 393-407.

MOSLEY, P. N. 1993. Geological evolution of the late Proterozoic "Mozambique Belt" of Kenya. *Tectonophysics,* 221**,** 223-250.

MUIRHEAD, J. D., KATTENHORN, S. A., LEE, H., MANA, S., TURRIN, B. D., FISCHER, T. P., KIANJI, G., DINDI, E. & STAMPS, D. S. 2016. Evolution of upper crustal faulting assisted by magmatic volatile release during early-stage continental rift development in the East African Rift. *Geosphere,* 12**,** 1670-1700.

NEEDHAM, T., YIELDING, G. & FOX, R. 1996. Fault population description and prediction using examples from the offshore U.K. *Journal of Structural Geology,* 18**,** 155-167.

NICOL, A., CHILDS, C., WALSH, J. J., MANZOCCHI, T. & SCHÖPFER, M. P. J. 2016. Interactions and growth of faults in an outcrop-scale system. *Geological Society, London, Special Publications,* 439.

NICOL, A., WALSH, J., VILLAMOR, P., SEEBECK, H. & BERRYMAN, K. 2010. Normal fault interactions, paleoearthquakes and growth in an active rift. *Journal of Structural Geology,* 32**,** 1101-1113.

NICOL, A., WALSH, J., WATTERSON, J. & UNDERHILL, J. 1997. Displacement rates of normal faults. *Nature,* 390**,** 157-159.

NICOL, A., WATTERSON, J., WALSH, J. J. & CHILDS, C. 1996. The shapes, major axis orientations and displacement patterns of fault surfaces. *Journal of Structural Geology,* 18**,** 235-248.

NIXON, C. W., BULL, J. M. & SANDERSON, D. J. 2014. Localized vs distributed deformation associated with the linkage history of an active normal fault, Whakatane Graben, New Zealand. *Journal of Structural Geology,* 69, Part A**,** 266-280.

ODLING, N., GILLESPIE, P., BOURGINE, B., CASTAING, C., CHILES, J., CHRISTENSEN, N., FILLION, E., GENTER, A., OLSEN, C. & THRANE, L. 1999. Variations in fracture system geometry and their implications for fluid flow in fractured hydrocarbon reservoirs. *Petroleum Geoscience,* 5**,** 373-384.

OLSEN, K. H. 1995. continental rifts:evolution, structure, Tectonics. 213-231.

OMENDA, P. A. 2010. THE GEOLOGY AND GEOTHERMAL ACTIVITY OF THE EAST AFRICAN RIFT.

OUILLON, G., CASTAING, C. & SORNETTE, D. 1996. Hierarchical geometry of faulting. *Journal of Geophysical Research: Solid Earth,* 101**,** 5477-5487.

PATON, D. A. 2006. Influence of crustal heterogeneity on normal fault dimensions and evolution: southern South Africa extensional system. *Journal of Structural Geology,* 28**,** 868-886.

PAVONI, N. 1992. RIFTING OF AFRICA AND PATTERN OF MANTLE CONVECTION BENEATH THE AFRICAN PLATE. *Tectonophysics,* 215**,** 35-53.

PEACOCK, D. 2002. Propagation, interaction and linkage in normal fault systems. *Earth-Science Reviews,* 58**,** 121-142.

PEACOCK, D. & SANDERSON, D. 1994. Geometry and development of relay ramps in normal fault systems. *AAPG bulletin,* 78**,** 147-165.

PEACOCK, D. C. P. & SANDERSON, D. J. 1991. Displacements, segment linkage and relay ramps in normal fault zones. *Journal of Structural Geology,* 13**,** 721-733.

PEACOCK, D. C. P. & SANDERSON, D. J. 1996. Effects of propagation rate on displacement variations along faults. *Journal of Structural Geology,* 18**,** 311-320.

PETIT, C. & EBINGER, C. 2000. Flexure and mechanical behavior of cratonic lithosphere: Gravity models of the East African and Baikal rifts. *Journal of Geophysical Research: Solid Earth,* 105**,** 19151-19162.

PHILLIPS, L. F. & SCHUMM, S. A. 1987. Effect of regional slope on drainage networks. *Geology,* 15**,** 813-816.

PICKERING, G., BULL, J. M. & SANDERSON, D. J. 1995. Sampling power-law distributions. *Tectonophysics,* 248**,** 1-20.

PICKERING, G., BULL, J. M. & SANDERSON, D. J. 1996. Scaling of fault displacements and implications for the estimation of sub-seismic strain. *Geological Society, London, Special Publications,* 99**,** 11-26.

POINTING, A. J., MAGUIRE, P. K. H., KHAN, M. A., FRANCIS, D. J., SWAIN, C. J., SHAH, E. R. & GRIFFITHS, D. H. 1985. Seismicity of the northern part of the Kenya Rift Valley. *Journal of Geodynamics,* 3**,** 23-37.

POLIT, A. T., SCHULTZ, R. A. & SOLIVA, R. 2009. Geometry, displacement–length scaling, and extensional strain of normal faults on Mars with inferences on mechanical stratigraphy of the Martian crust. *Journal of Structural Geology,* 31**,** 662-673.

POULIMENOS, G. 2000. Scaling properties of normal fault populations in the western Corinth Graben, Greece: implications for fault growth in large strain settings. *Journal of Structural Geology,* 22**,** 307-322.

PUTZ-PERRIER, M. W. & SANDERSON, D. J. 2008a. The distribution of faults and fractures and their importance in accommodating extensional strain at Kimmeridge Bay, Dorset, UK. *Geological Society, London, Special Publications,* 299**,** 97-111.

PUTZ-PERRIER, M. W. & SANDERSON, D. J. 2008b. Spatial distribution of brittle strain in layered sequences. *Journal of Structural Geology,* 30**,** 50-64.

RIBOLINI, A. & SPAGNOLO, M. 2008. Drainage network geometry versus tectonics in the Argentera Massif (French–Italian Alps). *Geomorphology,* 93**,** 253-266.

ROBERTSON, E. A. M., BIGGS, J., CASHMAN, K. V., FLOYD, M. A. & VYE-BROWN, C. 2015. Influence of regional tectonics and pre-existing structures on the formation of elliptical calderas in the Kenyan Rift. *Geological Society, London, Special Publications,* 420.

RYKOUNOV, L. N., SEDOV, V. V., SAVRINA, L. A. & BOURMIN, V. J. 1972. Study of microearthquakes in the rift zones of East Africa. *Tectonophysics,* 15**,** 123-130.

SCHLISCHE, R. W., YOUNG, S. S., ACKERMANN, R. V. & GUPTA, A. 1996. Geometry and scaling relations of a population of very small rift-related normal faults. *Geology,* 24**,** 683-686.

SCHOENBOHM, L. M., WHIPPLE, K. X., BURCHFIEL, B. C. & CHEN, L. 2004. Geomorphic constraints on surface uplift, exhumation, and plateau growth in the Red River region, Yunnan Province, China. *GSA Bulletin,* 116**,** 895-909.

SCHOLZ, C. H. & CONTRERAS, J. C. 1998. Mechanics of continental rift architecture. *Geology* 26, 967–970.

SCHOLZ, C. H. & COWIE, P. A. 1990. Determination of total strain from faulting using slip measurements. *Nature,* 346**,** 837-839.

SCHOLZ, C. H., DAWERS, N. H., YU, J. Z., ANDERS, M. H. & COWIE, P. A. 1993. Fault growth and fault scaling laws: Preliminary results. *Journal of Geophysical Research: Solid Earth,* 98**,** 21951-21961.

SCHOLZ, C. H. & SHAW, B. E. 1999. Experimental evidence for different strain regimes of crack populations in a clay model. *Geophysical Research Letters,* 26**,** 1081-1084.

SCHULTZ, R. A. & FOSSEN, H. 2002. Displacement–length scaling in three dimensions: the importance of aspect ratio and application to deformation bands. *Journal of Structural Geology,* 24**,** 1389-1411.

SERRA, S. & NELSON, R. A. 1988. Clay modeling of rift asymmetry and associated structures. *Tectonophysics,* 153**,** 307-312.

SHAHZAD, F., MAHMOOD, S. A. & GLOAGUEN, R. Drainage network and seismological analysis of active tectonics in Nanga Parbat Haramosh Massif, Pakistan. Geoscience and Remote Sensing Symposium,2009 IEEE International,IGARSS 2009, 12-17 July 2009 2009. I-9-I-12.

SIMONET, C., PAQUETTE, J. L., PIN, C., LASNIER, B. & FRITSCH, E. 2004. The Dusi (Garba Tula) sapphire deposit, Central Kenya—a unique Pan-African corundum-bearing monzonite. *Journal of African Earth Sciences,* 38**,** 401-410.

SLAMA, T., DEFFONTAINES, B. & TURKI, M. M. 2015. Morphotectonic and Morphodynamic investigations revealed by isobase surfaces analysis and derived differential mapping using GIS, Teboursouk area, northern Tunisia. *Earth Science Informatics,* 8**,** 759-773.

SMITH, M. & MOSLEY, P. 1993. Crustal heterogeneity and basement influence on the development of the Kenya Rift, East Africa. *Tectonics,* 12**,** 591-606.

SOLIVA, R. & BENEDICTO, A. 2004. A linkage criterion for segmented normal faults. *Journal of Structural Geology,* 26**,** 2251-2267.

SOLIVA, R. & BENEDICTO, A. 2005. Geometry, scaling relations and spacing of vertically restricted normal faults. *Journal of Structural Geology,* 27**,** 317-325.

SOLIVA, R., BENEDICTO, A. & MAERTEN, L. 2006. Spacing and linkage of confined normal faults: Importance of mechanical thickness. *Journal of Geophysical Research: Solid Earth,* 111**,** n/a-n/a.

SOLIVA, R. & SCHULTZ, R. A. 2008. Distributed and localized faulting in extensional settings: Insight from the North Ethiopian Rift–Afar transition area. *Tectonics,* 27**,** n/a-n/a.

SORNETTE, A., DAVY, P. & SORNETTE, D. 1993. Fault growth in brittle-ductile experiments and the mechanics of continental collisions. *Journal of Geophysical Research: Solid Earth,* 98**,** 12111-12139.

STEWART, I. S. & HANCOCK, P. L. 1990. What is a fault scarp. *Episodes,* 13**,** 256-263.

STOYAN, D. & GLOAGUEN, R. 2011. Nucleation and growth of geological faults. *Nonlin. Processes Geophys.,* 18**,** 529-536.

STRAHLER, A. N. 1952. Hypsometric (area-altitude) analysis of erosional topography. *Geological Society of America Bulletin,* 63**,** 1117-1142.

STRECKER, M. & BLISNIUK, P. 1992. Integration of East African Paleostress and Present-Day Stress Data'Implications for Continental Stress Field Dynamics. *Journal of Geophysical Research,* 97**,** 11,851-11,865.

STRECKER, M. & BOSWORTH, W. 1991. Quaternary stress-field change in the Gregory Rift, Kenya. *Eos,* 72.

STRECKER, M. R., BLISNIUK, P. M. & EISBACHER, G. H. 1990. Rotation of extension direction in the central Kenya Rift. *Geology,* 18**,** 299-302.

STUART, G., BASTOW, I. & EBINGER, C. 2006. Crustal structure of the northern Main Ethiopian Rift from receiver function studies. *Geological Society, London, Special Publications,* 259**,** 253-267.

TEYSSIER, C. & TIKOFF, B. 1999. Fabric stability in oblique convergence and divergence. *Journal of Structural Geology,* 21**,** 969-974.

TORABI, A. & BERG, S. S. 2011. Scaling of fault attributes: A review. *Marine and Petroleum Geology,* 28**,** 1444-1460.

TRUDGILL, B. & CARTWRIGHT, J. 1994. Relay-ramp forms and normal-fault linkages, Canyonlands National Park, Utah. *Geological Society of America Bulletin,* 106**,** 1143-1157.

VALLIANATOS, F. & SAMMONDS, P. 2011. A non-extensive statistics of the fault-population at the Valles Marineris extensional province, Mars. *Tectonophysics,* 509**,** 50-54.

VERSFELT, J. & ROSENDAHL, B. R. 1989. Relationships between pre-rift structure and rift architecture in Lakes Tanganyika and Malawi, East Africa. *Nature,* 337**,** 354-357.

VÉTEL, W., LE GALL, B. & WALSH, J. J. 2005. Geometry and growth of an inner rift fault pattern: the Kino Sogo Fault Belt, Turkana Rift (North Kenya). *Journal of Structural Geology,* 27**,** 2204-2222.

VIMAL, S., D. NAGESH KUMAR, AND INDU JAYA INTERNATIONAL PROCEEDINGS OF CHEMICAL, BIOLOGICAL & ENVIRONMENTAL ENGINEERING 33 (2012). 2012. Extraction of Drainage Pattern from ASTER and SRTM Data for a River Basin using GIS Tools.

WALSH, J., NICOL, A. & CHILDS, C. A New Model for the Growth of Faults. 64th EAGE Conference & Exhibition, 2002b.

WALSH, J., WATTERSON, J. & YIELDING, G. 1991. The importance of small-scale faulting in regional extension. *Nature,* 351**,** 391-393.

WALSH, J. J., BAILEY, W. R., CHILDS, C., NICOL, A. & BONSON, C. G. 2003a. Formation of segmented normal faults: a 3-D perspective. *Journal of Structural Geology,* 25**,** 1251-1262.

WALSH, J. J., CHILDS, C., IMBER, J., MANZOCCHI, T., WATTERSON, J. & NELL, P. A. R. 2003b. Strain localisation and population changes during fault system growth within the Inner Moray Firth, Northern North Sea. *Journal of Structural Geology,* 25**,** 307-315.

WALSH, J. J., CHILDS, C., MEYER, V., MANZOCCHI, T., IMBER, J., NICOL, A., TUCKWELL, G., BAILEY, W. R., BONSON, C. G., WATTERSON, J., NELL, P. A. & STRAND, J. 2001. Geometric controls on the evolution of normal fault systems. *Geological Society, London, Special Publications,* 186**,** 157-170.

WALSH, J. J., NICOL, A. & CHILDS, C. 2002a. An alternative model for the growth of faults. *Journal of Structural Geology,* 24**,** 1669-1675.

WALSH, J. J. & WATTERSON, J. 1988. Analysis of the relationship between displacements and dimensions of faults. *Journal of Structural Geology,* 10**,** 239-247.

WALSH, J. J., WATTERSON, J., CHILDS, C. & NICOL, A. 1996. Ductile strain effects in the analysis of seismic interpretations of normal fault systems. *Geological Society, London, Special Publications,* 99**,** 27-40.

WATTERSON, J. 1986. Fault dimensions, displacements and growth. *pure and applied geophysics,* 124**,** 365-373.

WATTERSON, J., WALSH, J. J., GILLESPIE, P. A. & EASTON, S. 1996. Scaling systematics of fault sizes on a large-scale range fault map. *Journal of Structural Geology,* 18**,** 199-214.

WHIPPLE, K. X. 2004. BEDROCK RIVERS AND THE GEOMORPHOLOGY OF ACTIVE OROGENS. *Annual Review of Earth and Planetary Sciences,* 32**,** 151-185.

WILKINS, S. J. & GROSS, M. R. 2002. Normal fault growth in layered rocks at Split Mountain, Utah: influence of mechanical stratigraphy on dip linkage, fault restriction and fault scaling. *Journal of Structural Geology,* 24**,** 1413-1429.

WITHJACK, M. O. & JAMISON, W. R. 1986. Deformation produced by oblique rifting. *Tectonophysics,* 126**,** 99-124.

WOBUS, C. W., HODGES, K. V. & WHIPPLE, K. X. 2003. Has focused denudation sustained active thrusting at the Himalayan topographic front? *Geology,* 31**,** 861-864.

WOLDE, B. 1989. Cenozoic volcanism and riftdevelopment in Ethiopia. *Journal of African Earth Sciences (and the Middle East),* 8**,** 99-105.

WOLDEGABRIAL, G., ARONSON, J. L. & WALTER, R. C. 1990. Geology, geochronology, and rift basin development in the central sector of the Main Ethiopia Rift. *Geological Society of America Bulletin,* 102**,** 439-458.

WOLFENDEN, E., EBINGER, C., YIRGU, G., DEINO, A. & AYALEW, D. 2004. Evolution of the northern Main Ethiopian rift: birth of a triple junction. *Earth and Planetary Science Letters,* 224**,** 213-228.

WU, H. & POLLARD, D. D. 1995. An experimental study of the relationship between joint spacing and layer thickness. *Journal of Structural Geology,* 17**,** 887-905.

YALE, D. P. 2003. Fault and stress magnitude controls on variations in the orientation of in situ stress. *Geological Society, London, Special Publications,* 209**,** 55-64.

YIELDING, G., NEEDHAM, T. & JONES, H. 1996. Sampling of fault populations using sub-surface data: a review. *Journal of Structural Geology,* 18**,** 135-146.

YIN, Z. M. & RANALLI, G. 1992. Critical stress difference, fault orientation and slip direction in anisotropic rocks under non-Andersonian stress systems. *Journal of Structural Geology,* 14**,** 237-244.

YOUNG, P. A. V. 1989. *A local earthquake study near lake bogoria in the kenya rift.* U017947 Ph.D., University of Leicester (United Kingdom).

ZHANG, L. & EINSTEIN, H. H. 2000. Estimating the intensity of rock discontinuities. *International Journal of Rock Mechanics and Mining Sciences,* 37**,** 819-837.

ZIEGLER, P. A. 1993. Plate-moving mechanisms: their relative importance: William Smith Lecture 1992. *Journal of the Geological Society,* 150**,** 927-940.

ZIEGLER, P. A. & CLOETINGH, S. 2004. Dynamic processes controlling evolution of rifted basins. *Earth-Science Reviews,* 64**,** 1-50.

Appendix A

Fault trace length and throw measurements from the three study areas

Table A.1 shows a sample of fault length and corresponding fault throw data picked using 30m resolution DEM for the central Kenya rift.

Zone	Fault No.	Length	Throw	D\L ratio	Log length	log throw	Angle	Strike
2	1	12662.81	213.71	0.02	4.103	2.330	178.16	178
2	2	11366.93	82.92	0.01	4.056	1.919	180.69	1
2	3	5825.85	266.46	0.05	3.765	2.426	167.38	167
2	4	10132.47	142.44	0.01	4.006	2.154	187.20	7
2	5	9495.94	148.67	0.02	3.978	2.172	183.37	3
2	6	9382.31	147.06	0.02	3.972	2.167	196.93	17
2	7	5837.50	142.27	0.02	3.766	2.153	187.55	8
2	8	18756.56	249.57	0.01	4.273	2.397	3.19	3
2	9	6466.10	94.65	0.01	3.811	1.976	187.10	7
2	10	8152.97	79.79	0.01	3.911	1.902	2.30	2
2	11	6340.04	124.94	0.02	3.802	2.097	171.24	171
2	12	5757.21	50.66	0.01	3.760	1.705	177.70	178
2	14	2562.48	51.01	0.02	3.409	1.708	188.60	9
2	15	9755.51	182.61	0.02	3.989	2.262	178.16	178
2	16	8331.24	177.86	0.02	3.921	2.250	180.66	1
2	17	14673.32	118.38	0.01	4.167	2.073	7.14	7
2	18	4504.06	63.38	0.01	3.654	1.802	6.06	6
2	19	7640.45	225.83	0.03	3.883	2.354	358.95	179
2	20	12499.44	100.29	0.01	4.097	2.001	357.51	178
2	21	9445.07	95.60	0.01	3.975	1.980	1.70	2
2	22	7061.69	27.37	0.00	3.849	1.437	354.66	175
2	23	10160.99	98.36	0.01	4.007	1.993	354.03	174
2	24	5067.44	81.75	0.02	3.705	1.912	355.69	176
2	25	1557.81	54.40	0.03	3.193	1.736	16.32	16
2	26	4607.99	108.31	0.02	3.664	2.035	356.12	176
2	27	5171.08	16.72	0.00	3.714	1.223	356.11	176
2	28	4300.06	60.76	0.01	3.633	1.784	358.01	178
2	29	4712.27	47.46	0.01	3.673	1.676	347.26	167
2	30	1561.05	30.19	0.02	3.193	1.480	353.63	174

Table A.1 Continued from previous page

Zone	Fault No.	Length	Throw	D\L ratio	Log length	log throw	Angle	Strike
2	31	1510.66	36.68	0.02	3.179	1.564	348.22	168
2	32	13707.27	97.66	0.01	4.137	1.990	358.07	178
2	33	1962.42	67.05	0.03	3.293	1.826	353.05	173
2	34	1962.42	67.05	0.03	3.293	1.826	336.10	156
2	35	4749.57	101.59	0.02	3.677	2.007	354.83	175
2	36	6852.44	79.13	0.01	3.836	1.898	2.74	3
2	37	1639.21	60.44	0.04	3.215	1.781	4.20	4
2	38	1117.43	49.45	0.04	3.048	1.694	14.18	14
2	39	4461.71	79.91	0.02	3.650	1.903	5.37	5
2	40	2473.95	58.50	0.02	3.393	1.767	355.91	176
2	41	5917.62	62.46	0.01	3.772	1.796	358.20	178
2	42	6300.62	93.48	0.01	3.799	1.971	357.08	177
2	43	4879.48	132.01	0.03	3.688	2.121	7.16	7
2	44	3389.73	128.75	0.04	3.530	2.110	0.67	1
2	45	3730.36	117.57	0.03	3.572	2.070	341.38	161
2	46	7071.60	74.17	0.01	3.850	1.870	354.66	175
2	47	2063.07	125.74	0.06	3.315	2.099	353.14	173
2	48	2216.10	51.05	0.02	3.346	1.708	339.65	160
2	49	2078.09	53.13	0.03	3.318	1.725	356.68	177
2	50	7201.01	168.35	0.02	3.857	2.226	356.48	176
2	51	3915.99	54.31	0.01	3.593	1.735	347.93	168
2	52	3915.99	54.31	0.01	3.593	1.735	34.03	34
2	53	5094.24	48.32	0.01	3.707	1.684	359.24	179
2	54	2709.36	42.57	0.02	3.433	1.629	0.07	0
2	55	6317.03	40.74	0.01	3.801	1.610	349.34	169
2	56	4375.07	28.49	0.01	3.641	1.455	352.95	173
2	57	2227.97	33.92	0.02	3.348	1.530	350.05	170
2	58	5571.08	33.55	0.01	3.746	1.526	353.01	173
2	59	16728.99	148.35	0.01	4.223	2.171	194.14	14
2	60	4729.83	87.31	0.02	3.675	1.941	184.47	4
2	61	10535.34	122.09	0.01	4.023	2.087	190.16	10
2	62	2895.45	44.46	0.02	3.462	1.648	180.37	0
2	63	24750.46	208.74	0.01	4.394	2.320	194.19	14
2	64	10709.41	108.25	0.01	4.030	2.034	194.79	15
2	65	5875.71	113.84	0.02	3.769	2.056	199.32	19
2	66	4459.90	72.31	0.02	3.649	1.859	187.37	7

Table A.1 Continued from previous page

Zone	Fault No.	Length	Throw	D\L ratio	Log length	log throw	Angle	Strike
1	257	23588.50	301.49	0.01	4.373	2.479	16.48	16
1	258	1956.84	69.57	0.04	3.292	1.842	3.15	3
1	259	6418.60	146.62	0.02	3.807	2.166	12.63	13
1	260	1005.00	74.52	0.07	3.002	1.872	6.43	6
1	261	6205.40	112.66	0.02	3.793	2.052	26.47	26
1	262	6109.54	93.16	0.02	3.786	1.969	0.57	1
1	263	3399.76	65.05	0.02	3.531	1.813	11.23	11
1	264	4240.09	41.18	0.01	3.627	1.615	20.00	20
1	265	4793.29	88.40	0.02	3.681	1.946	13.34	13
1	266	1105.52	64.49	0.06	3.044	1.809	34.54	35
1	267	2372.84	51.54	0.02	3.375	1.712	20.85	21
1	268	7951.17	88.09	0.01	3.900	1.945	16.04	16
1	269	6945.81	173.92	0.03	3.842	2.240	12.04	12
1	270	4833.78	136.27	0.03	3.684	2.134	20.25	20
1	271	4833.78	136.27	0.03	3.684	2.134	30.65	31
1	272	6448.06	47.91	0.01	3.809	1.680	11.28	11
1	273	2733.13	56.31	0.02	3.437	1.751	12.67	13
1	274	4369.80	76.26	0.02	3.640	1.882	15.37	15
1	275	13635.61	133.10	0.01	4.135	2.124	11.62	12
1	276	3581.15	99.36	0.03	3.554	1.997	14.79	15
1	277	2268.64	43.62	0.02	3.356	1.640	13.78	14
1	278	4033.84	90.32	0.02	3.606	1.956	18.35	18
1	279	11993.56	121.56	0.01	4.079	2.085	11.52	12
1	280	3481.96	52.01	0.01	3.542	1.716	21.30	21
1	281	2711.44	26.75	0.01	3.433	1.427	14.72	15
1	282	7596.52	66.22	0.01	3.881	1.821	189.88	10
1	283	11221.37	98.52	0.01	4.050	1.994	185.24	5
1	284	1870.71	35.99	0.02	3.272	1.556	180.68	1
1	285	4323.93	47.83	0.01	3.636	1.680	180.52	1
1	286	2067.63	111.67	0.05	3.315	2.048	172.75	173
1	287	3130.81	29.53	0.01	3.496	1.470	189.80	10
1	288	2336.20	61.02	0.03	3.369	1.785	182.47	2
1	289	3364.18	49.07	0.01	3.527	1.691	191.80	12
1	290	2580.45	52.87	0.02	3.412	1.723	198.00	18
1	291	3083.67	57.80	0.02	3.489	1.762	197.38	17
1	292	1315.40	45.68	0.03	3.119	1.660	194.88	15
1	293	3136.46	62.27	0.02	3.496	1.794	182.50	3
1	294	4017.81	96.34	0.02	3.604	1.984	196.77	17
1	295	2261.04	51.46	0.02	3.354	1.711	199.93	20
1	296	2200.56	34.13	0.02	3.343	1.533	190.18	10
1	297	990.45	26.01	0.03	2.996	1.415	173.30	173
1	298	2422.18	34.64	0.01	3.384	1.540	199.14	19
1	299	1465.61	34.99	0.02	3.166	1.544	198.12	18
1	300	1666.87	33.28	0.02	3.222	1.522	204.16	24
1	301	1594.18	47.50	0.03	3.203	1.677	193.44	13
1	302	65840.30	1560.84	0.02	4.818	3.193	179.49	179
1	303	28127.15	1335.78	0.05	4.449	3.126	182.22	2
1	304	21856.28	636.76	0.03	4.340	2.804	191.46	11
1	305	3590.36	302.87	0.08	3.555	2.481	150.20	150

Table A.1 Continued from previous page

Zone	Fault No.	Length	Throw	D\L ratio	Log length	log throw	Angle	Strike
1	306	34245.85	363.14	0.01	4.535	2.560	197.50	18
1	319	10269.587	61.05	0.01	4.012	1.786	9.54	10
1	402	2824.507	148.5	0.05	3.451	2.172	10.14	10
1	404	2359.824	398.52	0.17	3.373	2.600	6.64	7
1	405	1853.595	310.27	0.17	3.268	2.492	352.88	173
1	406	736.575	135.84	0.18	2.867	2.133	2.06	2
1	407	8565.496	156.48	0.02	3.933	2.194	0.70	1
1	409	4024.94	106.9	0.03	3.605	2.029	172.93	173
1	410	4326.732	244.98	0.06	3.636	2.389	189.45	9
1	411	2238.251	60.45	0.03	3.350	1.781	355.94	176
1	412	1204.531	71.32	0.06	3.081	1.853	358.86	179
1	413	1258.688	70.45	0.06	3.100	1.848	349.37	169
1	414	2221.307	115.21	0.05	3.347	2.061	359.54	180
1	415	816.141	42.04	0.05	2.912	1.624	356.44	176
1	416	2508.414	125.79	0.05	3.399	2.100	348.76	169
1	417	1522.549	53.49	0.04	3.183	1.728	4.96	5
1	418	1342.081	37.48	0.03	3.128	1.574	337.73	158
1	506	4174.110	244.000	0.058	3.621	2.387	345.69	166
1	507	1414.000	83.270	0.059	3.150	1.920	20.77	21
1	508	1300.000	137.170	0.106	3.114	2.137	178.99	179
1	509	2470.000	186.980	0.076	3.393	2.272	158.77	159
1	512	5035.000	276.710	0.055	3.702	2.442	23.85	24
1	513	1943.230	531.730	0.274	3.289	2.726	349.60	170
3	123	16492.68	125.41	0.01	4.217	2.098	334.55	155
3	124	3809.06	97.52	0.03	3.581	1.989	344.65	165
3	125	6698.97	72.77	0.01	3.826	1.862	339.82	160
3	126	1918.46	28.06	0.01	3.283	1.448	348.67	169
3	127	10324.82	261.11	0.03	4.014	2.417	352.08	172
3	128	5621.50	137.80	0.02	3.750	2.139	350.28	170
3	129	17647.69	192.03	0.01	4.247	2.283	343.75	164
3	130	6162.67	137.38	0.02	3.790	2.138	348.02	168
3	131	4685.46	77.52	0.02	3.671	1.889	352.47	172
3	132	16780.52	114.75	0.01	4.225	2.060	345.27	165
3	133	11033.09	160.36	0.01	4.043	2.205	338.07	158
3	134	9558.44	236.37	0.02	3.980	2.374	310.49	130
3	161	9689.92	331.84	0.03	3.986	2.521	0.64	1
3	162	2579.72	228.93	0.09	3.412	2.360	357.69	178
3	163	1178.64	97.82	0.08	3.071	1.990	354.42	174
3	164	3903.44	105.50	0.03	3.591	2.023	359.78	180
3	165	2370.43	97.10	0.04	3.375	1.987	1.83	2
3	166	5405.67	51.22	0.01	3.733	1.709	343.93	164
3	167	1750.88	52.69	0.03	3.243	1.722	0.86	1
3	168	2227.25	59.37	0.03	3.348	1.774	349.11	169
3	169	1438.14	52.83	0.04	3.158	1.723	352.81	173
3	170	2426.07	47.83	0.02	3.385	1.680	354.22	174

Table A.1 Continued from previous page

Zone	Fault No.	Length	Throw	D\L ratio	Log length	log throw	Angle	Strike
3	171	5344.83	83.23	0.02	3.728	1.920	7.58	8
3	172	3590.10	65.77	0.02	3.555	1.818	357.67	178
3	173	1551.63	152.11	0.10	3.191	2.182	11.24	11
3	174	2972.36	69.69	0.02	3.473	1.843	359.94	180
3	175	2605.37	86.05	0.03	3.416	1.935	2.88	3
3	176	1298.40	53.19	0.04	3.113	1.726	9.55	10
3	177	2584.90	67.56	0.03	3.412	1.830	3.27	3
3	178	6450.05	223.86	0.03	3.810	2.350	345.64	166
3	179	3838.44	141.18	0.04	3.584	2.150	340.64	161
3	180	805.63	69.81	0.09	2.906	1.844	351.00	171
3	181	1004.49	70.33	0.07	3.002	1.847	347.17	167
3	182	3029.27	101.16	0.03	3.481	2.005	353.35	173
3	183	3608.85	139.87	0.04	3.557	2.146	340.34	160
3	184	2154.97	124.40	0.06	3.333	2.095	349.29	169
3	185	2154.97	124.40	0.06	3.333	2.095	281.93	102
3	186	1400.76	52.44	0.04	3.146	1.720	339.56	160
3	187	3979.80	81.16	0.02	3.600	1.909	345.36	165
3	188	1046.00	52.48	0.05	3.020	1.720	15.17	15
3	189	832.96	63.37	0.08	2.921	1.802	354.50	175
3	190	3757.83	142.77	0.04	3.575	2.155	341.58	162
3	191	3757.83	142.77	0.04	3.575	2.155	6.03	6
3	192	1843.90	71.61	0.04	3.266	1.855	331.31	151
3	193	4402.62	117.17	0.03	3.644	2.069	181.92	2
3	194	760.87	89.15	0.12	2.881	1.950	162.81	163
3	195	4055.54	216.94	0.05	3.608	2.336	164.57	165
3	196	7682.32	236.01	0.03	3.885	2.373	173.96	174
3	197	3167.27	127.03	0.04	3.501	2.104	165.23	165
3	198	2733.93	97.82	0.04	3.437	1.990	168.99	169
3	199	1767.03	58.22	0.03	3.247	1.765	171.70	172
3	209	15343.73	263.24	0.02	4.186	2.420	149.65	150
3	210	37484.67	471.20	0.01	4.574	2.673	166.96	167
3	211	18064.62	402.83	0.02	4.257	2.605	173.04	173
3	212	6808.84	335.91	0.05	3.833	2.526	161.51	162
3	213	10369.71	446.03	0.04	4.016	2.649	172.87	173
3	214	22614.24	450.00	0.02	4.354	2.653	170.20	170
3	215	10082.81	296.25	0.03	4.004	2.472	177.88	178
3	216	40638.75	429.07	0.01	4.609	2.633	138.31	138
3	217	13687.72	209.55	0.02	4.136	2.321	185.67	6
3	218	2991.88	64.28	0.02	3.476	1.808	158.29	158
3	219	2991.88	64.28	0.02	3.476	1.808	206.02	26
3	220	2991.88	64.28	0.02	3.476	1.808	175.36	175
3	221	5806.49	128.56	0.02	3.764	2.109	164.84	165
3	222	2480.01	70.22	0.03	3.394	1.846	173.22	173
3	223	6391.54	87.94	0.01	3.806	1.944	165.20	165
3	224	12998.24	144.75	0.01	4.114	2.161	342.55	163
3	225	3753.09	96.91	0.03	3.574	1.986	347.92	168
3	226	39216.93	376.81	0.01	4.593	2.576	340.54	161
3	227	17593.04	121.22	0.01	4.245	2.084	338.82	159
3	228	12174.09	111.13	0.01	4.085	2.046	335.80	156

Table A.2 shows a sample of fault length and corresponding fault throw data picked using 30m resolution DEM for the central main Ethiopian rift (CMER).

Fault No.	Length	Throw	D\L ratio	Log length	log throw	Angle	Strike
500	3989	91	0.02	3.60	1.96	36.38	36
501	4737	126	0.03	3.68	2.10	32.60	33
502	3793	155	0.04	3.58	2.19	17.99	18
503	7572	114	0.02	3.88	2.06	26.49	26
504	1641	93	0.06	3.22	1.97	26.97	27
505	4207	83	0.02	3.62	1.92	38.91	39
506	755	38	0.05	2.88	1.58	29.52	30
507	556	34	0.06	2.75	1.54	40.68	41
508	2688	51	0.02	3.43	1.71	17.82	18
509	1124	31	0.03	3.05	1.50	234.31	54
510	6953	131	0.02	3.84	2.12	34.16	34
511	5284	77	0.01	3.72	1.88	14.50	14
512	3294	55	0.02	3.52	1.74	26.68	27
513	8770	237	0.03	3.94	2.37	36.60	37
514	1842	51	0.03	3.27	1.71	48.54	49
515	1729	107	0.06	3.24	2.03	24.39	24
516	1939	56	0.03	3.29	1.75	17.21	17
517	2344	62	0.03	3.37	1.79	58.93	59
518	3994	31	0.01	3.60	1.50	63.93	64
519	3958	59	0.01	3.60	1.77	43.82	44
520	1852	49	0.03	3.27	1.69	51.77	52
521	3895	31	0.01	3.59	1.49	37.10	37
522	8552	85	0.01	3.93	1.93	36.40	36
523	1601	27	0.02	3.20	1.44	35.14	35
524	1984	49	0.02	3.30	1.69	32.43	32
525	858	54	0.06	2.93	1.73	38.05	38
526	2946	39	0.01	3.47	1.59	37.14	37
527	19434	343	0.02	4.29	2.54	35.36	35
528	13452	163	0.01	4.13	2.21	32.39	32
529	1721	94	0.05	3.24	1.97	52.03	52
530	2393	146	0.06	3.38	2.16	60.65	61
531	7703	204	0.03	3.89	2.31	28.04	28
532	3083	41	0.01	3.49	1.61	32.65	33
533	5032	39	0.01	3.70	1.60	39.89	40
534	2920	43	0.01	3.47	1.64	36.35	36
535	1235	16	0.01	3.09	1.20	42.47	42
536	12552	71	0.01	4.10	1.85	37.47	37
537	4263	98	0.02	3.63	1.99	32.78	33
538	5823	47	0.01	3.77	1.67	14.54	15
539	2400	49	0.02	3.38	1.69	28.12	28
540	2776	64	0.02	3.44	1.81	200.68	21
541	2601	43	0.02	3.42	1.63	195.34	15
542	21641	174	0.01	4.34	2.24	208.87	29

Table A.2 Continued from previous page

Fault No.	Length	Throw	D\L ratio	Log length	log throw	Angle	Strike
543	2265	43	0.02	3.36	1.63	209.50	30
544	4927	60	0.01	3.69	1.78	222.19	42
545	3079	41	0.01	3.49	1.62	219.03	39
546	1566	30	0.02	3.19	1.48	222.29	42
547	1082	66	0.06	3.03	1.82	212.05	32
548	2036	48	0.02	3.31	1.68	212.78	33
549	5324	63	0.01	3.73	1.80	213.90	34
550	6626	71	0.01	3.82	1.85	207.42	27
551	737	28	0.04	2.87	1.45	212.45	32
552	1818	42	0.02	3.26	1.62	208.92	29
553	2627	33	0.01	3.42	1.52	199.24	19
554	1974	22	0.01	3.30	1.34	209.59	30
555	4150	43	0.01	3.62	1.63	208.39	28
556	1844	77	0.04	3.27	1.89	210.02	30
557	929	31	0.03	2.97	1.49	216.53	37
558	2297	90	0.04	3.36	1.95	208.87	29
559	2880	60	0.02	3.46	1.78	205.71	26
560	1863	34	0.02	3.27	1.53	223.22	43
561	11872	115	0.01	4.07	2.06	211.04	31
562	5267	86	0.02	3.72	1.93	214.41	34
563	6158	51	0.01	3.79	1.71	215.52	36
564	3256	61	0.02	3.51	1.79	216.26	36
565	3627	77	0.02	3.56	1.89	215.20	35
566	3141	45	0.01	3.50	1.65	197.01	17
567	3355	25	0.01	3.53	1.39	223.23	43
568	2855	65	0.02	3.46	1.81	196.75	17
569	919	81	0.09	2.96	1.91	195.07	15
570	3795	121	0.03	3.58	2.08	210.44	30
571	6630	184	0.03	3.82	2.26	185.02	5
572	1320	48	0.04	3.12	1.68	184.23	4
573	3322	70	0.02	3.52	1.85	179.86	180
574	1954	51	0.03	3.29	1.71	222.12	42
575	10602	160	0.02	4.03	2.20	206.01	26
576	1456	32	0.02	3.16	1.50	198.33	18
577	4519	121	0.03	3.66	2.08	209.01	29
578	3448	125	0.04	3.54	2.10	207.98	28
579	5142	123	0.02	3.71	2.09	204.74	25
580	2547	68	0.03	3.41	1.83	216.25	36
581	1764	51	0.03	3.25	1.71	208.29	28
582	1051	50	0.05	3.02	1.70	184.24	4
583	2246	27	0.01	3.35	1.43	230.04	50
584	4637	56	0.01	3.67	1.75	204.50	24
585	3186	161	0.05	3.50	2.21	184.72	5
586	827	66	0.08	2.92	1.82	206.66	27
587	2630	39	0.01	3.42	1.59	219.25	39
588	2100	33	0.02	3.32	1.51	220.45	40
589	5499	64	0.01	3.74	1.81	230.77	51
590	8614	54	0.01	3.94	1.73	209.46	29

Table A.2 Continued from previous page

Fault No.	Length	Throw	D\L ratio	Log length	log throw	Angle	Strike
591	968	22	0.02	2.99	1.33	214.37	34
592	4307	45	0.01	3.63	1.65	217.02	37
593	6734	108	0.02	3.83	2.03	220.83	41
594	2057	33	0.02	3.31	1.51	227.57	48
595	3051	45	0.01	3.48	1.66	204.40	24
596	8734	85	0.01	3.94	1.93	206.35	26
597	4642	157	0.03	3.67	2.19	19.72	20
598	2910	86	0.03	3.46	1.93	350.15	170
599	1700	123	0.07	3.23	2.09	8.52	9
600	1627	81	0.05	3.21	1.91	8.06	8
601	2291	77	0.03	3.36	1.89	37.43	37
602	2558	47	0.02	3.41	1.68	29.44	29
603	12534	468	0.04	4.10	2.67	25.90	26
604	4353	305	0.07	3.64	2.48	34.25	34
605	2510	214	0.09	3.40	2.33	15.94	16
606	2890	151	0.05	3.46	2.18	21.82	22
607	1194	71	0.06	3.08	1.85	351.01	171
608	3549	96	0.03	3.55	1.98	359.13	179
609	5095	189	0.04	3.71	2.28	21.24	21
610	4428	106	0.02	3.65	2.03	3.77	4
611	5557	126	0.02	3.74	2.10	20.57	21
612	2324	122	0.05	3.37	2.09	27.51	28
613	1110	93	0.08	3.05	1.97	44.21	44
614	539	43	0.08	2.73	1.63	23.22	23
615	1367	48	0.03	3.14	1.68	18.07	18
616	6971	76	0.01	3.84	1.88	26.48	26
617	5780	81	0.01	3.76	1.91	27.78	28
618	4329	210	0.05	3.64	2.32	35.83	36
619	4910	143	0.03	3.69	2.15	24.45	24
620	10471	208	0.02	4.02	2.32	16.33	16
621	10360	322	0.03	4.02	2.51	8.37	8
622	1874	51	0.03	3.27	1.71	203.45	23
623	2650	102	0.04	3.42	2.01	26.72	27
624	1366	84	0.06	3.14	1.93	9.53	10
625	1312	65	0.05	3.12	1.81	359.50	179
626	1860	120	0.06	3.27	2.08	17.15	17
627	1399	82	0.06	3.15	1.91	29.85	30

Table A.2 Continued from previous page

Fault No.	Length	Throw	D\L ratio	Log length	log throw	Angle	Strike
628	4003	34	0.01	3.60	1.53	22.39	22
629	5440	41	0.01	3.74	1.61	24.63	25
630	2972	62	0.02	3.47	1.79	188.20	8
631	3194	51	0.02	3.50	1.71	185.00	5
632	8634	95	0.01	3.94	1.98	199.84	20
633	4783	44	0.01	3.68	1.64	196.91	17
634	14616	368	0.03	4.16	2.57	209.15	29
635	3180	52	0.02	3.50	1.71	189.98	10
636	920	41	0.04	2.96	1.61	206.00	26
637	5191	88	0.02	3.72	1.95	17.02	17
638	4732	264	0.06	3.68	2.42	203.90	24
639	3044	139	0.05	3.48	2.14	213.30	33
640	2526	88	0.03	3.40	1.94	187.73	8
641	2351	45	0.02	3.37	1.66	195.29	15
642	2481	64	0.03	3.39	1.81	189.53	10
643	10687	150	0.01	4.03	2.18	10.37	10
644	4007	133	0.03	3.60	2.12	17.12	17
645	6021	78	0.01	3.78	1.89	9.05	9
646	3690	71	0.02	3.57	1.85	8.09	8
647	6608	51	0.01	3.82	1.71	10.73	11
648	5833	68	0.01	3.77	1.83	20.05	20
649	2955	49	0.02	3.47	1.69	17.88	18
650	3573	33	0.01	3.55	1.51	14.25	14
651	3474	36	0.01	3.54	1.55	22.91	23
652	4200	37	0.01	3.62	1.57	30.76	31
653	8305	159	0.02	3.92	2.20	209.20	29
654	2063	144	0.07	3.31	2.16	197.73	18
655	5590	189	0.03	3.75	2.28	202.21	22
656	3933	193	0.05	3.59	2.29	210.27	30
657	2209	122	0.06	3.34	2.08	221.17	41
658	10345	470	0.05	4.01	2.67	205.93	26
659	7852	465	0.06	3.89	2.67	219.77	40
660	8583	183	0.02	3.93	2.26	37.65	38
661	6686	208	0.03	3.83	2.32	40.73	41
662	12113	155	0.01	4.08	2.19	39.13	39
663	5654	167	0.03	3.75	2.22	43.46	43
664	2450	62	0.03	3.39	1.79	37.73	38
665	2293	102	0.04	3.36	2.01	29.03	29
666	2189	59	0.03	3.34	1.77	21.31	21
667	4057	69	0.02	3.61	1.84	19.02	19
668	4857	209	0.04	3.69	2.32	200.67	21
669	8580	172	0.02	3.93	2.23	195.05	15
670	3222	146	0.05	3.51	2.16	194.99	15
671	18068	229	0.01	4.26	2.36	206.40	26
672	12989	142	0.01	4.11	2.15	220.40	40
673	1984	86	0.04	3.30	1.93	240.55	61
674	10054	58	0.01	4.00	1.76	223.06	43
675	3744	44	0.01	3.57	1.64	218.60	39

Table A.2 Continued from previous page

Fault No.	Length	Throw	D\L ratio	Log length	log throw	Angle	Strike
676	4909	178	0.04	3.69	2.25	212.76	33
677	6119	146	0.02	3.79	2.17	216.90	37
678	11230	181	0.02	4.05	2.26	195.44	15
679	1019	76	0.08	3.01	1.88	211.57	32
680	5487	81	0.01	3.74	1.91	200.58	21
681	3621	101	0.03	3.56	2.01	24.76	25
682	7468	111	0.01	3.87	2.05	28.90	29
683	2473	62	0.03	3.39	1.79	33.68	34
684	5880	130	0.02	3.77	2.11	24.93	25
685	2751	71	0.03	3.44	1.85	37.14	37
686	1312	78	0.06	3.12	1.89	13.61	14
687	13871	73	0.01	4.14	1.87	33.36	33
688	19622	200	0.01	4.29	2.30	35.39	35
689	2686	70	0.03	3.43	1.85	202.67	23
690	2434	118	0.05	3.39	2.07	211.82	32
691	2379	96	0.04	3.38	1.98	224.96	45
692	3440	112	0.03	3.54	2.05	217.13	37
693	4240	122	0.03	3.63	2.09	212.28	32
694	4167	87	0.02	3.62	1.94	201.15	21
695	14300	207	0.01	4.16	2.32	203.22	23
696	4589	263	0.06	3.66	2.42	234.10	54
697	2993	247	0.08	3.48	2.39	223.19	43
699	2904	339	0.12	3.46	2.53	209.52	30
700	6417	475	0.07	3.81	2.68	216.22	36
701	6106	223	0.04	3.79	2.35	209.80	30
702	3481	85	0.02	3.54	1.93	234.01	54
703	1227	103	0.08	3.09	2.01	220.50	41
704	3081	73	0.02	3.49	1.87	55.93	56
705	3632	116	0.03	3.56	2.07	193.16	13
706	9994	147	0.01	4.00	2.17	231.79	52
707	5998	85	0.01	3.78	1.93	237.61	58
708	2658	145	0.05	3.42	2.16	248.53	69
709	15617	200	0.01	4.19	2.30	210.45	30
710	15028	46	0.00	4.18	1.66	213.68	34
711	1314	41	0.03	3.12	1.61	215.98	36
712	68615	606	0.01	4.84	2.78	211.71	32
713	27160	206	0.01	4.43	2.31	202.72	23
714	5427	90	0.02	3.73	1.95	217.85	38
715	2126	88	0.04	3.33	1.95	211.26	31
716	2291	99	0.04	3.36	2.00	34.39	34
717	3305	89	0.03	3.52	1.95	39.86	40
718	6080	101	0.02	3.78	2.00	226.48	46
719	8082	102	0.01	3.91	2.01	234.71	55
720	4606	80	0.02	3.66	1.90	238.48	58
721	31070	175	0.01	4.49	2.24	214.58	35
722	18252	458	0.03	4.26	2.66	227.58	48
723	13151	239	0.02	4.12	2.38	189.17	9
724	7001	222	0.03	3.85	2.35	200.16	20
725	6606	108	0.02	3.82	2.03	195.61	16

Table A.3 shows a sample of fault length and corresponding fault throw data picked using 30m resolution DEM for the northern main Ethiopian rift (NMER).

Fault No.	Length	Throw	D\L ratio	Log length	log throw	Angle	Strike
1	4157.96	80.38	0.02	3.62	1.91	206.63	27
2	5493.12	73.79	0.01	3.74	1.87	201.95	22
3	1466.60	25.48	0.02	3.17	1.41	185.97	6
4	5947.30	139.07	0.02	3.77	2.14	203.93	24
5	1736.95	70.09	0.04	3.24	1.85	213.73	34
6	1426.21	73.83	0.05	3.15	1.87	197.22	17
7	937.98	47.84	0.05	2.97	1.68	208.77	29
8	2177.81	110.74	0.05	3.34	2.04	207.09	27
9	1707.67	133.17	0.08	3.23	2.12	233.52	54
10	5129.62	124.65	0.02	3.71	2.10	212.44	32
11	2141.82	48.98	0.02	3.33	1.69	201.99	22
12	4417.15	212.70	0.05	3.65	2.33	206.27	26
13	2175.09	197.30	0.09	3.34	2.30	201.51	22
14	6813.53	239.18	0.04	3.83	2.38	205.88	26
15	5863.67	430.94	0.07	3.77	2.63	213.82	34
16	4782.35	219.70	0.05	3.68	2.34	206.81	27
17	6344.32	183.42	0.03	3.80	2.26	213.88	34
18	15883.75	355.99	0.02	4.20	2.55	210.19	30
19	3555.62	203.90	0.06	3.55	2.31	216.14	36
20	10250.59	295.46	0.03	4.01	2.47	206.80	27
21	8865.32	318.87	0.04	3.95	2.50	199.07	19
22	3725.38	173.56	0.05	3.57	2.24	198.72	19
23	1644.25	126.68	0.08	3.22	2.10	209.24	29
24	3158.79	166.44	0.05	3.50	2.22	198.74	19
25	10283.79	203.35	0.02	4.01	2.31	209.16	29
26	2251.91	117.56	0.05	3.35	2.07	183.81	4
27	3818.67	245.73	0.06	3.58	2.39	202.55	23
28	3213.45	66.43	0.02	3.51	1.82	198.42	18
29	4000.34	129.71	0.03	3.60	2.11	216.48	36
30	886.43	83.75	0.09	2.95	1.92	205.23	25
31	4406.24	30.13	0.01	3.64	1.48	52.47	52
32	903.83	149.15	0.17	2.96	2.17	231.85	52
33	4082.52	49.05	0.01	3.61	1.69	209.77	30
34	6931.83	76.78	0.01	3.84	1.89	219.82	40
35	3119.81	373.54	0.12	3.49	2.57	193.62	14
36	2850.55	39.50	0.01	3.45	1.60	202.16	22
37	5705.03	45.03	0.01	3.76	1.65	222.30	42
38	14339.06	115.50	0.01	4.16	2.06	204.12	24
39	2050.05	144.69	0.07	3.31	2.16	202.49	22
40	6074.45	47.89	0.01	3.78	1.68	204.55	25
41	845.10	22.84	0.03	2.93	1.36	203.80	24
42	3287.04	222.28	0.07	3.52	2.35	204.11	24
43	1089.92	183.21	0.17	3.04	2.26	215.81	36
44	855.53	151.82	0.18	2.93	2.18	227.99	48
45	1902.41	88.47	0.05	3.28	1.95	213.41	33
46	3745.74	240.47	0.06	3.57	2.38	215.24	35

Table A.3 Continued from previous page

Fault No.	Length	Throw	D\L ratio	Log length	log throw	Angle	Strike
48	529.09	127.42	0.24	2.72	2.11	237.12	57
49	8737.52	282.01	0.03	3.94	2.45	216.32	36
50	1731.65	97.94	0.06	3.24	1.99	219.96	40
51	15407.61	204.24	0.01	4.19	2.31	212.56	33
52	21929.47	395.75	0.02	4.34	2.60	209.82	30
53	7206.92	242.14	0.03	3.86	2.38	210.40	30
54	1761.74	120.21	0.07	3.25	2.08	189.35	9
55	1478.92	58.68	0.04	3.17	1.77	200.80	21
56	1920.09	127.69	0.07	3.28	2.11	201.39	21
57	5570.81	206.86	0.04	3.75	2.32	211.43	31
58	8945.29	288.94	0.03	3.95	2.46	205.37	25
59	10455.56	135.37	0.01	4.02	2.13	200.79	21
60	13975.63	181.23	0.01	4.15	2.26	207.15	27
61	3112.46	85.24	0.03	3.49	1.93	197.08	17
62	5284.28	121.42	0.02	3.72	2.08	186.95	7
63	3772.62	121.92	0.03	3.58	2.09	181.52	2
64	4697.91	201.66	0.04	3.67	2.30	31.60	32
65	7161.24	117.15	0.02	3.85	2.07	231.48	51
66	5405.21	52.34	0.01	3.73	1.72	211.75	32
67	3003.30	86.22	0.03	3.48	1.94	209.74	30
68	1317.25	30.37	0.02	3.12	1.48	196.56	17
69	1421.74	73.33	0.05	3.15	1.87	200.57	21
70	3273.53	105.53	0.03	3.52	2.02	211.13	31
71	2129.88	148.20	0.07	3.33	2.17	20.84	21
72	2705.66	78.03	0.03	3.43	1.89	208.52	29
73	3019.36	145.31	0.05	3.48	2.16	22.21	22
74	2358.78	108.25	0.05	3.37	2.03	33.28	33
75	1497.39	114.69	0.08	3.18	2.06	31.56	32
76	903.27	93.63	0.10	2.96	1.97	340.94	161
77	3652.44	98.38	0.03	3.56	1.99	218.19	38
78	4692.79	81.66	0.02	3.67	1.91	210.95	31
79	3427.17	120.68	0.04	3.53	2.08	205.03	25
80	1011.06	79.99	0.08	3.00	1.90	207.72	28
81	1526.64	59.66	0.04	3.18	1.78	213.87	34
82	5266.51	109.43	0.02	3.72	2.04	217.36	37
83	2364.99	151.16	0.06	3.37	2.18	195.85	16
84	2238.73	133.86	0.06	3.35	2.13	184.96	5
85	2066.73	211.84	0.10	3.32	2.33	198.61	19
86	2377.62	42.63	0.02	3.38	1.63	203.31	23
87	2023.68	62.43	0.03	3.31	1.80	202.06	22
88	2572.69	50.33	0.02	3.41	1.70	225.92	46
89	2819.66	50.54	0.02	3.45	1.70	203.66	24
90	4439.03	143.57	0.03	3.65	2.16	226.33	46
91	3766.53	63.86	0.02	3.58	1.81	224.92	45
92	3815.29	92.10	0.02	3.58	1.96	199.21	19
93	2367.41	131.75	0.06	3.37	2.12	214.26	34
94	1501.98	80.76	0.05	3.18	1.91	203.71	24
95	1531.04	148.61	0.10	3.18	2.17	206.37	26
96	2292.45	244.77	0.11	3.36	2.39	209.93	30

Table A.3 Continued from previous page

Fault No.	Length	Throw	D\L ratio	Log length	log throw	Angle	Strike
98	925.10	238.65	0.26	2.97	2.38	201.13	21
99	1194.66	332.73	0.28	3.08	2.52	195.37	15
100	324.12	281.36	0.87	2.51	2.45	212.68	33
101	1009.68	88.28	0.09	3.00	1.95	37.62	38
102	1450.57	65.72	0.05	3.16	1.82	16.69	17
103	2066.81	141.63	0.07	3.32	2.15	225.72	46
104	1342.55	134.89	0.10	3.13	2.13	200.00	20
105	1223.18	45.73	0.04	3.09	1.66	222.86	43
106	2935.19	97.93	0.03	3.47	1.99	23.04	23
107	7913.55	167.35	0.02	3.90	2.22	29.29	29
108	1943.32	47.93	0.02	3.29	1.68	36.99	37
109	7376.76	109.83	0.01	3.87	2.04	27.47	27
110	4179.23	56.34	0.01	3.62	1.75	30.85	31
111	5496.17	105.59	0.02	3.74	2.02	223.67	44
112	3257.04	93.99	0.03	3.51	1.97	209.50	30
113	1679.71	65.00	0.04	3.23	1.81	219.03	39
114	11345.06	103.72	0.01	4.05	2.02	220.54	41
115	6032.37	35.83	0.01	3.78	1.55	45.20	45
116	9715.70	75.57	0.01	3.99	1.88	232.14	52
117	8903.96	138.39	0.02	3.95	2.14	234.76	55
118	3338.22	76.42	0.02	3.52	1.88	241.47	61
119	4872.56	115.57	0.02	3.69	2.06	47.51	48
120	5524.49	64.10	0.01	3.74	1.81	234.03	54
121	5607.93	120.48	0.02	3.75	2.08	229.74	50
122	2104.84	59.45	0.03	3.32	1.77	48.58	49
123	2745.50	37.14	0.01	3.44	1.57	60.44	60
124	6616.02	63.50	0.01	3.82	1.80	247.00	67
125	3350.91	65.90	0.02	3.53	1.82	233.22	53
126	3961.68	115.08	0.03	3.60	2.06	236.44	56
127	1433.11	67.86	0.05	3.16	1.83	208.53	29
128	5393.74	233.20	0.04	3.73	2.37	215.73	36
129	1028.82	64.01	0.06	3.01	1.81	237.69	58
130	4656.35	109.22	0.02	3.67	2.04	217.23	37
131	4994.00	215.19	0.04	3.70	2.33	209.67	30
132	1896.36	106.73	0.06	3.28	2.03	230.66	51
133	928.28	108.54	0.12	2.97	2.04	241.92	62
134	2886.27	155.00	0.05	3.46	2.19	241.84	62
135	2969.61	151.38	0.05	3.47	2.18	217.93	38
136	2683.72	111.84	0.04	3.43	2.05	219.89	40
137	7086.47	85.22	0.01	3.85	1.93	229.82	50
138	3999.29	70.30	0.02	3.60	1.85	231.74	52
139	935.49	40.66	0.04	2.97	1.61	231.42	51
140	1760.38	51.43	0.03	3.25	1.71	233.91	54
141	1327.07	144.49	0.11	3.12	2.16	248.64	69
142	2632.51	130.94	0.05	3.42	2.12	255.67	76
143	1386.88	110.41	0.08	3.14	2.04	265.92	86
144	2111.77	110.49	0.05	3.32	2.04	235.78	56
145	2378.36	62.15	0.03	3.38	1.79	57.44	57
146	2456.18	60.34	0.02	3.39	1.78	231.02	51

Table A.3 Continued from previous page

Fault No.	Length	Throw	D\L ratio	Log length	log throw	Angle	Strike
148	4075.40	139.55	0.03	3.61	2.14	230.37	50
149	6449.96	50.18	0.01	3.81	1.70	218.02	38
150	5037.57	48.78	0.01	3.70	1.69	207.70	28
151	5203.94	62.14	0.01	3.72	1.79	196.09	16
152	3177.55	51.51	0.02	3.50	1.71	181.82	2
153	2064.69	51.56	0.02	3.31	1.71	216.10	36
154	1012.97	78.26	0.08	3.01	1.89	218.59	39
155	2031.96	44.35	0.02	3.31	1.65	221.04	41
156	2614.22	69.84	0.03	3.42	1.84	53.81	54
157	4204.52	56.33	0.01	3.62	1.75	52.56	53
158	984.33	61.83	0.06	2.99	1.79	52.56	53
159	6722.12	76.06	0.01	3.83	1.88	40.82	41
160	1562.31	52.65	0.03	3.19	1.72	49.06	49
161	2742.92	44.48	0.02	3.44	1.65	43.77	44
162	4604.17	71.31	0.02	3.66	1.85	46.99	47
163	4014.53	58.44	0.01	3.60	1.77	43.80	44
164	1367.22	46.64	0.03	3.14	1.67	26.12	26
165	5897.46	63.03	0.01	3.77	1.80	45.95	46
166	1961.60	64.47	0.03	3.29	1.81	46.02	46
167	3604.92	56.67	0.02	3.56	1.75	208.64	29
168	2005.13	72.45	0.04	3.30	1.86	205.68	26
169	1186.10	74.67	0.06	3.07	1.87	225.46	45
170	1185.68	34.20	0.03	3.07	1.53	192.70	13
171	5212.78	154.41	0.03	3.72	2.19	219.19	39
172	2018.38	207.83	0.10	3.31	2.32	30.95	31
173	6180.33	70.30	0.01	3.79	1.85	202.39	22
174	2156.91	27.02	0.01	3.33	1.43	200.81	21
175	1805.97	44.40	0.02	3.26	1.65	215.91	36
176	2053.30	85.15	0.04	3.31	1.93	196.56	17
177	1095.50	35.75	0.03	3.04	1.55	33.50	33
178	10741.87	55.98	0.01	4.03	1.75	23.44	23
179	3965.71	37.54	0.01	3.60	1.57	21.09	21
180	2618.57	22.07	0.01	3.42	1.34	18.92	19
181	2502.56	33.57	0.01	3.40	1.53	13.09	13
182	5684.21	89.36	0.02	3.75	1.95	40.69	41
183	4692.11	57.80	0.01	3.67	1.76	23.52	24
184	2852.61	224.49	0.08	3.46	2.35	196.94	17
185	5089.95	135.91	0.03	3.71	2.13	200.88	21
186	2357.90	132.24	0.06	3.37	2.12	189.14	9
187	5210.65	117.02	0.02	3.72	2.07	206.12	26
188	1385.27	77.85	0.06	3.14	1.89	18.43	18
189	8545.04	68.49	0.01	3.93	1.84	21.72	22
190	2408.09	85.38	0.04	3.38	1.93	199.12	19
191	4976.71	171.29	0.03	3.70	2.23	71.29	71
192	5724.24	151.70	0.03	3.76	2.18	36.07	36
193	2546.85	94.02	0.04	3.41	1.97	36.85	37
194	4487.53	70.96	0.02	3.65	1.85	33.01	33
195	704.56	39.92	0.06	2.85	1.60	36.85	37
196	4721.69	78.64	0.02	3.67	1.90	49.57	50

Table A.3 Continued from previous page

Fault No.	Length	Throw	D\L ratio	Log length	log throw	Angle	Strike
198	1889.50	106.66	0.06	3.28	2.03	43.94	44
199	2401.87	84.75	0.04	3.38	1.93	35.37	35
200	2987.91	64.02	0.02	3.48	1.81	39.68	40
201	3098.59	110.34	0.04	3.49	2.04	36.76	37
202	5835.30	121.52	0.02	3.77	2.08	27.53	28
203	3324.89	53.83	0.02	3.52	1.73	215.68	36
204	3057.75	61.05	0.02	3.49	1.79	216.34	36
205	4784.58	106.27	0.02	3.68	2.03	23.87	24
206	16966.47	217.15	0.01	4.23	2.34	42.19	42
207	4017.28	82.25	0.02	3.60	1.92	19.82	20
208	1418.67	60.46	0.04	3.15	1.78	49.74	50
209	6158.60	54.26	0.01	3.79	1.73	210.19	30
210	2508.09	58.94	0.02	3.40	1.77	24.40	24
211	18526.84	116.47	0.01	4.27	2.07	33.16	33
212	3829.49	44.91	0.01	3.58	1.65	31.65	32
213	15541.02	66.29	0.00	4.19	1.82	38.41	38
214	3571.91	61.82	0.02	3.55	1.79	29.49	29
215	4022.77	82.64	0.02	3.60	1.92	31.09	31
216	1378.19	43.82	0.03	3.14	1.64	39.68	40
217	2292.46	41.48	0.02	3.36	1.62	25.34	25
218	1564.50	32.04	0.02	3.19	1.51	28.98	29
219	1052.83	45.92	0.04	3.02	1.66	30.93	31
220	1805.20	43.48	0.02	3.26	1.64	20.45	20
221	6294.01	79.30	0.01	3.80	1.90	45.61	46
222	294.23	47.84	0.16	2.47	1.68	14.76	15
223	866.75	46.89	0.05	2.94	1.67	27.89	28
224	5660.32	45.73	0.01	3.75	1.66	217.28	37
225	18832.81	113.46	0.01	4.27	2.05	221.10	41
226	1290.69	54.25	0.04	3.11	1.73	214.57	35
227	4659.60	58.75	0.01	3.67	1.77	227.65	48
228	7656.24	78.31	0.01	3.88	1.89	56.34	56
229	2138.93	63.09	0.03	3.33	1.80	41.96	42
230	1691.18	113.20	0.07	3.23	2.05	53.41	53
231	1186.38	71.97	0.06	3.07	1.86	67.94	68
232	2467.66	99.48	0.04	3.39	2.00	53.80	54
233	1701.36	83.50	0.05	3.23	1.92	48.77	49
234	1246.17	72.81	0.06	3.10	1.86	35.34	35
235	1426.99	52.51	0.04	3.15	1.72	46.05	46
236	3339.96	47.96	0.01	3.52	1.68	34.58	35
237	2503.14	83.04	0.03	3.40	1.92	43.80	44
238	1928.89	37.47	0.02	3.29	1.57	47.40	47
239	12808.42	126.17	0.01	4.11	2.10	55.81	56
240	4117.99	50.06	0.01	3.61	1.70	235.60	56
241	4278.93	60.93	0.01	3.63	1.78	232.49	52
242	1854.46	82.43	0.04	3.27	1.92	245.04	65
243	9290.62	127.59	0.01	3.97	2.11	87.78	88
244	11552.12	119.32	0.01	4.06	2.08	88.03	88
245	5196.19	113.73	0.02	3.72	2.06	76.16	76
246	4731.33	120.80	0.03	3.67	2.08	64.74	65
247	8964.41	81.67	0.01	3.95	1.91	251.32	71